

INFORMATION TO USERS

This manuscript has been reproduced from the microfilm master. UMI films the text directly from the original or copy submitted. Thus, some thesis and dissertation copies are in typewriter face, while others may be from any type of computer printer.

The quality of this reproduction is dependent upon the quality of the copy submitted. Broken or indistinct print, colored or poor quality illustrations and photographs, print bleedthrough, substandard margins, and improper alignment can adversely affect reproduction.

In the unlikely event that the author did not send UMI a complete manuscript and there are missing pages, these will be noted. Also, if unauthorized copyright material had to be removed, a note will indicate the deletion.

Oversize materials (e.g., maps, drawings, charts) are reproduced by sectioning the original, beginning at the upper left-hand corner and continuing from left to right in equal sections with small overlaps. Each original is also photographed in one exposure and is included in reduced form at the back of the book.

Photographs included in the original manuscript have been reproduced xerographically in this copy. Higher quality 6" x 9" black and white photographic prints are available for any photographs or illustrations appearing in this copy for an additional charge. Contact UMI directly to order.

UMI

A Bell & Howell Information Company
300 North Zeeb Road, Ann Arbor MI 48106-1346 USA
313/761-4700 800/521-0600

RICE UNIVERSITY
DIFFERENCE FREQUENCY GENERATION:
SPECTROMETERS AND SPECTROSCOPY

BY
WADE CHARLES ECKHOFF

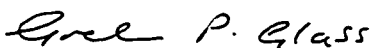
A THESIS SUBMITTED
IN PARTIAL FULFILLMENT OF THE
REQUIREMENTS FOR THE DEGREE

DOCTOR OF PHILOSOPHY

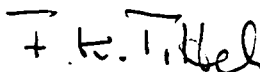
APPROVED, THESIS COMMITTEE



R. F. Curl, Professor, Chair
Department of Chemistry



G. P. Glass, Professor, Department Chair
Department of Chemistry



F. K. Tittel, Professor, J. S. Abercrombie Chair
Department of Electrical and
Computer Engineering

Houston, Texas

April, 1997

UMI Number: 9727547

UMI Microform 9727547

Copyright 1997, by UMI Company. All rights reserved.

**This microform edition is protected against unauthorized
copying under Title 17, United States Code.**

UMI

**300 North Zeeb Road
Ann Arbor, MI 48103**

DIFFERENCE FREQUENCY GENERATION: SPECTROMETERS AND SPECTROSCOPY

by

WADE CHARLES ECKHOFF

ABSTRACT

The theory of difference frequency generation has been further developed. Derived from basic principles, the equations developed here accurately predict the conversion of power to the idler wave. Critical phasematching can now be modeled with ellipticity in both beams and the effects of double refraction and non-normal incidence upon the crystal treated. It is no longer necessary to focus the beams into the center of the crystal nor is it necessary to have an equal confocal parameter in the two drive beams.

A mid-infrared spectrometer based on titanium:sapphire pumped difference frequency generation in silver thiogallate (AgGaS_2) has been constructed in order to conduct high resolution spectroscopy on free radicals. Detector limited sensitivity has been demonstrated with an estimated source bandwidth of 0.00003 cm^{-1} . The process used to calibrate scans has been improved and calibration accuracy of 0.001 cm^{-1} is now routine.

With the silver thiogallate spectrometer, the infrared spectrum of the monodeuterated propargyl radical (CH_2CCD) has been acquired. Approximately 250 lines have been positively identified and assigned to the ν_1 C-D stretch in the region between 2300 cm^{-1} and 2400 cm^{-1} . The spectrum consists of a-type transitions ($\Delta K_a = 0$) with a fully resolved K subband structure, in contrast to the CH stretch of the normal radical. This resolved structure is due to a P_a -type Coriolis interaction or a Fermi resonance in the molecule. These interactions may be responsible for the fact that we were unable to identify the odd K subbands, though positive identification of the $K_a = 0, 2, 4,$ and 6 subbands was made and used to determine rotational constants for the radical.

A spectrometer based on difference frequency generation in gallium selenide (GaSe) was constructed. Precise phasematching characteristics were determined as well as the potential power produced in the process. The instrument is continuously tunable in the $8.8 - 15.0\text{ }\mu\text{m}$ wavelength region.

TABLE OF CONTENTS

LIST OF FIGURES

LIST OF TABLES

1. Introduction	1
1.1 Infrared Spectrometers	3
1.2 Nonlinear Frequency Conversion	9
1.2.1 Difference Frequency Generation	9
1.2.2 Optical Parametric Oscillators (OPOs)	10
2. Difference Frequency Generation	12
2.1 The Index of Refraction	12
2.2 Wave Propagation and Polarization	14
2.3 Difference Frequency Generation	17
2.3.1 Maxwell's Equations and the Paraxial Wave Equation	17
2.3.2 Profile of the Drive Beams	24
2.4 Power Generated in the DFG Process	27
2.4.1 The Phasematching Condition	30
2.5 Alternative Formulations for DFG Power	31
2.5.1 Plane Wave Theory	32
2.5.2 Chu and Broyer's Theory	34
2.5.3 Lera and Nieto-Vesperinas' Theory	38
2.5.4 Quasiphasematching	39
2.6 Crystals Used in Mid-Infrared Down-Conversion	42

2.6.1	Cadmium Germanium Arsenide (CdGeAs_2)	44
2.6.2	Cadmium Selenide (CdSe)	47
2.6.3	Cinnabar ($\alpha\text{-HgS}$)	49
2.6.4	Gallium Selenide (GaSe)	52
2.6.5	Indium Antimonide (InSb)	54
2.6.6	Lithium Iodate (LiIO_3)	54
2.6.7	Lithium Niobate (LiNbO_3)	56
2.6.8	Mercury Thiogallate (HgGa_2S_4)	58
2.6.9	Proustite (Ag_3AsS_3)	63
2.6.10	Pyrargyrite (Ag_3SbS_3)	66
2.6.11	Silver Gallium Selenide (AgGaSe_2)	68
2.6.12	Silver Thiogallate (AgGaS_2)	71
2.6.13	Tellurium (Te)	73
2.6.14	Zinc Germanium Phosphide (ZnGeP_2)	76
2.7	Summary of Implications for DFG	78
3.	Equipment used in Difference Frequency Generation	81
3.1	The Argon Ion Laser	85
3.2	The Tunable Pump Lasers	87
3.2.1	Daily Operation of the 899-21 Laser	90
3.2.2	Causes of Instabilities in the Ti:Sapphire Output Power	91
3.2.2	Alignment of the 899-29 Lasers	95
3.3	Autoscan	96
3.3.1	Optical Activity Monochrometer (OAM)	96
3.3.2	Vernier Etalons (VETs)	99

3.3.3 Scanning of the Autoscanner Laser	101
3.4 The External Etalon	102
3.5 Reference Gas Calibration	106
3.6 The Michelson Interferometer	107
3.6.1 Gross Alignment of the Interferometer	109
3.6.2 Fine Alignment of the Interferometer	112
3.6.3 Alignment of the Unknown Beam	113
3.7 The Excimer Laser	114
3.8 Detectors	115
3.9 Software	116
3.9.1 Software used in Obtaining a Frequency Spectrum	117
3.9.2 Software Used in Obtaining Temporal Information	120
Chapter 4 - Difference Frequency Generation in AgGaS₂ ...	121
4.1 Gross Physical Properties	121
4.2 The Growth of AgGaS ₂	125
4.3 The Index of Refraction	126
4.4 The History of Downconversion in AgGaS ₂	128
4.5 Frequency Tuning in Difference Frequency Generation	131
4.6 Phasematching Bandwidth	135
4.7 Power Scaling in AgGaS ₂	138
4.7.1 Problems Encountered in Power Scaling	138
4.7.2 Power Scaling Analysis	142
4.7.3 Thermal Loading	143
4.7.4 Conclusions	147

4.7.5	Corrections to the Above	148
4.8	Noise and Sensitivity in the AgGaS ₂ System	154
4.8.1	Balancing Photovoltaic Detectors	155
4.8.2	Balancing Photoconductive Detectors	158
4.8.3	Excimer Noise	162
4.8.4	Infrared Emissions	163
4.8.5	Theoretical Noise Limitations	163
4.8.6	Sensitivity of the AgGaS ₂ DFG Spectrometer	167
4.9	Summary of the AgGaS ₂ Spectrometer	171
Chapter 5	- Difference Frequency Generation in GaSe	173
5.1	Background	173
5.2	Experimental	174
5.3	Spectroscopy of Ethylene	185
5.4	Conclusion	188
Chapter 6	- The ν_2 Stretch of the Monodeuterated	
	Propargyl Radical (CH₂CCD)	190
6.1	Propargyl Background	190
6.2	Experimental	193
6.3	Results and Discussion	194
6.4	Conclusions on the Propargyl Radical	207
Chapter 7	- Concluding Remarks	211
7.1	Advances in Difference Frequency Generation	211

7.2 Future Directions	213
7.3 Conclusion	216

Appendices

A.1 Derivation of the Power Generated in the Difference Frequency Generation Process	217
A.2 The Index of Refraction in Silver Thiogallate	230
A.3 Synthesis of 3-d Propargyl Bromide	233

Bibliography	235
---------------------------	-----

LIST OF FIGURES

2.1	Energy Level Diagram of the DFG Process	29
2.2	The $\text{Sinc}^2(x)$ Function	33
2.3	Chu and Broyer's h-function	37
2.4	Type-I Phasematching in CdGeAs_2	45
2.5	Type-II Phasematching in CdGeAs_2	46
2.6	Type-II Noncritical Phasematching in CdGeAs_2	46
2.7	Type-II Phasematching in CdSe	48
2.8	Type-II Noncritical Phasematching in CdSe	49
2.9	Type-I Phasematching in $\alpha\text{-HgS}$	51
2.10	Type-II Phasematching in $\alpha\text{-HgS}$	51
2.11	Type-I Phasematching in GaSe	53
2.12	Type-II Phasematching in GaSe	53
2.13	Type-I Phasematching in LiIO_3	55
2.14	Type-I Noncritical Temperature Dependent Phasematching in LiNbO_3	58
2.15	Type-I Phasematching in the Orange Phase of HgGa_2S_4	60
2.16	Type-I Noncritical Phasematching in the Orange Phase of HgGa_2S_4	61
2.17	Type-II Phasematching in the Orange Phase of HgGa_2S_4	61
2.18	Type-I Phasematching in the Yellow Phase of HgGa_2S_4	62
2.19	Type-I Noncritical Phasematching in the Yellow Phase of HgGa_2S_4	62

2.20	Type-II Phasematching in the Yellow Phase of HgGa_2S_4	63
2.21	Type-I Phasematching in Ag_3AsS_3	64
2.22	Type-I Noncritical Phasematching in Ag_3AsS_3	65
2.23	Type-II Phasematching in Ag_3AsS_3	65
2.24	Type-I Phasematching in Ag_3SbS_3	67
2.25	Type-II Phasematching in Ag_3SbS_3	67
2.26	Type-I Phasematching in AgGaSe_2	69
2.27	Type-I Noncritical Phasematching in AgGaSe_2	70
2.28	Type-II Phasematching in AgGaSe_2	70
2.29	Type-I Phasematching in AgGaS_2	72
2.30	Type-I Noncritical Phasematching in AgGaS_2	72
2.31	Type-II Phasematching in AgGaS_2	73
2.32	Type-I Phasematching in Te	75
2.33	Type-II Phasematching in Te	76
2.34	Type-I Phasematching in ZnGeP_2	77
2.35	Type-II Phasematching in ZnGeP_2	78
2.36	Characteristics of Mid-IR Nonlinear Optical Crystals	79
3.1	General Experimental Setup - Infrared Generation	81
3.2	General Experimental Setup - Wavelength Calibration and Spectroscopy	82
3.3	White Cell Geometry	84
3.4	Coherent 899 Single Frequency Power versus Wavelength ..	88
3.5	Coherent 899 Single Frequency Power versus Coherent Power Meter Model 212 Response	89
3.6	Vernier Etalon (VET) Spectrum	100

3.7	External Etalon Retrace and Wavelength Correction	103
3.8	Michelson Scanning Interferometer Setup	108
3.9	Michelson Interferometer Spot Arrangement	110
3.10	Indium Antimonide Detector Response Time	117
4.1	The Index of Refraction Comparison in AgGaS ₂	128
4.2	Optimized Phasematching Wavelengths for Type-I DFG in Silver Thiogallate	131
4.3	The Phasematching Bandwidth in a 45 mm long Silver Thiogallate Crystal	136
4.4	Theoretical Power in AgGaS ₂ versus Wavelength: Unfocused versus Focused Beams	137
4.5	Infrared Power for Unfocused Beams	139
4.6	Infrared Power for Focussed Beams	141
4.7	Frequency Offset versus Signal Power	145
4.8	Infrared Power Generation versus Input Power in AgGaS ₂ ...	152
4.9	Peak Phasematching Frequency Offset versus Input Power	154
4.10	Comparison of Detector, Laser, and Balanced Detection Noise	157
4.11	Noise Power Spectrum	159
4.12	Noise in Mercury Cadmium Telluride Detectors	160
4.13	Effect of Time Delay in Mercury Cadmium Telluride Detectors	161
4.14	Spatial Concentration of Radicals in the White Cell	170
4.15	Optimization of the $\sigma_{UV} \cdot c_{pre}$ Parameter	171
5.1	Schematic Diagram of a DFG spectroscopic source based on GaSe crystal	175

5.2	Indices of Refraction in GaSe	177
5.3	External Phasematching Angles in GaSe	178
5.4	Phasematching in GaSe	180
5.5	Coherence Length in GaSe	181
5.6	IR Power Scaling with Input Powers	185
5.7	Survey Spectrum of a Sampling of Gases Important to Atmospheric Chemistry	186
5.8	Ethylene Absorption Spectrum	188
6.1	Sample Spectrum of the Deuterated Propargyl Radical	194
6.2	Q-Branch of the Propargyl $K_a = 4 \leftarrow 4$ Subband	195
6.3	Normal Propargyl Spectrum in the C-H Stretch Region	200
6.4	Propargyl Time Trace	201
6.5	$K_a = 0 \leftarrow 0$ Ground State Combination Differences Residuals ..	202
6.6	Subband Origins in the CH ₂ CCD Spectrum	203
6.7	$(B_{\text{eff}}' - \Delta_{NK'} \cdot K^2)$ vs. K^2	205
6.8	Perturbations in the $K_a=0$ Subband	206
6.9	Attempted Fit of the $K_a = 3$ Subband	207

LIST OF TABLES

4.1	Damage Threshold of Silver Thiogallate	122
4.2	Nonlinear Coefficient of Silver Thiogallate	124
4.3	AgGaS ₂ Peak Experimental Phasematching Wavelengths	132
4.4	Experimental and Calculated Infrared Powers	140
5.1	GaSe Peak Experimental Phasematching Wavelengths	179
6.1	Observed $K_a = 0 \Leftarrow 0$ Frequencies (cm ⁻¹)	196
6.2	Observed $K_a = 2 \Leftarrow 2$ Frequencies (cm ⁻¹)	197
6.3	Observed $K_a = 4 \Leftarrow 4$ Frequencies (cm ⁻¹)	198
6.4	Observed $K_a = 6 \Leftarrow 6$ Frequencies (cm ⁻¹)	199
6.5	Rotational Constants of the Propargyl Radical	204
6.6	Unassigned Lines in the ν_2 Region of the Propargyl Spectrum ..	209

Chapter 1 - Introduction

In chemistry today it is a great challenge to list every detail of chemical reactions. Years ago, chemists were forced to initiate a reaction and analyze the resultant materials after a while, leaving the intermediate steps as a unexplored region on the map of scientific progress. All that could be done was to change the reaction conditions by changing the temperature or pressure. Such variations, or perhaps the substitution of different but related reactants, could suggest some insight into the ways molecules reacted and the identity of the molecules that formed the intermediate steps, but in most chemical systems it was impossible to directly observe the intermediate steps. In more modern times, it has become possible to observe and measure the properties of some of these intermediate steps that used to comprise this magical black box.

It is now possible to observe molecules that exist for less than a microsecond and at total concentrations measured in parts per trillion. Optimally, the detection method would be a universal sensor able to differentiate between close chemical species with absolute specificity, would positively identify the species under study, provide temporal information on the progress of the reaction, and would not affect the reaction under study. Spectroscopy provides a method that fulfills all the above requirements in many systems.

The infrared region is attractive to chemists in identifying and following the reaction progress of transient species because this region "fingerprints" molecules. Almost every molecule has absorptions in the

infrared, corresponding to transitions of vibrational fundamental, overtones, and low-lying electronic states. With high resolution infrared spectroscopy, accurate molecular parameters and hence the structure and identity of small transient species can be determined.

A number of new techniques and methods have been introduced since the advent of flash photolysis kinetic spectroscopy in the 1940s by Norrish and Porter. The most significant scientific advance leading to improved spectroscopic methods was the advent of the laser in the 1960's. Laser sources have provided the wavelength control and output intensity that have enabled scientists to devise experiment that are orders of magnitude more sensitive than those previously possible.

The following sections of this chapter outline the basic advantages and disadvantages of each infrared probe and hence the motivation for the development of a new source for use in the infrared. Chapter 2 will derive the fundamental equations upon which the new instruments are based while Chapter 3 will describe the elaborate equipment necessary for operation of these spectrometers. Chapters 4 and 5 will detail the characteristics of two spectrometers based on the difference frequency generation method and Chapter 6 will give an example of the use of the method in the original high-resolution spectrum of the monodeuterated propargyl (CH_2CCD) radical.

1.1 Infrared Spectrometers

Raman Spectroscopy

Though not an infrared source, Raman spectroscopy can be used to probe rotational-vibrational transitions. When light of frequency ν_0 (usually from a visible wavelength laser or mercury arc lamp) irradiates a sample, it is scattered. The frequency of the scattered light can either be at the original frequency (Rayleigh scattering) or at some shifted frequency $\nu_s = \nu_0 \pm \nu_{\text{internal}}$ (Raman scattering). The frequency ν_{internal} is an internal frequency corresponding to rotational, vibrational, or electronic transitions.

One advantage of the method is the ability to use visible laser technology to probe infrared transitions. Since visible laser technology is very advanced compared to that in the infrared, this is an enormous advantage. The other advantage of the method is its ability to collect information about the entire spectrum of a molecule simultaneously when coupled with an interferometer. The disadvantage of the method is that Raman scattering is relatively weak (typically less than one photon out of a million incident upon a sample is Raman scattered). Detection therefore is often difficult and requires long integration times.

Color-Center Lasers

A color center laser operates on the principle that optical absorption in certain crystals will excite an electron trapped by an anion vacancy in

those crystals and that the relaxation of this excited state will lead to emission at longer wavelengths than the pump wavelength.

Color center lasers typically operate in the 0.82 to 3.5 μm spectral region [1,2] with powers ranging from a few milliwatts to several watts [3]. They can be operated in continuous wave (cw) mode with a linewidth on the order of a MHz, and have proven to be a very versatile and useful source within their wavelength range. Beyond its limited tuning range in the mid-infrared, its other drawback is the need for constant liquid nitrogen cooling of the color center crystal to prevent reorganization of the color centers with degradation of the crystal and the laser performance.

Spin-flip Raman Lasers

The Spin-Flip Raman Laser (SFRL) is based on stimulated Raman scattering of pump radiation from a fixed frequency source by conduction electrons in low-temperature semiconductors. The doubly degenerate energy levels in the conduction band are split with electronic spins parallel and antiparallel to an applied magnetic field. The scattering frequency is

$$\nu = \nu_p \pm \frac{g^* \cdot \mu_B \cdot B}{2\pi\hbar}$$

where ν_p is the pump laser frequency, g^* the effective Lande factor, μ_B the Bohr magneton, and B the magnetic field strength. In InSb, for example, $g^* = -50$. When pumped near the energy of the direct band gap,

the threshold energy dramatically decreases and threshold pump powers as low as 5 mW have been observed.

InSb cw lasers pumped with a CO laser have a demonstrated tuning range of 5.0 - 6.5 μm , a linewidth of less than 1 kHz [4,5], and a power conversion efficiency in excess of 50% for the Stokes lines [6,7] (5% for the anti-Stokes lines). A pulsed InSb SFRL has a demonstrated tuning range of 9 - 14.6 μm using magnetic fields of up to 10 Tesla [8], had an output powers of up to 1 Watt for Stokes lines [9], and a bandwidth of less than 0.03 cm^{-1} [10], though it should be noted that the authors attribute the linewidth to problems with the pump laser. HgCdTe or InSb crystals can be pumped with a CO₂ laser and InAs by a HF laser in order to extend the tuning range to longer and shorter wavelengths, respectively.

The drawback of the Spin-Flip Raman laser is the equipment startup cost: a single-frequency CO or CO₂ laser, a liquid helium refrigeration system, and a superconducting magnet capable of at least 1 Tesla and up to 10 Tesla. The latter was the limiting factor at the time of its original development, but magnet technology has progressed sufficiently in the last 25 years that the required magnetic fields are now routine (a 500 MHz NMR contains a 14 Tesla magnet while the Spin-Flip Raman laser is largely limited to field strengths less than 10 Tesla).

CO and CO₂ Lasers

Tunable single-frequency radiation can be generated from CO and CO₂ lasers centered near 5.3 and 10.6 μm , respectively. Using a dispersive

element within a low-pressure laser cavity, it is possible to tune the lasers to operate in cw mode on a single CO or CO₂ rotational-vibrational transition. Lines in this operation are spaced by approximately 4 cm⁻¹, making this source unsuitable for most spectroscopic investigations. The traditional method of overcoming this limitation is to electrooptically modulate the laser radiation (frequency ν_l) with tunable microwave radiation (ν_m) in a CdTe or GaAs crystal to generate laser sidebands at frequency $\nu_l \pm \nu_m$. Applied to both CO [11] and CO₂ [12] lasers, it allows tuning of almost a wavenumber on either side of the laser lines and 50% wavelength coverage within the tuning range of both lasers.

True continuous tuning of CO and CO₂ lasers is accomplished by increasing the pressure in the laser tube to 10-20 atmospheres and using pressure-broadening to allow continuous tuning between the most intense laser transitions. Because the discharge becomes filamentary at voltages below threshold, continuous-wave operation is impossible and pulse durations must be kept shorter than the arc formation time [13]. The smallest laser linewidth achieved is 0.018 cm⁻¹, which is too large for high-resolution spectroscopy.

Time Resolved Fourier-transform Spectrometers

Fourier-transform infrared spectrometers (FTIRs) are the workhorse of most infrared spectroscopic applications. Their wavelength coverage is limited only by detector responsivity and the power distribution of blackbody sources. The resolution of the instrument ($\Delta\nu$) is

determined by its maximum retardation Δ_{max} (the maximum change in pathlength which is typically twice the distance traveled by the mirror).

$$\Delta\nu = (\Delta_{\text{max}})^{-1}$$

For complete resolution of lines differing in position by 0.010 cm^{-1} (the Doppler width of lines is typically 0.007 cm^{-1}) without apodization, a 1 meter retardation is required. This is routinely available in research grade instruments.

Because the typical lifetime of a free radical studied in this laboratory is far shorter than either the scan time of a Fourier-transform spectrometer or the repetition rate of an excimer laser, spectroscopy on many free radicals is impossible using a standard Fourier-transform spectrometer in the classic pump-probe experiment. Using a microwave discharge to initiate atom extraction and creating a constant concentration of free-radicals is one method of conducting free radical spectroscopy, but because radical concentrations generated in atom abstraction are rather low, the lifetime of the radical has to be on the order of a millisecond in order to increase the concentration of most radicals to a detectable level.

Fourier-transform spectrometers can be used to collect both spectroscopic and kinetic information about free radicals in a pump-probe experiment using a technique called Time-Resolved Fourier Transform Spectroscopy (TRFTS). There are two main approaches under this heading: step scan and continuous scan. In a step scan method, the scanning mirror is fixed at a precisely known position while transient absorptions are recorded and then the mirror is stepped to another position and the process repeated. The data is processed in the traditional fashion

by performing the FFT on all points taken at a fixed time delay from the pump source. A continuous scan is conceptually similar; the mirror is continuously scanned and the data stored as a function of mirror position and time and sorted after the entire scan is completed. This latter method is computationally more challenging but avoids the problems associated with maintaining a constant mirror position. Products are commercially available to turn a standard FTIR into a time-resolved instrument of either type at a relatively low cost [14,15].

Although the source brightness is low compared with laser-based sources, the Fourier-transform spectrometer has the advantage of simultaneously acquiring information about the entire spectrum as limited by the responsivity of the detectors used. Because it relies on a black-body source, the minimum detectable absorption is on the order of magnitude of 1%.

Lead-Salt Diode Lasers

Lead salt diode lasers cover the 3-30 μm wavelength range with relatively good output power ($\sim 1\text{-}10\text{ mW}$) and quantum noise limited amplitude stability [16]. Because these diode lasers are based upon a Fabry-Perot cavity, they have a rather short continuous tuning range (typically less than 1 cm^{-1}) and will not operate between cavity modes (typically spaced by $4\text{ - }5\text{ cm}^{-1}$). A good total tuning range for these lasers is 100 cm^{-1} . They must be cryogenically cooled to less than 100 K and exhibit irregular tuning characteristics upon heating and cooling. Often, a

diode laser capable of tuning to a particular frequency will be unable to do so after a heating and cooling cycle.

Because of the above technical difficulties associated with diode lasers, multiple diode lasers are necessary to cover each 100 cm^{-1} region.

1.2 Nonlinear Frequency Conversion

The above sources all suffer from severe wavelength limitations, an inability to tune continuously, or a low spectral brightness that leads to low sensitivity. In light of this, scientists have experimented with an additional source for infrared spectroscopy - nonlinear frequency conversion.

1.2.1 Difference Frequency Generation

Difference frequency generation (DFG) is a stimulated nonlinear optical process in which the conversion of a photon of light at frequency ν_p into two photons of light at frequencies ν_s and ν_i such that the sum of the frequencies of the two created photons equals the frequency of the original photon ($\nu_p = \nu_s + \nu_i$) is stimulated. In this fashion, a portion of tunable visible laser light can be converted to tunable infrared light. The process relies on the high intensity of laser sources for radiation at ν_p and either ν_s or ν_i .

By utilizing visible laser technology, DFG has the same frequency stability and tunability as the well developed visible laser technology. The method suffers from relatively low output power (usually measured in

nano or microwatts) and a relatively complex setup. In addition to the benefits of the visible laser technology, DFG offers tunability from the visible wavelengths to 30 μm and requires no cryogenic cooling.

1.2.2 Optical Parametric Oscillators (OPOs)

Optical parametric oscillators are based on the same principles as difference frequency generation. The large difference between the two methods is that in difference frequency generation two laser beams are used to stimulate the production of a third beam whose frequency is equal to the difference in the frequencies of the two input waves. In an OPO, only the high frequency beam is used as a drive source. The other two beams are created in the crystal by placing it in a resonant cavity and amplifying the spontaneous emission. An OPO can be singly, doubly, or triply resonant depending on the number of beams amplified in the cavity.

The obvious advantage of OPOs is the need for only a single pump source, versus the two necessary for DFG. Its primary disadvantage is the high threshold intensity needed for operation that often precludes continuous-wave operation. Part of the need for a high threshold intensity is caused by absorption in the nonlinear crystals and part is due to the difficulty in manufacturing mirrors with appropriate broadband coatings for all appropriate wavelengths.

To date, the production of a cw OPO capable of locking to a single-frequency has eluded scientists. The current record at this time is an instrument capable of locking to a line for ~50 milliseconds [17].

In the next chapter the theory of difference frequency generation will be developed from first principles and the implications of the theory discussed.

Chapter 2 - Difference Frequency Generation

Difference Frequency Generation (DFG) is the optical process of stimulating the conversion of a high frequency light photon into two lower frequency photons the sum of whose frequencies is equal to the original frequency. The purpose of this text is to derive the equations governing the DFG process, explain their application to the present experiments, and discuss the basic assumptions that went into their derivation. The reader is urged to refer to the references or one of the numerous texts written on the subject for a more complete physical description.

2.1 The Index of Refraction

The basis for all nonlinear optical processes is the fact that when an electrical field is applied to a molecule, a polarization is induced. Consider a single electron and a nucleus. As a weak applied electric field oscillates, the polarization of the molecule oscillates at the same frequency as the driving field. This oscillating dipole radiates an electromagnetic wave with the same frequency but with a phase dependent on the restoring force of the electrons in the molecule and differing from the phase of the initial wave. If we take two parallel waves with the same initial phase and frequency and let one of these waves pass through N atoms, at a point on the other side of these atoms the two waves will still have the same frequency but the phase difference will be proportional to N . Since the number of atoms in a given distance is fixed by the density of a material, the phase delay induced by a material is determined by its thickness d .

Thus, the wave inside the material appears to propagate more slowly than one in a vacuum and is material dependent. The ratio between these velocities is known as the index of refraction of the material.

Of course, in the above we have assumed the interaction between atoms is isotropic. This sometimes not the case and the optical anisotropy leads to an index of refraction that is dependent on the orientation of the input light polarization with respect to the crystallographic axes. If the index of refraction of the crystal is invariant upon rotation about one crystallographic axis but not the other two, the crystal is called *uniaxial* and the unique axis the *optical axis*. If there are two such unique axis, the crystal is *biaxial*.

In this text, we will restrict the discussion of birefringence to uniaxial crystals as research to date in this laboratory has involved uniaxial crystals exclusively. The direction of polarization perpendicular to the optic axis is known as the *ordinary* direction and the other direction of polarization *extraordinary*. The indices of refraction are denoted n_o and n_e , respectively. When $(n_e - n_o) > 0$, the crystal birefringence is said to be positive, and when $(n_e - n_o) < 0$, the crystal birefringence is said to be negative.

As earlier mentioned, when a uniaxial birefringent crystal is rotated by an angle θ about one of the two identical axis, the index of refraction experienced by light polarized in the ordinary direction is invariant to the rotation, but the index experienced by the wave in the plane of the extraordinary axis changes according to the following formula:

$$n_e^{\text{eff}}(\lambda) = \sqrt{\frac{1}{\frac{\sin^2\theta}{n_e^2(\lambda)} + \frac{\cos^2\theta}{n_o^2(\lambda)}}} \quad (2.1.1)$$

where θ is the angle of the beam in the crystal with respect to the optical axis

n_e and n_o are the extraordinary and ordinary indices of refraction of the crystal

To this point it has been tacitly assumed that the light propagates only in the forward direction and that the emitted wave propagates only in the forward direction. The latter occurs because any radiation not radiated in the forward direction is out of phase with the radiation in that same direction from other dipoles and does not build up. Only in the forward direction are the dipoles correctly phased.

2.2 Wave Propagation and Polarization

In order to proceed with the development of nonlinear optics, we must now introduce the mathematical form of the dependence of the induced polarization on the applied field strength. Classically, the induced polarization $\mathbf{P}(t)$ by a wave at frequency ω in the crystal over time is given as:

$$\mathbf{P}(t) = \epsilon_0 \cdot \chi^{(1)} \cdot \mathbf{E}(t) \quad (2.2.1)$$

where the constant of proportionality $\chi^{(1)}$ is known as the linear susceptibility and is a second-rank tensor and the polarization and electric field terms are vector quantities. Nonlinear optics is based on the fact that the polarization responds in a nonlinear fashion to large applied electric fields. The polarization is most often expressed as a power series in the field strength $\mathbf{E}(t)$:

$$\mathbf{P}(t) = \epsilon_0 \cdot (\chi^{(1)} \mathbf{E}(t) + \chi^{(2)} \mathbf{E}^2(t) + \chi^{(3)} \mathbf{E}^3(t) + \dots) \quad (2.2.2)$$

where the variables $\chi^{(2)}$ and $\chi^{(3)}$ are known as the second- and third-order nonlinear optical susceptibilities and are third- and fourth-rank tensors respectively. For the purposes of this text, we will assume that the third-order and higher nonlinear optical susceptibilities are negligible and that their effects can be ignored.

In a first approximation, we can imagine a light source whose electric field strength is represented as

$$\mathbf{E}(t) = \mathbf{E}e^{j\omega t} + \text{complex conjugate (c.c.)} \quad (2.2.3)$$

is incident upon a crystal whose second order nonlinear susceptibility is nonzero. Note: in this text, the imaginary number $\sqrt{-1}$ is denoted by j as is standard in most of the nonlinear texts. The polarization is given by

$$\begin{aligned} \mathbf{P}(t) &= \epsilon_0 \cdot (\chi^{(1)} \mathbf{E}(t) + 2\chi^{(2)} \mathbf{E}\mathbf{E}^* + (\chi^{(2)} \mathbf{E}^2 e^{-j\omega t} + \text{c.c.})) \\ &= \epsilon_0 \cdot (\mathbf{P}^{(1)}(t) + \mathbf{P}^{(2)}(t)) \end{aligned} \quad (2.2.4)$$

where $\mathbf{P}^{(2)}(t) = 2\chi^{(2)} \cdot \epsilon_0 \cdot \mathbf{E}\mathbf{E}^* + (\chi^{(2)} \cdot \epsilon_0 \cdot \mathbf{E}^2 e^{-j\omega t} + \text{c.c.})$

$\mathbf{P}^{(2)}(t)$ is known as the second order nonlinear polarization; it is this term that is the basis of the present discussion.

Now consider what happens when two distinct light sources at frequencies ω_1 and ω_2 are incident upon the crystal. The electric field is:

$$\mathbf{E}(t) = \mathbf{E}_1 e^{-j\omega_1 t} + \mathbf{E}_2 e^{-j\omega_2 t} + \text{c.c.} \quad (2.2.5)$$

and the second order nonlinear polarization is given as

$$\begin{aligned} \mathbf{P}^{(2)}(t) = & \chi^{(2)} \cdot \epsilon_0 \cdot (\mathbf{E}_1^2 e^{-2j\omega_1 t} + \mathbf{E}_2^2 e^{-2j\omega_2 t} + 2\mathbf{E}_1 \mathbf{E}_2 e^{-(\omega_1 + \omega_2)t} \\ & + 2\mathbf{E}_1 \mathbf{E}_2^* e^{-(\omega_1 - \omega_2)t} + \text{c.c.}) + 2\chi^{(2)} \cdot \epsilon_0 \cdot (\mathbf{E}_1^* \mathbf{E}_1 + \mathbf{E}_2 \mathbf{E}_2^*) \end{aligned} \quad (2.2.6)$$

The complex amplitudes of the various frequency components of the above polarization describe various second-order nonlinear optical mixing processes and are respectively:

$$\begin{aligned} \mathbf{P}(2\omega_1) &= \chi^{(2)} \cdot \epsilon_0 \cdot \mathbf{E}_1^2 + \text{c.c.} && \text{Second Harmonic Generation} \\ \mathbf{P}(2\omega_2) &= \chi^{(2)} \cdot \epsilon_0 \cdot \mathbf{E}_2^2 + \text{c.c.} && \text{Second Harmonic Generation} \\ \mathbf{P}(\omega_1 + \omega_2) &= 2\chi^{(2)} \cdot \epsilon_0 \cdot \mathbf{E}_1 \mathbf{E}_2 + \text{c.c.} && \text{Sum Frequency Generation} \\ \mathbf{P}(\omega_1 - \omega_2) &= 2\chi^{(2)} \cdot \epsilon_0 \cdot \mathbf{E}_1 \mathbf{E}_2^* + \text{c.c.} && \text{Difference Frequency Generation} \\ \mathbf{P}(0) &= 2\chi^{(2)} \cdot \epsilon_0 \cdot (\mathbf{E}_1 \mathbf{E}_1^* + \mathbf{E}_2 \mathbf{E}_2^*) && \text{Optical Rectification} \end{aligned} \quad (2.2.7)$$

The last term describes a process called optical rectification by which a static electric field is created within the nonlinear crystal. As it does not lead to the generation of electromagnetic radiation (its second time derivative vanishes), the process will no longer be considered. The rest of

the above terms describe oscillations of the polarization in a material caused by incidence of radiation at up to two distinct frequencies. According to Larmor's theorem from electromagnetism, accelerated charges generate electromagnetic radiation. Thus, in a very superficial way, the method for conversion of two photons of light into sums and differences of their frequencies has been thus far described.

The theory of difference frequency generation will now be developed in a more complete and rigorous fashion.

2.3 Difference Frequency Generation

The equations detailing the transfer of power between the drive sources and the output wave will here be derived.

2.3.1 Maxwell's Equations and the Paraxial Wave Equation

To consider the form of the wave equation for the propagation of light through a nonlinear optical medium, begin with Maxwell's equations in the MKS form

$$\nabla \cdot \mathbf{D} = \rho \quad (2.3.1)$$

$$\nabla \cdot \mathbf{B} = 0 \quad (2.3.2)$$

$$\nabla \times \mathbf{E} = - \frac{\partial \mathbf{B}}{\partial t} \quad (2.3.3)$$

$$\nabla \times \mathbf{H} = \partial \mathbf{D} / \partial t + \mathbf{J} \quad (2.3.4)$$

We will now assume we are operating in a medium where the polarization vector \mathbf{P} depends nonlinearly upon the local value of the electric field strength:

$$\mathbf{D} = \epsilon_0 \mathbf{E} + \mathbf{P} \quad (2.3.5)$$

and we will treat the magnetic field and induction differently, writing:

$$\mathbf{B} = \mu_0 \cdot \mu_p \cdot \mathbf{H} \quad (2.3.6)$$

The definitions of the above variables follow those of Flygare [18] and are as follows: \mathbf{E} and \mathbf{H} are the electric and magnetic field vectors, respectively, \mathbf{D} is the electric induction or displacement field, ϵ is the relative electric permittivity (dielectric constant) of the system, \mathbf{B} is the magnetic induction or magnetic flux density and μ_p the relative magnetic permeability of the medium, ϵ_0 is the permittivity of free space, μ_0 the permeability of free space, ρ is the electric charge density, and \mathbf{J} is the electric current density. For an isotropic medium, the scalars ϵ and μ_p are used in place of ϵ and μ_p . $\epsilon = \mu_p = 1$ for a vacuum and μ_p is very near unity for most substances.

Assume that there are no free space charges ($\rho = 0$) and that there is no free current ($\mathbf{J} = 0$). Take the curl of the curl-E Maxwell equation (Equation 2.3.3), insert Equations 2.3.4 and 2.3.6, and interchange the order of space and time derivatives on the right-hand side of the resulting equation; and one can obtain the equation

$$\nabla \times \nabla \times \mathbf{E} = -\frac{\partial^2 \mathbf{D}}{\partial t^2} = -\mu_0 \cdot \mu_p \cdot \left\{ \epsilon_0 \frac{\partial^2 \mathbf{E}}{\partial t^2} - \frac{\partial^2 \mathbf{P}}{\partial t^2} \right\} \quad (2.3.7)$$

The left hand side of the above equation can be transformed by an identity operation from calculus to:

$$\nabla \times \nabla \times \mathbf{E} = \nabla(\nabla \cdot \mathbf{E}) - \nabla^2 \mathbf{E} \quad (2.3.8)$$

In classical linear optics the first term on the right side of the equation is exactly equal to zero because the Maxwell equation $\nabla \cdot \mathbf{D} = \rho = 0$ (Equation 2.3.1) implies that $\nabla \cdot \mathbf{E} = 0$. In nonlinear optics, however, this term is nonvanishing due to the relation between the electric induction, the electric field, and the polarization given in Equation 2.3.5. This term can be shown [19] to be small when the slowly-varying approximation is valid. Under the slowly-varying-amplitude approximation, the second derivative of the electric field amplitude with respect to the longitudinal coordinate is much smaller than the first derivative. This assertion is valid when the fractional changes in the electric field amplitude in a distance of the order of magnitude of an optical wavelength is much smaller than unity.

Combining Equations 2.3.7 and 2.3.8 and the slowly-varying-amplitude approximation, we find that:

$$-\nabla^2 \mathbf{E} + \epsilon_0 \cdot \mu_0 \cdot \mu_p \cdot \frac{\partial^2 \mathbf{E}}{\partial t^2} = \mu_0 \cdot \mu_p \cdot \frac{\partial^2 \mathbf{P}}{\partial t^2} \quad (2.3.9)$$

But $\epsilon_0 \cdot \mu_0 = c^{-2}$ and μ_p is, to a fair approximation, unity for most substances. Now the electric field and polarization at each frequency (simply indexed by the subscript n) is represented by

$$\mathbf{E}_{\mathbf{n}}(x,y,z,t) = \mathbf{A}_{\mathbf{n}}(x,y,z)e^{j(k_{\mathbf{n}}z - \omega_{\mathbf{n}}t)} + \text{c.c.} \quad (2.3.10)$$

$$\mathbf{P}_{\mathbf{n}}(x,y,z,t) = \mathbf{p}_{\mathbf{n}}(x,y,z)e^{j(k_{\mathbf{n}}'z - \omega_{\mathbf{n}}t)} + \text{c.c.} \quad (2.3.11)$$

where the waves explicitly propagate at different speeds by allowing the wave vector of P to be different from that of E. In this formulation, we have assumed cw (*continuous wave*) beams and therefore that the amplitude of the electric field and the polarization is time independent. These results are independent of the choice of beam profile, as the transverse character of the electromagnetic wave is contained within the Cartesian functionality of $\mathbf{A}_{\mathbf{n}}$ and $\mathbf{p}_{\mathbf{n}}$. Redefine the Laplacian operator

$$\nabla^2 = \frac{\partial^2}{\partial z^2} + \nabla_2^T \text{ where } \nabla_2^T = \frac{\partial^2}{\partial x^2} + \frac{\partial^2}{\partial y^2} \quad (2.3.12)$$

and define the wavevector mismatch:

$$\Delta k = k_{\mathbf{n}}' - k_{\mathbf{n}} \quad (2.3.13)$$

If we substitute Equations 9 through 13 into Equation 8 and make the slowly-varying-amplitude approximation ($\partial^2/\partial z^2 \mathbf{A} = 0$) we finally have derived the paraxial wave equation.

$$-2jk_{\mathbf{n}} \frac{\partial \mathbf{A}_{\mathbf{n}}}{\partial z} + \nabla_2^T \mathbf{A}_{\mathbf{n}} = \frac{-\omega_{\mathbf{n}}^2}{2 \cdot \epsilon_0 \cdot c^2} \cdot \mathbf{p}_{\mathbf{n}} e^{-j\Delta k z} \quad (2.3.14)$$

This is known as the paraxial equation because the neglect of the contribution of $\partial^2/\partial z^2 \mathbf{A}$ on the left hand side is justifiable as long as the wave \mathbf{E}_n is propagating primarily along the z axis.

To properly set the stage for difference frequency generation, the complex amplitude \mathbf{p}_n and \mathbf{A}_n are assumed to be collinear with the other beams and the time averaged scalar values of their projections onto one of the crystallographic axes are substituted. The polarization p_n for DFG is equal to $2\chi^{(2)} \cdot \epsilon_0 \cdot E_1 E_2^*$ (Equation 2.2.7). Usually, the symbol for the effective nonlinear susceptibility in DFG is given by $d_{\text{eff}} = 2\chi^{(2)}$. The d_{eff} value is a trigonometric function of the angle of incidence of the beams with respect to the crystallographic axes that is dependent upon the space group symmetry of the crystal. The reader is urged to consult any of a number of texts on this matter [19-21] for a more complete definition of the terms involved.

$$-2jk_n \frac{\partial \mathbf{A}_n}{\partial z} + \nabla_T^2 \mathbf{A}_n = \frac{-\omega_n^2 \cdot d_{\text{eff}} \cdot \epsilon_0 \cdot E_1 \cdot E_2^* \cdot e^{i\Delta k z}}{\epsilon_0 \cdot c^2} \quad (2.3.15)$$

The wavevector Δk in Equation 2.3.15 refers to:

$$\mathbf{k} = \frac{n\omega}{c} \mathbf{v} \quad (2.3.16)$$

which is a vector quantity with n the index of refraction specific to the wave at circular frequency ω and \mathbf{v} is a unit vector in the direction of propagation. Again, we have assumed collinearity of the wavefronts throughout this text and will simply use the scalar k .

By substituting the form of the the wavevector of Equation 2.3.16 into Equation 2.3.15, replacing the generic n subscripts by i (for reasons we will soon discuss), and with some slight rearrangement, the paraxial wave equation can be recast into its usual form:

$$\left(\frac{\partial}{\partial z} - \frac{j}{2 \cdot k_i} \cdot \nabla_T^2 \right) \cdot A_i = \frac{j \cdot \omega_i \cdot d_{\text{eff}} \cdot E_1 \cdot E_2^* \cdot e^{-j\Delta k z}}{\epsilon_0 \cdot c \cdot n_i} \quad (2.3.17)$$

Quite obviously, since the electric field of the infrared beam is a measurable quantity, we will need to use the real portion of the above function. By solving Equation 2.3.17 for the amplitude of the infrared beam and integrating the square of the amplitude across the transverse coordinates at some arbitrary distance beyond the nonlinear crystal, it is possible to determine the total power in the generated beam:

$$P_i(z) = \frac{n_i \cdot c}{2 \cdot \epsilon_0} \cdot \int_{-\infty}^{\infty} dx \cdot dy \cdot |A_i(x, y, z)|^2 \quad (2.3.19)$$

The standard method for solving this inhomogeneous second order differential equation is to find the Green's function (G) for the homogeneous equation and then to integrate the Green's function across the inhomogeneous part:

$$A_i(x,y,z) = \frac{j \cdot \omega_i \cdot d_{eff}}{\epsilon_0 \cdot c \cdot n_i} \cdot \int_0^z dz' \cdot \int_{-\infty}^{\infty} dx' dy' \cdot G(x,x',y,y',z,z') \cdot A_p(x',y',z') \cdot A_s^*(x',y',z') \cdot e^{-j\Delta k z'} \quad (2.3.20)$$

In the research to date in this laboratory, it is the lowest frequency wave (the *idler* wave) that is generated and so we will solve for the amplitude of this term. The other two waves are the *pump* (the highest frequency) and *signal* (the intermediate frequency) waves.

Fisher *et. al.* [22] have determined the Green's Function for this situation:

$$G_i(x,x',y,y',z,z') = \frac{-j \cdot k_i}{2\pi(z-z')} \exp\left(\frac{j \cdot k_i}{2\pi(z-z')} \{ (x-x')^2 + (y-y')^2 \} \right) \quad (2.3.21)$$

The Green's Function describes the electric field produced at point z due to an impulse of radiation at point z' . This approach has been used by Kleinman *et. al.* in various papers [21,23-25] to describe the process of second-harmonic generation.

The power produced in difference frequency generation is then:

$$\begin{aligned} P_i(Z) &= \frac{n_i \cdot c}{2 \cdot \epsilon_0} \cdot \int_{-\infty}^{\infty} dx \cdot dy \cdot |A_i(x,y,Z)|^2 \\ &= \frac{n_i \cdot c}{2 \cdot \epsilon_0} \cdot \int_{-\infty}^{\infty} dx \cdot dy \cdot A_i(x,y,Z) \cdot A_i^*(x,y,Z) \end{aligned}$$

$$\begin{aligned}
&= \frac{n_i \cdot c}{2 \cdot \epsilon_0} \cdot \left(\frac{j \cdot \omega_i \cdot d_{eff}}{\epsilon_0 \cdot c \cdot n_i} \right)^2 \cdot \int_0^Z dz \cdot \int_{-\infty}^{\infty} dx \cdot dy \cdot A_p(x, y, z) \cdot A_s^*(x, y, z) \cdot e^{-j\Delta k z} \cdot \\
&\quad \int_0^z dz' \cdot \int_{-\infty}^{\infty} dx' \cdot dy' \cdot G^*(x, x', y, y', z, z') \cdot A_p^*(x', y', z') \cdot A_s(x', y', z') \cdot e^{-j\Delta k z'}
\end{aligned}
\tag{2.3.22}$$

where the last equality was taken directly from Fischer *et. al.* This equation amounts to determining the total power in the beam at the exit face of the crystal by integrating the product of the amplitude of the three beams over the length of the entire crystal. It is assumed that the crystal transverse dimensions x and y are large compared with the beam diameter d at all points in the crystal so that vignetting effects are negligible.

It is implicit in the formulation of Equation 2.3.22 that power conversion into the infrared is considered negligible so that the amplitude of the pump and signal waves is independent of the power produced. This is called the undepleted pump and signal approximation and will be shown to be valid in Chapter 4. When this assumption is no longer valid, one must take into account the transfer of power out of the signal and idler waves and back into the pump wave.

2.3.2 Profile of the Drive Beams

In order to calculate the output power of difference frequency generation, we will have to assign certain characteristics to the pump and

signal laser beams. We will assume that they are monochromatic and that the transverse horizontal and vertical profiles both beams are individually in the lowest order Gaussian (hereafter simply called Gaussian), though we do not assume the beams are circular in shape (this is called *elliptical* focusing). It has been shown [21] that Gaussian beams transfer the greatest power to the infrared and hence represents an upper limit for infrared production. The form used for the pump and signal amplitudes ($a=p$ or s) is:

$$A_a(x,y,z) = N_a \cdot \exp \left(\frac{-\left\{ x - \rho_x(z-z_{ax}^0) + x_0 \right\}^2}{w_{ax}^2 \cdot (1+j \cdot (\tau_{ax}-\tau_{ax}^0))} + \frac{-y^2}{w_{ay}^2 \cdot (1+j \cdot (\tau_{ax}-\tau_{ay}^0))} \right) \quad (2.3.23)$$

where

$$N_a = \frac{A_{a0}}{(1+j \cdot (\tau_{ax}-\tau_{ax}^0)) \cdot (1+j \cdot (\tau_{ax}-\tau_{ay}^0))} \quad (2.3.24)$$

is a normalization factor for the wavefunction

$$\rho_a = \tan^{-1} \left(\frac{1}{2} \cdot \sin(2\theta) \cdot n_{eff} \left| \frac{1}{n_e^2} - \frac{1}{n_o^2} \right| \right) \quad (2.3.25)$$

is the double refraction angle for the beam. The Cartesian coordinates are chosen so that double refraction occurs in the x - z plane. In a biaxial crystal the angle ρ_a is nonzero only for extraordinary polarized beams.

z_{ax}^0 the z position of the focus in the x dimension for the a^{th} wave. In the case of nonastigmatic beams, this will equal the z_{ay}^0 value.

w_{ax} The beam waist in the x dimension.

τ_{ax} $2 \cdot z / b_a$

τ_{ax}^0 $2 \cdot z_{ax}^0 / b_a$

b_a The confocal parameter (twice the Raleigh Range) is a measure of the depth of the focus of the beam. $b_a = w_{ay} \cdot w_{ax} \cdot k_a$

$$A_{a0} = \frac{2 \cdot \epsilon_0 \cdot P_a}{n_a \cdot c \cdot w_{ay} \cdot w_{ax}}$$

The peak amplitude of the wave (see Appendix 1).

P_a The total power carried by wave a

x_0 The displacement of the center of the extraordinary polarized beam from the ordinary polarized beam at the entrance face of the crystal.

We also explicitly ignore the effects of reflection inside the crystal. This allows us to ignore the complex conjugate of Equation 2.3.15 and makes the calculations more manageable.

The most fundamental requirement of any wave function is that it fulfill the paraxial wave equation for vacuum propagation. In vacuum, the right hand side of Equation 2.3.14 is equal to zero (there is no polarization in a vacuum). It can be shown that this is the case for the function given in Equation 2.3.19 if and only if the double refraction angle ρ is equal to zero. This is the result expected (double refraction does not occur in a vacuum).

2.4 Power Generated in the DFG Process

By substituting the form of the wave equation in Equation 2.3.23 into Equation 2.3.22, it is possible to calculate the net power transferred to the infrared beam. The final answer of this calculation will be simply be presented here while the derivation of this result is contained within Appendix 1.

$$P_i = \frac{16P_p P_s k_i \omega_i^2 d_{eff}^2}{\pi^3 \epsilon_0 n_p n_s n_i c^3 w_{px} w_{py} w_{sx} w_{sy}} \cdot \text{Im} \int_0^L \int_0^z \frac{C_x \cdot C_y \cdot I_x \cdot I_y \cdot e^{j\Delta k(z-z')}}{2(z-z')} dz' dz \quad (2.4.1)$$

where the τ' terms refer to substitution of z by z' ,

$$a_x = \frac{1}{w_{sx}^2 \cdot (1 + j(\tau_s - \tau_{sx}^0))} \quad (2.4.2)$$

$$b_x = \frac{1}{w_{px}^2 \cdot (1 - j(\tau_p - \tau_{px}^0))} \quad (2.4.3)$$

$$c_x = \frac{1}{w_{sx}^2 \cdot (1 - j(\tau_s' - \tau_{sx}^0))} \quad (2.4.4)$$

$$d_x = \frac{1}{w_{px}^2 \cdot (1 + j(\tau_p' - \tau_{px}^0))} \quad (2.4.5)$$

$$a_y = \frac{1}{w_{sy}^2 \cdot (1 + j(\tau_s - \tau_{sy}^0))} \quad (2.4.6)$$

$$b_y = \frac{1}{w_{py}^2 \cdot (1 - j \cdot (\tau_p - \tau_{py}^0))} \quad (2.4.7)$$

$$c_y = \frac{1}{w_{sy}^2 \cdot (1 - j \cdot (\tau_s' - \tau_{sy}^0))} \quad (2.4.8)$$

$$d_y = \frac{1}{w_{py}^2 \cdot (1 + j \cdot (\tau_p' - \tau_{py}^0))} \quad (2.4.9)$$

$$E = \frac{k_i}{2(z - z')} \quad (2.4.10)$$

$$x_0 = \rho_x(z - z_{px}^0) \quad (2.4.11)$$

$$x_1 = \rho_x(z' - z_{px}^0) \quad (2.4.12)$$

$$C_x = \frac{1}{\sqrt{(1-j(\tau_p-\tau_{px}^0)) \cdot (1+j(\tau_s-\tau_{sx}^0)) \cdot (1+j(\tau_p'-\tau_{px}^0)) \cdot (1-j(\tau_s'-\tau_{sx}^0))}} \quad (2.4.13)$$

$$C_y = \frac{1}{\sqrt{(1-j(\tau_p-\tau_{py}^0)) (1+j(\tau_s-\tau_{sy}^0)) (1+j(\tau_p'-\tau_{py}^0)) (1-j(\tau_s'-\tau_{sy}^0))}} \quad (2.4.14)$$

$$\mathbf{M}_x = \begin{pmatrix} a_x + b_x - j \cdot E & -j \cdot E \\ -j \cdot E & c_x + d_x - j \cdot E \end{pmatrix} \quad (2.4.15)$$

$$\mathbf{M}_y = \begin{pmatrix} a_y + b_y - j \cdot E & -j \cdot E \\ -j \cdot E & c_y + d_y - j \cdot E \end{pmatrix} \quad (2.4.16)$$

$$I_x = \frac{\pi}{\sqrt{|\mathbf{M}_x|}} e^{-b_x \cdot x_0^2 - d_x \cdot x_1^2} \cdot e^{(b_x \cdot x_0 \ d_x \cdot x_1) \cdot \mathbf{M}_x^{-1} \cdot \begin{pmatrix} b_x \cdot x_0 \\ d_x \cdot x_1 \end{pmatrix}} \quad (2.4.17)$$

$$I_y = \frac{\pi}{\sqrt{|\mathbf{M}_y|}} \quad (2.4.18)$$

In this second-order parametric process, the highest frequency wave is called the pump wave and its frequency denoted ω_p . The second highest frequency wave is called the signal wave and the lower frequency the idler wave, denoted ω_s and ω_i , respectively. These frequencies are the circular frequencies (frequency in Hertz multiplied by 2π). The energy level diagram of their interaction is given in Figure 2.1.

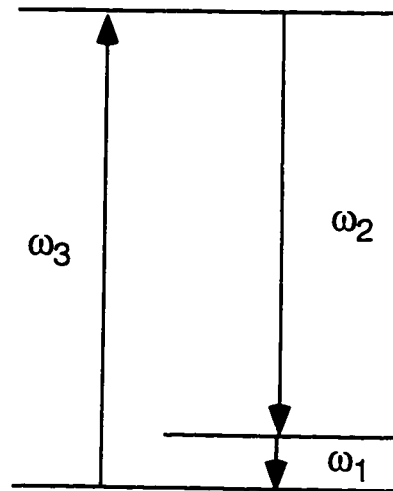


Figure 2.1 - Energy Level Diagram of the DFG Process

2.4.1 - The Phasematching Condition

The wavevector mismatch (or momentum mismatch) is a scalar measure of the difference in momentum between the pump and the sum of the signal and idler waves:

$$\Delta k = k_p - k_s - k_i = \frac{n_p \cdot \omega_p}{c} - \frac{n_s \cdot \omega_s}{c} - \frac{n_i \cdot \omega_i}{c} \quad (2.4.19)$$

For a given combination of frequencies, there is sometimes an angle θ with respect to the optical axis such that the wavevector mismatch is equal to zero. This occurs because of the angular dependence of the index of refraction (Equation 2.1.1) that changes the effective index of refraction for the radiation polarized in the extraordinary plane but leaves the ordinary plane polarized index of refraction unchanged. This angle is measured internal to the crystal and is found utilizing Equation 2.3.19 and the conservation of energy ($\omega_p = \omega_s + \omega_i$).

There are often two ways in which phasematching can occur. The pump wave always is associated with the lower index of refraction (n_{eff}^e for negative uniaxial crystals, n_o for positive). The signal wave is always associated with the other polarization. The idler wave can be polarized in either direction. If it is polarized in the same plane as the signal wave, it is called a *type-I* interaction. If it is polarized in the same direction as the pump wave, it is called a *type-II* interaction. Using the numbering system $\omega_p = \omega_3$, $\omega_s = \omega_2$, and $\omega_i = \omega_1$, it is common to see the method of interaction simply given by the directions of polarizations of the three waves listed in increasing numerical order. For example, in a negative

uniauxial crystal type-I interaction, where the pump wave is polarized with a component along the extraordinary axis and the signal and idler waves are purely polarized in the ordinary direction, the interaction is listed as ooe.

In Equation 2.3.18, the wavevector mismatch appears in the term $e^{-j\Delta k(z-z')}$. This is equivalent to $\cos(-j\Delta k(z-z'))$. If one wavelength is scanned about the perfect phasematching wavelength and all other parameters remain fixed, Δk will vary around zero. Therefore, the infrared power produced oscillates from a maximum value to zero as one drive wavelength is scanned and if all other parameters remain unchanged. This is called the *phasematching condition* and the oscillation period is called the *phasematching bandwidth*. All the nonlinear optical processes listed in Section 2.2 (Second Harmonic Generation, Sum Frequency Generation, etc.) with the exception of Optical Rectification have wavevector mismatch terms. Because of this, usually only one of these processes is active at any time for a given combination of input frequencies and crystal orientation.

2.5 Alternative formulations for DFG Power

Others have calculated the theoretical yield for down conversion of laser light into difference frequency generation with different approximations. These are useful in that they illustrate aspects of the nonlinear mixing process that are sometimes difficult to envision in the above formulation.

2.5.1 Plane Wave Theory

The simplest theory developed to describe the difference frequency generation process is the Plane Wave Limit. Equation 2.3.15 is replaced by an infinite plane wave

$$E_a(z,t) = A_a e^{j(k_a z - \omega_a t)} + \text{c.c.} \quad (2.5.1)$$

where the amplitude of the wave A_a is invariant with respect to the Cartesian coordinates. It is a relatively straightforward operation to derive the infrared power produced by such incident waves [19,26] and the results give easy insight into the process of parametric amplification.

$$P_i = \frac{(2 \cdot \omega_i \cdot d_{\text{eff}} \cdot L)^2 \cdot P_p \cdot P_s}{n_p \cdot n_s \cdot n_i \cdot c^3 \cdot \pi \cdot \epsilon_0 \cdot (\omega_s^2 + \omega_p^2)} \cdot \text{sinc}^2\left(\frac{\Delta k L}{2}\right) \quad (2.5.2)$$

It can be seen that in order to maximize the infrared power produced, it is desirable to use high pump and signal powers, a long crystal, and to increase the intensity of the input beams by using small beam waists.

The phasematching bandwidth in the plane wave limit can be seen in the form of the sinc^2 ($\text{sinc}(x) = \sin(x) / x$) function of Equation 2.5.2. As seen in Figure 2.2, the sinc^2 function exhibits a maximum at 0. This corresponds to the condition of all three waves moving at the same velocity through the crystal. When this occurs, the idler wave builds quadratically along the entire length of the crystal, but as Δk is changed from zero, the waves no longer move exactly in phase and if $\Delta k L$ is equal to π , the waves

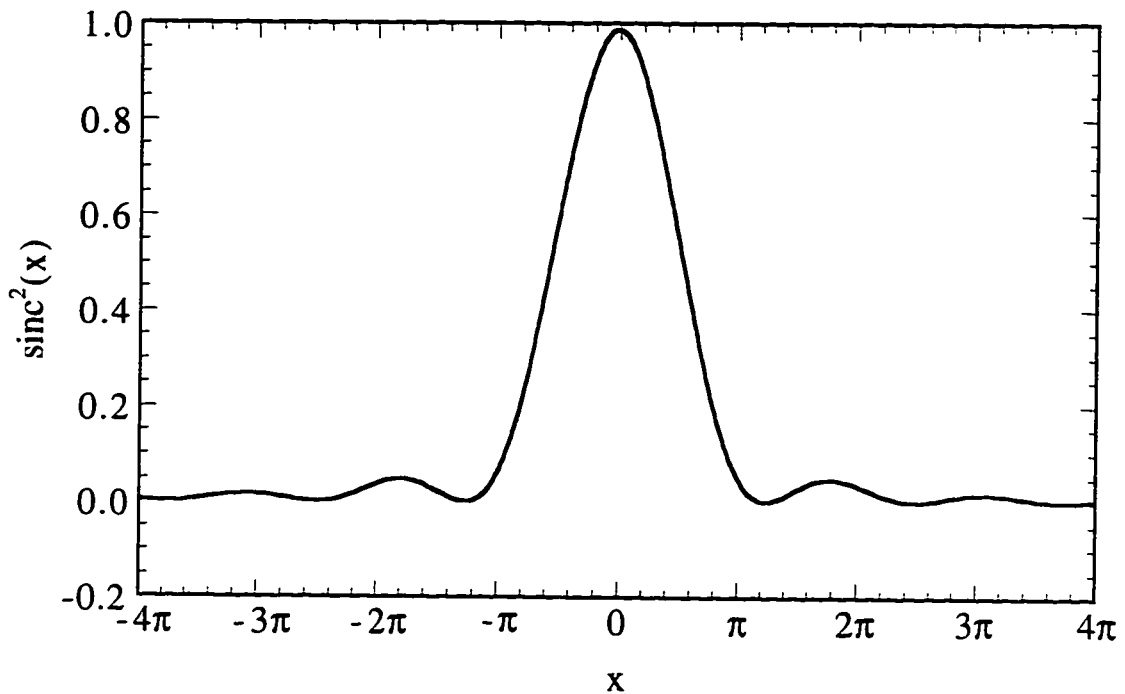


Figure 2.2 - The $\text{Sinc}^2(x)$ Function

have moved 180° out of phase by the end of the crystal. According to Equation 2.3.18, the infrared power produced is the product of the amplitude of all three waves. If one wave is out of phase by 180° with respect to the other two waves, power is transferred from the idler and signal waves back into the pump beam (sum frequency generation). The net result when $(\Delta kL/2) = \pi$ is that no infrared power is produced.

The decreasing amplitude of the oscillations from perfect phasematching also has a simple explanation. The second largest pair of peaks at $x=\pm 3\pi/2$ correspond to infrared power that is generated by waves that stay in phase for the first third of the crystal ($\{\Delta kL/6\} \leq \pi$). The infrared power is then converted back to the pump beam in the middle third of the crystal as the phase difference is greater than π , and regenerated in the last third of the crystal with less than perfect

phasematching. Thus, the satellite peaks each generate less than 10% of the power of perfect phasematching.

It is also seen that as the crystal length is increased, the peak infrared power produced is increased by the square of the length. It is also true that as the crystal length is increased, the phasematching bandwidth decreases proportionately. Physically, this means that for peak phasematching, the tolerance for a difference in phase velocity is tighter (the waves have to travel a longer distance at the same velocity). This is a valid concern when trying to construct a spectrometer - while it would be nice to consider an infinitely long crystal, the phasematching bandwidth would become infinitely narrow and the instrument is largely transformed into a fixed frequency source with little spectroscopic application.

While the plane wave theory can be used for unfocussed beams with beam diameters much larger than the wavelength, it ignores double refraction, ellipticity in the drive beams, and, most importantly, diffraction effects. It will later be shown that focusing the laser beams can lead to dramatic improvement in the parametric conversion efficiency. The plane wave theory correctly shows that as the drive beam intensity is increased (the beam waists decrease), infrared power increases, but this then approaches the regime in which the plane wave theory is invalid.

2.5.2 Chu and Broyer's Theory

Chu and Broyer have addressed the problem of diffraction-limited DFG [27]. By assuming an equal confocal parameter for the two drive

beams, a lossless crystal, and locating the foci of the two beams in the center of the crystal; they have generated a formula [Equation 32 in their text] that applies to focused, circular, gaussian beams (transformed to MKS units).

$$P_i = \frac{(2 \cdot \omega_i \cdot d_{eff} \cdot L)^2 \cdot P_p \cdot P_s}{c^3 \cdot n_p \cdot n_s \cdot n_i \cdot \pi \cdot \epsilon_0 \cdot (w_p^2 + w_s^2)} \cdot \frac{h^{DF}(B, \sigma, \mu, \xi)}{\xi} \quad (2.5.3)$$

with

$$h^{DF}(B, \sigma, \mu, \xi) = \frac{1}{2\xi} \int_0^\xi d\tau \int_0^\xi d\tau' \cdot \frac{e^{-j\sigma(\tau-\tau')} F(B, \mu, \xi)}{1 - \frac{j}{2} \left[\frac{1+\mu}{1-\mu} + \frac{1-\mu}{1+\mu} \right] \cdot (\tau-\tau') + \tau\tau'} \quad (2.5.4)$$

$$B = \frac{\rho}{2} \cdot \sqrt{L \cdot k_p} \quad (2.5.5)$$

$$\sigma = \frac{-\Delta k b}{2} \quad (2.5.6)$$

$$\xi = \frac{L}{b} \quad (2.5.7)$$

$$\mu = \frac{k_s}{k_p} \quad (2.5.8)$$

$$F(B, \mu, \xi) = \exp \left\{ -\frac{B}{\xi} \left(\frac{\tau'^2}{1+j\tau'} \left[1 - \frac{j(1-j\tau')(\tau-\tau')}{(1-\mu)[1]} \right] + \frac{\tau^2}{1-j\tau} \right) - \right. \\ \left. - \left[\frac{\tau'(1-j\tau')}{[1]} - \frac{\tau}{1-j\tau} \right]^2 \cdot \frac{1+\tau^2 \cdot [1]}{2(1+\mu) \{ \}_4} \right\} \quad (2.5.9)$$

$$[]_1 = 1 + j \cdot \frac{1+\mu}{1-\mu} (\tau - \tau') + \tau \tau' \quad (2.5.10)$$

$$\{ \} _4 = 1 - \frac{j}{2} \cdot \left[\frac{1+\mu}{1-\mu} + \frac{1+\mu}{1-\mu} \right] \cdot (\tau - \tau') + \tau \tau' \quad (2.5.11)$$

Note: the above equations have been exactly reproduced from Chu and Broyer's paper. It is this author's opinion, unsupported that it is, that the second minus sign between lines in Equation 2.5.9 is spurious. This author also suspects that Equation 2.5.11 should read.

$$\{ \} _4 = 1 - \frac{j}{2} \cdot \left[\frac{1+\mu}{1-\mu} + \frac{1-\mu}{1+\mu} \right] \cdot (\tau - \tau') + \tau \tau' \quad (2.5.12)$$

In the case of noncritical phasematching at the perfect phasematching condition ($\Delta k = 0$), their equations can be reformulated in a simpler form [3].

$$P_i = \frac{(2 \cdot \omega_i \cdot d_{eff})^2 \cdot P_p \cdot P_s \cdot L}{c^3 \cdot n_p \cdot n_s \cdot n_i \cdot \pi \cdot \epsilon_0 \cdot (k_p^{-1} + k_s^{-1})} \cdot h(\mu, \xi) \quad (2.5.13)$$

with

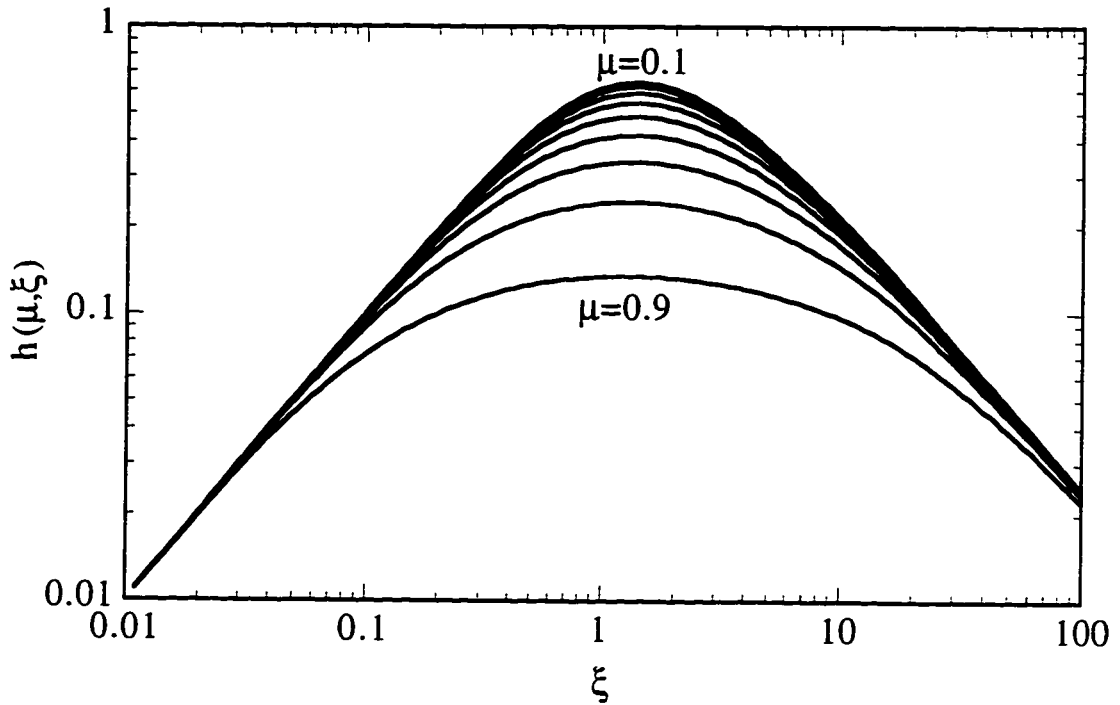


Figure 2.3 - Chu and Broyer's h-function

$$h(\mu, \xi) = \frac{1}{2\xi} \int_0^\xi d\tau \int_{-\xi}^\xi d\tau' \cdot \frac{1+\tau\tau'}{(1+\tau\tau')^2 \cdot \frac{1}{4} \left[\frac{1+\mu}{1-\mu} + \frac{1-\mu}{1+\mu} \right]^2 \cdot (\tau-\tau')^2} \quad (2.5.14)$$

This h-function contains all the beam focussing information. Figure 2.3 displays the h-function for various values of μ as a function of ξ . From this, it can be seen that for a wide range of pump and signal wavelengths (various μ 's), the focusing parameter ξ is maximized with virtually the same value, indicating that the optimum focusing condition is only weakly dependent upon the drive wavelengths used.

Focussing the drive beams greatly increases the infrared power produced over the plane wave limit. There can be more than an order of magnitude difference in the power produced. A concrete example of the advantage of focusing the drive beams into the crystal will be shown in Chapter 4.

It can be shown numerically that Equations 2.4.1 and 2.5.13 are nearly identical. The results with a variety of input parameters match to within 4% when all the variables in 2.4.1 correspond to those in 2.5.13:

$$\Delta k = 0$$

$$z_{px}^0 = z_{py}^0 = z_{sx}^0 = z_{sy}^0 = \frac{L}{2}$$

$$w_{px} = w_{py}, w_{sx} = w_{sy}$$

$$\rho_p = \rho_s = 0$$

2.5.3 Lera and Nieto-Vesperinas' Theory

Lera and Nieto-Vesperinas [28] have established a method for the non-paraxial formulation for difference frequency generation. It is based on the angular spectrum representation of wavefields and considers depletion and birefringent effects of gaussian beams. Their model is based on one dimensional drive beams of equal beam waists and, while it gives different spatial distributions of the generated idler beam than does the theory of Chu and Broyer, the total power produced in the process is virtually identical. The equations produced by this non-paraxial

formulation are rather complicated and will not be reproduced here - instead the reader is urged to directly consult their article.

The importance of this work is that it serves as a confirmation that even under extreme focusing conditions, the paraxial approximation is still valid when calculating the total power transferred to the infrared in the DFG process.

2.5.4 - Quasiphasematching

In a technique called quasiphasematching, some nonlinear materials can be specifically tailored for noncritical phasematching for any given combination of drive wavelengths. For a given combination of drive wavelengths, the distance over which the relative phase of the three waves changes by π is the *coherence length* l_c .

From Equation 2.3.18, it can be seen that if the product of the amplitude terms is allowed to vary by π radians, the sign of the integral will change and the signal and idler waves will be converted back into the pump wave. If one could invert the amplitude of the waves after each coherence length, the infrared would build monotonically along the entire crystal. This sort of control of optical waves is rather impractical, so instead the sign of the nonlinear coefficient d_{eff} is alternated. To this point in the text, no mention of the fact that d_{eff} is a signed value has been made because the equations were invariant to the sign: the infrared power is proportional to the square of d_{eff} . This process of inverting the relative phases of the electromagnetic waves is called *quasiphasematching*. The

phase is thus reset periodically so that, on average, the proper phase relationship is maintained for growth of the idler wave.

Two methods have been used to create an inversion in the d_{eff} value. The older method involves stacking thin layers of the nonlinear material, each rotated from its neighbors by 180° . A more recent approach involves permanently forming regions of periodically reversed spontaneous polarization (*domains*) in ferroelectric materials (like lithium niobate and RTA) with strong electric fields.

By allowing the phase to slip by $m\pi$ each coherence period where m is an odd integer, we find:

$$\Delta k \cdot l_c = m \cdot \pi \quad (2.5.15)$$

rearranged slightly gives

$$l_c = \frac{m \cdot \pi}{\Delta k} \quad (2.5.16)$$

Thus, the sign of the nonlinear coefficient must be inverted each coherence length l_c to maintain the monotonic increase in idler power. The period of the domains Λ (the *domain period* or *grating period*) is equal to twice the coherence length

$$\Lambda = 2 \cdot l_c \quad (2.5.17)$$

It can be shown [29] that by representing the wavevector mismatch for quasiphasematching by:

$$\Delta k_Q = \Delta k - \frac{2\pi}{\Lambda} = \frac{n_p \cdot \omega_p}{c} - \frac{n_s \cdot \omega_s}{c} - \frac{n_i \cdot \omega_i}{c} - \frac{2\pi}{\Lambda} \quad (2.5.18)$$

the effective quasiphasematched nonlinear coefficient d_Q is:

$$d_Q = \frac{2 \cdot d_{eff}}{m \cdot \pi} \quad (2.5.19)$$

By substituting Δk_Q for Δk and d_Q for d_{eff} into any of the above power calculations, Armstrong *et. al.* [30] and Baumgartner *et. al.* [31] have shown that the infrared power can be calculated in the same way as in the bulk material. From the form of Equation 2.5.19, it is clear that it is most efficient to use the lowest order quasiphasematching ($m=1$) whenever possible.

The advantages of quasiphasematching are profound. Since the material is engineered to fit the drive wavelengths, the phasematching condition can be tailored to utilize convenient drive wavelengths. In lithium niobate, it is common to employ a Nd:YAG and a titanium:sapphire laser. Though the nonlinear coefficient is at most $2/\pi$ of the bulk value, it is possible to design crystals utilizing nonlinear coefficients that are inaccessible to bulk phasematching and thus higher conversion efficiencies are attainable than can be achieved in the bulk material. Finally, by choosing an angle of incidence θ with respect to the grating period of the crystal such that

$$\frac{d}{d\lambda_i} \cdot \frac{\Lambda}{\cos\theta} = 0 \quad (2.5.20)$$

it is possible to increase the phasematching bandwidth to hundreds of wavenumbers [32,33]. Compare this with a typical phasematching bandwidth of 1 cm^{-1} in the bulk for a 50 mm long crystal.

2.6 Crystals Used in Mid-Infrared Down-Conversion

There are a number of requirements for any material that is to be used in a nonlinear frequency down-conversion scheme. Clearly, the crystal should be transparent at all three wavelengths. From the form of Equation 2.4.1, it should have a high damage threshold so that high pump intensities can be used to increase the produced power. It should also have a high nonlinear coefficient. Large, optical quality samples must be produced, cleaved, and polished in such a fashion as to allow phasematching. There are only a handful of crystals produced that fulfill all the above requirements. Sections 2.6.1 through 2.6.13 detail the relevant characteristics of most of the suitable materials that fulfill the above requirements.

To be used in a convenient, versatile spectrometer, phasematching wavelengths need to be in spectral regions accessible by powerful, broadly tunable, single frequency sources. This suggests using at least one pump laser in the near ultraviolet to near infrared regions of the spectrum (300 nm - 1050 nm) where dye lasers and titanium sapphire lasers and their frequency doubled counterparts fulfill all the above requirements.

It is also desirable for the nonlinear crystal to be noncritically phasematchable (the phasematching condition can be met at $\theta=\pi/2$) to remove the effects of double refraction of the pump from the signal beam. Noncritical phasematching may be fulfilled by changing the wavelength of both pump sources or by changing the index of refraction of the material through temperature or pressure changes.

Finally, the material should be mechanically and chemically robust. To avoid the difficulties of vacuum systems, the material should be stable in the atmosphere and non-hygroscopic. If temperature tuning is to be used, the material should have a large change in the index of refraction with temperature. Similarly, pressure tuning is impractical if the material is either a brittle or soft crystal.

The diagrams on the following pages display the results of calculating the perfect phasematching conditions ($\Delta k = 0$) for a variety of crystals. Critical phasematching diagrams have been constructed in the following manner. For a given pump wavelength (displayed in the legend), the signal and idler wavelengths are calculated as a function of the phasematching angle.

Notes: the d_{eff} value is measured by the efficiency of second-harmonic generation pumped at the wavelength given in parenthesis. For many materials, noncritical phasematching ($\theta=\pi/2$) is impossible because d_{eff} at this angle equals zero. In these cases, d_{eff} rapidly approaches zero. This situation will be indicated in the listing of the effective nonlinear coefficients section. The angle ϕ is the angle of the beams with respect to the crystallographic a-axis and the angle θ is

measured with respect to the optical axis. The damage threshold is dependent upon pulse length and wavelength, so these are given in the parenthesis. All dispersion relations assume that wavelength λ is given in microns.

2.6.1 Cadmium Germanium Arsenide (CdGeAs₂)

Transparency: 2.4 - 18 μm [34,35]

Damage Threshold: 38 MW/cm² ($\tau = 160$ ns, 10.6 μm) [36]

Nonlinear Coefficient: [37]

$$d_{oeo} = d_{36} \cdot \sin(\theta) \cdot \sin(2\phi)$$

$$d_{eoo} = d_{36} \cdot \sin(2\theta) \cdot \cos(2\phi) \quad [\text{Not critically phasematchable}]$$

$$d_{36}(10.6 \mu\text{m}) = 234 \pm 38 \text{ pm/V}$$

Index of Refraction:[38]

$$n_o^2 = 10.1064 + \frac{2.2988 \cdot \lambda^2}{\lambda^2 - 1.0872} + \frac{1.6247 \cdot \lambda^2}{\lambda^2 - 1370}$$

$$n_e^2 = 11.8018 + \frac{1.2152 \cdot \lambda^2}{\lambda^2 - 2.6971} + \frac{1.6922 \cdot \lambda^2}{\lambda^2 - 1370}$$

Other index relations: [34,36]

Positive uniaxial crystal: $n_o < n_e$

Using grating-tuned cw CO and CO₂ lasers, tunable infrared radiation between 11.4 and 16.8 μm was generated using type-II difference frequency generation [36]. The linewidth of this source was 500 kHz and generated several microwatts of power, making it a potentially attractive source for spectroscopy but for the fact that tunable frequencies were

spaced a bit less than 1 cm^{-1} apart [39]. CdGeAs_2 can be noncritically type-II phasematched (Figure 2.6) but the wavelengths required are beyond most presently available continuously tunable sources.

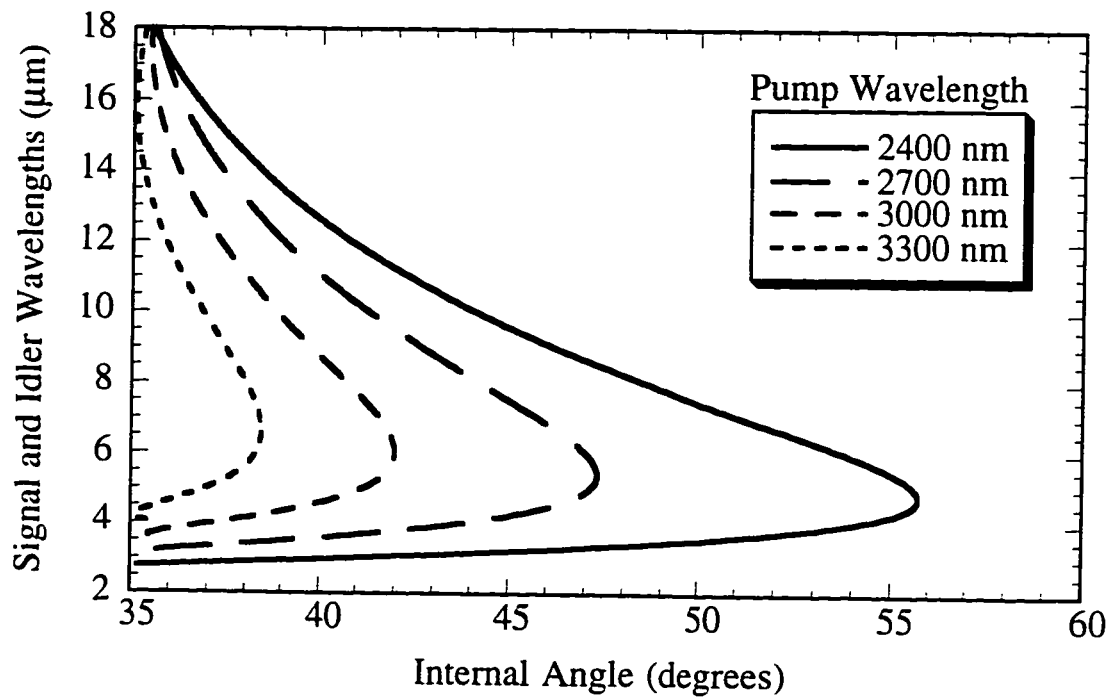


Figure 2.4 - Type-I Phasematching in CdGeAs_2 ($o \Rightarrow e+e$)

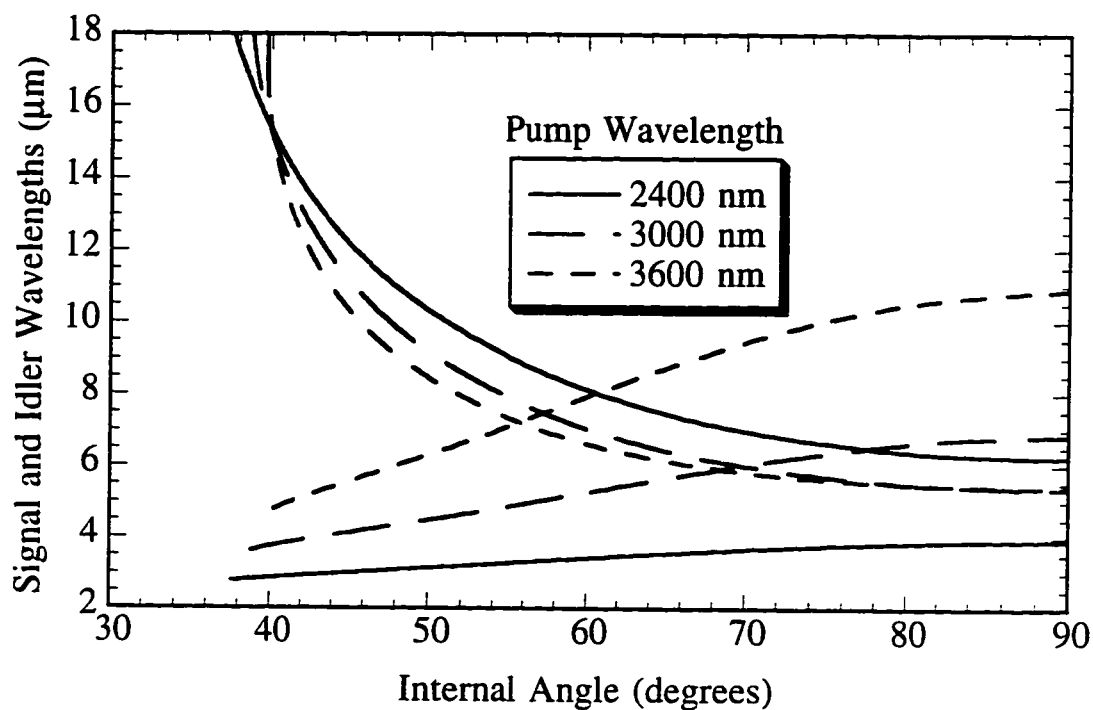


Figure 2.5 - Type-II Phasematching in CdGeAs₂ ($o \Rightarrow e+e$)

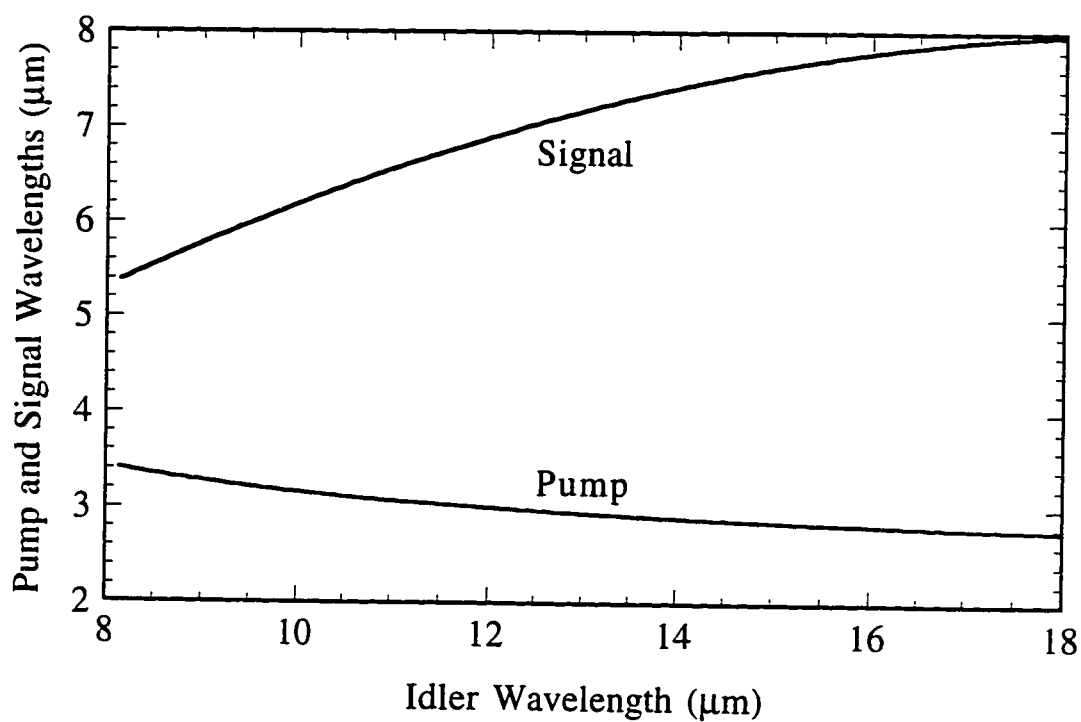


Figure 2.6 - Type-II Noncritical Phasematching in CdGeAs₂ ($o \Rightarrow e+e$)

2.6.2 Cadmium Selenide (CdSe)

Transparency: 0.75 - 20 μm [40]

Damage Threshold: 30 MW/cm² ($\tau = 300$ ns, 1.833 μm) [41]

30 MW/cm² ($\tau = 35$ ns, 2.36 μm) [40]

Nonlinear Coefficient: [37]

$$d_{oeo} = d_{15} \cdot \sin(\theta)$$

$$d_{15}(10.6 \mu\text{m}) = 18 \pm 1.8 \text{ pm/V}$$

Index of Refraction: [38]

$$n_o^2 = 4.2243 + \frac{1.768 \cdot \lambda^2}{\lambda^2 - 0.227} + \frac{3.12 \cdot \lambda^2}{\lambda^2 - 3380}$$

$$n_e^2 = 4.2009 + \frac{1.8875 \cdot \lambda^2}{\lambda^2 - 0.2171} + \frac{3.6461 \cdot \lambda^2}{\lambda^2 - 3629}$$

Other relations published: [42]

Positive uniaxial crystal: $n_o < n_e$

CdSe has been used as a nonlinear material for infrared parametric oscillators in the mid-infrared. Experimenters have generated radiation in singly resonant OPOs with various degrees of success (9.6 - 14 μm pumped by the 1.833 μm line of a Q-switched Nd:YAG [41,43], 2.8 - 3.36 μm and 7.88 to 13.7 μm pumped with a CaF₂:Dy²⁺ laser [40,44], 4.3 - 4.5 and 8.1 - 8.3 μm pumped by an HF laser [45], and between 14.1 and 16.4 μm with a grating tuned HF laser [46]). Hanna *et. al.* demonstrated downconversion of the output of a proustite OPO with CdSe that gave continuous tunability between 9.4 to 24.3 μm [47]. Andreou mixed the output of a lithium niobate OPO to yield 16 μm radiation [48] suitable for

laser isotope separation, while Dhirine et. al. generated tunable radiation from 10 to 20 μm by mixing the 1.064 μm line of a Nd:YAG laser with the output of a Nd:YAG pumped KTP OPO seeded by a doubled Nd:YAG pumped BBO OPO [49].

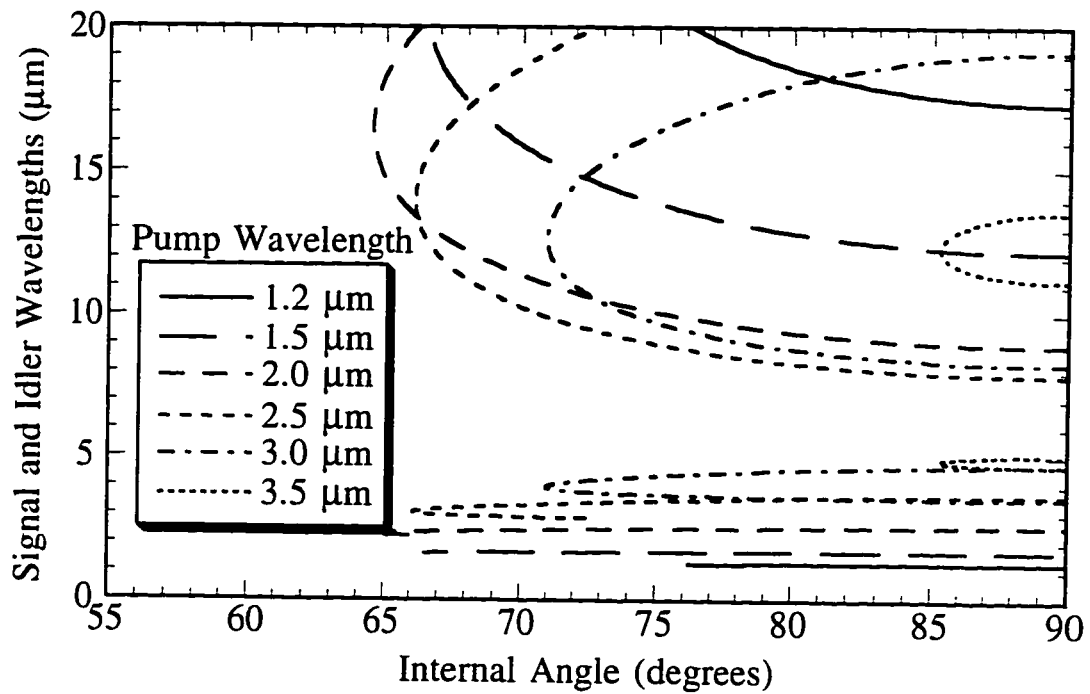


Figure 2.7 - Type-II Phasematching in CdSe ($o \Rightarrow e+o$)

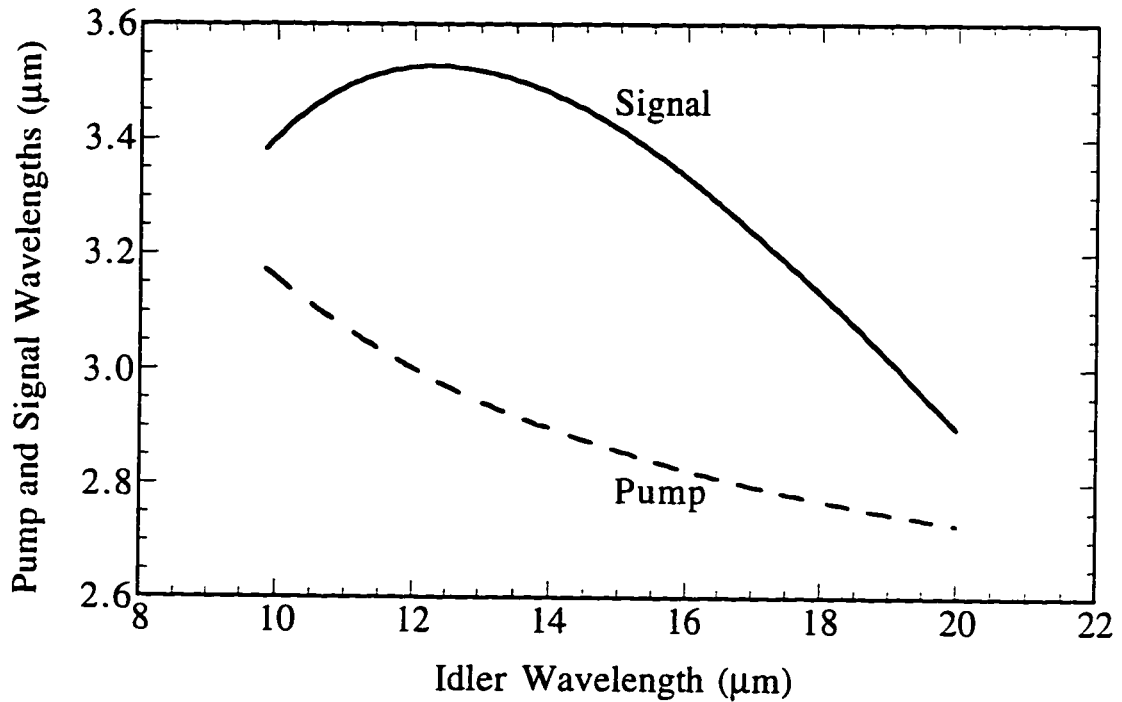


Figure 2.8 - Type-II Noncritical Phasematching in CdSe ($o \Rightarrow e+o$)

2.6.3 Cinnabar (α -HgS)

Transparency: 0.63 - 13.5 μm [50]

Damage Threshold: 40 MW/cm² ($\tau = 17$ ns, 1.064 μm) [51]

Nonlinear Coefficient: [37]

$$d_{oeo} = d_{11} \cdot \cos(\theta) \cdot \cos(3\phi) \quad [\text{Not critically phasematchable}]$$

$$d_{eeo} = d_{11} \cdot \cos^2(\theta) \cdot \sin(3\phi) \quad [\text{Not critically phasematchable}]$$

$$d_{11}(10.6 \mu\text{m}) = 50 \pm 17 \text{ pm/V}$$

Index of Refraction:[38]

$$n_o^2 = 4.1506 + \frac{2.7896 \cdot \lambda^2}{\lambda^2 - 0.1328} + \frac{1.1378 \cdot \lambda^2}{\lambda^2 - 705}$$

$$n_e^2 = 4.0101 + \frac{4.3736 \cdot \lambda^2}{\lambda^2 - 0.1284} + \frac{1.5604 \cdot \lambda^2}{\lambda^2 - 705}$$

Other index equations: [50,52,53]

Positive uniaxial crystal: $n_o < n_e$

There have been no experiments to date using α -HgS in the downconversion of light, but there is no fundamental reason it couldn't be done. The pump and signal wavelengths are easily attainable and would allow generation of wavelengths between 2 and 13.5 μm , though with the phasematching angles required for phasematching, double refraction effects would dominate the conversion process near the long wavelength absorption edge (the internal angles can be as small as 20 degrees). Boyd *et. al.* demonstrated it was possible to use α -HgS in the upconversion of 10.6 μm radiation to visible wavelengths utilizing a CO₂ and a HeNe laser through sum frequency generation and the reverse process of down-conversion in difference frequency generation would rather easily follow [54].

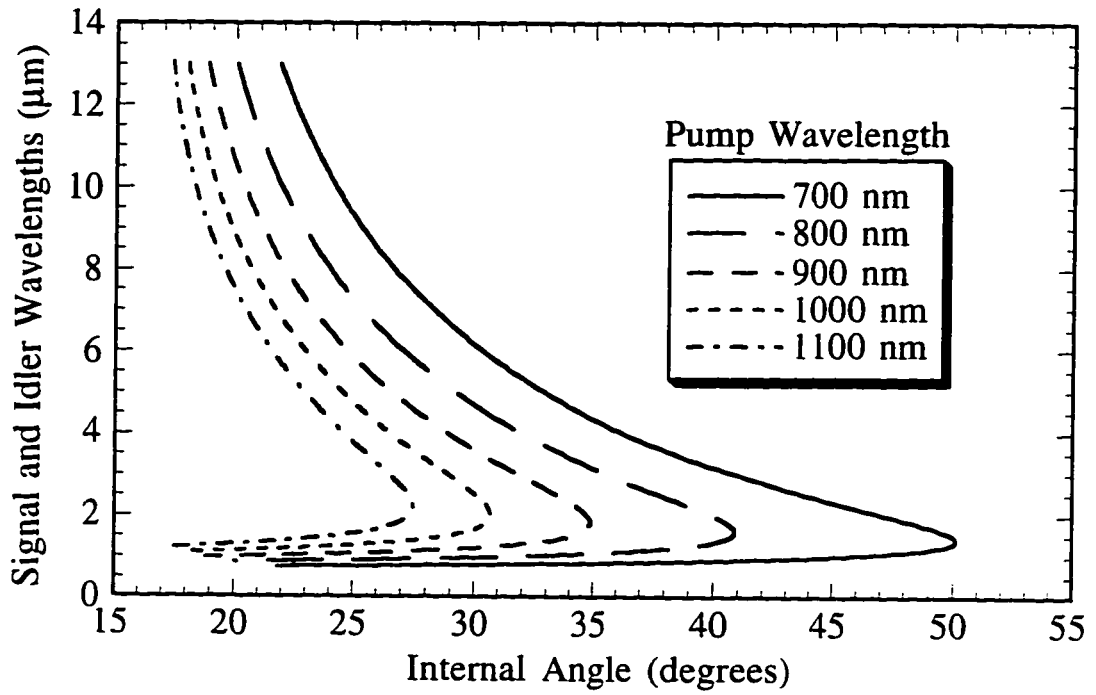


Figure 2.9 - Type-I Phasematching in α -HgS ($o \Rightarrow e+e$)

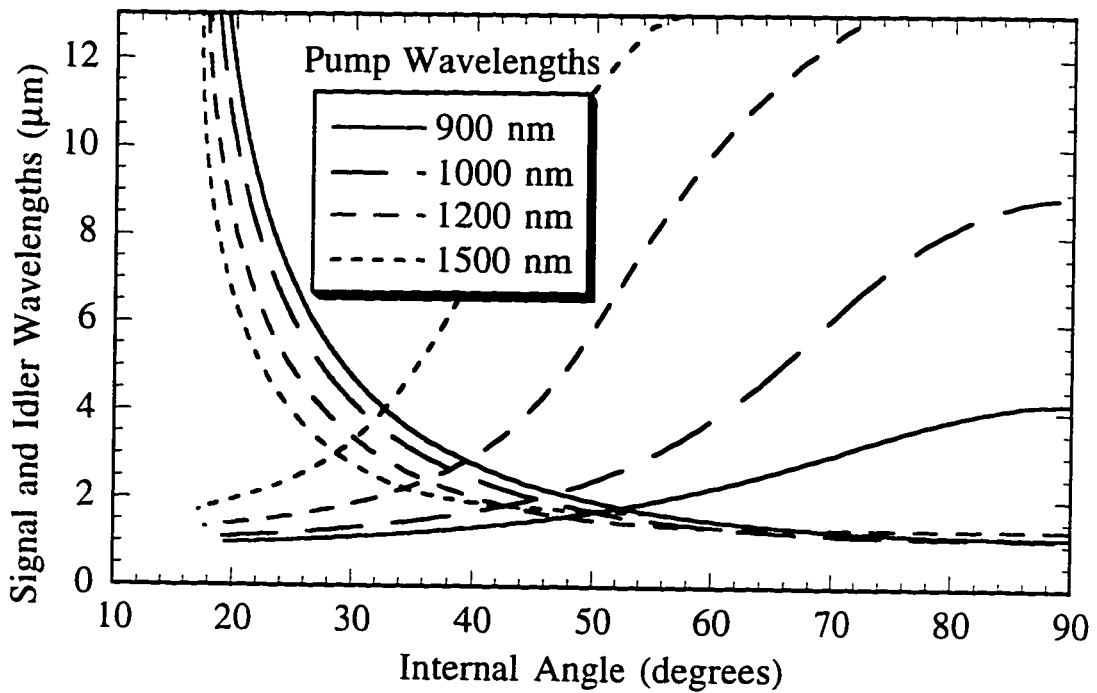


Figure 2.10 - Type-II Phasematching in α -HgS ($o \Rightarrow e+o$)

2.6.4 Gallium Selenide (GaSe)

Transparency: 0.65 - 18 μm [55]

Damage Threshold: 20 MW/cm^2 ($\tau = 25$ ns, 0.694 μm) [56]

35 MW/cm^2 ($\tau = 10$ ns, 1.064 μm) [57]

Nonlinear Coefficient:

$$d_{\text{ooe}} = d_{22} \cdot \cos(\theta) \cdot \sin(3\phi) \quad [\text{Not critically phasematchable}]$$

$$d_{\text{eoe}} = d_{22} \cdot \cos^2(2\theta) \cdot \cos(3\phi)$$

$$d_{22}(10.6 \mu\text{m}) = 54.4 \pm 10.9 \text{ pm/V} [55]$$

Index of Refraction: [38]

$$n_o^2 = -\frac{0.06}{\lambda^4} + \frac{0.526}{\lambda^2} + 8038 - 8.2 \cdot 10^{-4} \cdot \lambda^2 - 2.7 \cdot 10^{-6} \cdot \lambda^4$$

$$n_e^2 = 6.06 + \frac{0.5754}{\lambda^2 - 0.04353} - 1.04 \cdot 10^{-3} \cdot \lambda^2$$

Other index equations: [58-61]

Negative uniaxial crystal: $n_o > n_e$

There have been a number of experiments involving the successful downconversion to the mid-infrared involving GaSe. A discussion of these experiments will be deferred until Chapter 5.

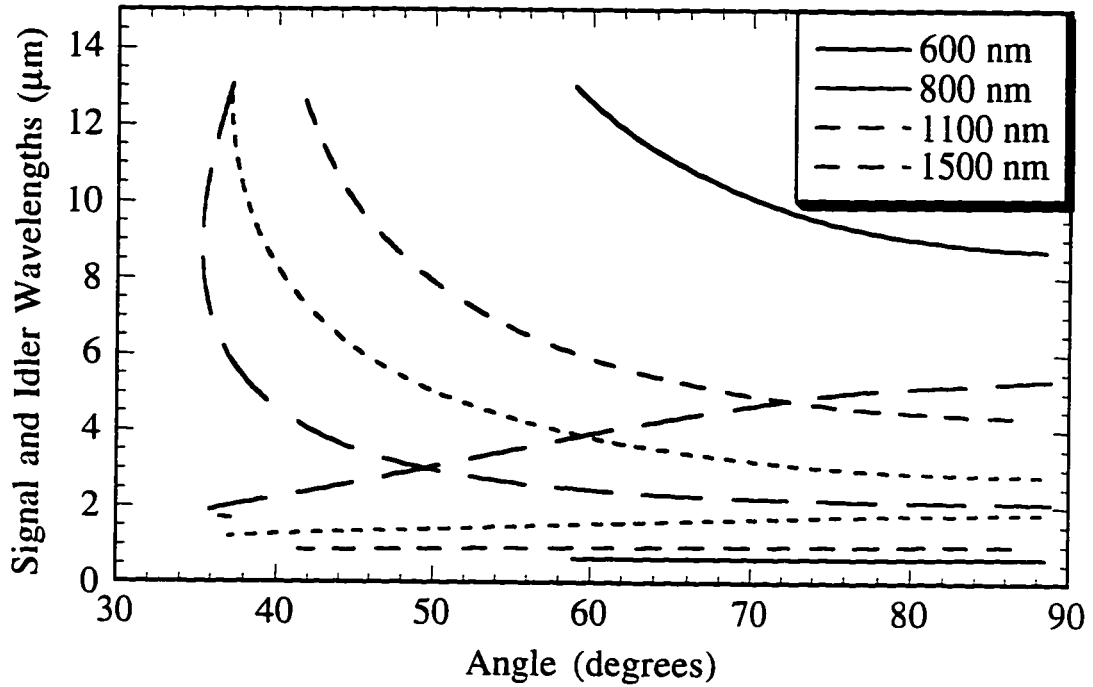


Figure 2.11 - Type-I Phasematching in GaSe ($e \Rightarrow o+o$). The pump wavelengths are presented in the legend.

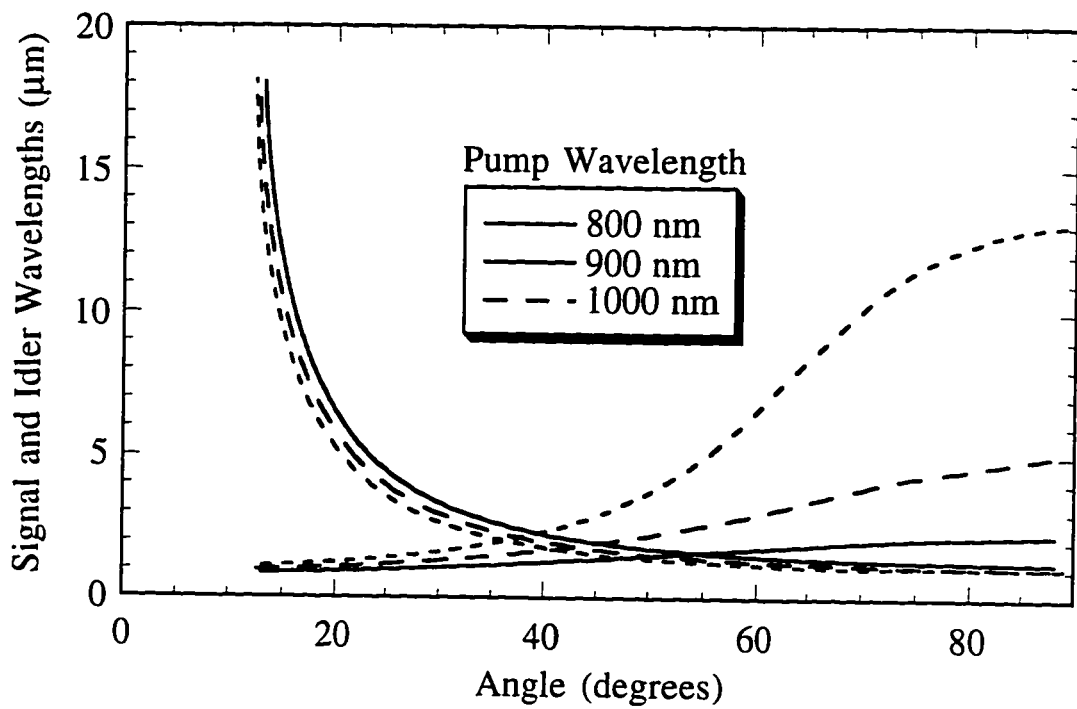


Figure 2.12 - Type-II Phasematching in GaSe ($e \Rightarrow o+e$)

2.6.5 Indium Antimonide (InSb)

Though data on the physical characteristics of InSb is available, it can be considered almost unusable in most frequency mixing experiments because the transparency of the material is typically 0.5% / cm.

Comparatively few experimental results have been published regarding the difference frequency generation in indium antimonide. Marginally transparent from 8 to 25 μm and with an effective nonlinear coefficient of approximately 500 pm/V [62], indium antimonide is potentially a viable far infrared DFG source but difficult to use because of a dearth of pump sources beyond 8 μm . Using the 946 and 1047 cm^{-1} lines of a CO_2 laser, idler frequencies near 100 cm^{-1} have been generated [63,64].

2.6.6 Lithium Iodate (LiIO_3)

Transparency: 0.3 - 6.0 μm [65]

Damage Threshold: 45 MW/cm^2 ($\tau = 15$ ps, 532 nm) [66,67]

>60 MW/cm^2 ($\tau = 20$ ps, 1.064 μm) [68]

<130 MW/cm^2 (τ unknown, 694 nm) [69]

Nonlinear Coefficient:

$$d_{\text{ooe}} = d_{15} \cdot \sin(\theta)$$

$$d_{15} (1.06 \mu\text{m}) = 5.53 \pm 0.3 \text{ pm/V} [20]$$

$$d_{15} (514.5 \text{ nm}) = 7.31 \pm 0.62 \text{ pm/V} [70]$$

Index of Refraction:[71]

$$n_o^2 = 9.220 + \frac{0.4454}{\lambda^2 - 0.1264} - \frac{1733}{1000 - \lambda^2}$$

$$n_e^2 = 7.007 + \frac{0.3230}{\lambda^2 - 0.1192} - \frac{660}{1000 - \lambda^2}$$

Negative uniaxial crystal: $n_o > n_e$

Lithium Iodate has been widely used as a nonlinear mixing crystal. Usually mentioned in conjunction with lithium niobate, it shares most of the properties of this crystal with a greater transmission range and similar d_{eff} value [72]. The index of refraction of this material does not allow noncritical phasematching and the internal angles of critical phasematching tend to be rather extreme (typically 20 - 45 degrees as seen in Figure 2.13).

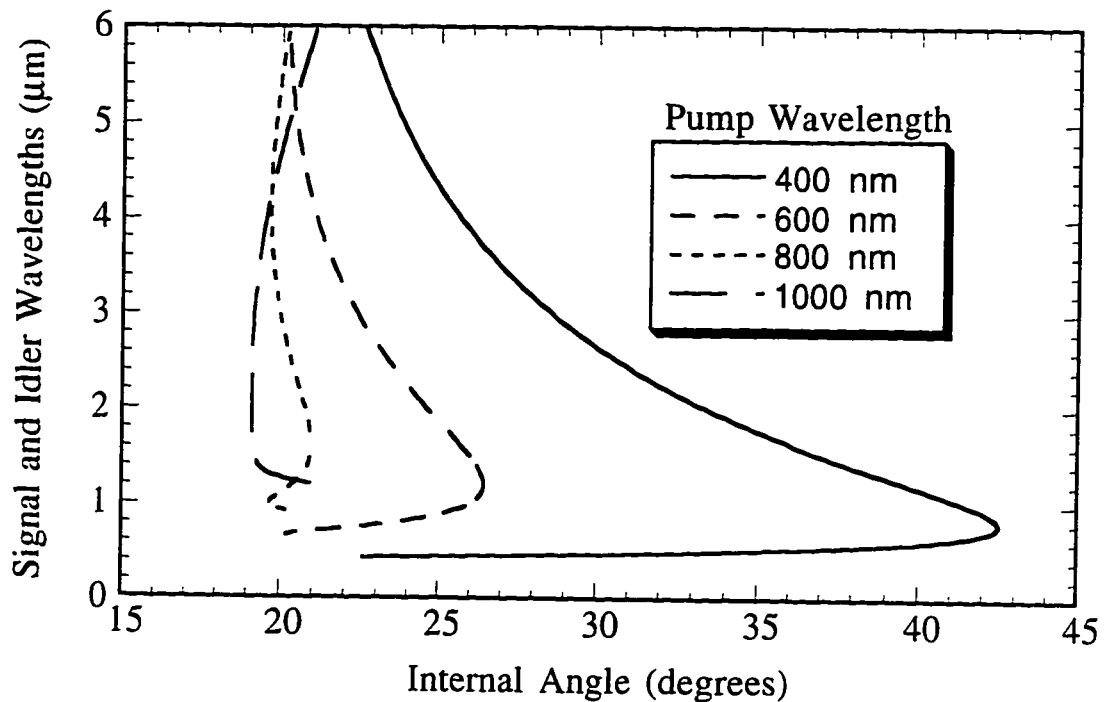


Figure 2.13 - Type-I Phasematching in LiIO_3 ($e \Rightarrow o+o$)

2.6.7 Lithium Niobate (LiNbO₃)

Transparency: 0.4 - 5.0 μm [73]

Damage Threshold: 50 MW/cm² [66]

>1 MW/cm² [74]

Nonlinear Coefficient:

$$d_{\text{ooe}} = d_{15} \cdot \sin(\theta) - d_{22} \cdot \cos(\theta) \cdot \sin(3\phi)$$

$$d_{\text{eoe}} = d_{22} \cdot \cos^2(\theta) \cdot \cos(3\phi) \quad [\text{Not critically phasematchable}]$$

$$d_{15} (514.5 \text{ nm}) = 5.82 \pm 0.70 \text{ pm/V} [70]$$

$$d_{15} (1.064 \text{ } \mu\text{m}) = 5.44 \pm 0.29 \text{ pm/V} [72]$$

$$d_{22} (1.064 \text{ } \mu\text{m}) = 2.8 \pm 0.2 \text{ pm/V} [72]$$

$$d_{33} (1.064 \text{ } \mu\text{m}) = 27 \text{ pm/V} [33]$$

Index of Refraction: [75]

$$n_o^2 = 4.9048 + \frac{0.11775 + 2.2314 \cdot 10^{-8} \cdot F(T)}{\lambda^2 - (0.21802 - 2.9671 \cdot 10^{-8} \cdot F(T))^2 + 2.1429 \cdot 10^{-8} \cdot F(T) - 0.027153 \cdot \lambda^2}$$

$$n_e^2 = 4.5820 + \frac{0.09921 + 5.2716 \cdot 10^{-8} \cdot F(T)}{\lambda^2 - (0.21090 - 4.9143 \cdot 10^{-8} \cdot F(T))^2 + 2.2971 \cdot 10^{-8} \cdot F(T) - 0.021940 \cdot \lambda^2}$$

where $F(T) = (T - 24.5) \cdot (T + 570.5)$
and T is the temperature of the crystal in °C

other relations published: [71,76-79]

Negative uniaxial crystal: $n_o > n_e$

Perhaps the most widely used crystal for achieving mid-infrared wavelengths from difference frequency generation, its transparency range,

high damage threshold, and excellent optical quality with large dimensions make it a natural choice for frequency mixing. Though it can be noncritically phasematched using two tunable input lasers, the classical method of phasematching in this crystal is to use temperature tuning to phasematch two arbitrary wavelengths - usually the output of a single frequency argon ion laser and a dye / Titanium:sapphire laser.

Visible light incident upon LiNbO_3 crystals changes the index of refraction in an effect called photorefraction. Stimulated parametric interactions (such as difference frequency generation) are particularly sensitive to changes in the index of refraction and the effect is highly detrimental in these processes. Photorefractive effects are annealed out at temperatures above 170°C [80], usually setting the lower temperature limit for phasematching of the bulk crystal.

Because of these effects, the type-I and type-II critical phasematching curves are not presented here. Instead, we simply present a type-I temperature tuned noncritical phasematching curve (Figure 2.14). The first DFG spectroscopic source developed by Alan Pine was based on LiNbO_3 [81]. Since that early experiment, numerous groups have used spectrometers based on lithium niobate as practical instruments. Recent improvements in fabrication of the crystal have allowed the development of quasi-phasematching in the crystal (Section 2.5.4) as well as quasi-phasematched waveguides [82]. For infrared wavelengths shorter than $4\text{ }\mu\text{m}$, it is probably the easiest material to work with and is preferred over all other crystals.

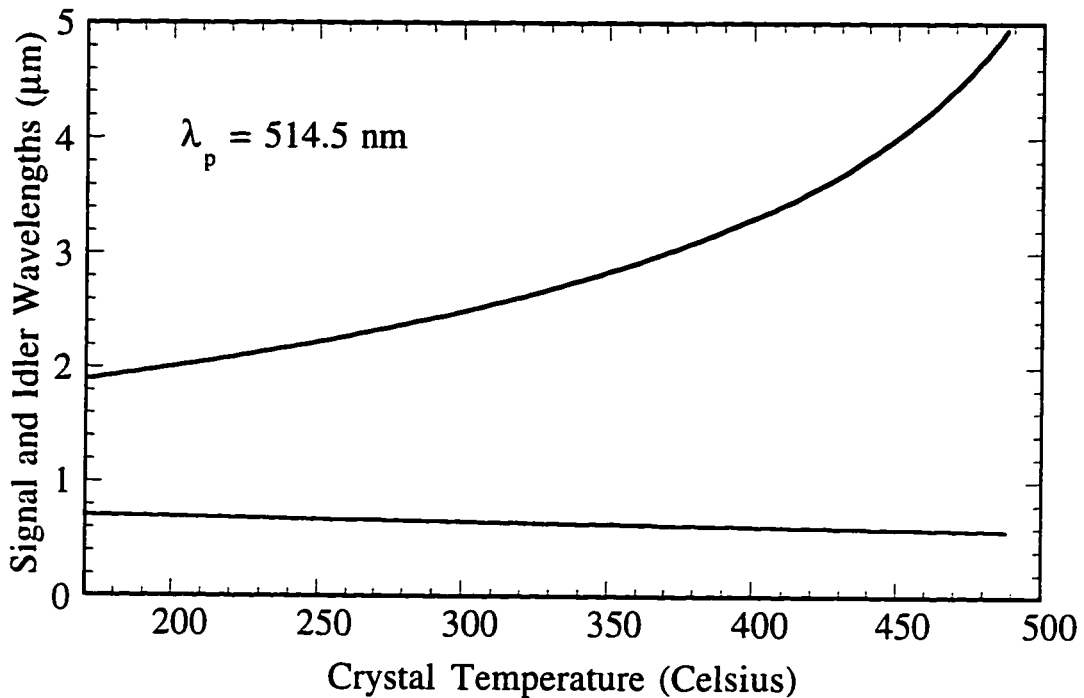


Figure 2.14 - Type-I Temperature Dependent Noncritical Phasematching in LiNbO₃ (e \Rightarrow o+o). The pump wavelength has been fixed to 514.5 nm, the strongest line of the argon ion laser.

2.6.8 Mercury Thiogallate (HgGa₂S₄)

Transparency: 0.5 - 13 μm [83]

Damage Threshold: 60-90 MW/cm² (τ = 10 ns, 1.064 μm) [84]

Nonlinear Coefficient:

$$d_{ooe} = d_{31} \cdot \sin(\theta) \cdot \cos(2\phi) - d_{36} \cdot \sin(\theta) \cdot \sin(2\phi)$$

$$d_{eoe} = (d_{31}^2 + d_{36}^2) \cdot \sin^2(2\theta) \quad [\text{Not critically phasematchable}]$$

Orange Phase [85]

$$d_{31}(1.064 \mu\text{m}) = 65 \pm 10 \text{ pm/V}$$

$$d_{36}(1.064 \mu\text{m}) = 21.9 \pm 3.3 \text{ pm/V}$$

Yellow Phase

Unknown

Index of Refraction:

Orange Phase [86]

$$n_o^2 = 6.20815221 - \frac{63.70629851}{\lambda^2 - 225.00000000} - \frac{0.23698804}{0.09568646 - \lambda^2}$$

$$n_e^2 = 6.00902670 - \frac{63.28065920}{\lambda^2 - 225.00000000} - \frac{0.21489656}{0.09214633 - \lambda^2}$$

Yellow Phase [84]

$$n_o^2 = 9.804044 - \frac{5702.08}{\lambda^2 - 1500} - \frac{0.246244}{0.092169 - \lambda^2}$$

$$n_e^2 = 9.518129 - \frac{5797.5}{\lambda^2 - 1500} - \frac{0.225103}{0.0852637 - \lambda^2}$$

Negative uniaxial crystal: $n_o > n_e$

Mercury thiogallate can be produced in two phases. One is yellow in color and is deficient in HgS while the other is orange and is rich in HgS in comparison to the stoichiometric ratios [83]. Phasematching curves have been calculated for both phases (Figures 2.15 through 2.18) and indicate that noncritical type-I phasematching is possible for the 3-5 μm region with dye/titanium:sapphire lasers. Though the noncritical phasematching wavelength range is comparable with that of lithium niobate and considerably less than that of silver thiogallate, the conversion efficiency

per crystal length should be higher than either due to its higher effective nonlinear coefficients.

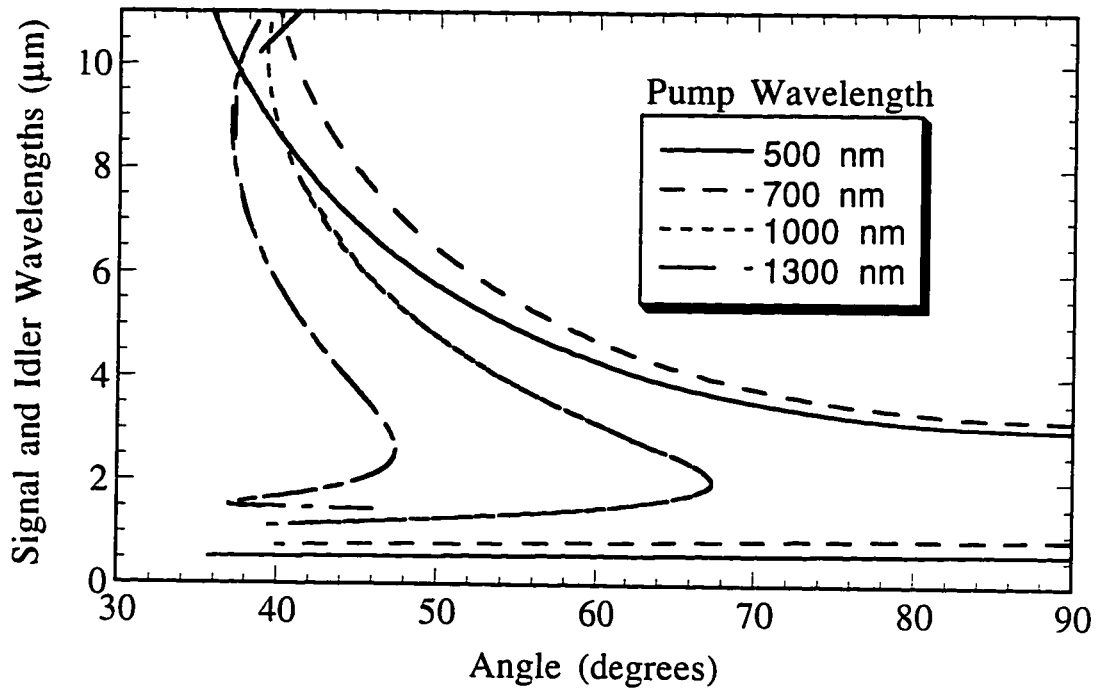


Figure 2.15 - Type-I Phasematching in the Orange Phase of HgGa₂S₄ (e⇒o+o)

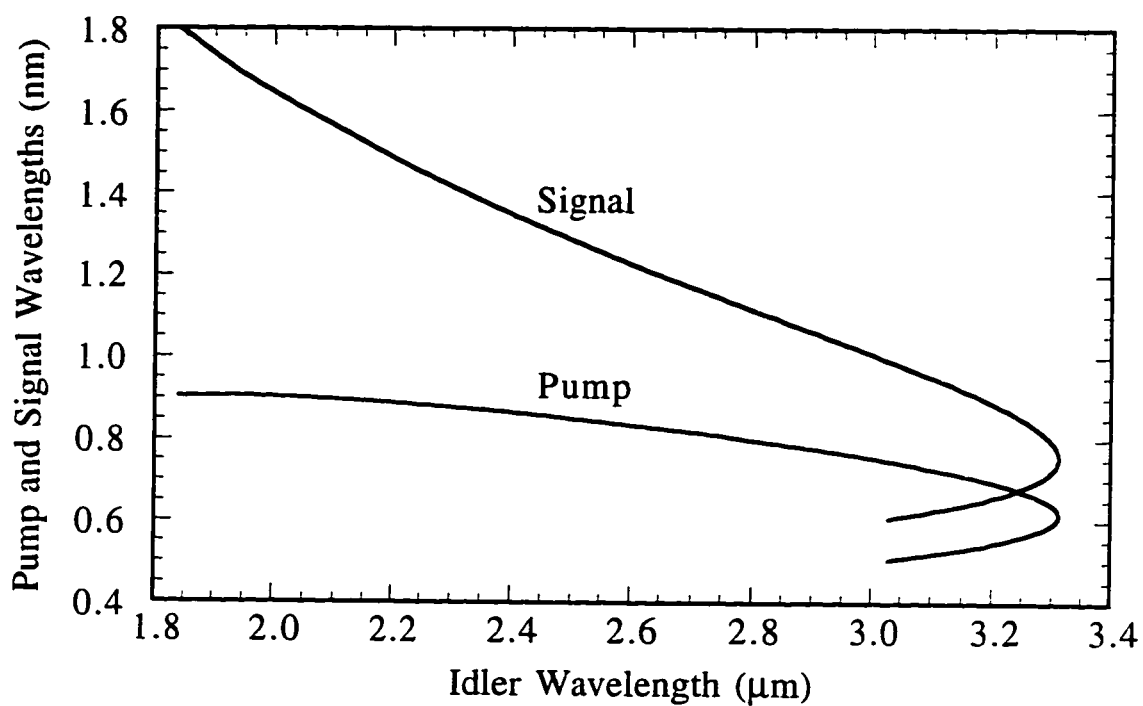


Figure 2.16 - Type-I Noncritical Phasematching in the Orange Phase of HgGa_2S_4 ($e \Rightarrow o+o$)

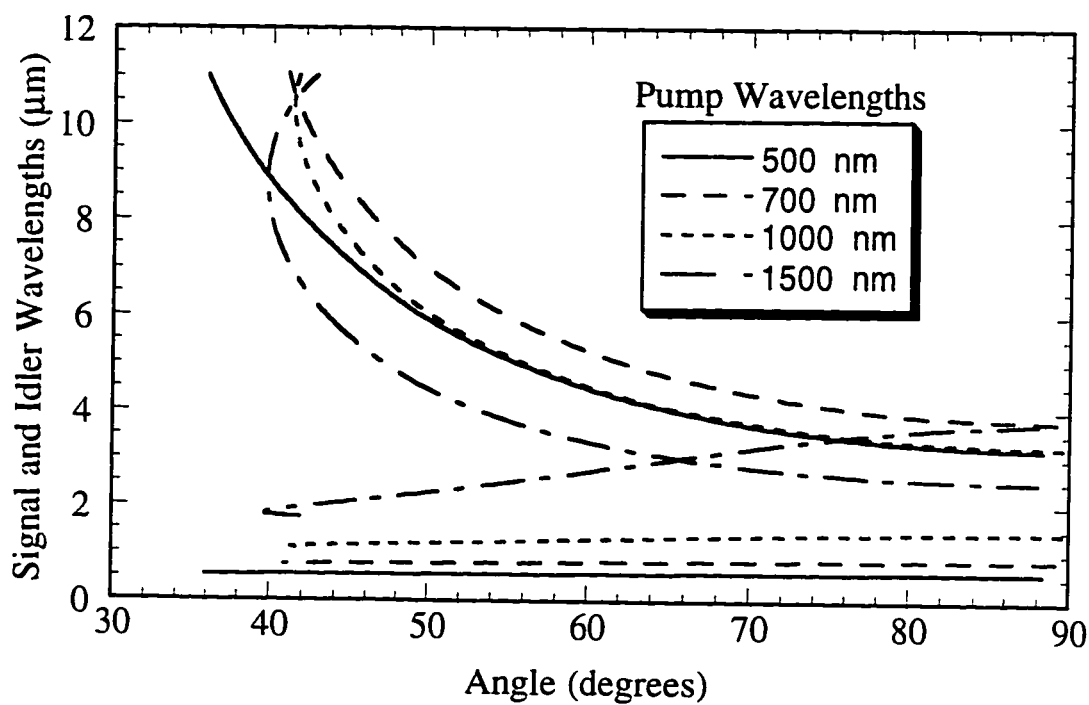


Figure 2.17 - Type-II Phasematching in the Orange Phase of HgGa_2S_4 ($e \Rightarrow o+e$)

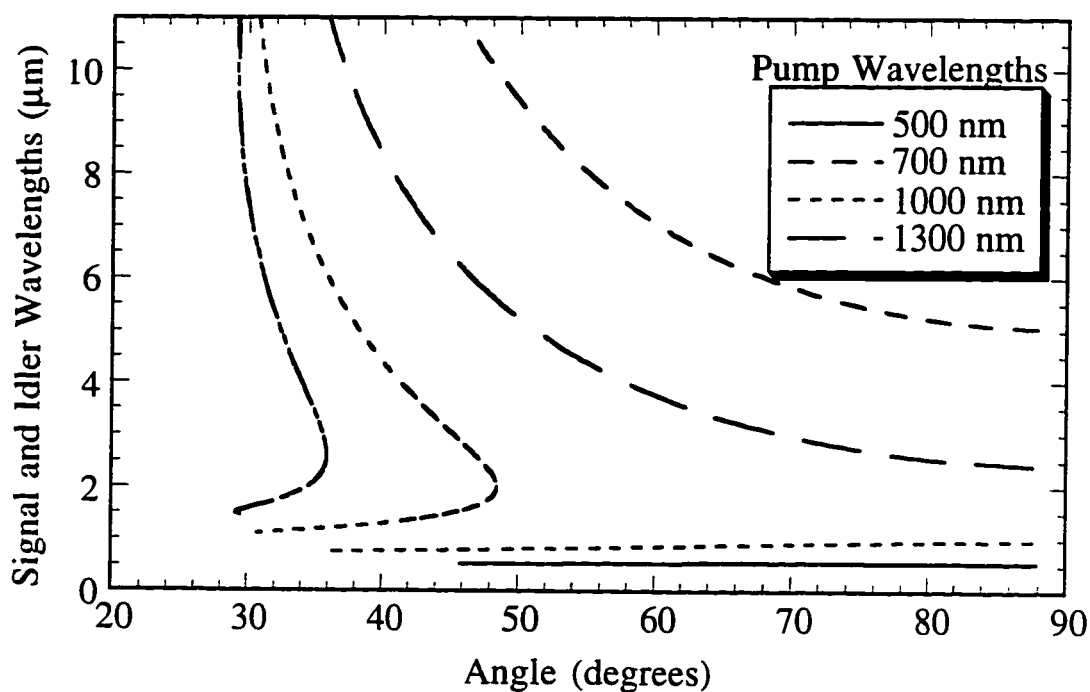


Figure 2.18 - Type-I Phasematching in the Yellow Phase of HgGa_2S_4 ($e \Rightarrow o+o$)

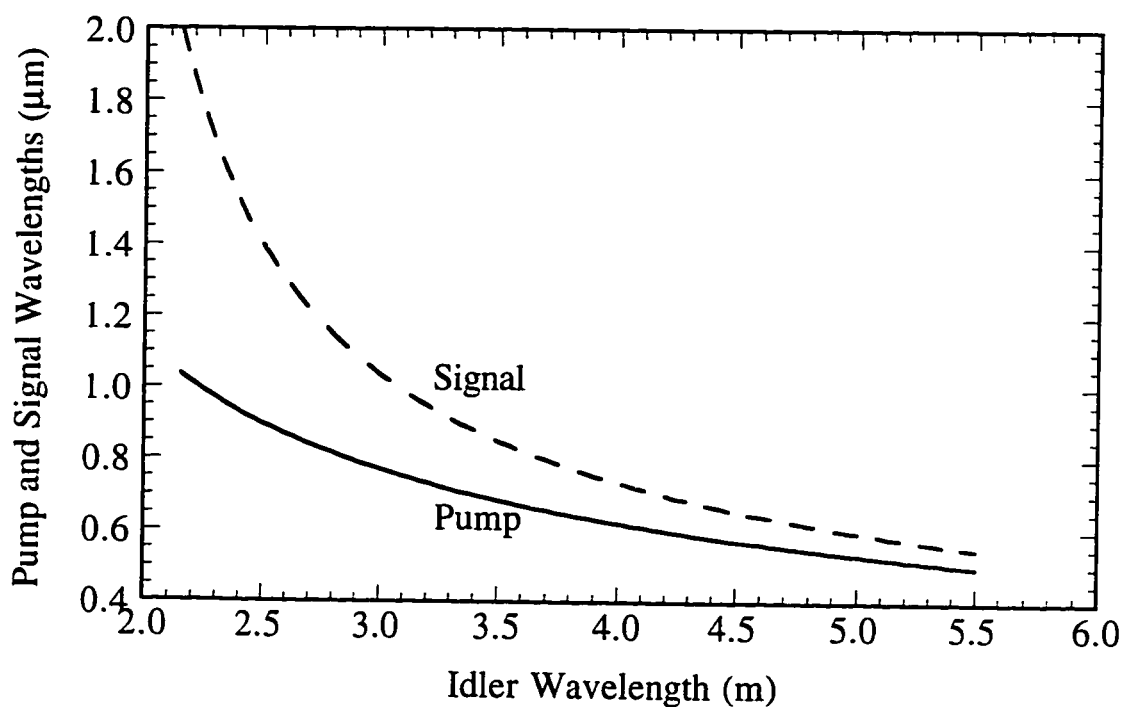


Figure 2.19 - Type-I Noncritical Phasematching in the Yellow Phase of HgGa_2S_4 ($e \Rightarrow o+o$)

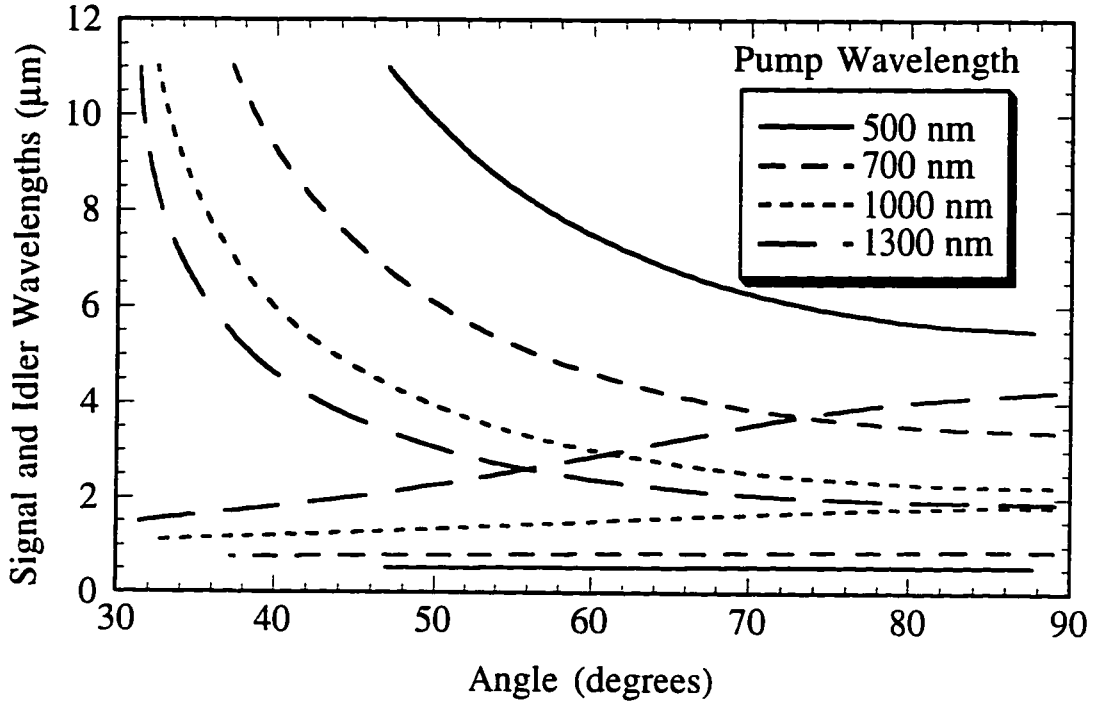


Figure 2.20 - Type-II Phasematching in the Yellow Phase of HgGa_2S_4 ($e \Rightarrow o+o$)

2.6.9 Proustite (Ag_3AsS_3)

Transparency: 0.6 - 13 μm [87,88]

Damage Threshold: 20 MW/cm^2 [51]

Nonlinear Coefficient: [72,89]

$$d_{ooe} = d_{15} \cdot \sin(\theta) - d_{22} \cdot \cos(\theta) \cdot \sin(3\phi)$$

$$d_{eoe} = d_{22} \cdot \cos^2(\theta) \cdot \cos(3\phi) \quad [\text{Not critically phasematchable}]$$

$$d_{15} (10.6 \mu\text{m}) = 11 \pm 2 \text{ pm/V}$$

$$d_{22} (10.6 \mu\text{m}) = 18 \pm 2 \text{ pm/V}$$

Index of Refraction: [90,91]

$$n_o^2 = 9.220 + \frac{0.4454}{\lambda^2 - 0.1264} - \frac{1733}{1000 - \lambda^2}$$

$$n_e^2 = 7.007 + \frac{0.3230}{\lambda^2 - 0.1192} - \frac{660}{1000 - \lambda^2}$$

Negative uniaxial crystal: $n_o > n_e$

Similar in many respects to AgGaS₂, proustite is a negative uniaxial crystal with good birefringence and an adequate transparency range for many mixing combinations. It has been used in pulsed mid-infrared DFG processes [92-94] to generate light tunable from 3.2 to 23 μm , though realistically the crystal probably absorbs too much light to efficiently generate infrared light past the 10 μm absorption edge in cw operation. Based on the index of refraction data of Hobden [90], the material can be noncritically phasematched within the stated transparency range (see Figures 2.21 - 2.23), but is commercially unavailable at the present time.

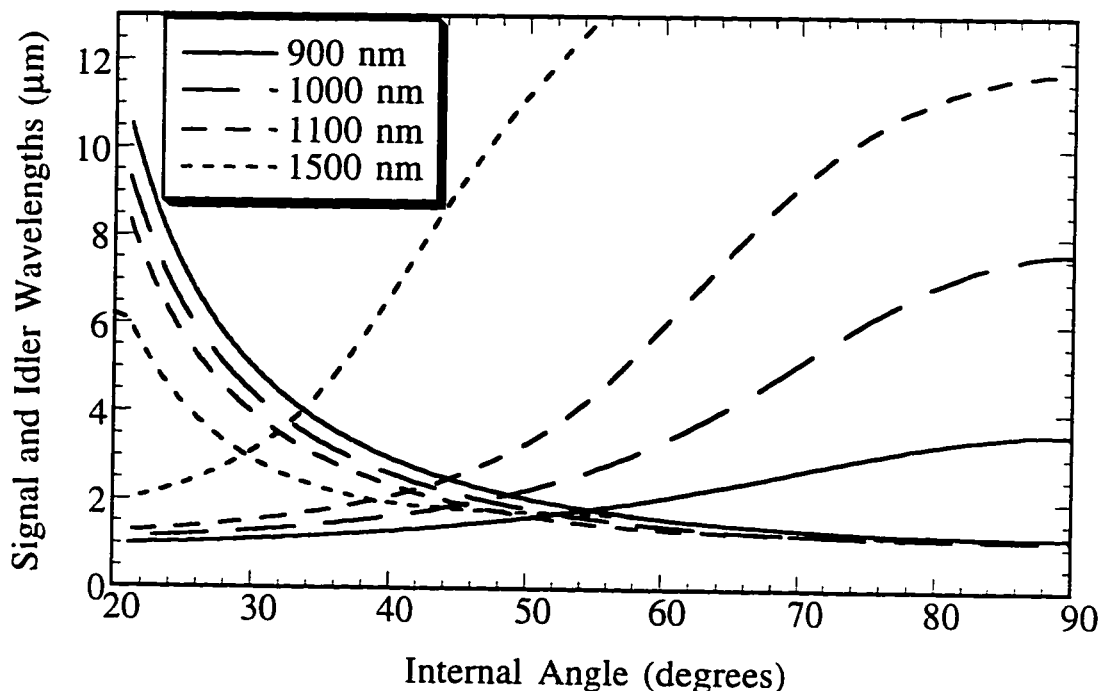


Figure 2.21 - Type-I Phasematching in Ag₃AsS₃ (e⇒o+o). The pump wavelength is held fixed at the wavelength given in the legend.

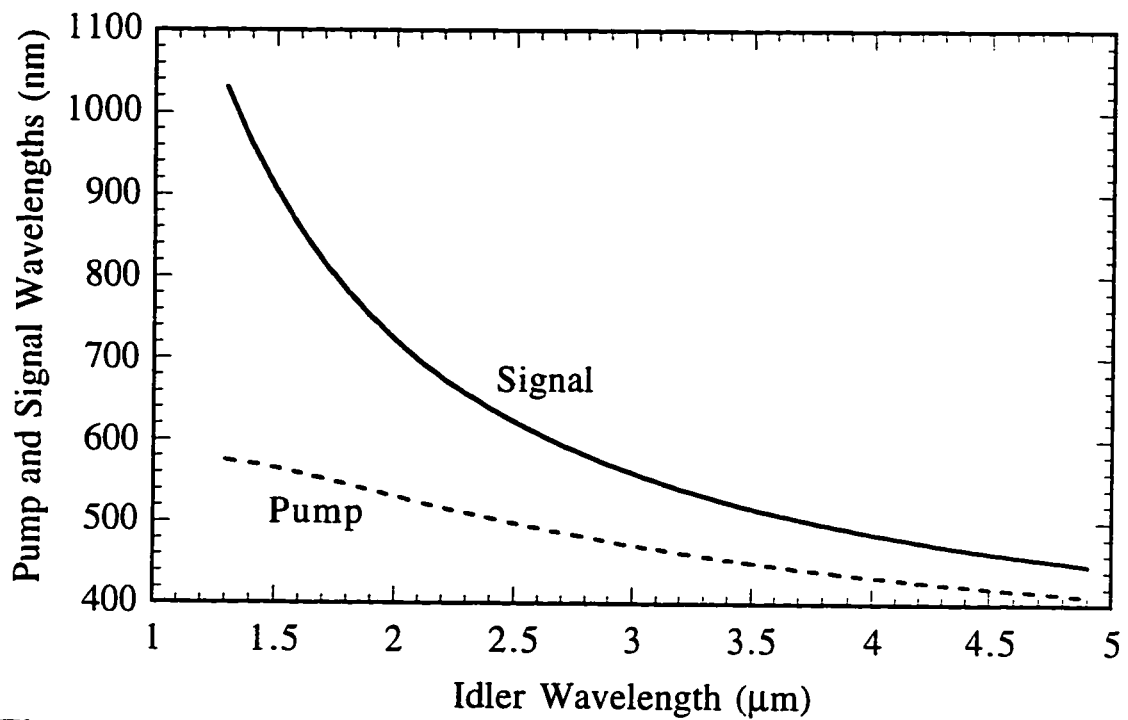


Figure 2.22 - Type-I Noncritical Phasematching in Ag_3AsS_3 ($e \Rightarrow o+o$).

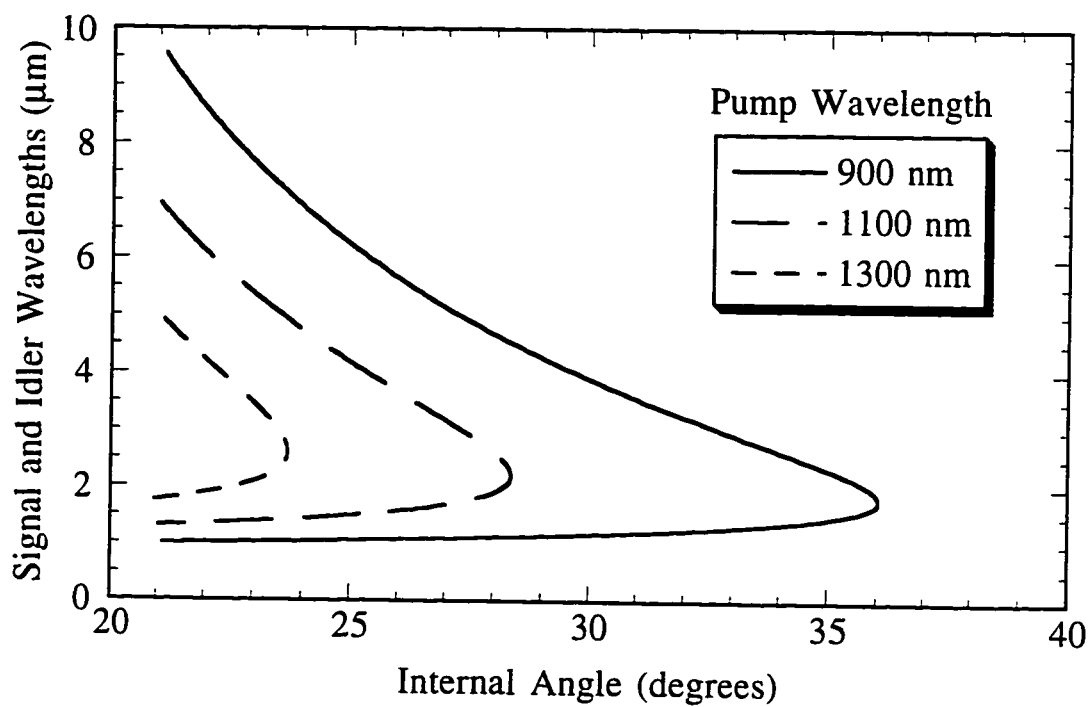


Figure 2.23 - Type-I Phasematching in Ag_3AsS_3 ($e \Rightarrow o+o$).

2.6.10 Pyrargyrite (Ag_3SbS_3)

Transparency: 2.4 - 18 μm [95,96]

Damage Threshold [51]: 20 MW/cm^2 ($\tau = 17.5$ ns, 1.06 μm)

50 MW/cm^2 ($\tau = 200$ ns, 10.6 μm)

Nonlinear Coefficient:

$$d_{\text{ooe}} = d_{15} \cdot \sin(\theta) - d_{22} \cdot \cos(\theta) \cdot \sin(3\phi)$$

$$d_{\text{eoe}} = d_{22} \cdot \cos^2(\theta) \cdot \cos(3\phi) \quad [\text{Not critically phasematchable}]$$

$$d_{36}(10.6 \mu\text{m}) = 8.4 \pm 2.8 \text{ pm/V} [97]$$

$$d_{36}(10.6 \mu\text{m}) = 9.2 \pm 3.0 \text{ pm/V} [98]$$

Index of Refraction:[95]

$$n_o^2 = 3.6280 + \frac{2.1686 \cdot \lambda^2}{\lambda^2 - 0.1003} + \frac{2.1753 \cdot \lambda^2}{\lambda^2 - 950}$$

$$n_e^2 = 4.0172 + \frac{1.5274 \cdot \lambda^2}{\lambda^2 - 0.1310} + \frac{2.1699 \cdot \lambda^2}{\lambda^2 - 950}$$

Negative uniaxial crystal: $n_o > n_e$

No literature mention of difference frequency generation in pyrargyrite was found - probably because of the extreme angles required for phasematching (Figures 2.24 and 2.25).

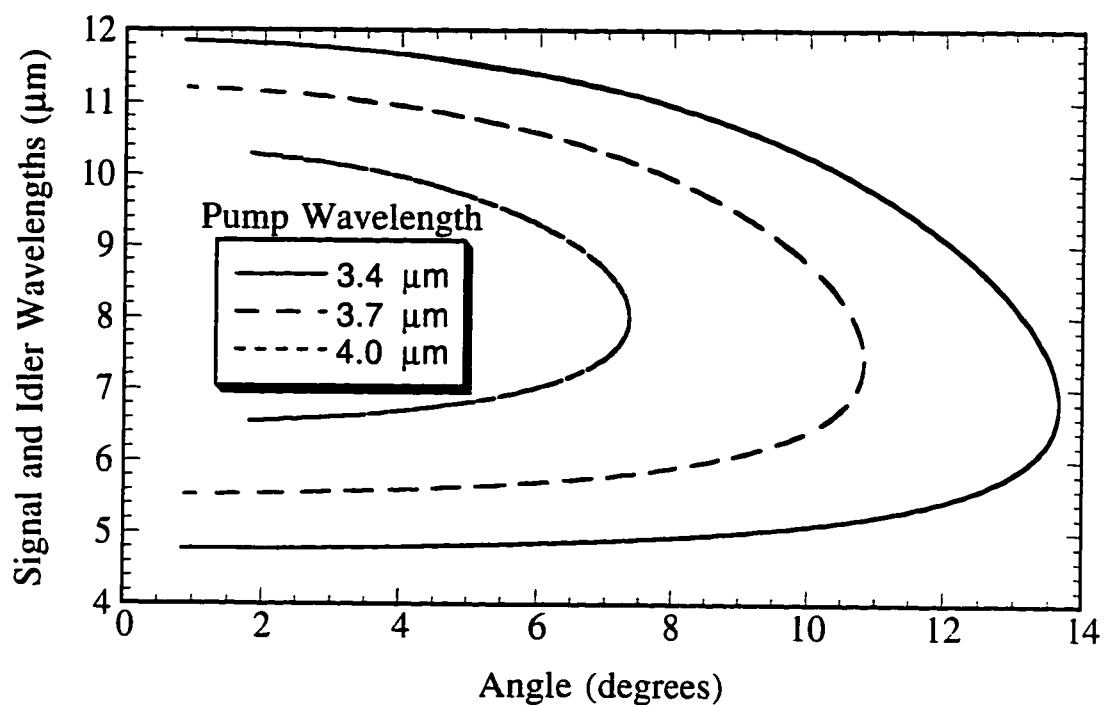


Figure 2.24 - Type-I Phasematching in Ag_3SbS_3 ($e \Rightarrow o+o$)

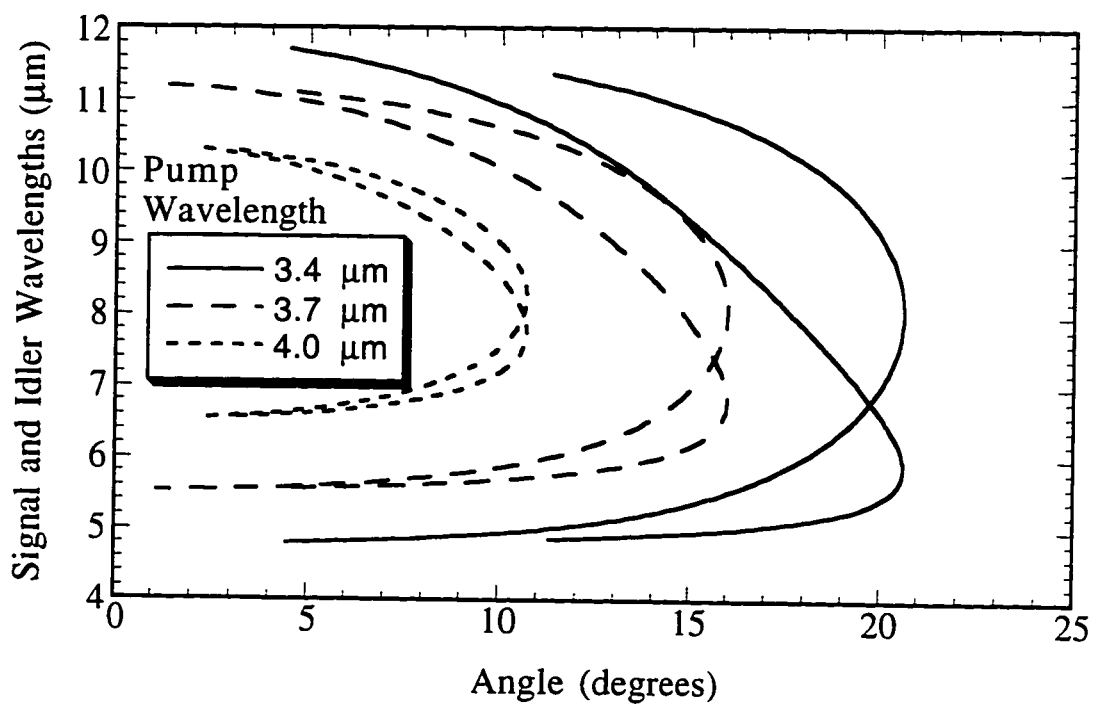


Figure 2.25 - Type-II Phasematching in Ag_3SbS_3 ($e \Rightarrow o+e$)

2.6.11 Silver Gallium Selenide (AgGaSe₂)

Transparency: 0.71 μm to 18 μm [99]

Damage Threshold: 10-20 MW/cm² [100]

Nonlinear Coefficient: [72]

$$d_{\text{ooe}} = d_{36} \cdot \sin(\theta) \cdot \sin(2\phi)$$

$$d_{\text{eoe}} = d_{36} \cdot \sin(2\theta) \cdot \cos(2\phi) \quad [\text{Not critically phasematchable}]$$

$$d_{36}(10.6 \mu\text{m}) = 33 \pm 3 \text{ pm/V}$$

Index of Refraction: [38]

$$n_o^2 = 4.6453 + \frac{2.2057 \cdot \lambda^2}{\lambda^2 - 0.1879} + \frac{1.8377 \cdot \lambda^2}{\lambda^2 - 1600}$$

$$n_e^2 = 5.2912 + \frac{1.3970 \cdot \lambda^2}{\lambda^2 - 0.2845} + \frac{1.9282 \cdot \lambda^2}{\lambda^2 - 1600}$$

Negative uniaxial crystal: $n_o > n_e$

The ternary chalcopyrite AgGaSe₂ exhibits a wide transparency range from 0.71 μm to 18 μm [99]. Available in large dimensions and with good optical quality [101], its physical characteristics make it a very attractive source for difference frequency generation. Unfortunately, noncritical phasematching in this material necessitates the use of pump wavelengths greater than 1000 nm [102].

Many groups have successfully used the AgGaSe₂ crystal to generate infrared radiation. A number of Optical Parametric Oscillators have been built in recent years, tunable from 2.65 to 9.02 μm [103,104] and 2.49 - 12.05 μm . Komine *et. al.* have used noncritical phasematching in

AgGaSe₂ to generate tunable light from 8 to 13 μm [105]. Recently, a spectrometer has been built utilizing an Er/Yb codoped fiber laser at 1.554 μm and the 1.319 μm line of a Nd:YAG laser to generate infrared radiation at 8.7 μm [106]. With an internal phasematching angle of 65° with respect to the optic axis, an effective crystal length of 2.5 mm generated a maximum power of 100 nW. At present time, however, none of these spectrometers are suitable for high-resolution spectroscopy of transient species.

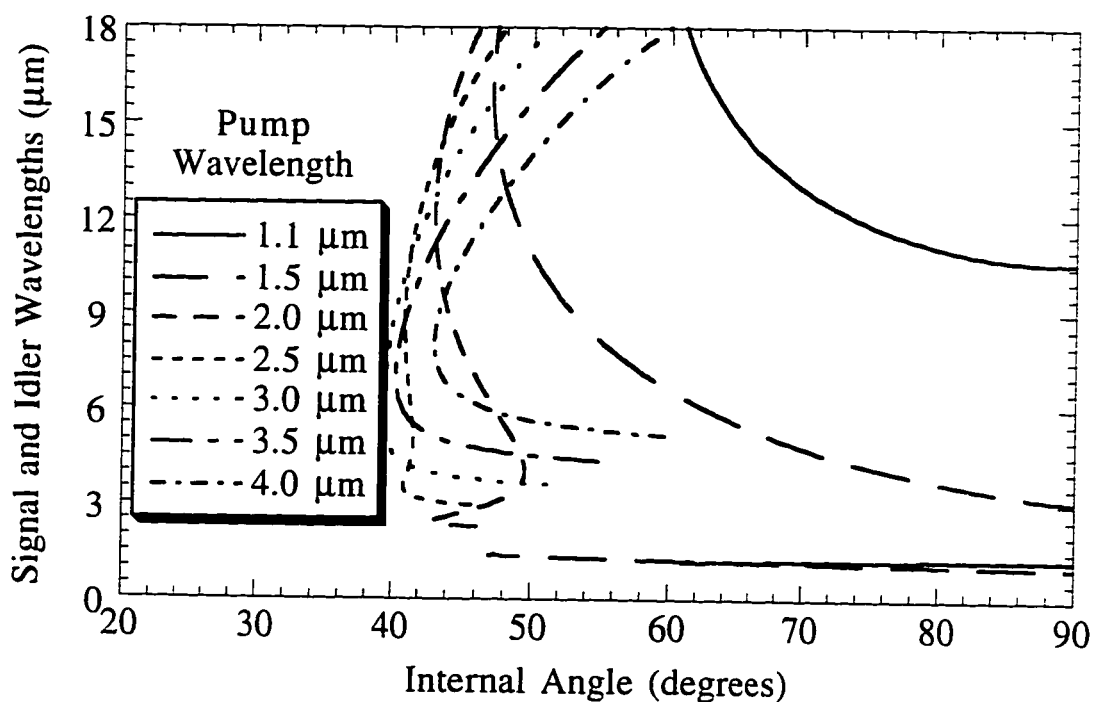


Figure 2.26 - Type-I Phasematching in AgGaSe₂ (e \Rightarrow o+o)

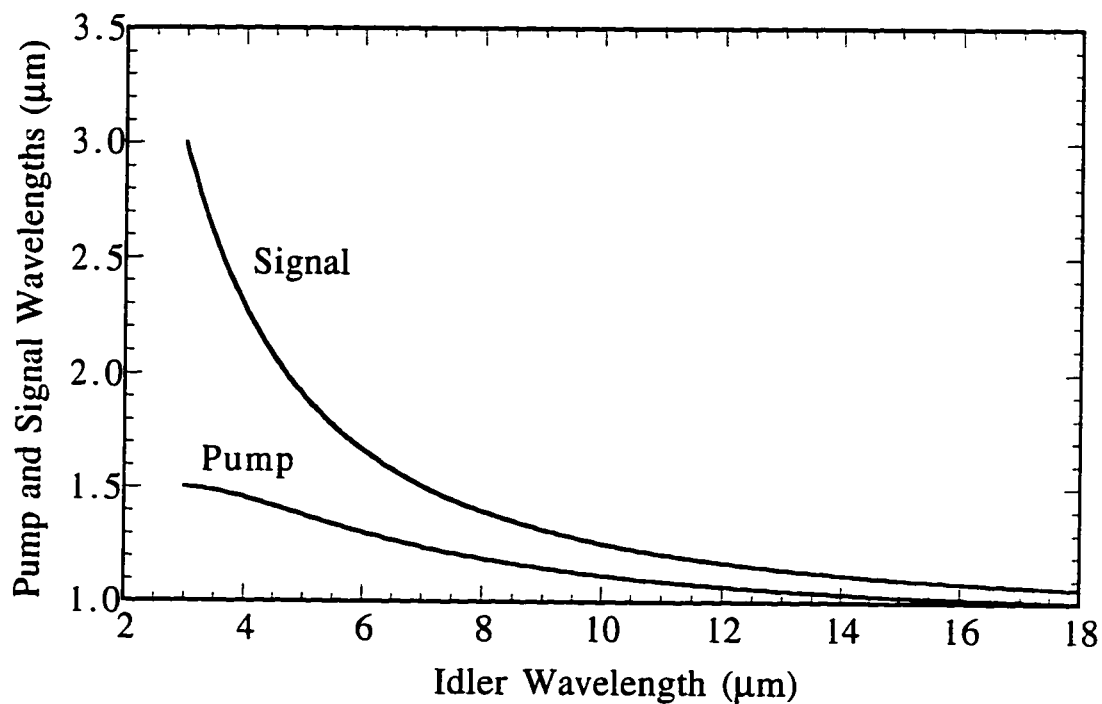


Figure 2.27 - Type-I Noncritical Phasematching in AgGaSe₂ ($e \Rightarrow o+o$)

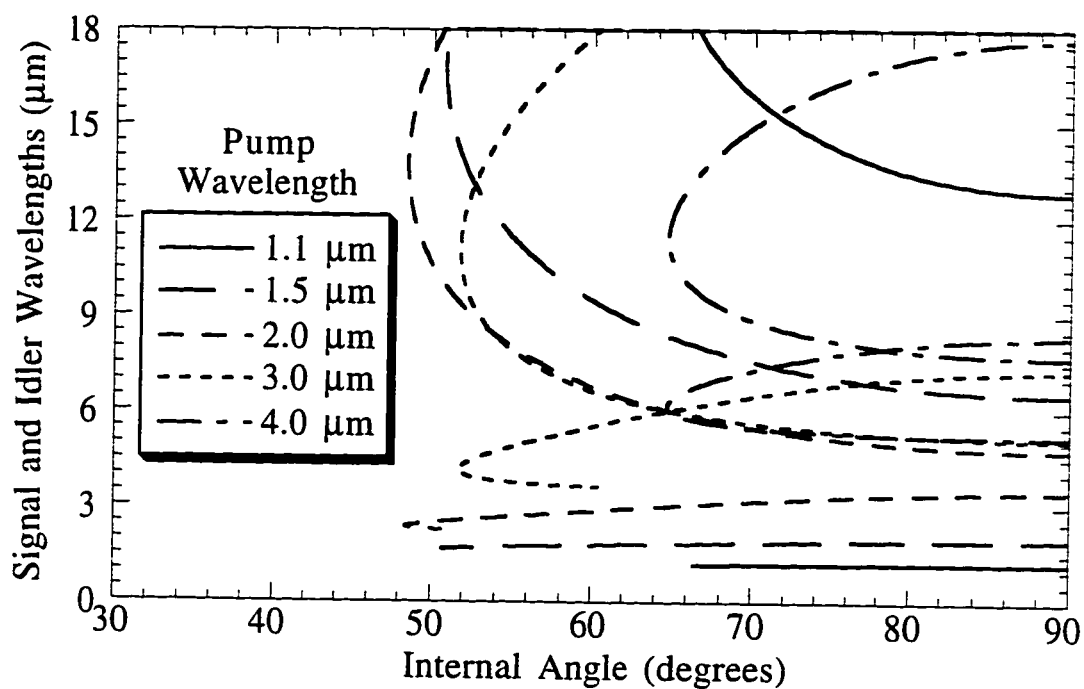


Figure 2.28 - Type-II Phasematching in AgGaSe₂ ($e \Rightarrow o+e$)

2.6.12 Silver Thiogallate (AgGaS₂)

Transparency: 0.5 μm to 13 μm [107]

Damage Threshold: 2 MW/cm² (0.590 μm , $\tau_p = 1 \mu\text{sec}$) [51]

Nonlinear Coefficient: [108]

$$d_{ooe} = d_{36} \cdot \sin(\theta) \cdot \sin(2\phi)$$

$$d_{eoe} = d_{36} \cdot \sin(2\theta) \cdot \cos(2\phi) \quad [\text{Not critically phasematchable}]$$

$$d_{36}(10.6 \mu\text{m}) = 12.4 \pm 1.7 \text{ pm/V}$$

Index of Refraction: [109]

$$n_o^2 = 3.3970 + \frac{1.3758 \cdot \lambda^2}{\lambda^2 - 0.09311} + \frac{2.1640 \cdot \lambda^2}{\lambda^2 - 950}$$

$$n_e^2 = 3.5873 + \frac{1.9533 \cdot \lambda^2}{\lambda^2 - 0.11066} + \frac{2.3391 \cdot \lambda^2}{\lambda^2 - 1030.7}$$

Negative uniaxial crystal: $n_o > n_e$

Numerous experimenters have used silver thiogallate for the downconversion of mid-infrared light. A discussion of these experiments will be deferred until Chapter 4.

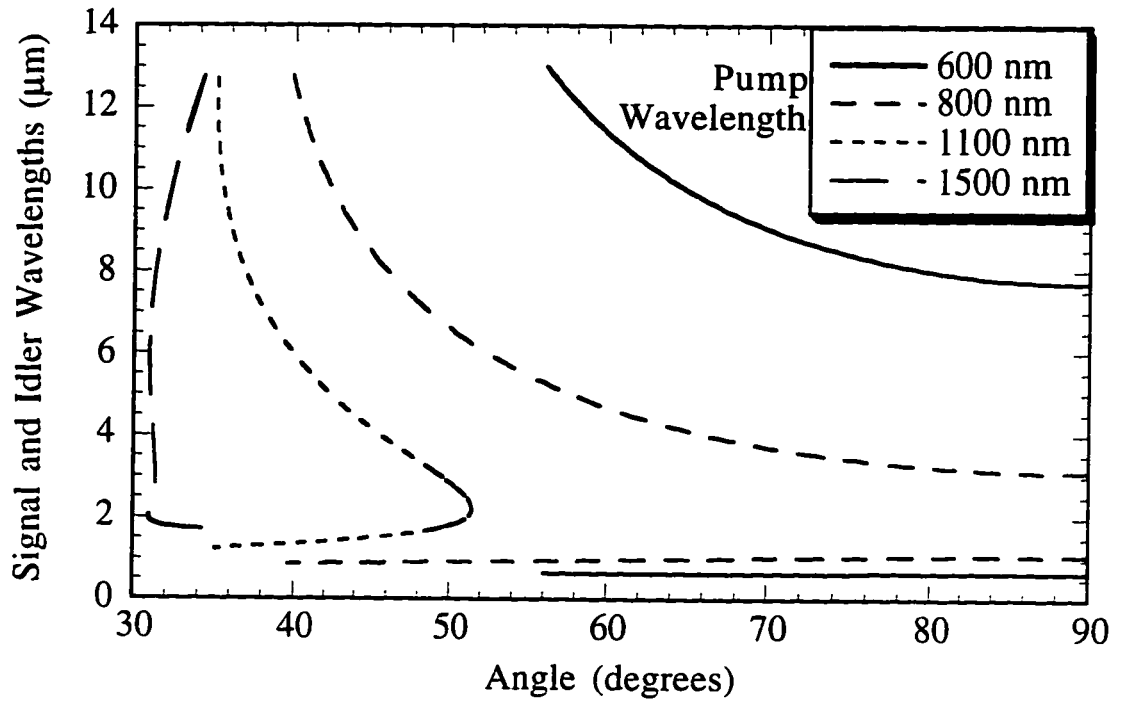


Figure 2.29 - Type-I Phasematching in AgGaS_2 ($e \Rightarrow o+o$)

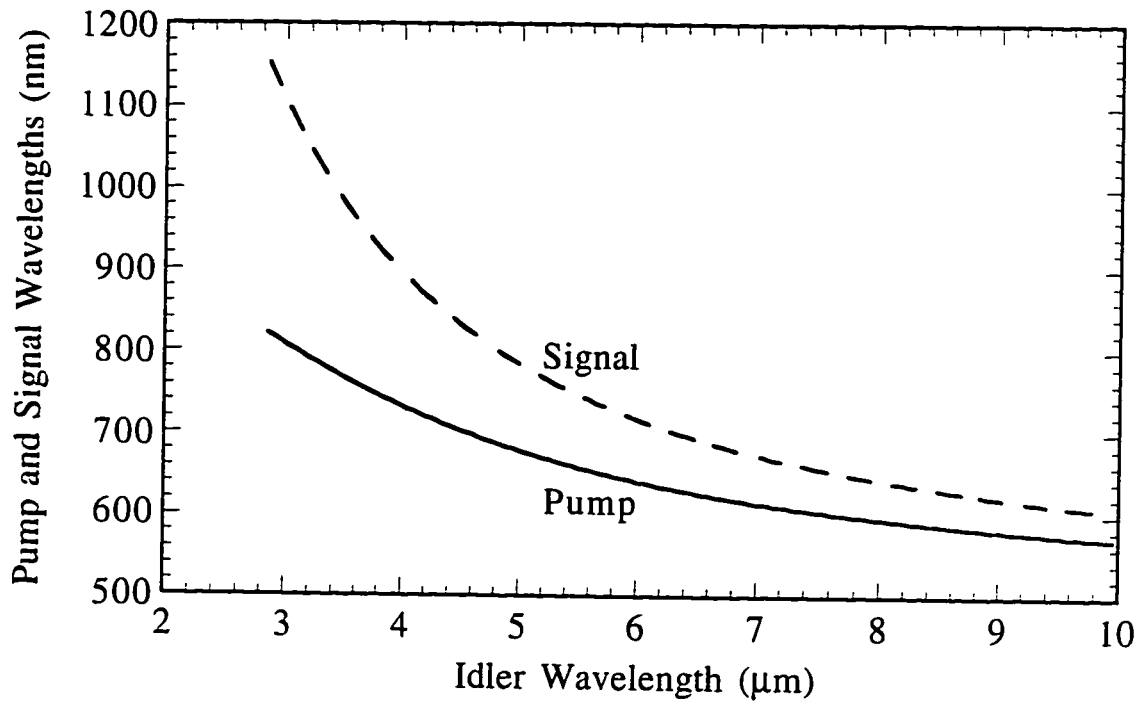


Figure 2.30 - Type-I Noncritical Phasematching in AgGaS_2 ($e \Rightarrow o+o$)

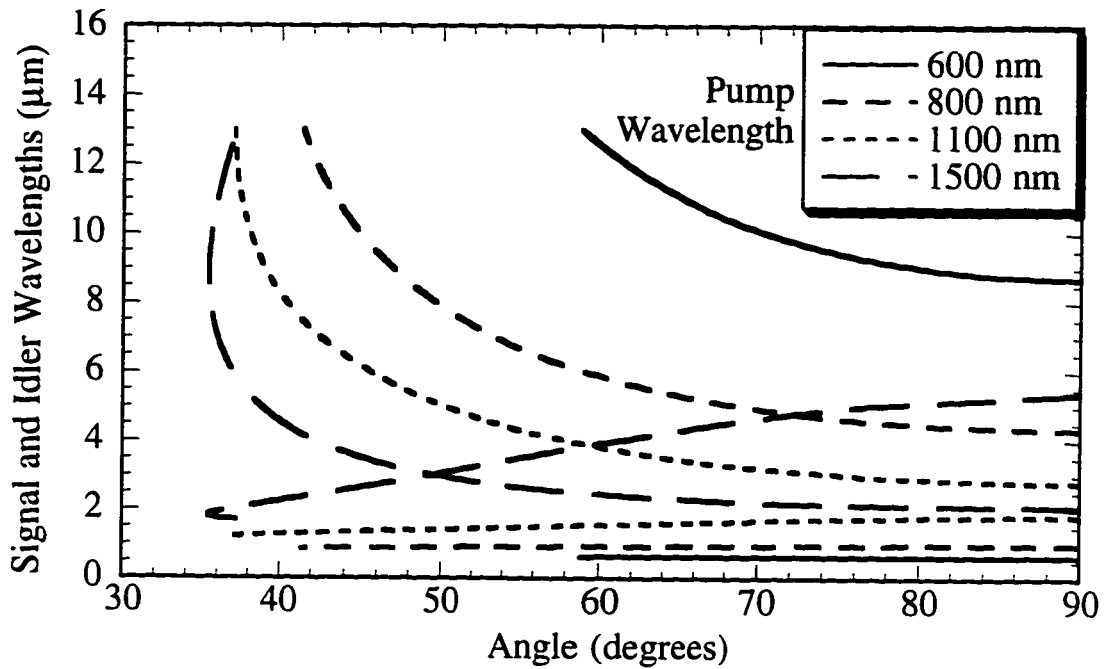


Figure 2.31 - Type-II Phasematching in AgGaS₂ (e⇒o+e)

2.6.13 Tellurium (Te)

Transparency: 3.8 - 32 μm [62]

Damage Threshold: 45 kW/cm² (τ = 17 ns, 1.064 μm) [51]

Nonlinear Coefficient:

$$d_{oeo} = d_{11} \cdot \cos(\theta) \cdot \cos(3\phi)$$

$$d_{eeo} = d_{11} \cdot \cos^2(2\theta) \cdot \sin(3\phi) \quad [\text{Not critically phasematchable}]$$

$$d_{11}(10.6 \mu\text{m}) = 649 \pm 33 \text{ pm/V} [72]$$

$$d_{11}(10.6 \mu\text{m}) = 92 \pm 30 \text{ pm/V} [110]$$

$$d_{11}(28.0 \mu\text{m}) = 570 \pm 190 \text{ pm/V} [111]$$

Index of Refraction: [38]

for λ in the range of 4 - 14 μm

$$n_o^2 = 18.5346 + \frac{4.3289 \cdot \lambda^2}{\lambda^2 - 3.9810} + \frac{3.7800 \cdot \lambda^2}{\lambda^2 - 11.813}$$

$$n_e^2 = 29.5222 + \frac{9.3068 \cdot \lambda^2}{\lambda^2 - 2.5766} + \frac{9.2350 \cdot \lambda^2}{\lambda^2 - 13.521}$$

for λ in the range of 8.5 - 30.5 μm

$$n_o^2 = 4.0164 + \frac{18.8133 \cdot \lambda^2}{\lambda^2 - 1.1572} + \frac{7.3729 \cdot \lambda^2}{\lambda^2 - 10.0000}$$

$$n_e^2 = 1.9041 + \frac{36.8133 \cdot \lambda^2}{\lambda^2 - 1.0803} + \frac{6.2456 \cdot \lambda^2}{\lambda^2 - 10.0000}$$

Positive uniaxial crystal: $n_o < n_e$

Using the output of a line-tunable CO₂ laser and a CO-laser-pumped InSb Spin Flip Raman laser (tunable near 5.3 μm), infrared radiation tunable from 10.95 to 11.11 μm was generated [112]. Approximately 10 μW of power was generated with a bandwidth of $< 0.01 \text{ cm}^{-1}$. Because the two lasers were only line-tunable, continuously tunable radiation was not possible, though wavelength coverage exceeded 60%. The tuning range of the instrument was hampered by the high magnetic field requirements of the spin flip raman laser which made it difficult to operate (see Section 1.1). The phasematching curves calculated for Figures 2.32 and 2.33 were calculated in the following manner: the index of refraction for the 4 - 30 μm range was calculated by averaging the ordinary indices of

refraction from the two dispersion relations in the 8.5 - 14 μm region and using a cubic spline algorithm to fit the index from 4 to 30 μm . Similarly, the extraordinary index of refraction was fit with another cubic spline function. These cubic spline functions were used to calculate the index of refraction for the entire wavelength range, and thence the phasematching characteristics.

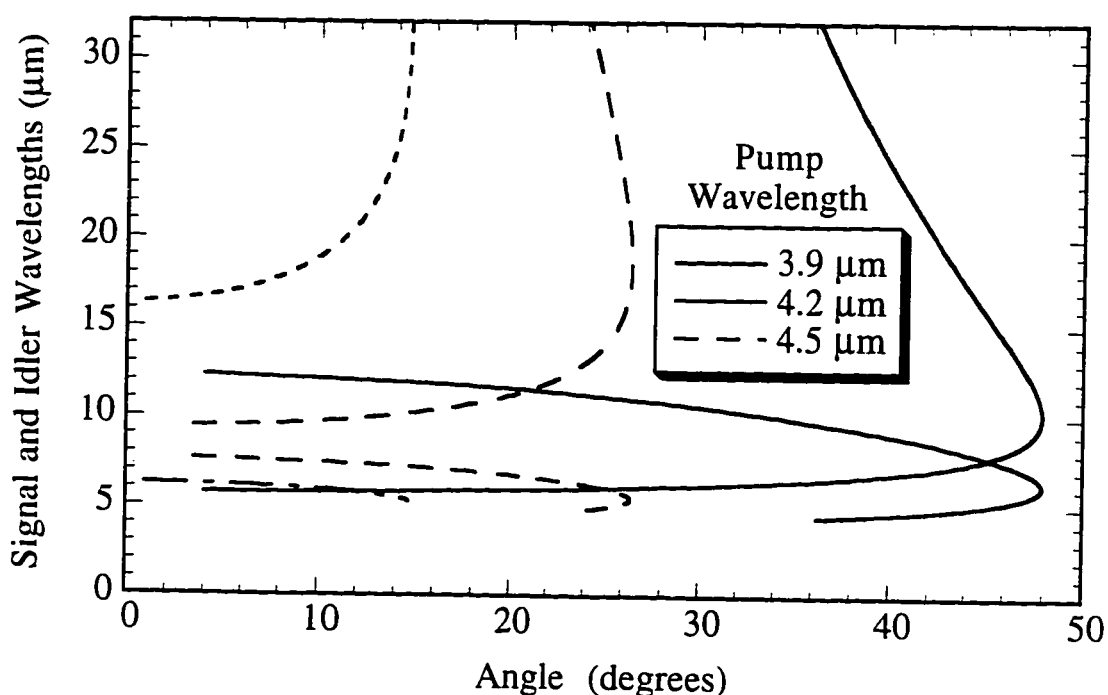


Figure 2.32 - Type I Phasematching in Te ($o \Rightarrow e+e$)

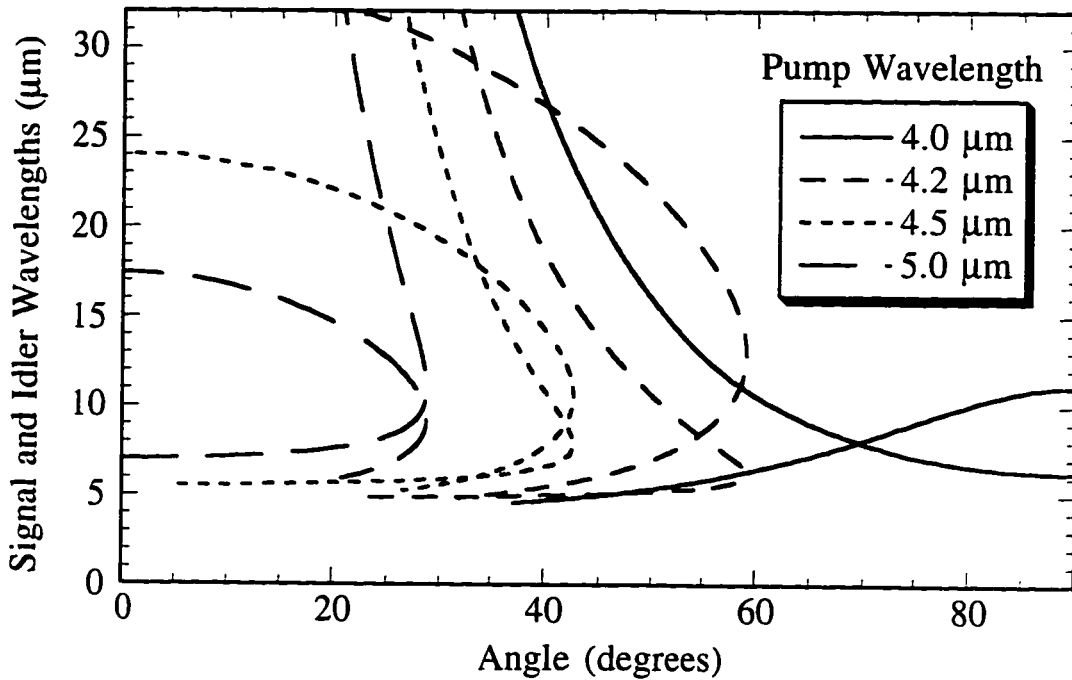


Figure 2.33 - Type II Phasematching in Te ($o \Rightarrow e+o$)

2.6.14 Zinc Germanium Phosphide (ZnGeP_2)

Transparency: 0.74 to 12 μm ($\alpha < 1.0 \text{ cm}^{-1}$) and

2.1 to 10.6 μm ($\alpha < 0.2 \text{ cm}^{-1}$) [113]

Damage Threshold: 60 MW/cm^2 ($\tau = 100 \text{ ns}$, 10.6 μm) [114]

Nonlinear Coefficient: [72]

$$d_{oeo} = d_{36} \cdot \sin(\theta) \cdot \sin(2\phi)$$

$$d_{eoo} = d_{36} \cdot \sin(2\theta) \cdot \cos(2\phi) \quad [\text{Not critically phasematchable}]$$

$$d_{36}(10.6 \mu\text{m}) = 111 \text{ pm/V} [60]$$

Index of Refraction:[38]

$$n_o^2 = 4.5069 + \frac{5.2334 \cdot \lambda^2}{\lambda^2 - 0.1343} + \frac{1.7367 \cdot \lambda^2}{\lambda^2 - 750}$$

$$n_e^2 = 4.6613 + \frac{5.3153 \cdot \lambda^2}{\lambda^2 - 0.1430} + \frac{1.6982 \cdot \lambda^2}{\lambda^2 - 750}$$

Other relations given: [42]

Positive uniaxial crystal: $n_o < n_e$

With its high nonlinear coefficient and transparency range, ZnGeP_2 would seem to be an attractive nonlinear crystal, but as in the case of silver gallium selenide, its usefulness has largely been limited by pump source wavelength requirements. Noncritical phasematching is only possible over a narrow tuning range in Type II phasematching and not at all in Type I. Using an optical parametric oscillator, Vodopyanov and Voevodin have generated tunable radiation from 3.9 to 10 μm [115], but this instrument suffers from a linewidth limited only by the acceptance angle of the crystal and thus had output wavelengths microns wide.

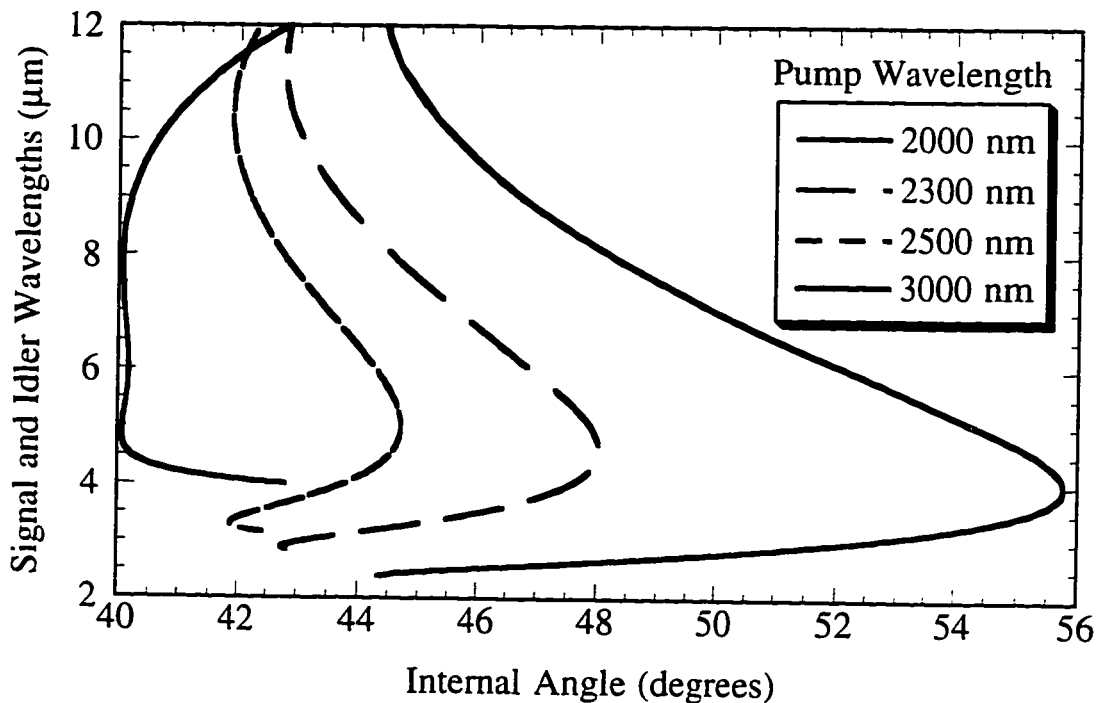


Figure 2.34 - Type-I Phasematching in ZnGeP_2 ($o \Rightarrow e+e$)

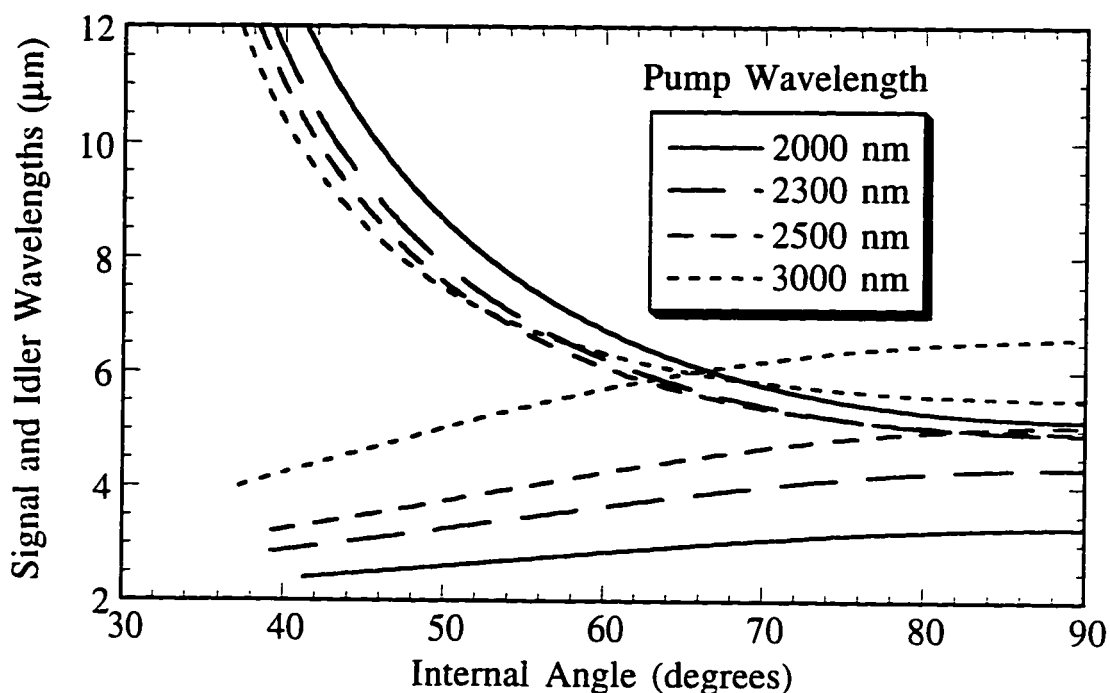


Figure 2.35 - Type-II Phasematching in ZnGeP_2 ($o \Rightarrow e+o$)

2.7 Summary of Implications for DFG

For all the nonlinear crystals produced to date, most are unsuitable for use in a high-resolution spectrometer. Figure 2.36 displays the average nonlinear coefficient d_{eff} for Type-I and Type-II phasematching (neglecting the wavelength dependence) versus wavelength. It is clear that many of the mid-infrared mixing crystals are immediately ruled out because they are not transparent in the optimum pump laser region. Most of the remaining crystals either cannot be phasematched at all or require extreme internal angles for critical phasematching. Again, it is desirable that the crystal be oriented reasonably close to noncritical phasematching in order to increase the interaction length of the drive beams and therefore increase the infrared power.

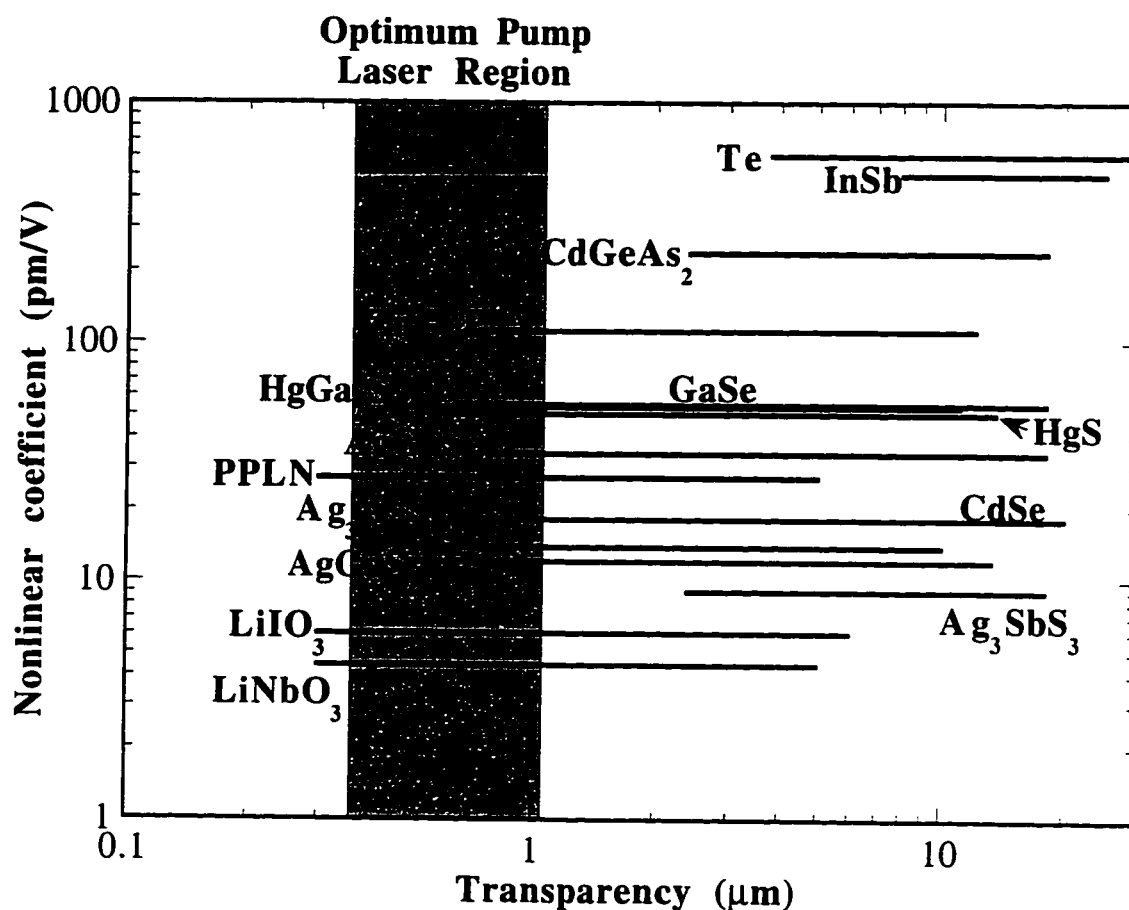


Figure 2.36 - Transmission Ranges and Nonlinear Coefficients of Mid-Infrared Nonlinear Optical Crystals

To date, there are only four or five crystals that are suitable for a mid-infrared spectrometer. Lithium niobate and its close analog periodically-poled lithium niobate are already proven infrared sources and are presently used in numerous laboratories. Silver thiogallate is commercially available in large crystals and has all the properties necessary for daily use in the 3 - 10 μm range. Gallium selenide has possibilities for wavelengths longer than 10 μm , but the angles necessary for phasematching and high absorption coefficients make it difficult to obtain appreciable

output power. Proustite is suitable for generation of infrared light with visible and near-IR pump sources, but is commercially unavailable at the present time and would cover the same wavelength range as lithium niobate and silver thiogallate. Mercury thiogallate would also cover this same range with greater power per crystal length, but to date it remains an unproven frequency converter.

Chapter 4 will detail the efforts of this laboratory in the creation of a spectrometer based on silver thiogallate while Chapter 5 explores the physical characteristics of gallium selenide. Next is Chapter 3 and a description of the equipment used in the difference frequency process.

Chapter 3 - Equipment used in Difference Frequency Generation

The most current experimental setup for infrared kinetic spectroscopy is presented in Figures 3.1 and 3.2. Typically, the 20 - 25 W all lines output of an argon ion laser (Coherent Innova 200-20) passes through a wedged beamsplitter designed to reflect 40% of the incoming light. Both beams separately pump single frequency ring lasers (Coherent 899-29 and Coherent 899-21) locked to external etalons. The

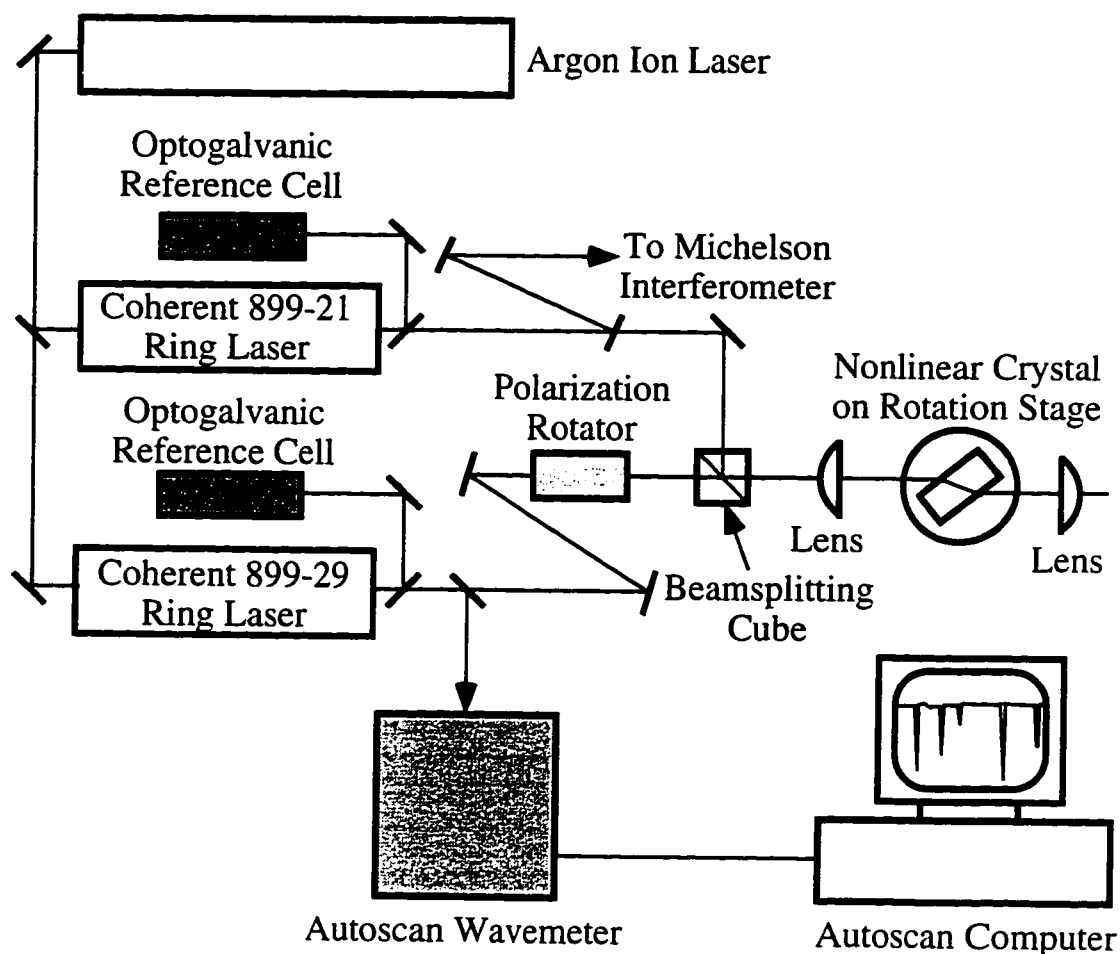


Figure 3.1 Experimental Setup - Infrared Generation

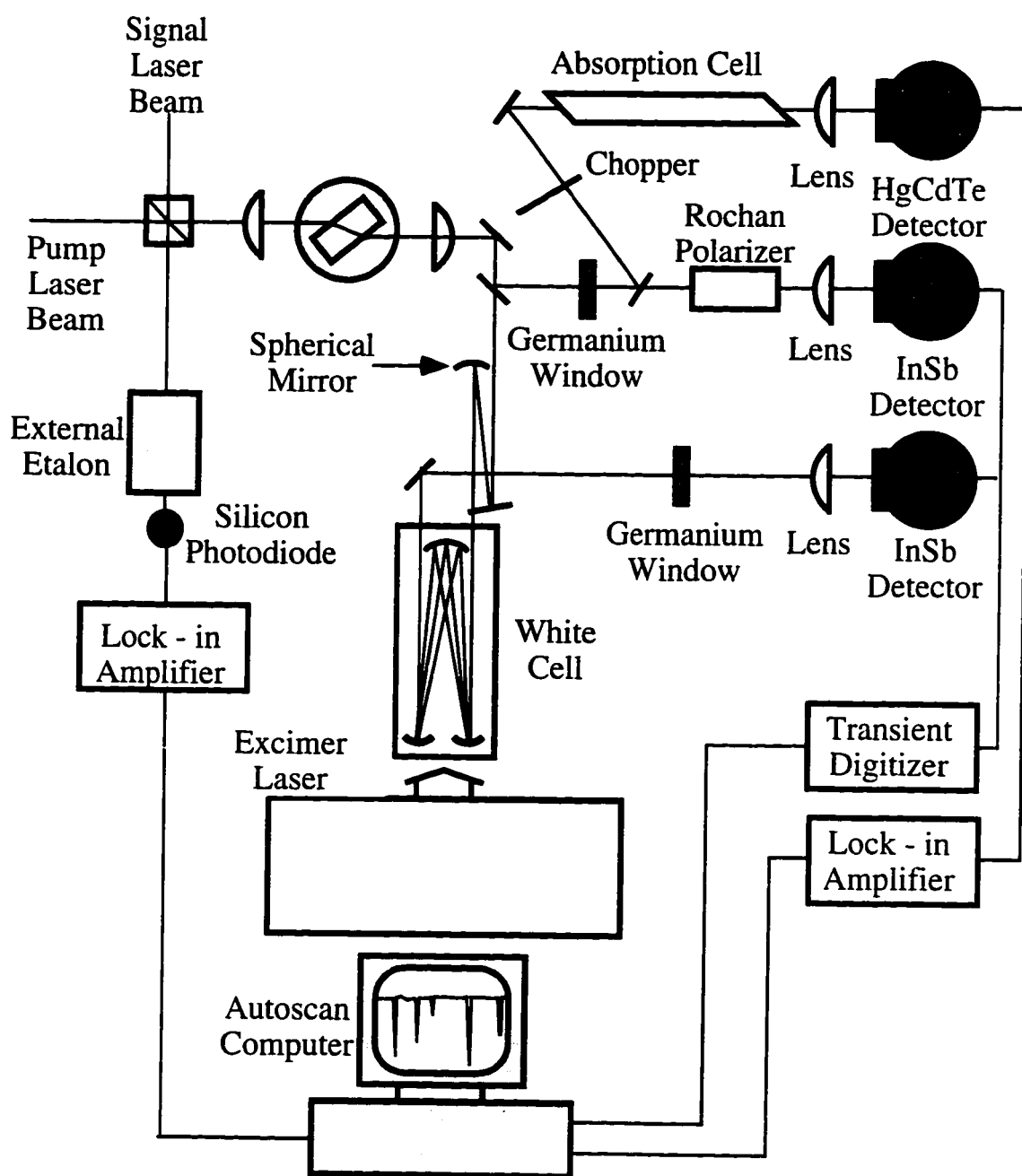


Figure 3.2 - Experimental Setup - Spectroscopy and Wavelength Calibration

899-29 is computer controlled through the Autoscan II (Coherent) system and can be scanned through its tuning range under computer control. By

rotating the polarization of one beam by 90° with a polarization rotator the orthogonally polarized beams are spatially overlapped with a polarization cube. The collinearly propagating beams are focused into a $4 \times 4 \times 45 \text{ mm}^3$ AgGaS₂ crystal (Cleveland Crystals) where type-I noncritical collinear phasematching takes place and infrared radiation is generated at the difference between the two input frequencies. Infrared light is collimated with a BaF₂ lens and split with a beamsplitter constructed of a silicon substrate antireflection coated (3 - 13 μm) on one side. The Fresnel losses from the uncoated side average 30% over the tuning range of the DFG spectrometer. Light that passes through the Si beamsplitter is reflected by a spherical mirror that allows efficient coupling into a 1 meter long multipass cell (White configuration [116-119]).

The pulsed output of an excimer laser (Lambda Physik EMG 101-E) photolyzes an appropriate precursor gas within the multipass cell where transient absorptions can be measured (Figure 3.3). Infrared light enters the cell slightly below an aluminum baffle that blocks the excimer pulse and traverses the cell at a slight incline such that the d-mirrors are placed slightly above the quartz window where the UV light enters the cell. The intensity of the transmitted infrared light is measured by a liquid nitrogen cooled infrared detector. An antireflective coated germanium window (3 - 13 μm) placed immediately in front of the detector blocks the excimer light scattered in the cell.

Light that was originally split off the beam before the multipass cell is again split by a ZnSe beamsplitter designed with one side broad-band

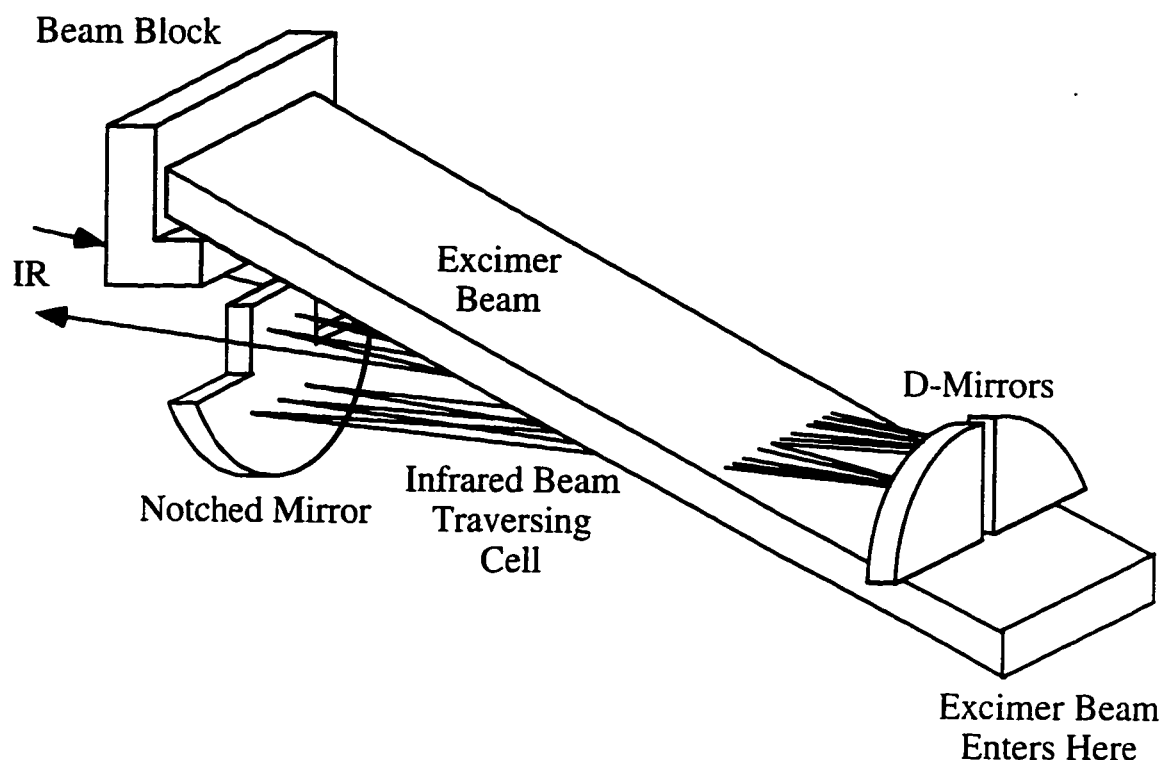


Figure 3.3 - White Cell Configuration

antireflective coated ($3 - 13 \mu\text{m}$) and the other uncoated such that 80% of the power (approximately 24% of the total infrared power) is transmitted. The light reflected from the ZnSe beamsplitter is chopped and passes through a 50 cm cell containing a few torr of a gas(es) whose infrared absorption frequencies are accurately known. The power transmitted through the reference cell is focused onto a HgCdTe detector and the output connected to a lock-in amplifier. The output of the lock-in amplifier is recorded as a function of frequency to provide calibration of spectra. The visible transmission signal of a confocal etalon is recorded as the laser is scanned in order to properly linearize the scans.

To reduce the noise that arises from fluctuations in the infrared intensity, transmitted power from the ZnSe beamsplitter is focused onto a second detector and the two signals are subtracted. The intensity of the light passing into this second detector was manually adjusted with a MgF₂ Rochan polarizer such that the outputs of the two detectors are nulled out prior to the excimer flash and the noise is minimized.

To obtain the absorption signal of a transient free radical, a transient digitizer acts as a dual-gated integrator, averaging the signal both before and after the excimer to remove the high-frequency noise. Low frequency noise is largely eliminated by subtracting the pretrigger signal from the postsignal and the S/N ratio is thereby roughly tripled.

3.1 - The Argon Ion Laser

The argon ion laser is a Coherent Innova 200-20. Equipped with the PowerTrack system, the laser continually maximizes the laser power. The operation and characteristics of the laser are straightforward and will not be discussed here. Under standard operating conditions, the laser is operated in current regulation mode to reduce the Poynting vector instabilities.

It has been found that protecting the argon ion beam path from dust and stray air currents is vital to stable operation of the DFG apparatus. A forced air hood has been constructed over the entire optical table to cut down on the dust, but the lasers pumped by the argon ion laser are especially susceptible to changes in the argon ion intensity. Fluctuations

caused by dust particles passing through the beam path as well as the displacement of the beam caused by heating of the air due to atmospheric absorption of the argon ion beam can be greatly reduced by enclosing the beam. Placing tubes around the beam reduces noise in the ring lasers by a factor of approximately 15.

Approximately once each fifteen months, the argon ion laser power will begin to fluctuate. At this time, the PowerTrack system will indicate the mirror actuators are out of range. The source of the power fluctuations is intercavity creation of ozone through plasma emissions and subsequent absorptions of the laser lines by the Chappuis ozone bands [120]. Due to stray air currents, a steady state is not reached and the power fluctuates. This problem can be positively diagnosed by slipping the dust filters off the end of the Brewster window (thus allowing ozone to freely diffuse from the laser cavity), turning off the PowerTrack system, and observing a decrease in the amplitude of the fluctuations. The dust filters contain silver oxide that reacts with ozone until all surfaces are coated. When ordering replacements, be sure to specify dust filters suitable for a single frequency argon ion laser. Though the laser is usually operated in multiline mode, it has the capability for single frequency operation and contains a spacer where the intercavity etalon would otherwise be placed, precluding the use of the standard filter.

Due to contaminants (primarily rust) in the chilled water system in the Space Science building, a closed loop water system has been constructed to isolate all lasers from the contaminated water. It uses two

water-to-water heat exchangers to dissipate the 50 kW of heat generated in the laser system.

3.2 - The Tunable Pump Lasers

The lasers used in this experiment are commercially available single frequency ring lasers. Though listing the full details of these lasers is beyond the scope of this work, the basics of the operational characteristics will be briefly discussed. The reader is urged to read the manuals accompanying the lasers for further details [121,122].

One laser is a Coherent 899-21 and the other a Coherent 899-29. The -29 designation denotes a -21 equipped with the Autoscan system (discussed in Section 3.3). For the purposes of the following section the lasers will be considered interchangeable. Both are cw lasers that can be converted to run on a variety of dyes or on a titanium:sapphire gain media. The tuning range and output power of the various gain media used to date in these lasers is given in Figure 3.4 where all curves but for that of Rhodamine 6G are experimentally determined. The Rhodamine 6G curve was taken from the 899-21 manual and is included for completeness. Figure 3.4 takes into account the wavelength dependant responsivity of the power meter (Coherent Model 212) and is on average 75% of the display reading. The detector response expected for single frequency laser operation is given in Figure 3.5 and reflects the wavelength dependence of the silicon detector.

The lasers are actively stabilized by locking the cavities to external etalons and linewidths of 500 kHz are typical. Approximate selection of

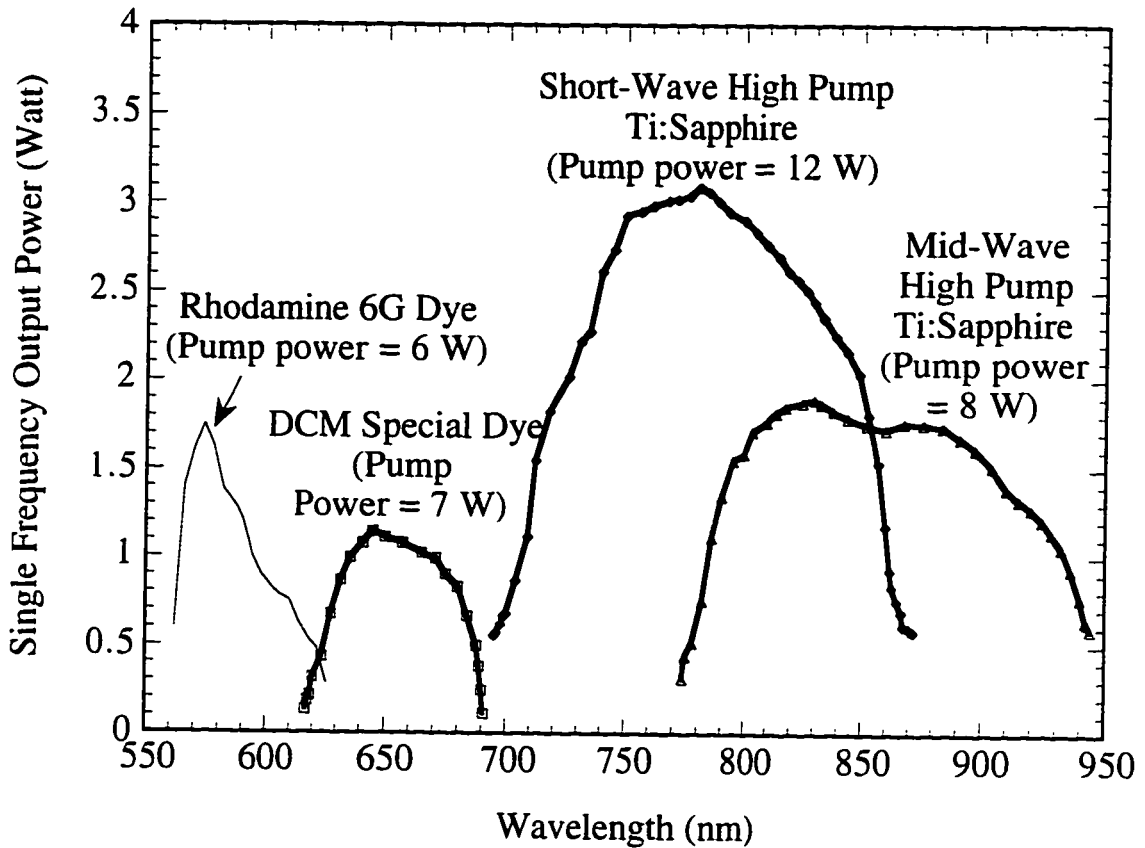


Figure 3.4 - Coherent 899 Single-Frequency Power Versus Wavelength

the output frequency is made possible through the use of three birefringent plates (inside the Bifrefringant Filter or BRF) and two etalons within the intercavity assembly (ICA). Frequency locking is accomplished by fringe-side monitoring of a normalized transmission signal through a thermally stabilized external etalon. The transmission signal is fed back through a cross-over network that separates the high from the low frequency noise. Fast frequency fluctuations in the laser are compensated by the tweeter mirror - a piezoelectrically controlled mirror that responds at 1500 Hz. Slow frequency drift in the laser is compensated by a glass plate tipped near Brewster's angle. As the plate is tipped the effective

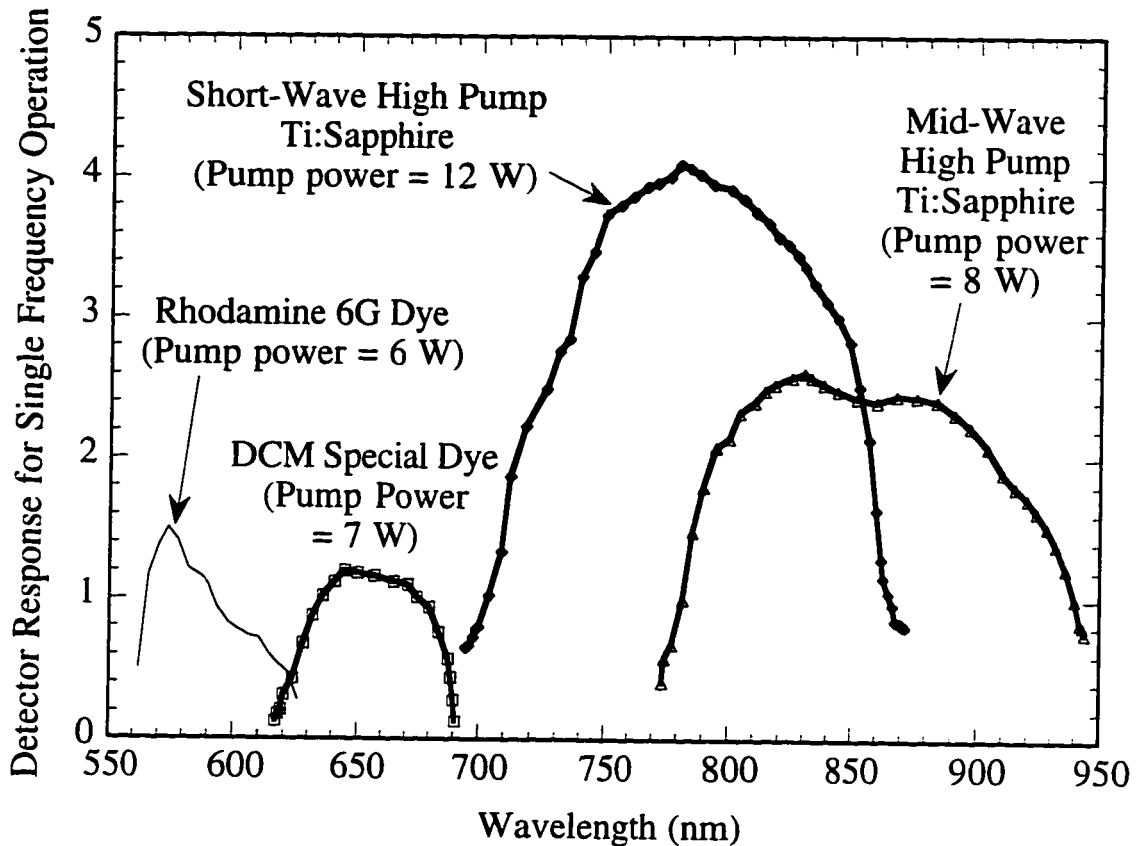


Figure 3.5 - Expected Power Meter Reading versus Wavelength for Coherent 899 Lasers in Single Frequency Operation

cavity length is changed and the laser frequency adjusted. Because the glass plate is located near the output coupler and photons pass through the plate twice during their round trip, the net offset of the beam within the cavity is zero, though the beam is slightly offset during the course of scanning the laser. The effect of the beam offset can be observed as a 5% change in the infrared power during a DFG scan because the infrared power is a sensitive function of the overlap of the two laser beams.

The typical linewidth of the stabilized laser output is 500 kHz, but the long-term stability of this system is closer to 5 or 6 MHz due to incomplete atmospheric seals on the external reference cavities that allows

atmospheric pressure changes to change the effective cavity length. Power stability of the lasers is 0.2% RMS as measured by a silicon photodiode and transient digitizer.

3.2.1 - Daily Operation of the 899-21 laser

The key to successful operation of the lasers is extreme attention to detail:

- 1). One should not attempt to optimize the ring lasers before the argon ion laser has warmed for at least half an hour (preferably an hour) because the poynting vector of the argon ion laser changes as the Brewster window heats.
- 2). All optical surfaces inside the ring lasers should be cleaned on a daily basis and only after the warm-up time has been completed. Inside the cavity, there are four mirrors and nine intercavity surfaces which need to be cleaned daily as even trace amounts of dust on optics will rapidly degrade the performance of a laser with twenty-four intercavity surfaces (eleven surfaces cannot be accessed). It is also a good idea to clean the optics coupling the argon ion laser into the cavity, though care should be taken with the new mounts fastened with clips as they can easily fall out of the mounts if even slight pressure is applied (be especially careful of the lens as the mount is poorly designed and rotates easily).

- 3). Generally, it is a good idea to clean the laser only after it is operating because optics often move during the cleaning process and it is much easier to tweak the cavity when the misaligned optic can positively identified.
- 4). Test the feed-forward adjustments. "Feed forward" is the name applied to the slopes of the voltage ramps applied to the thick etalon, the scanning Brewster plate, and the thin etalon. If the laser is to successfully lock and/or scan, the above elements must all track at rates that allow for synchronous compenstion of all tuning elements. If one element scans at a rate not matching the other two, mode hops will occur. The pots controlling these voltage ramps are sensitive to day-to-day changes in the room temperature. If the laser cannot lock to a full 29.99 GHz scan, the voltages need to be adjusted. Note: the ring laser electronics will not reliably lock to 29.99 GHz at a 4 Hz repetition rate and will go into "spasm" - characterized by full range fluctuations in the lock error signal over a repeatable portion of the scan. Briefly unlock the laser, change the scan time to one second, and again try to lock the laser.

3.2.2 - Causes of Instabilities in the Ti:Sapphire Output Power

When the cavity is exhibiting rapid power fluctuations and the argon ion laser power is stable, there are eight standard causes:

- 1). The etalons have not been "walked-off" properly. This means that a surface in the etalon assembly is perpendicular to the cavity mode and reflections are causing feedback in the cavity that allows the laser to briefly lase in both the forward and backward directions. The laser manual gives explicit instructions on the etalon alignment procedures.
- 2). Either the pump beam or the lowest order cavity mode is being clipped. While clipping of the pump beam is usually obvious the spatial tolerances inside the cavity are rather tight and the locations of the constrictions in the cavity are rather difficult to observe. The most common places for the beam to be clipped are at the top of the BRF, the Faraday rotator, the clips holding the input coupler in place, and the Brewster galvo plate. While the rest of the locations can be visually inspected, one must loosen the screws holding the Faraday rotator in place and lift the assembly. If the power changes as the rotator is lifted two or three millimeters, the beam is striking the Faraday rotator.
- 3). The cavity is nonplanar. If the laser cavity is nonplanar, the laser power will fluctuate wildly with the slightest touch of any horizontal mirror controls. Most commonly, the beam is not horizontally centered on the output coupler. This can easily be fixed by simultaneously adjusting the horizontal controls of the tweeter and upper-fold mirrors. If this

adjustment is properly executed the laser will continue to lase during the entire procedure.

- 4). An optical surface is not clean and a dust particle is increasing the losses in the TEM₀₀ mode enough to make the higher transverse modes competitive. Clean all surfaces again and check the laser power. Though many of the ICA surfaces cannot be cleaned in the laboratory, there is sufficient play to utilize a different portion of the optical surface. The ICA should be sent to Coherent every two years for a thorough cleaning.
- 5). Excessive dust is passing through the focusing region in the laser cavity. Replace the cover and observe the stability.
- 6). The focusing elements in the laser are at improper distances. The upper-fold mirror (M5) needs to be at precisely the correct distance from the intermediate fold mirror (M1) to recollimate the beam or the laser will form an unstable resonator. If the pump beam's waist position (determined by the third pump mirror P3) does not precisely match that of the cavity, the gain that is undepleted by the lowest order gaussian mode of the cavity will briefly lase in higher transverse modes, again leading to unstable operation.

There are two quick tests of the focusing in the cavity that have been discovered in this laboratory. The crystal is heated by absorption of the pump laser beam, forming a positive thermal lens and changing the focusing of the cavity

mode. This can be used for diagnostic purposes. In the first test, block the argon ion beam for several seconds and allow the Ti:Sapphire crystal to cool down. Unblock the pump beam and observe the laser power for several seconds. If the laser power first increases and then slowly decreases to a steady state level, the upper-fold mirror is too far from the intermediate fold mirror and should be brought forward. In the second test, block the cavity near the output coupler for half a minute so that lack of optical cooling causes the crystal to heat above standard operating temperature. Unblock the cavity and if the power increases and then decreases to a steady state level, the upper-fold mirror is too close to the intermediate fold mirror. Only after the above tests should the P3 mirror position be adjusted to maximize the laser output power.

- 7). The cooling water is not reaching the Ti:Sapphire crystals and the lasers are unsuccessfully mode-locking. To test, place your finger on the mount holding the crystal. If it does not feel cool, immediately check the cooling water connections.
- 8). The laser is mode-hopping. This occurs either because the feed-forward adjustments have not been properly made or the laser is being tuned to a wavelength where the cavity losses are increasing and the gain is decreasing enough to allow another cavity mode to become competitive. Lock the laser, turn the front panel display to "Reference Cavity", and observe the

error signal over the period of several minutes. If the needle swings quickly the laser is indeed mode-hopping. Tune the laser to a frequency known to operate stably, adjust the feed-forwards, then tune to the desired frequency. Note: though Figure 3.4 depicts the short-wave Ti:Sapphire laser as capable of tuning to 697 nm, it cannot scan near that wavelength and the operator will have to search for stable cavity modes. The Ti:Sapphire laser will only reliably scan at wavelengths longer than 702 nm.

3.2.3 - Alignment of the 899-21 lasers

It has been found that the Poynting vector stability of the argon ion laser is absolutely critical to operation of the ring lasers. It can be shown that a movement of the ion laser cavity by 30 μm can cause the ring lasers to stop lasing. In order to prevent this sort of movement in the pump laser a number of steps have been taken:

- 1). Gluing the legs of the argon ion laser to the optical table with 5-minute epoxy helps to immobilize the cavity. To remove the epoxy, it is only necessary to apply acetone to the epoxy spots and wait five minutes for the glue to soften. Simply placing magnetic mounts around the case allows the cavity to flex.
- 2). To prevent excessing coupling of vibrations due to surges in the cooling water pressure to the laser and to prevent the laser umbilical cord from pulling the laser askew when the optical

table floats and flexes, the cord is clamped directly to the table and sufficient slack is given on either side of the clamp to allow the table to float properly.

- 3). When the height of the argon ion laser is adjusted, care must be taken that the legs remain securely fastened to the laser base plate and that the laser is not lowered so much that the legs directly contact the cavity. To check for the latter condition, the operator can place his/her entire weight on the argon ion laser case. Not only should the power of the argon ion laser remain unchanged, but the ring laser powers should also remain unaffected.

3.3 - Autoscan

The Autoscan system on the 899-29 laser is rather elaborate and will be discussed in some detail.

The heart of the system is an on-board wavelength meter, a device capable of determining the laser wavelength to an absolute accuracy of 200 MHz (0.007 cm^{-1}). Interfaced to a PC, the system can automatically tune to any desired wavelength within the bandwidth of the laser gain medium. The entire assembly is mounted in a box directly attached to the frame of the laser and cannot be moved to the 899-21.

3.3.1 - Optical Activity Monochromator (OAM)

Gross wavelength calibration in Autoscan is accomplished using the specific rotation of quartz. The relationship between the optical frequency

(v) and specific rotation (ρ) can be described in terms of a modified Sellmeier equation:

$$\rho(v) = \frac{A_1 v^2}{B_1 - v^2} - A_2 \quad (3.3.1)$$

A tiny fraction of the laser light is separately passed through two pieces of quartz and then through a polaroid sheet mounted on a wheel spinning at a constant speed, producing a time-varying signal that reproduces itself every π rotation. By measuring the delay from a timing mark on the wheel, the polarization of the light can be determined to within 0.1 degrees. The lengths of quartz are carefully chosen such that the total rotation within quartz pieces is greater than 1000 degrees over the entire scanning range of the ring laser system. Because the polarization angle only has a range of values from 0 to 180 degrees, the measured rotation is only a modulus of the total. To determine the total angular rotation, the quartz pieces are of different lengths (typically differing by approximately 4 mm) and the difference between the two angles ($\theta_1 - \theta_2$) is a measure of the rotation that occurs within the difference in lengths (ΔL). This gives an approximation of the specific rotation:

$$\rho_{\text{coarse}} = \frac{\theta_1 - \theta_2}{\Delta L} \quad (3.3.2)$$

From ρ_{coarse} , the computer calculates an estimate of the total rotation through each piece of quartz. The number of 180° rotations in the short and long piece, respectively, is:

$$n_1 = \text{integer}\left(\frac{(\rho_{\text{coarse}} \cdot L) - \theta_1}{180^\circ}\right) \quad (3.3.3)$$

$$n_2 = \text{integer}\left(\frac{(\rho_{\text{coarse}} \cdot (L + \Delta L)) - \theta_2}{180^\circ}\right) \quad (3.3.4)$$

where the "integer" in Equations 3.3.3 and 3.3.4 is the integer truncation function. A refined value of specific rotation, ρ_{refined} , is computed by combining the above information in an average over the two crystals:

$$\rho_{\text{refined}} = \frac{(n_1 + n_2) \cdot 180^\circ + (\theta_1 + \theta_2)}{2L + \Delta L} \quad (3.3.5)$$

This refined value of the specific rotation is then used to determine the frequency to within approximately 2.5 cm^{-1} . The entire specific rotation assembly is known as the Optical Activity Monochromator (OAM). Autoscan is limited to wavelengths shorter than 900 nm because the specific rotation of quartz monotonically drops with increasing wavelength and beyond 900 nm has fallen to a value so low that the OAM system cannot achieve the required 2.5 cm^{-1} accuracy.

In order to measure the time delay from the timing mark to the maximum transmission of the polarization wheel the number of 8 MHz cycles is counted. This 8 MHz timing signal is taken directly from the computer bus and prevents the use of most modern computers, which typically operate at up to 200 MHz clock speeds. The computer used in the system is a 286-8 personal computer.

3.3.2 - Vernier Etalons (VETs)

To determine the frequency of the laser to an accuracy of at least 2.5 cm^{-1} , vernier etalons are used. Theoretically, if one scanned a laser over an etalon transmission peak of known free spectral range (FSR) one could determine the difference ($\Delta\nu$) between the laser frequency and the peak and thus obtain the frequency - assuming the laser frequency was reproducible and one knew the absolute order number of the etalon.

$$\nu_{\text{laser}} = n_{\text{etalon}} \cdot \text{FSR} + \Delta\nu \quad (3.3.6)$$

In practice, however, the uncertainty in $\Delta\nu$ is typically on the order of 1% of the FSR. Since the etalon order uncertainty is on the order of 2.5 cm^{-1} (the uncertainty in the frequency ν_{OAM} determined by the OAM), the frequency could only be determined to an accuracy of 0.025 cm^{-1} (1% of 2.5 cm^{-1}). This accuracy is improved using a parallel pair of etalons of slightly different FSR. As the laser is scanned, transmission data from both etalons is recorded and the difference (D) between the transmission peaks of the two etalons determined.

$$D = n_{\text{VET1}} \cdot \text{FSR}_{\text{VET1}} - n_{\text{VET2}} \cdot \text{FSR}_{\text{VET2}} \quad (3.3.7)$$

where n_{VET1} and n_{VET2} are the absolute order numbers of the two vernier etalons (VETs) and FSR_{VET1} and FSR_{VET2} are their corresponding free spectral ranges. A typical spectrum of these etalons is given in Figure 3.6. To determine the estimated orders of the etalons:

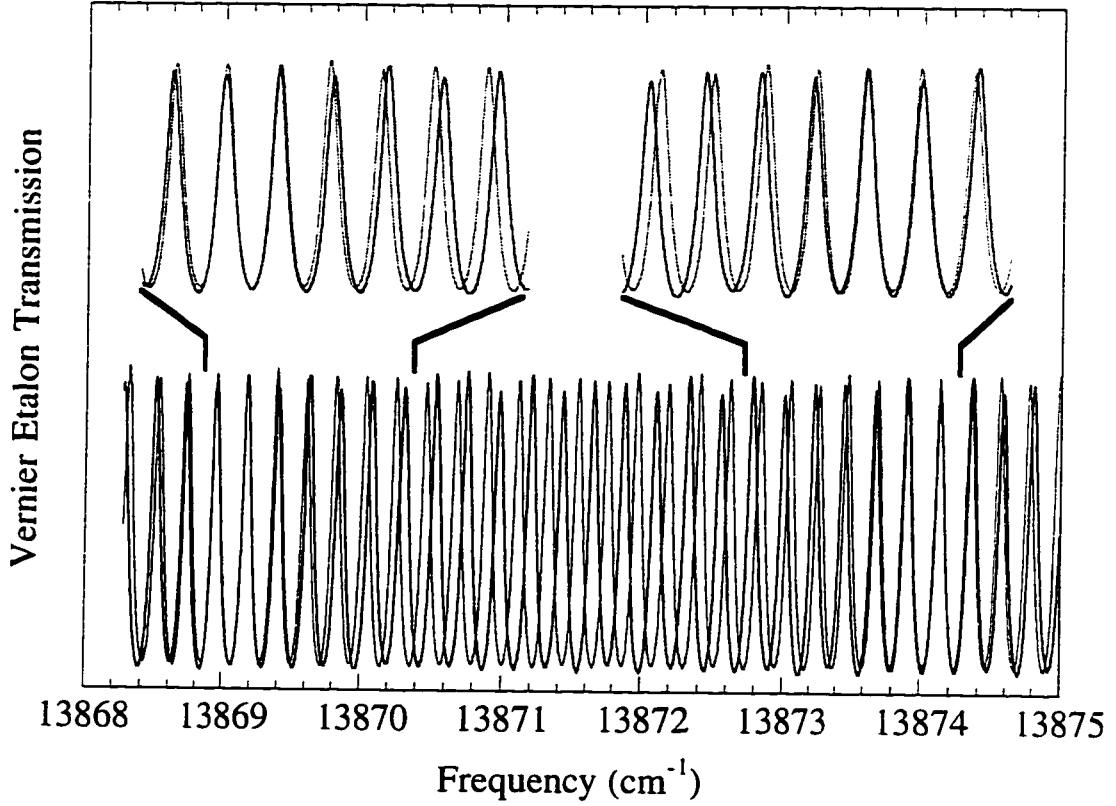


Figure 3.6 - Vernier Etalon (VET) Data

$$n_{\text{VET1,est}} = \text{integer} \left(\frac{\text{VOAM}}{\text{FSR}_{\text{VET1}}} \right) \quad (3.3.8)$$

$$n_{\text{VET2,est}} = \text{integer} \left(\frac{\text{VOAM}}{\text{FSR}_{\text{VET2}}} \right) \quad (3.3.9)$$

Since the OAM data is not perfect, these estimations of the VET orders may be in error, but they will be in error by the same amount (Δn) if we assume the FSR of both etalons is a constant. The Δn term is added to both terms above (Equations 3.3.8 and 3.3.9).

The difference D in the transmission frequencies is:

$$D = (n_{\text{VET1,est}} + \Delta n) \cdot \text{FSR}_{\text{VET1}} - (n_{\text{VET2,est}} + \Delta n) \cdot \text{FSR}_{\text{VET2}} \quad (3.3.10)$$

The difference between the expected difference at the OAM frequency (D_{expected}) and the measured difference D is an integral multiple of the difference of the two FSRs, and therefore the error in the etalon orders Δn is:

$$\Delta n = \text{integer} \left(\frac{D_{\text{expected}} - D}{\text{FSR}_{\text{VET1}} - \text{FSR}_{\text{VET1}}} \right) \quad (3.3.11)$$

The final laser wavelength is simply:

$$\nu = (n_{\text{VET1,est}} + \Delta n) \cdot \text{FSR}_{\text{VET1}} + \Delta \nu \quad (3.3.12)$$

Using this VET / OAM system, it is possible to obtain absolute frequency accuracy of 200 MHz (0.007 cm^{-1}) and reproducibility of 50 MHz.

3.3.3 - Scanning of the Autoscan Laser

Scanning in the Autoscan system is accomplished automatically under computer control. After the starting frequency for a scan is input by the operator, the laser changes all the tuning elements in the laser to move to their calculated positions, locks the laser to the reference cavity in mid-travel, and peaks the BRF and thin etalon. After the wavemeter determines the wavelength the computer calculates new positions for all tuning elements and iterates on this process. When the laser locks to the target wavelength, the glass plate in the reference cavity is tipped slightly by a calculated amount (based on the step size of the scan), changing the

effective length of the cavity. The laser scans the thick etalon and Brewster galvo to stay locked to the reference cavity signal as described in Section 3.2.

The entire tuning range of the reference cavity Brewster galvo (called the scan drive in the Autoscan software) is approximately one wavenumber, but as this cavity element must be tuned by up to 0.50 wavenumbers to attain the proper start frequency (the FSR of the thin etalon), the starting position is variable and in the worst case scenario could limit a scan length to 0.5 cm^{-1} . Therefore, scans are standardized to just over 10 GHz (0.33 cm^{-1}) before a reset. Longer scans are built up by scanning the laser over a 10.25 GHz segment (called a panel), unlocking the laser, changing the frequency to 250 MHz below the end of the last panel, scanning another 10.25 GHz, and repeating the process. This 250 MHz overlap in the panels should ensure that all frequencies are scanned during the course of data collection.. Because the frequency accuracy of the restart after unlocking the laser is limited by the uncertainty in the wavemeter, there is an uncertainty of 200 MHz in the absolute frequency of each panel that is uncorrelated with the uncertainty in all other panels during a scan.

3.4 - The External Etalon

Because of the above mentioned 200 MHz uncertainty encountered in scanning the laser, the transmission spectrum of an external etalon is acquired as the laser is scanned. The etalon is a vacuum confocal etalon with a mirror spacing of 100 mm. The calculated FSR for $c/2L$ mode is

1.5 GHz but is most often operated in $c/4L$ mode ($\text{FSR} = 750 \text{ MHz}$) by using unfocused beams. The etalon is not temperature stabilized and the FSR changes from day to day but does not change significantly over the course of an hour or two.

The transmission spectrum of the external etalon (Figure 3.7)

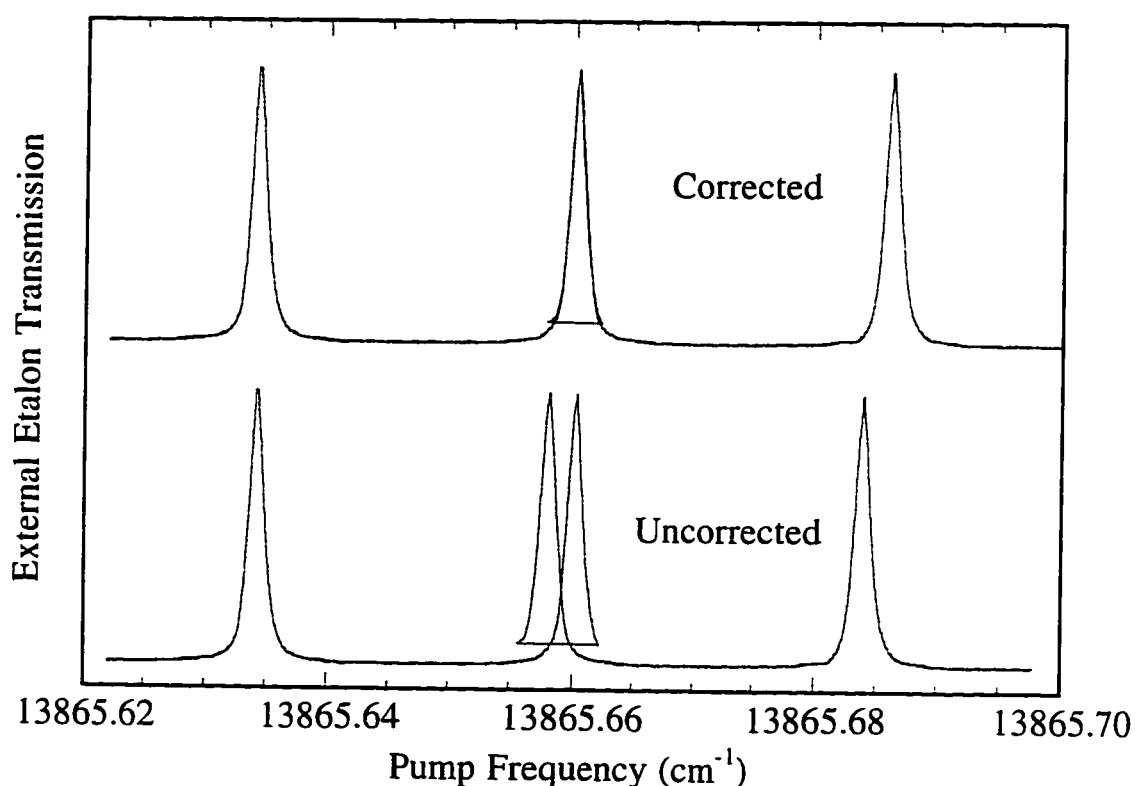


Figure 3.7 - External Etalon Retrace and Wavelength Correction

illustrates the 200 MHz uncertainty in determining the beginning frequency of a panel with respect to the previous panel and the 250 MHz overlap of the panels. The lower trace shows an uncorrected portion of a scan centered on a panel-panel overlap region where the retrace of the scanning frequency is clearly seen in the horizontal line. The apparent frequency

error upon restart of the scan is also clearly shown, leading to the double image of the transmission peak. Transforming the lower trace into the upper is implemented within a computer program named ANALYZE written in Microsoft's Visual Basic. The procedure used is as follows:

- 1). The program determines the average voltage level of the scan and uses this as a baseline. This is not a base line in the true sense of the word as transmission peaks are included in the average. It is simply a reference point upon which the presence of transmission peaks will be tested. The program has the capability of fitting points with a higher polynomial in case an infrared etalon is used (in which case the true baseline will change during the course of a scan due to the phasematching condition and incomplete interference of the etalon).
- 2). Data is examined point-by-point and compared with the baseline voltage. Any group of four or more consecutive data points that lie above this baseline are assumed to comprise a transmission peak. The next data point that dips below the average is the end of the peak.
- 3). If the data does not drop below the baseline before the end of a panel is reached, it is noted that a peak was observed but that its position could not be properly determined.

- 4). A centroid is determined for the transmission peak and its frequency stored along with the number of the panel in which it is contained.
- 5). After the peakfinding algorithm has finished, the user is given a chance to delete unwanted peaks and identify peaks missed by the search algorithm.
- 6). An approximate FSR of the etalon is determined by dividing the difference in frequency between the first and last peaks of the scan by the total number of peaks (identified frequency peaks + unidentified peaks) and the theoretical frequencies of etalon peaks are calculated by simple interpolation between the first and last peaks.
- 7). Each panel is individually fit to a polynomial of user defined degree based on a least squares algorithm that transforms the measured frequencies to the theoretical frequencies. Usually, the polynomial contains only a constant term, as the linearity of the Autoscan system is quite good (typically better than 50 MHz).
- 8). The user is given another chance to change the measured etalon frequencies, refit the data, etc.
- 9). The data is transformed to the new linear frequency system.

The above procedure is able to remove the 200 MHz precision errors that occur when transitioning from one panel to another. It does not correct the inaccuracy of the system in determining the positions of the first and

last peaks, but does make the error linear in frequency. The final linear correction is made upon examination of the reference gas as described in the next section.

In addition to its above mentioned function, the external etalon provides a monitor of the frequency stability of the second ring laser. Driven by stray reflections off the beamsplitting cube, the etalon transmits both lasers. Since the 899-21 laser is frequency locked during a scan, the time dependence of its transmission through the etalon should be fixed and should not vary over the course of a scan. If the baseline of the etalon trace changes it is an indication that the fixed frequency laser has mode-hopped.

3.5 - Reference Gas Calibration

As earlier mentioned, after linearization of a scan has taken place by means of the external etalon, the infrared scan has not been properly calibrated. The Autoscan laser's frequency uncertainty is 200 MHz and the uncertainty in the 899-21 is 300 MHz. To properly determine the infrared frequencies generated in the nonlinear crystal, as the 899-29 laser is scanned the infrared spectrum of another gas is acquired whose transition frequencies are known to an accuracy of at least 0.001 cm^{-1} . After the scan has been linearized to the external etalon, the absorption lines of the reference gas are manually identified and their transition frequencies input to the ANALYZE program. A linear least-squares algorithm is used to transform the observed data to the literature frequencies. Preferably, at

least two reference gas lines can be identified in each scan and thus provide the linear fit. When this is not the case, it is possible to use a single absorption line and the FSR of the external etalon determined by another scan with at least two lines and taken as close in time as possible to minimize the effects of thermal expansion of the etalon to calibrate the scan.

3.6 - The Michelson Interferometer

A Michelson Interferometer operates on the principal that a beam that is split in two and then recombined will exhibit interference fringes as the path length difference between the two arms is varied. The fringe-counting or scanning Michelson interferometer is composed of a constant frequency reference source, a beamsplitter, two folding mirrors, a pair of moving retroreflectors, and a ratio frequency counter. The basic design is essentially that described by Hall and Lee [123] and modified by many others [124-126].

Displayed in Figure 3.8, corner cube reflectors are mounted on an air track and translated along the directions of the beams from either side. As the corner cube assembly is moved along the track between the folding mirrors, the path length difference between the two portions of the two laser beams is varied and as a result a series of interference maxima, minima, and nodes are generated at the photodiode. The number of interference fringe nodes for each laser wavelength generated for a given path length difference is given by the equation:

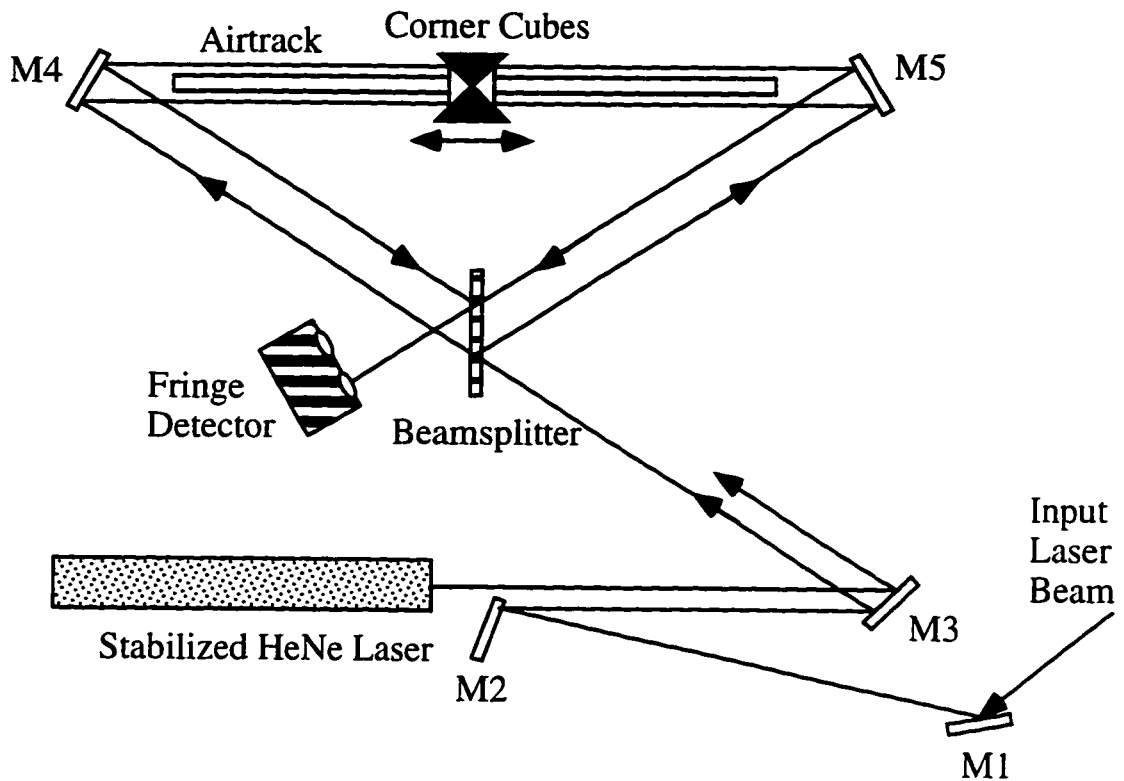


Figure 3.8 - Michelson Scanning Interferometer Setup

$$N_f = \frac{4 \cdot d}{\lambda} \quad (3.6.1)$$

where N_f is the number of fringes, d is the distance traveled by the retroreflectors, and λ is the wavelength of the laser light. Since the two input laser beams travel essentially the same path but are vertically displaced, the distance d of the two measurements is the same. From this, the relation between the two laser wavelengths can be derived:

$$\lambda_{\text{Unknown}} = \frac{n_{\text{known}}}{n_{\text{Unknown}}} \frac{N_{\text{known}}}{N_{\text{Unknown}}} \lambda_{\text{known}} \quad (3.6.2)$$

where the λ 's represent the input wavelengths, the n 's refractive indices of the beams in air, and N 's the relevant number of fringes counted for each laser.

In the present setup, the 632.991 nm line of a stabilized HeNe laser (Coherent Model 200) is used as the known frequency source. First suggested by Balhorn *et. al.* [127] and developed by Niebauer *et. al.* [128], the laser design supports two modes with orthogonal polarizations. The two modes supported within the Doppler width of the Ne line are separated in frequency by $c/2L$ (685 MHz [129]). As the cavity frequency drifts, the intensity of one polarization increases while the intensity of the orthogonal polarization decreases. The HeNe laser is frequency stabilized by locking the cavity length to keep the ratio of the intensities of the two output lines equal. Using a polarizing beamsplitter, a single line stable to within 5 MHz is selected for the output beam.

The accuracy of the Michelson Interferometer is highly dependent upon the alignment of the two beams. In practice, this interferometer is accurate to 300 MHz.

3.6.1 - Gross Alignment of the Interferometer

The following steps describe rough alignment of a Michelson Interferometer. This alignment should only be performed when the interferometer has been grossly misaligned (such as when the HeNe has been removed for maintenance). Designations for all mirrors are given in Figure 3.8 and the locations of all beams upon mirrors M3, M4, and M5

are given in Figure 3.9 (the beam locations on M5 should be mirrored across the mirror plane).

- 1). The HeNe laser should be aligned parallel to the table, just over the edge of M5, and onto M3 approximately 10 mm to the left and 3 mm above the mirror's center.
- 2). The beamsplitter should be placed in a position equidistant from M4 and M5.
- 3). Adjust M3 so that the HeNe beam passes through the beamsplitter (BS) and intersects M4 approximately 3 mm above the mirror's center and horizontally above the edge of the track support farthest from the HeNe laser.
- 4). The HeNe beam reflected from the beamsplitter should intersect M5 3 mm above center and above the edge of the track support farthest from the HeNe laser.

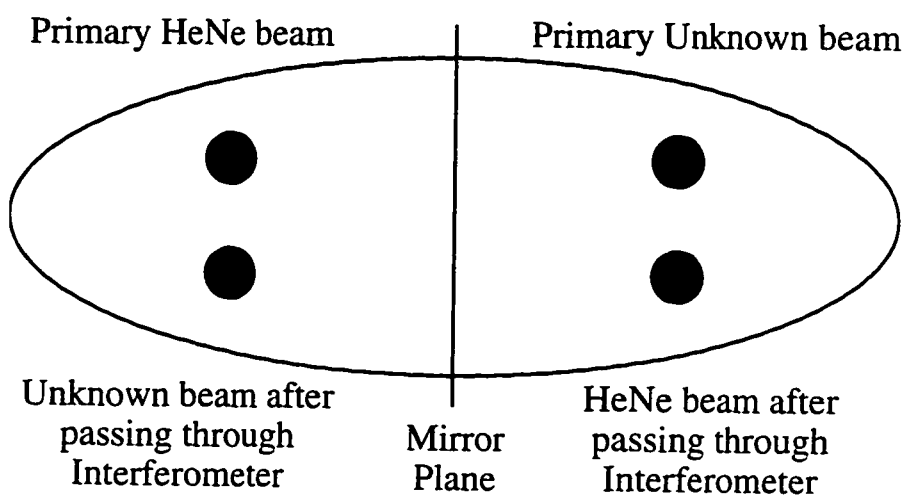


Figure 3.9 - Michelson Interferometer Spot Arrangement

- 5). M4 should be adjusted so that as the corner cube is manually moved along the track the reflected beam does not visibly move from its position on M4.
- 6). M3 is adjusted so that the beam returning from the M4 arm intersects the beamsplitter in the fourth quadrant as observed along the direction of the beam. Iterate between steps 5 and 6 until the alignment is visibly satisfactory.
- 7). Adjust the beamsplitter and M5 so that the beam does not move on M5 as the corner cube is moved along the track and the returning beam roughly overlaps the beam from the M4 arm at the beamsplitter. Iteration in this step almost certainly will be necessary.
- 8). Block the M5 arm.
- 9). Place an iris and a standard laser power detector between the beamsplitter and fringe detector. These should be adjusted so that when removed the fringe detector will be roughly aligned and so that the iris is carefully centered on the reflection from the M4 arm off the beamsplitter.
- 10). Move the corner cube to a position close to M4 and adjust the M3 mirror to maximize the light passing through the iris.
- 11). Move the corner cube to a position close to M5 and adjust M4 to maximize the light passing through the iris. The transmitted power will drop considerably from step 10 because of the increased path length and the divergence of the HeNe beam.
- 12). Repeat steps 10 and 11 until convergence is reached.

- 13). Block the M4 arm and unblock the M5 arm.
- 14). Optimize the M5 arm with the iris in the same position by moving the corner cube close to M5, adjusting the beamsplitter, moving the cube near M4, and then adjusting M5. Repeat this step until convergence has been reached.
- 15). Open the iris fully and remove the detector. Align the fringe detector so that the HeNe beam enters the left detector as observed from the beam. Turn on the air track. If the above steps have been correctly followed, a sine wave should be observed on the oscilloscope over the entire travel of the air track. If not, repeat the above steps.

3.6.2 - Fine alignment of the Interferometer

This procedure should be followed each day to ensure optimum performance of the system. Though theoretically the system should remain fixed and should not require daily realignment, empirically this has not proven to be the case.

Observe the amplitude of the reference output of the fringe detector as the air track moves the corner cube reflectors back and forth. This signal should remain constant, indicating the reflector is moving perpendicular to the beams from both arms of the interferometer. If necessary, make delicate adjustments to first M3 and then the beamsplitter to ensure that the amplitude of the signal remains constant as the corner cubes move along the air track. Either a maxima or minima in the center

of the corner cube travel indicates an error in both the horizontal and vertical directions.

3.6.3 - Alignment of the Unknown Beam

The following steps need to be followed each day for the proper use of the interferometer.

- 1). Direct the unknown beam onto M1 approximately 6 mm below the HeNe beam that is passing out of the interferometer.
- 2). Adjust M1 so that the beam contacts M2 approximately 6 mm below the before mentioned HeNe beam.
- 3). M2 should be adjusted so that the spots on M3 form a box pattern. See Figure 3.9.
- 4). Slight adjustments can now be made to M1 and M2 to ensure a box pattern on M4 and M5 similar to that on M3. Be careful not to adjust any elements inside the interferometer setup as this will destroy the HeNe alignment.
- 5). Observe the amplitude of the unknown output of the fringe detector and make fine adjustments to M1 and M2 to ensure the signal amplitude remains a constant as the corner cube reflectors are translated along the air track. If the signal is visibly truncated, the detector is saturating and filters should be placed immediately in front of the fringe detector block to attenuate the beam. Conversely, if the signal amplitude is below approximately 10 mV, insufficient light is reaching the

detector for adequate fringe detection. Typically, the interferometer requires only 1 mW of input radiation for proper operation.

If all the above steps have carefully been followed, the precision of the interferometer will be approximately 0.01 cm^{-1} . Variations greater than a tenth of a wavenumber indicate either unstable frequency operation of the unknown beam, improper alignment of the interferometer, or signal levels that are out of the fringe detector's acceptable range.

3.7 - The Excimer Laser

The excimer laser used is a Lambda Physik 101-E. It can be operated with a number of different halogen/inert gases as the lasing medium. Operating with an ArF mixture, it is capable of producing 260 mJ / pulse at a 1 Hz repetition rate. This has been made possible by the addition of a recirculating system designed to flush impurities from the laser gas. It is well established that impurities are the major cause of the decline of excimer laser power over time [130-133]. A recirculating system, patterned after the design by Stevens *et. al.* [134], removes gas from the excimer laser cavity and passes it through a liquid nitrogen trap where impurities are frozen out. To reduce the volume of liquid nitrogen used to maintain the cold trap and thus its maintenance demands, copper tubing was folded in half and the two halves silver soldered together to make good thermal contact in a counter-flow heat exchanger. As the hot

gas from the laser is pumped to the liquid nitrogen, it is cooled by the gas returning to the laser.

When the recirculation system is not engaged, the laser output power drops in half after 5 - 10 minutes at a 1 Hz repetition rate. With the recirculator turned on, we have seen no degradation in the pulse power even after 48 hours of continuous operation at 10 Hz. The maximum pulse power has increased from the former maximum of 100 mJ/pulse to 260 mJ/pulse, and the standard deviation of the pulse-to-pulse energy has decreased from 20% to 3% of the total power.

The internal recirculating fan of the excimer limits the pulsed output power at repetition rates above 1 Hz. The output power has been observed to decrease by 65% upon increasing the repetition rate to 10 Hz.

3.8 - Detectors

The detectors used in all experiments to date are liquid nitrogen cooled indium antimonide (InSb) or mercury cadmium telluride (HgCdTe) detectors. The noise characteristics and wavelength sensitivity of these detectors will be deferred until next chapter along with the implications of that noise upon the sensitivity of infrared experiments.

UV and visible radiation can, in a process called flashing, convert the surface of an exposed n-type material to p-type, enlarging the junction area. This will increase the active area of the detector at the cost of lowered impedance and excessive crosstalk and noise. As such, it is to be avoided at all costs. Even illumination from fluorescent lighting is to be

avoided. The effects are more pronounced when the detector is cooled and generally can be reversed by warming to room temperature and recooling. Prolonged exposures will result in irreversible damage detector. Special care should be taken that the ring laser tracer beam used in detector alignment is attenuated so that it is barely visible to the human eye (when working at visible wavelengths, obviously).

The typical response time ($1/e$ time) of the detectors is less than 1 μ second. As the InSb detectors are sensitive to light in the red portion of the visible spectrum, it is possible to measure the time response of the detectors using a excimer laser operating on fluorine atom transitions. Because the pulse duration of the laser operating on these transitions is typically less than 10 nanoseconds (an order of magnitude less than the response time of the infrared detectors), the source can be regarded as a Dirac delta source of light. The result of one such test is given in Figure 3.10. The response time of a pair of detectors connected in series to a single transimpedance amplifier is 0.74 μ seconds. The reason that two detectors are connected to a single amplifier will be deferred until Section 4.8.

3.9 - Software

Data collection in the current setup is handled by five software programs operating simultaneously on three computers in the laboratory.

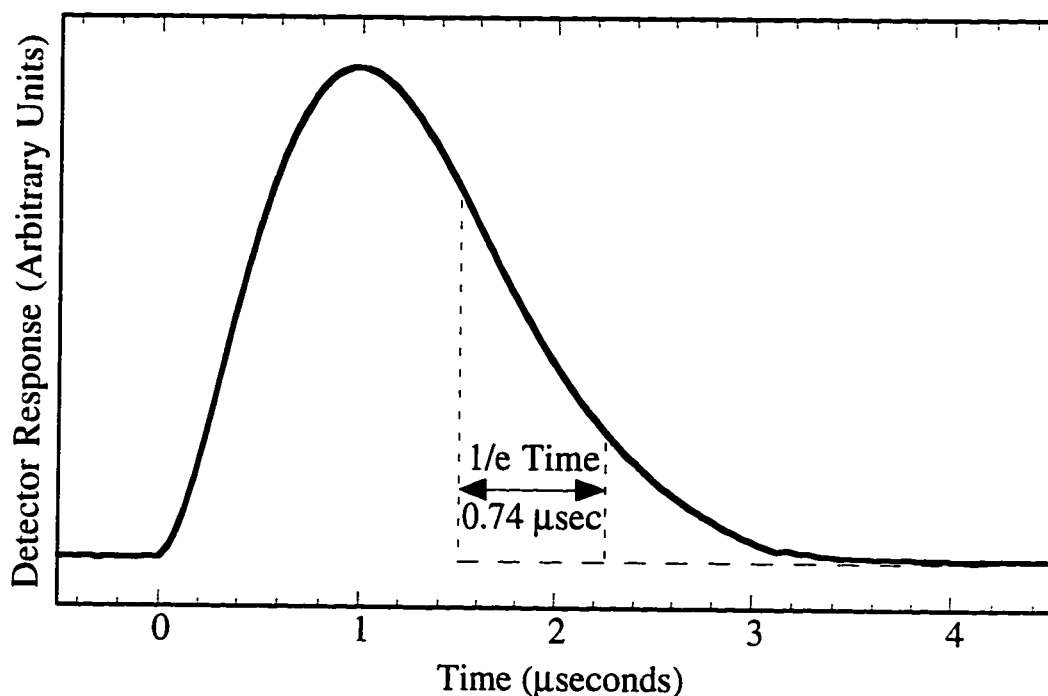


Figure 3.10 - Balanced Indium Antimonide Detector Response Time

3.9.1 - Software used in obtaining a Frequency Spectrum

In order to measure the wavelength of the fixed frequency laser, the fringes from the Michelson Interferometer must be counted, a correction for the index of refraction of air must be made, the unknown wavelength must be calculated from the formula in Equation 3.6.2, etc. All this is handled by a program called 699. The only submenu used (3. Adjust Control Positions) allows the operator to adjust the BRF position of the laser by controlling a stepper motor attached to the BRF micrometer. By hitting the ENTER key, the unknown laser wavelength is displayed. This is recorded at the beginning of each scan for use in the calibration of the spectrum - giving the user a rough idea of the infrared frequency generated.

As the AUTOSCAN.EXE program is performing a scan, it collects all the necessary internal data (VET Data, Laser Power, etc.) Note: the use of capitilization is deliberate - AUTOSCAN refers to the software that interfaces with the entire Autoscan system. No direct provision was made within the AUTOSCAN software for communication with external devices (like transient digitizers). Instead, the authors of the program allowed for the use of User Defined Interrupts (UDIs) which are memory resident interrupt driven programs that execute upon the command INT 61H, which is issued for AUTOSCAN data channels numbering above 10. The form of the interrupt called by 61H is left to the user.

In our particular situation, a 286-8 processor has insufficient speed to accomplish all the data collection and manipulation necessary in the 0.1 seconds between excimer shots so we have chosen to write a small program called TALK.EXE that sends the current channel number over the serial port, waits for a response over the serial line, and passes the returned channel voltage to AUTOSCAN.

The INTRPT program on another computer functions with the DFL.EXE program and directly controls the transient digitizer. Written in assembly language, it functions as a dual gated integrator. It loads the necessary values into the transient digitizer and waits for the digitizer to execute the data collection based on those loaded parameters. After control of the computer is relinquished by the transient digitizer, it sums the data values within user defined time windows, subtracts the pretrigger values, and passes the time channel values to the DFL.EXE program.

The DFL.EXE program runs on a 75 MHz Pentium processor equipped with a transient digitizer and a 12 bit A/D & D/A board (Analogic DAS-12/50) containing multiple input and output channels. This computer is responsible for control of all external data collection. Two A/D channels are used to acquire the reference gas spectra and the external etalon transmission spectrum. Though this function could be accomplished by the Autoscan interface box directly it has been found that there is sufficient noise in the Autoscan power supply so that the A/D converters in the interface box are only stable and accurate to 1 part in 16. By collecting these spectra on the Pentium computer, stability is limited only by signal levels.

The software programs work together to acquire spectra in the following fashion. The AUTOSCAN program on the 286 computer controls the scanning of the 899-29 laser. Upon initiation of a frequency scan, it collects all internal sensor readings and passes control to the TALK program. The TALK program passes the current channel number over the serial port to the Pentium computer and waits for a response over the same serial line. Upon receipt of the first channel number (11), the DFL program initiates the INTRPT program which acquires temporal information from the transient digitizer and sums it into the appropriate temporal bins before returning control back to DFL. The DFL program takes this information and returns channel 11 information to the TALK program over the serial cable. The TALK program conveys channel 11 information to the Autoscan program. Autoscan then asks TALK for the next channel value. TALK conveys the request to DFL and DFL returns

the channel information already collected. This process is repeated until information about each time channel has been acquired by AUTOSCAN. AUTOSCAN then scans the laser to the next frequency point, where the entire process is repeated until the scan is complete.

3.9.2 - Software Used in Obtaining Temporal Information

A short spectrum is required to locate an absorption peak prior to conducting kinetics experiments, but because signal levels are often too low to be visible on the AUTOSCAN screen, locating a peak is difficult under the software described in the previous section. By connecting the -5 to +5 volt output of the 12 bit D/A port to the External Scan connection in the back of the 899-21 laser control box the laser is tuned by up to 30 GHz. The DFL program controls the 899-21 scan, displays and stores the results, etc. The ultimate resolution of this arrangement is therefore $30 \text{ GHz} / 2^{12} = 7.3 \text{ MHz}$. This implies a maximum error off an absorption peak of 3.6 MHz (half the resolution size) - far too small to be detected under most circumstances.

When conducting kinetics experiments the 899-29 laser functions as the fixed frequency source and the 899-21 as the tunable laser, in contrast with the spectroscopic arrangement.

Chapter 4 - Difference Frequency Generation in AgGaS₂

AgGaS₂ belongs to the A^IB^{III}C^{VI} class of compound semiconductors. Commonly called silver thiogallate or silver gallium sulfide, it is formed in the chalcopyrite structure (point-group symmetry $\bar{4}2m$) and is both birefringent and acentric. It has a relatively wide range of optical transparency; it has a high damage threshold, and a high nonlinear coefficient. Silver thiogallate is phasematchable over a wide range of input and output frequencies.

4.1 Gross Physical Properties

Crystals of AgGaS₂, commonly referred to as silver thiogallate or silver gallium sulfide, are typically yellow to green. It is suspected that the variation in color is due to stoichiometric variations [135] or to Fe atom inclusions within the crystal [136].

The transmission range of AgGaS₂ is limited at the short wavelength end (near 500 nm) by the fundamental electronic band edge (band gap) and at long wavelengths ($\geq 13 \mu\text{m}$) by two-phonon absorption processes [137]. Detailed studies of the electronic absorption have been made by Tell *et. al.* [138,139] and by Yu *et. al.* [140]. The extraordinary polarization band edge is at a wavelength ~20 nm longer than the ordinary polarization edge. Holah *et. al.* [141,142] have investigated the Reststrahlen absorption, where the two-photon infrared cutoff is polarization independent.

AgGaS₂ exhibits optical activity off the optic axis near 497 nm where the crystal becomes temporarily loses its linear birefringence as a result of a change in the sign of the linear birefringence [143,144]. For wavelengths removed from this wavelength the much larger magnitude of the linear birefringence completely dominates the propagation polarization [145,146]. Optical activity is negligible for most nonlinear mixing experiments.

The cw damage threshold of the crystal is uncertain at the present date. Table 4.1 lists the damage threshold for various pulsed experiments where the damage threshold is listed according to peak power. It must be noted that the various lasers produced pulses of varying duration, and this accounts for some of the variations in damage threshold as does the quality of the various crystals tested. The damage threshold definitely decreases as the laser wavelength approaches the electronic band edge.

There is considerable disagreement among the measurements of the

Table 4.1 - Damage Threshold of AgGaS₂

Wavelength (μm)	Reference	Damage Threshold (MW/cm^2)	Pulse Duration
0.590	[147]	2	1 μs
0.625	[147]	3	500 ns
0.694	[148]	10	10 ns
0.694	[149]	0.6	30 ns
0.694	[135]	20	10 ns
1.06	[135]	23	35 ns
1.1 - 1.4	[150]	> 1000	< 1 ps
10.6	[51]	25	200 ns

effective nonlinear coefficient (d_{36}) in the AgGaS₂ crystal. As can be seen in Table 4.2, published values of the coefficient vary from 9 to 57 pm/V [107,108,151-157]. The frequency dependence of the nonlinear coefficient can mostly be removed through defining the quantity Miller's delta [158].

$$d_{36} = \delta_{36} \cdot \{ \epsilon_0 \cdot (n_p^2 - 1) \cdot (n_s^2 - 1) \cdot (n_i^2 - 1) \} \quad (4.1.1)$$

When this is done and the supposedly frequency independent δ_{36} is examined, the discrepancy rises to a factor of 8 between the highest and lowest values. The value reported from spontaneous parametric fluorescence (SPG) experiments are consistently twice as large as those from difference frequency generation, sum frequency generation, or second harmonic generation experiments. Maker fringe methods (non-phased matched second harmonic generation) usually give the highest values, equal to or greater than those obtained from SPG experiments. Early published values of KTP's nonlinear coefficient were overestimated in crystals of small dimension and/or poor quality [152,159,160]. A similar effect may be in evidence in the nonlinear measurements of AgGaS₂.

The problem in predicting the theoretical difference frequency power is compounded because one finds that the predicted generated infrared power depends on the square of the nonlinear coefficient (Equations 2.4.1, 2.5.2, and 2.5.3). Thus, there is a factor of 64 discrepancy in the theoretical conversion efficiency, depending on the coefficient used in the calculation. In this work a δ_{36} value of 12 pm/V will be used in order to be consistent with the results of stimulated

Table 4.2 - Nonlinear coefficient d_{36} in AgGaS₂

λ_1 (μm)	λ_2 (μm)	λ_3 (μm)	δ_{36} (pm/V)	d_{36} (pm/V)	Method (Year)	Ref.
5.1	1.6	0.88	0.08 ± 0.02	9 ± 2	DFG conversion efficiency (1991)	[107]
10.2	0.842	0.778	0.11 ± 0.02	12.4 ± 1.7	SFG conversion efficiency (1997)	[108]
2.53	1.265	0.842	0.12 ± 0.01	13.4 ± 1.5	DFG conversion efficiency (1997)	[108]
2.53	2.53	1.265	0.12 ± 0.03	13.9 ± 2.8	SHG relative to KTP (1994)	[151]
2.53	2.53	1.265	0.13 ± 0.02	13.7 ± 2.2	SHG conversion efficiency (1997)	[108]
6.0	1.30	1.06	0.13	14	DFG conversion efficiency (1984)	[152]
10.6	10.6	5.3	0.20 ± 0.07	18.6 ± 6	SHG wedge relative to GaAs (1971)	[153]
2.454	2.454	2.612	0.22 ± 0.05	20 ± 4	SHG Maker relative to GaAs (1974)	[154]
5.505	1.319	1.064	0.22 ± 0.02	23.6 ± 2.4	Spontaneous Parametric Fluorescence (type-II CPM) (1994)	[155]
7.8	0.65	0.6	0.22 ± 0.04	31 ± 5	Spontaneous Parametric Fluorescence (type-I NCPM) (1992)	[156]
1.06	1.06	0.53	0.23 ± 0.04	34 ± 5	SHG Maker relative to SiO ₂ (1974)	[154]
10.6	10.6	5.3	0.62 ± 0.19	57 ± 7	SHG Maker relative to GaAs (1971)	[157]

parametric processes and with the more recent nonlinear coefficient measurements.

The phasematching condition in AgGaS₂ is generally satisfied by angle tuning of the crystal or by tuning both input wavelengths. Due to a rather low change of the index of refraction with temperature [161] and the instability of the crystal at elevated temperatures, temperature tuning over any broad range is impractical. Canarelli *et. al.* [157] have determined a temperature tuning value of $0.65 \text{ cm}^{-1} / ^\circ\text{C}$ for collinear type-I noncritical phasematching near 1300 cm^{-1} . AgGaS₂ is mechanically brittle and expensive, making pressure tuning of the crystal impractical. A quasi-phasematched AgGaS₂ crystal has not been produced to date. The crystal presently employed in this laboratory measures $4 \times 4 \times 45 \text{ mm}$, limiting possible angle tuning so that two tunable sources are used to satisfy the phasematching condition.

4.2 The Growth of AgGaS₂

Produced by the Bridgman-Stockbarger method, initial crystal growth experiments on AgGaS₂ exhibited a number of problem areas [101]. The first crystals produced contained microcracks throughout the crystal, inclusions, composition gradients, and twinning. Because of these imperfections, crystals were often appeared milky in appearance and had poor optical quality due to small micrometer-size scattering centers [138,162-166]. Early crystals were highly colored.

Two breakthroughs made it possible to grow macroscopic single crystals of AgGaS_2 . The first was the discovery of Korczak and Staff [165] that the crystal expands along its c-axis upon cooling. Expansion was the cause of the microfracturing in the crystal as it cooled within the confines of the evacuated and sealed fused-quartz ampoules. This problem was solved by orienting seed crystals so that the crystallographic c-axis is close to the axis of the growth ampoule where there is sufficient room to expand after cooling. Ampoules are slightly tapered so that the diameter increases down the ampoule and mechanical restrictions along the crystal lengths are avoided.

The second important advance was the development of a heat-treatment procedure to eliminate the scattering centers in as-grown crystals [166]. Crystals, as grown, were found to have a milky appearance caused by micrometer wide one hundred micrometer long microcracks consisting of Ga and S rich precipitates surrounded by localized strain fields. Boules of the crystal were heat treated in a sealed quartz ampoule for 10 to 15 days at 900 °C in the presence of 0.5% weight excess Ag_2S . During this period, the Ga and S rich material volatilizes from the surface of the crystal and reacts with the excess Ag_2S to form AgGaS_2 , resulting in a crystal of optical quality.

4.3 The Index of Refraction

In part because the phasematching condition is so dependent upon the index of refraction, the index of refraction in AgGaS_2 has been studied by

many groups [104,109,135,154,167,168]. Traditionally, data on the index of refraction at a variety of wavelengths is acquired and the data is fit to modified versions of classical (Sellmeier) dispersion equations for an ensemble of uncoupled electronic and ionic oscillators [169], where

$$n(\lambda)^2 = A + \frac{B\lambda^2}{\lambda^2 - C} + \frac{D\lambda^2}{\lambda^2 - E} \quad (4.3.1)$$

This form (or modifications of the above) is sufficient to describe the wavelength dependence of the index of refraction of AgGaS₂ over its transparency range. Appendix 4.1 is a listing of the literature dispersion relations as well as details on the method used to acquire the data, the relevant wavelength ranges, etc.

Figure 4.1 displays the indices of refraction versus wavelength for the dispersion relations given in the literature. Using these equations to calculate the wavelengths necessary for noncritical phasematching, it is found that all these equations match the experimental results to within 3 nm for all data points. The equations developed by Roberts [104] are marginally more accurate and will henceforth be used for all calculations. It should be remembered that the phasematching wavelengths are not temperature independent and that the use of high power pump lasers will shift the phasematching wavelengths away from those calculated in the above equations because the crystal is heated by absorption.

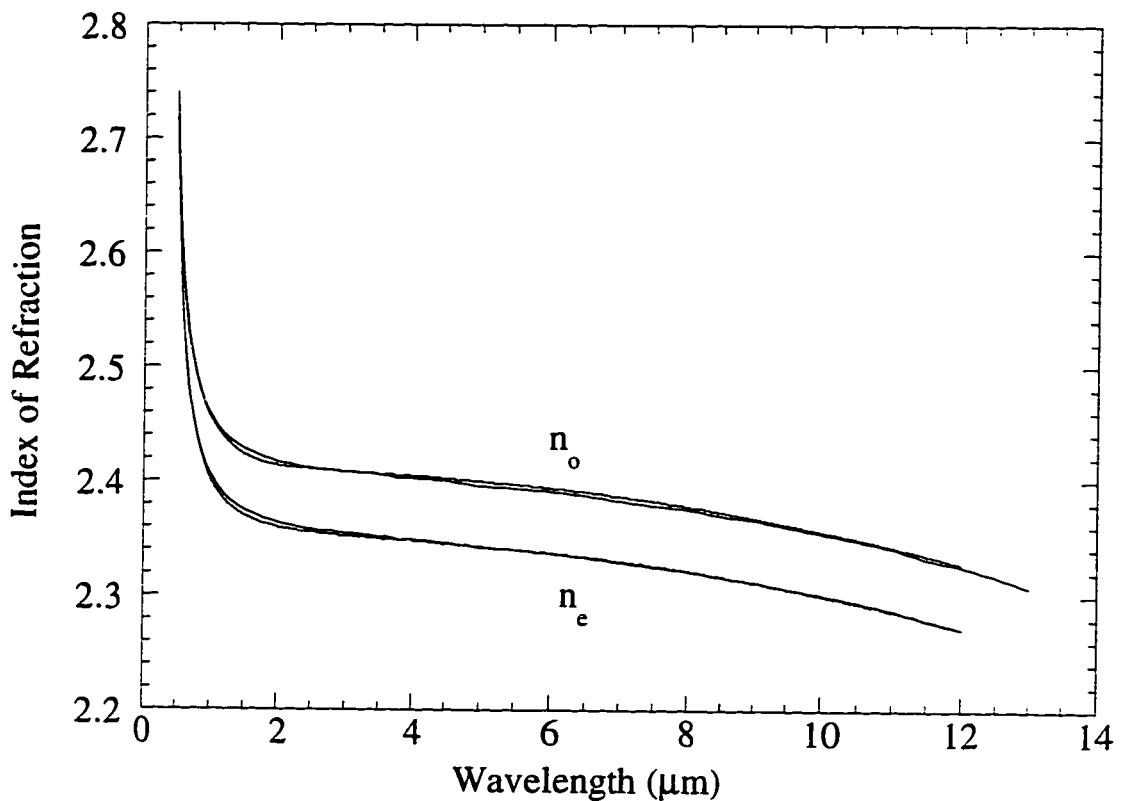


Figure 4.1 - Index of Refraction Comparison in AgGaS₂

4.4 The History of Downconversion in AgGaS₂

AgGaS₂ has been used for the down-conversion of light into the mid-infrared for over a decade. The first reported DFG experiment utilizing AgGaS₂ was conducted by Bethea *et. al.* [170], who mixed the 1.06 and 1.318 μm lines of a single Nd:YAG laser to generate radiation at 5.52 μm .

The first tunable mid-infrared spectrometer based on silver thiogallate was reported by Hanna *et. al.* [148], who mixed a ruby laser with ruby-pumped dye lasers to generate radiation from 4.6 to 12 μm . Though this work was a large step forward in source development, no

information was given in this regard on the applicability of this source to spectroscopy (e.g. linewidth, pulse-to-pulse reproducibility, etc.).

Elsaesser *et. al.* [171] reported the mixing of picosecond pulses from a mode-locked Nd:YAG laser and a traveling wave laser (1.20 - 1.46 μm) in a difference frequency generation configuration utilizing angle tuning of the crystal to generate tunable 3.9 - 9.4 μm idler wavelengths. The conversion efficiency on a photon basis was measured as a few percent, but the spectral resolution of this instrument ($\Delta\nu \sim 6.5 \text{ cm}^{-1}$) precludes its use in a standard high-resolution spectroscopic experiment. Pulsed mixing has been verified by other researchers with similar results in the picosecond [150,151,172,173] and nanosecond [174] regimes.

Seymour and Zernike [175] generated tunable radiation from 5.5 to 18.3 μm in AgGaS₂. Though the usual transparency range quoted for silver gallium sulfide is quoted as 500 nm through 13 μm , Seymour and Zernike point out (as did Bhar and Smith [137]) that the long wavelength absorption is a two-phonon process and another window of transparency exists beyond 14 μm . By mixing the output of nitrogen pumped pulsed dye lasers in a noncritically phasematched type-I DFG interaction, they were the first to demonstrate this window in a nonlinear process.

The first fully tunable, narrow linewidth source based on difference frequency generation in silver thiogallate was demonstrated at Rice in 1992 [176]. Argon ion pumped tunable DCM and Rhodamine 6G dye lasers were used in noncritical type-I phasematching to generate continuously tunable radiation from 7-9 μm (1100 - 1450 cm^{-1}) with an estimated linewidth of approximately 1 MHz. The experimental powers

produced were probably measured in nanowatts (though the paper quotes a value of 10 μW , later data on the responsivity of the detector used in the experiment indicates that the generated power was at least an order of magnitude less than this). The tuning range was later extended from 4.8 to 6.5 μm (1550 - 2100 cm^{-1}) by mixing a DCM dye laser with a titanium:sapphire laser [177]. In the most recent work in this laboratory, the tuning range has been extended to the 3.7 to 4.4 μm region (2250 - 2650 cm^{-1}), the infrared conversion efficiency increased by a factor of 11 with up to 172 μWatts measured at the detector, and fluctuations in the infrared source power decreased by 99%. These latest improvements will be described in detail in following sections of this chapter but remain otherwise unpublished.

Fan *et. al.* [109] demonstrated the first optical parametric oscillator based on the thiogallate crystal. Tunable from 1.4 to 4.0 μm , it utilized two flat mirrors in a singly resonant cavity and was pumped with the 1.064 μm output of a pulsed Nd:YAG laser. Since then other researchers have used the AgGaS_2 crystal in a variety of ways, from using it as in optical parametric amplifier (OPA) [178-180] to using diode lasers to create a prototype portable *in-situ* gas sensor [181-185]. These last, also pioneered at Rice University, are especially exciting, offering the possibility of using difference frequency generation in a practical setting rather than confined to the university research laboratory.

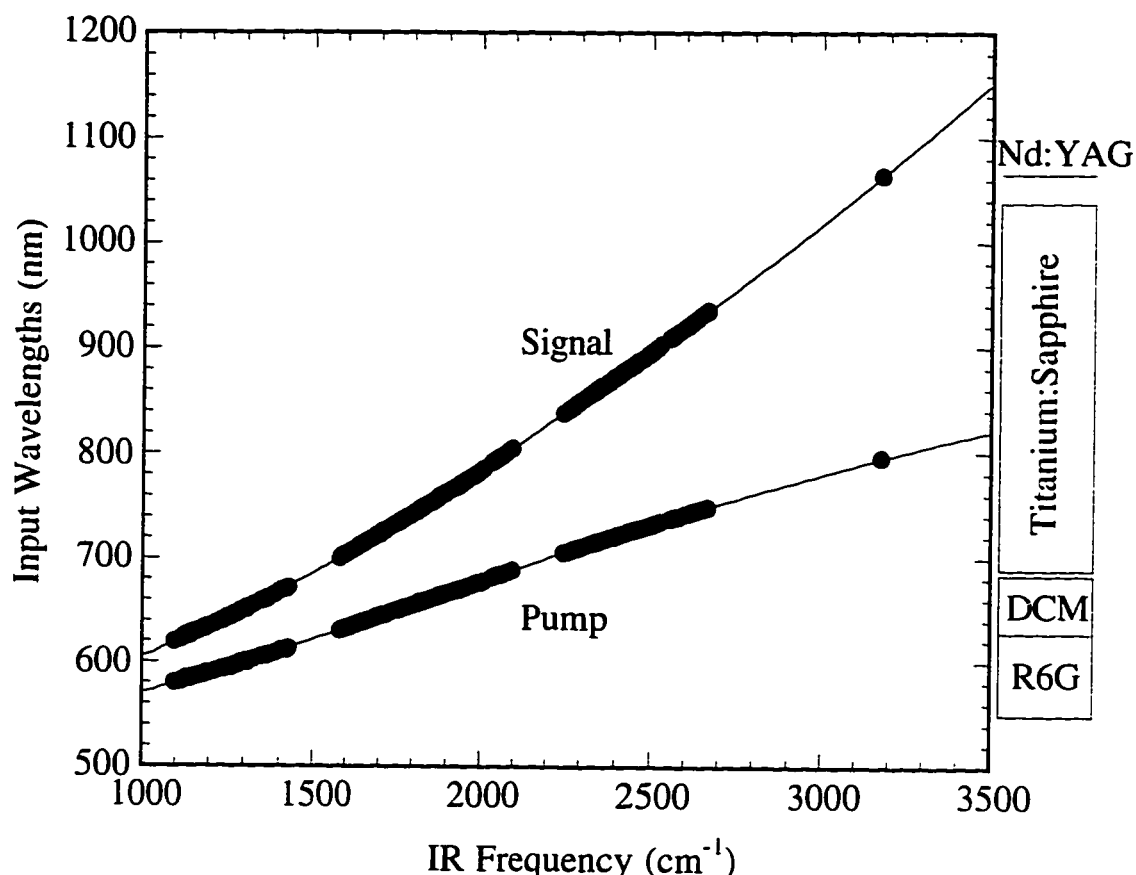


Figure 4.2 - Optimized Phasematching Wavelengths for Type-I DFG in Silver Thiogallate

4.5 Frequency Tuning in Difference Frequency Generation

Figure 4.2 displays the calculated versus theoretical wavelengths required for noncritical type-I phasematching and Table 4.3 lists the experimental points. The frequencies listed in Table 4.3 are optimized for approximately 0.5 watts in each laser (heating of the crystal due to the absorption at this power changes the phasematching frequencies by approximately one wavenumber). Circles in Figure 4.2 represent a sampling of experimentally determined points and lines the theoretically calculated points based on the Roberts' Sellmeier equations [104] and

Table 4.3 - Experimentally Determined Points for Peak IR Power in Noncritically Phasematched AgGaS₂

λ_p (nm)	λ_s (nm)	ν_i (cm ⁻¹)	λ_p (nm)	λ_s (nm)	ν_i (cm ⁻¹)
580.040	619.400	1095.536	609.000	665.300	1389.548
580.960	621.220	1115.531	611.010	668.410	1405.466
582.010	622.500	1117.578	612.000	670.600	1424.461
582.420	623.350	1122.028	613.010	671.660	1427.850
582.960	623.760	1127.388	630.254	699.936	1579.605
583.970	625.800	1131.199	630.254	699.936	1579.605
584.040	625.940	1144.622	631.119	701.377	1587.198
584.960	626.410	1146.143	631.119	701.377	1587.198
585.690	628.280	1149.684	632.259	703.262	1596.837
585.980	629.000	1157.409	633.131	704.777	1605.641
586.090	629.000	1163.974	634.290	706.717	1615.724
586.980	629.470	1167.178	635.221	708.249	1623.220
586.990	630.330	1171.651	636.168	709.889	1632.418
588.020	632.100	1183.051	637.272	711.742	1641.843
588.120	632.100	1185.942	638.340	713.534	1650.874
589.010	633.500	1192.321	639.228	715.075	1659.313
589.230	633.900	1195.944	640.214	716.651	1665.980
591.060	636.830	1215.979	641.093	718.172	1674.113
591.070	636.900	1217.418	642.284	720.307	1686.485
591.300	637.200	1218.230	643.185	721.864	1694.594
592.950	639.930	1234.019	644.078	723.406	1702.562
593.120	639.960	1238.119	645.284	725.401	1711.578
594.880	642.900	1251.839	646.206	727.042	1720.566
595.030	642.920	1255.595	647.132	728.671	1729.177
595.050	643.420	1263.363	648.180	730.498	1738.513
596.930	646.000	1272.507	649.181	732.273	1747.910
599.030	649.210	1290.318	650.175	734.099	1758.341
599.050	649.360	1293.319	651.182	735.791	1765.874
599.960	651.100	1309.153	652.180	737.590	1775.521
600.970	652.290	1309.161	653.181	739.328	1783.906
600.980	652.310	1309.355	654.179	741.167	1794.098
602.930	655.410	1328.048	655.170	742.933	1803.055
605.070	658.890	1349.973	656.181	744.734	1812.083
605.330	659.700	1361.509	656.196	744.759	1812.188
605.980	660.600	1364.441	656.196	744.759	1812.188
607.030	662.050	1369.050	657.180	746.512	1820.891

Table 4.3 - (continued)

λ_p (nm)	λ_s (nm)	ν_i (cm ⁻¹)	λ_p (nm)	λ_s (nm)	ν_i (cm ⁻¹)
658.174	748.285	1829.623	709.700	847.564	2291.940
658.176	748.289	1829.724	710.501	849.221	2299.080
659.189	750.114	1838.857	711.829	851.998	2311.189
660.183	751.893	1847.559	713.183	854.759	2322.450
661.183	753.682	1856.027	714.475	857.567	2335.399
661.191	753.705	1856.613	715.518	859.816	2345.479
662.216	755.580	1865.947	716.210	861.321	2352.310
663.189	757.327	1874.323	717.116	863.292	2361.180
664.184	758.918	1879.405	717.405	863.794	2362.290
665.218	760.768	1888.052	717.910	865.014	2368.830
666.090	762.577	1899.005	719.224	867.864	2381.330
666.517	763.105	1899.549	720.832	871.349	2396.400
667.459	765.287	1915.201	722.160	874.257	2409.060
668.750	767.620	1925.992	723.817	877.780	2423.260
669.724	769.430	1934.890	725.406	881.321	2438.790
670.702	771.250	1943.786	726.766	884.305	2451.280
672.006	773.630	1954.744	728.106	887.311	2464.250
672.989	775.210	1959.354	729.436	890.309	2477.181
673.955	777.290	1972.574	731.030	893.952	2493.040
674.945	779.120	1981.028	732.403	897.022	2505.680
676.265	781.600	1992.834	733.847	900.117	2517.150
677.261	783.500	2002.115	735.330	903.231	2527.970
678.245	785.330	2010.435	737.882	909.469	2556.870
681.593	791.240	2033.121	739.267	912.650	2569.811
682.607	793.204	2042.620	740.522	915.852	2585.181
683.631	795.280	2053.587	741.915	919.050	2597.840
684.653	797.240	2062.664	743.002	921.659	2608.920
685.322	798.530	2068.670	744.370	924.941	2622.680
686.347	800.507	2077.807	745.729	928.188	2636.021
687.376	802.490	2086.864	746.829	930.823	2646.771
688.409	804.500	2096.167	747.917	933.480	2657.860
705.255	838.335	2250.859	748.746	935.506	2666.260
706.239	840.484	2261.609	795.500	1064.504	3176.664
707.274	842.645	2271.399	708.371	844.823	2280.090

assuming that the power is maximized for perfect phasematching ($\Delta k = 0$). As seen in Figure 4.2, a wide infrared tuning range can be achieved at the cost of a correspondingly wide tuning range in both the pump and signal wavelengths. Coherent 899-21 ring lasers equipped with Rhodamine 6G dye, DCM Special dye, or a Titanium:Sapphire rod as the gain media can cover most of the range. The tuning range of these media are given on the right side of the graph for reference. Characteristics of these sources were discussed in detail in the previous chapter (Section 3.2). The highest idler frequency point in Figure 4.2 was obtained by mixing the output of a Ti:Sapphire laser with a Nd:YAG laser [181].

The gaps in the experimentally determined phasematching points in Figure 4.2 arise because of the difficulty in tuning these ring lasers between 690 and 695 nm. DCM dye gain is insufficient to lase at wavelengths above 690 nm and the reflectivity of broadband coatings of the short-wave Ti:Sapphire mirrors has become too low to provide stable operation below 695 nm. In fact, the standard broadband tuning range of the Ti:Sapphire laser extends only to 715 nm - to tune below this a DCM tweeter mirror and output coupler is used in the Ti:Sapphire ring laser to increase the losses at longer wavelengths and prevent mode-hopping. Coherent has developed mirrors with coatings suitable for single-frequency operation at wavelengths as short as 685 nm, but they are custom items and are not commercially available. Kiton Red dye is available to cover this wavelength range but requires a large frame krypton ion laser as a pump source.

4.6 Phasematching Bandwidth

A typical frequency spectrum is obtained by fixing the frequency of the 899-21 and scanning the 899-29 (the Autoscan laser). The spectrometer is limited to 2 cm^{-1} scans because the phasematching condition (Section 2.4.1) produces low infrared power at the beginning of a scan, reaches a maximum near the middle of the scan, and decreases again with a FWHM of 1 cm^{-1} . Figure 4.3 displays the result of a scan near 2461 cm^{-1} . Both theoretical predictions take into account the Fresnel losses on all surfaces, used a d_{eff} value of 12 pm/V [186] , the index of refraction values predicted from Roberts' Sellmeier coefficients [104], utilized a 45 mm crystal length, 500 mW in the pump laser, and 450 mW in the signal laser. A circular Gaussian beam with $w_s = 27.578 \text{ }\mu\text{m}$ and $w_p = 32.255 \text{ }\mu\text{m}$ was used in Equations 2.4.1, 2.5.2, and 2.5.13

The asymmetry in the phasematching peak is an artifact of focusing the drive beams into the crystal, reminiscent of the effects of overfocusing in second-harmonic generation studied by Boyd and Kleinman [21]. As a Gaussian beam passes through the focus region, the sign of the exponential term describing its transverse envelope is reversed. This is equivalent to shifting the phase of the wave by π in an effect called the Guoy phase shift [187]. In general, the nonlinear polarization p_n will experience a shift that is larger than that experienced by the incident wave of amplitude A_n . Thus, the nonlinear polarization will be unable to couple efficiently to the generated wave unless a negative wave vector mismatch Δk is introduced to compensate for the phase shift due to the passage of the

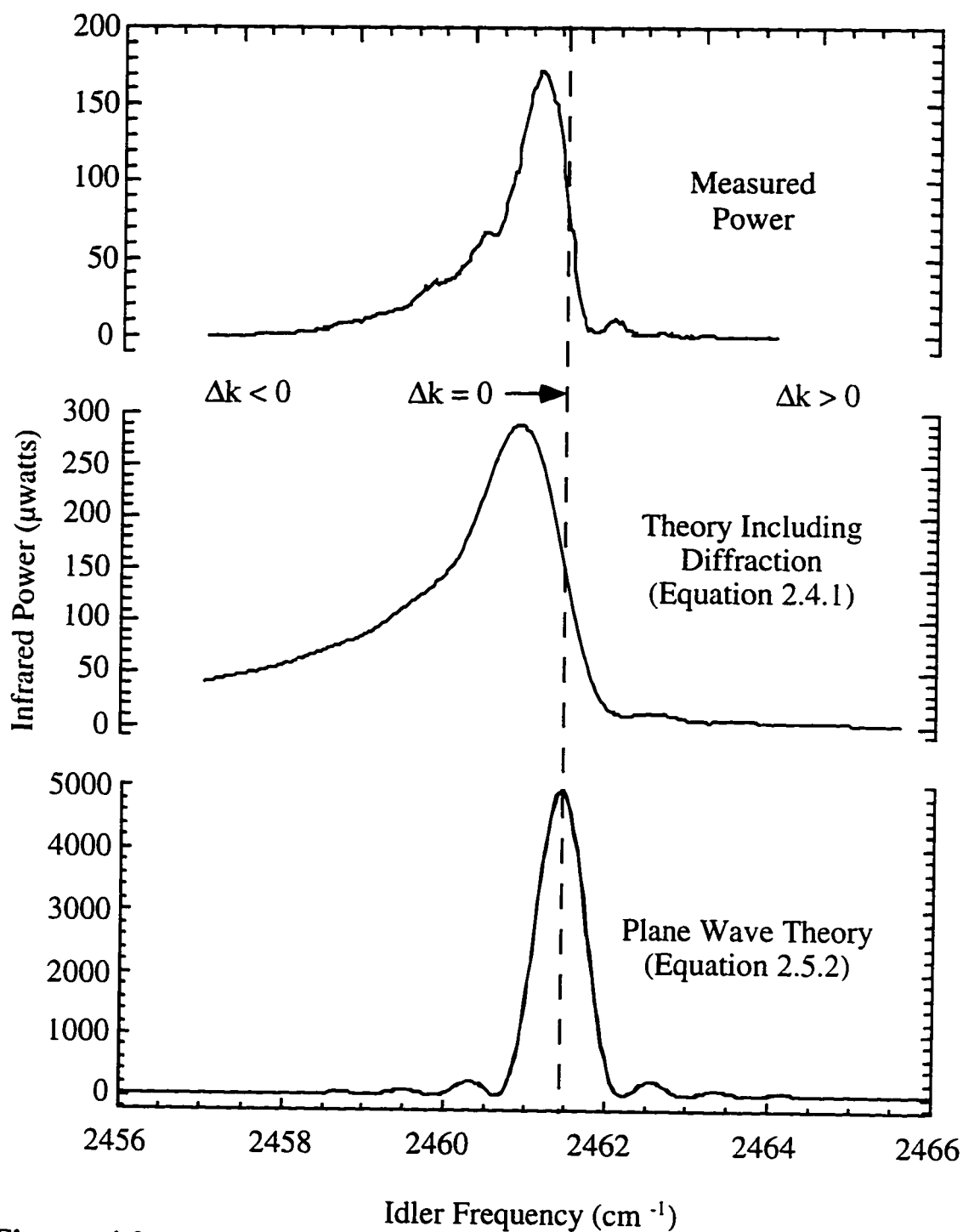


Figure 4.3 - The Phasematching Bandwidth in a 45 mm Long Silver Thiogallate Crystal

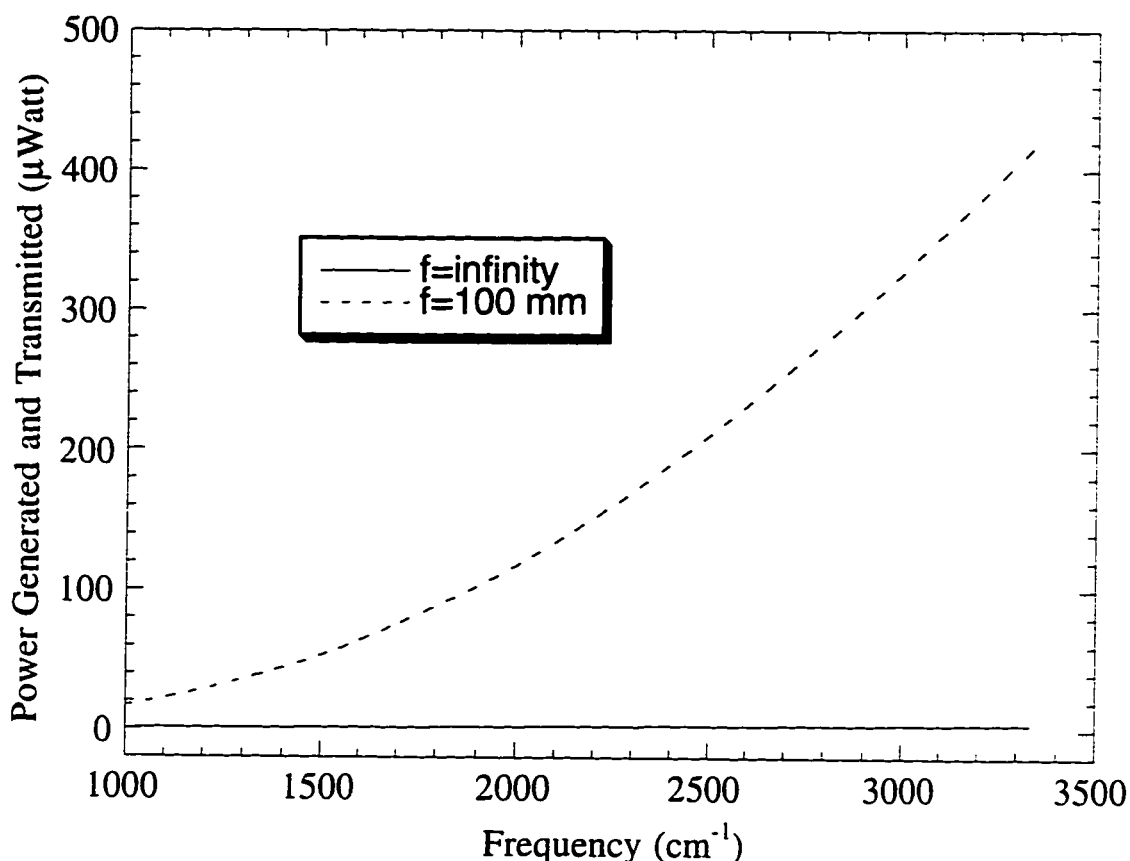


Figure 4.4 - Theoretical Power in AgGaS₂ versus Wavelength : Unfocused ($w_s = w_p = 300 \mu\text{m}$) versus Focused Beams ($f=100 \text{ mm}$)

incident wave through its focus.

As can be seen in Equation 2.4.1, the infrared power generated in the DFG process depends on all three wavelengths involved in the conversion process. Figure 4.4 displays a calculation of the theoretical power as a function of the transmitted idler frequency (accounting for Fresnel losses at the rear surface of the crystal), with the upper trace reflecting the power generated with focused gaussian beams ($f=100 \text{ mm}$) and the lower assuming the plane wave approximation ($w_s = w_p = 300$

μm). The transmitted pump and signal laser powers were both assumed to be 500 mW. Clearly, idler power depends a great deal not only on the wavelengths involved, but the focusing of the beam, and thus it is very important to understand this process.

4.7 Power Scaling in AgGaS₂

Much of the following text appears in the paper "CW difference frequency generation using AgGaS₂: problems encountered in power scaling" [188]. The text of the paper has been expanded upon in sections to clarify points and an effort has been made to correct the errors contained within the paper. A discussion of these errors will follow the text.

4.7.1 Problems Encountered in Power Scaling

IR power measurements were performed at 1903.3 cm^{-1} , the peak of the InSb detector spectral response function. The pump and signal waves required to produce IR at this frequency are $\nu_{\text{pump}} = 15013.3\text{ cm}^{-1}$ (666.076 nm) and $\nu_{\text{signal}} = 13110.0\text{ cm}^{-1}$ (762.776 nm). The corresponding value for μ (Equation 2.5.8) is 0.8775. The values of $h(\mu=0.8775, \xi)$ (Equation 2.5.14) are approximately shown for the $\mu = 0.9$ curve in Figure 2.3. The value $h_{\text{max}}(\mu=0.8775, \xi)$ occurs for $\xi \sim 1.125$ and the function displays minimal dependence on the focusing parameter for $\xi \sim 0.7$ to 2.2.

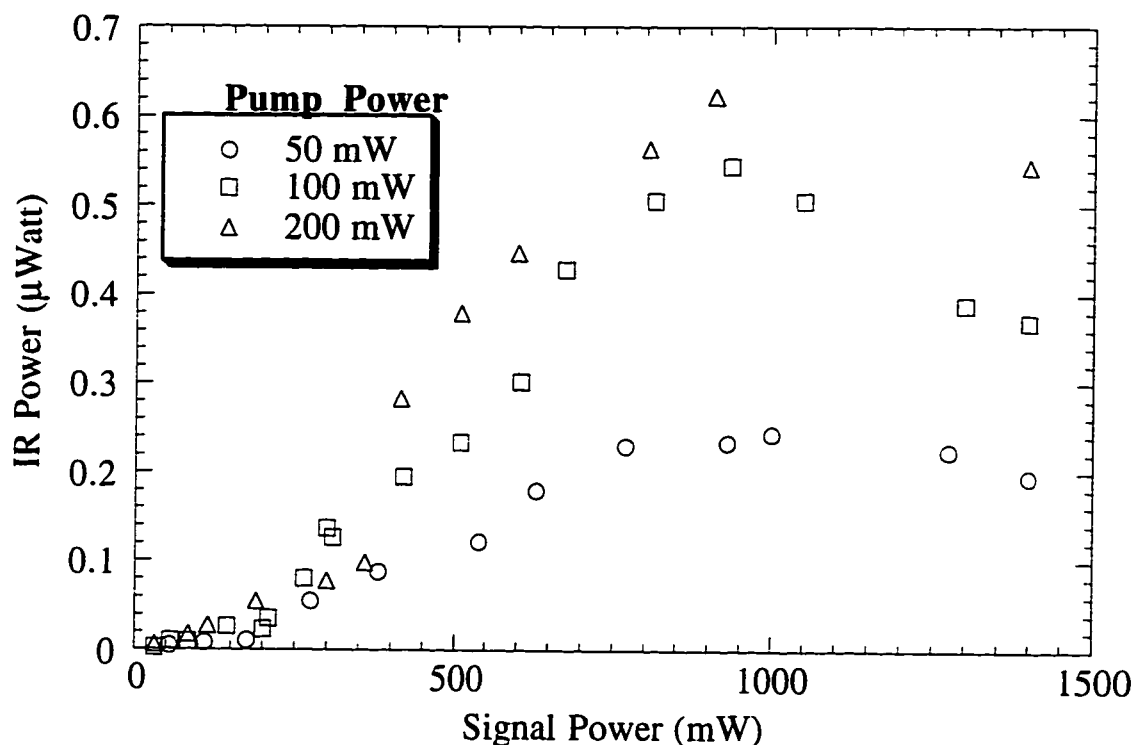


Figure 4.5 - Infrared Power for Unfocused Beams

IR powers were measured for a series of focusing conditions (focal lengths $f = \infty$, 400 mm, 250 mm, and 100 mm) by placing a lens in the path of the copropagating beams such that the calculated position of the beam waist was at the center of the AgGaS₂ crystal [assuming vacuum propagation]. The pump laser power (P_{pump}) was adjusted by introducing neutral density filters into its path and measuring the power just prior to the AgGaS₂ crystal. The signal laser power (P_{signal}) was subsequently varied using neutral density filters and the resulting IR power recorded as a function of f , P_{pump} , and P_{signal} . Results for the case of $F = \infty$ (no focusing lens or the plane wave approximation) and $F = 100$ mm are shown in Figures 4.5 and 4.6, respectively.

Table 4.4 lists the experimental and theoretical IR powers for all of the focusing conditions used in this study. For $\mu = 0.8775$, the maximum IR power yield predicted by Equation 2.5.14 occurs for $\xi = 1.125$. Using our experimental configuration, this would require a lens having $f \sim 165$ mm. It is apparent from the experimental results that slight over focusing provides increased IR power compared to the calculated optimum, although $h(\mu, \xi)$ for the most tightly focused case considered ($f = 100$ mm, $\xi = 1.893$) only differs by 1% from the maximum possible value.

The curves in Figures 4.5 and 4.6 illustrate the typical characteristics observed when attempting to maximize the IR power output. For a fixed value of P_{pump} , there are three distinct IR conversion regimes as a function of P_{signal} . For $P_{\text{signal}} \leq 200$ mW the IR power scales

Table 4.4. Experimental and Calculated IR Powers.

f (mm)	ξ	$h(\mu, \xi)$	^a Calc. P_i ($\mu\text{W}/\text{W}^2$)	^b Expt. P_i ($\mu\text{W}/\text{W}^2$)	<u>Expt.</u> <u>Calc.</u>
∞	0.003	0.003	7.1	5.5	0.775
400	0.063	0.056	101	22	0.218
250	0.224	0.118	215	42.7	0.198
100	1.893	0.159	288	109	0.378

- a. Calculated powers have been corrected for Fresnel losses at the entrance and exit surfaces of the crystal.
- b. Experimental IR power efficiencies were determined from the linear portion of the P_i vs. P_s curve, as described in the text.

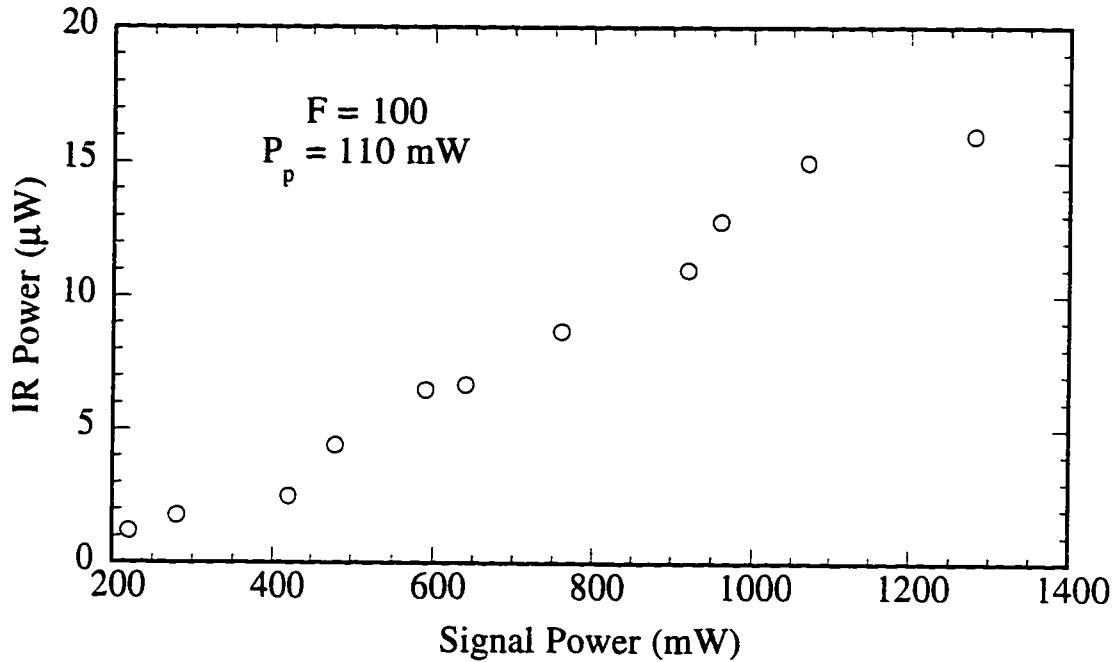


Figure 4.6 - Infrared Power for Focused Beams

linearly with P_{signal} , but the slope efficiency is less than that observed for the intermediate power regime. This is most likely due to the choice of phase matching frequencies which are optimized for higher input powers. For intermediate input power levels, $200 \text{ mW} \leq P_{\text{signal}} \leq 800 \text{ mW}$, the IR power output is still a linear function of P_s , but the conversion efficiency is improved. For $P_{\text{signal}} \geq 800 \text{ mW}$ there is a marked decrease in the IR power output. This decrease in power is usually accompanied by a noticeable "blooming" of the visible beams that have passed through the crystal. At higher input powers a slow, time dependent shift in the frequency associated with the maximum IR power output is also observed.

4.7.2 Power Scaling Analysis

The single mode ring lasers used in this work have excellent gaussian beam properties, although there may be some slight astigmatism when the laser cavities are optimized for maximum TEM₀₀ output power [189]. Measured values of M^2 for the lasers used in this study were 1.0 within the 5% experimental uncertainty of the measuring process using the Coherent Mode Master. Therefore, purely gaussian beam behavior was assumed in the analysis. The pump and signal beam parameters were calculated assuming that $\omega_0(\text{pump}) = 275 \mu\text{m}$, $\theta_{1/2}(\text{pump}) = 0.80 \text{ mrad}$, $\omega_0(\text{signal}) = 285 \mu\text{m}$, $\theta_{1/2}(\text{signal}) = 0.85 \text{ mrad}$ and that the ω_0 position for each laser was located inside the laser 5 cm from the output coupler. The desired beam properties at any point along the propagation path were then obtained by computing the appropriate ABCD matrix algebra. Of special interest are the confocal parameters

$$b_p = \frac{2 \cdot \pi \cdot n_e(\lambda_p) \cdot \omega_p^2}{\lambda_p} \quad b_s = \frac{2 \cdot \pi \cdot n_o(\lambda_s) \cdot \omega_s^2}{\lambda_s}$$

since these values determine ξ . We note that b is defined in the non-linear medium and must necessarily include the index of refraction. The propagation distances were adjusted so that the calculated ξ values for the pump and signal beams were approximately equal and a single value was used for both beams in subsequent power calculations.

The agreement between theory and experiment is quite good for the case of unfocused beams (Table 4.4). The experimental Pidler yield is 77.8% of the predicted IR power and there is very good consistency

between the determinations made for different values of the pump laser power. The calculated power levels obtained from Equations 2.4.1, 2.5.2 and 2.5.3 are essentially identical, as expected. We do not expect an exact agreement with the plane wave approximation since the input beams used in these measurements have beam waists back inside their respective lasers. However, each beam diverges slowly and the parametric interaction occurs within three Rayleigh lengths of each beam waist so that Equation 2.5.2 should be valid. Equation 2.5.3 applies to the beam waists located at the center of the crystal and should probably not be applied to the unfocused case. Equation 2.5.2 does not apply to the focused cases and Equation 2.5.3 must be used for these power calculations.

The agreement between experiment and theory is poor for all of the experiments using focused input beams. We observed approximately 20% of the calculated IR output power for the two experiments where ξ was less than the optimal value ($F = 400, 250$ mm) and 38% of the theoretical yield with nearly ideal focusing ($F = 100$ mm, $\xi = 1.893$). We note that the phase matching frequency of the signal laser was carefully optimized in the $F = 100$ mm experiments and this may partially explain the increased conversion efficiencies noted for these results.

4.7.3 Thermal Loading

We have several experimental indications that residual absorption in the AgGaS₂ crystal causes thermal loading and limits the maximum attainable IR output power. The observed turnover in P_{idler} as P_{signal}

increases, shown in Figure 4.6 and the blooming of the visible beams after the crystal imply a thermally induced effect.

We have used the approximations developed by Innocenzi *et al.* [190] and the loss measured calorimetrically to estimate the thermal lensing effects in our experiment. A temperature gradient along the propagation axis resulting from light absorption is expected. Such a temperature gradient might decrease the coherence length as result of the temperature dependence of the phase matching condition. Our calculations indicate that this effect is not important and may be ignored. However, the radial temperature gradient resulting from absorption causes pronounced thermal lensing of the pump and signal waves. Since dn/dT is positive for $AgGaS_2$, temperature increases create a positive thermal lens whose focal length is given by [190]

$$f_{\text{Thermal}} = \frac{\pi \cdot K_c \cdot \omega_p^2}{P \frac{dn}{dT}} \left(\frac{1}{1 - \exp[-\alpha L]} \right) \quad (4.7.1)$$

From Equation 4.7.1, we calculate a focal length of 6.33 mm for a thermal lens generated inside a 45 mm long $AgGaS_2$ crystal assuming $\alpha = 0.05 \text{ cm}^{-1}$, $K_c = 0.014 \text{ W/(cm}\cdot\text{K)}$, $\omega_p = 300 \text{ }\mu\text{m}$, $dn/dT = 1.55 \cdot 10^{-4} \text{ }^\circ\text{C}^{-1}$, and $P = 2 \text{ W}$. The calculated f_{Thermal} is much smaller than the crystal length, so the assumptions on which Equation 2.5.3 is based are invalid. However, this result suggests that overfocusing may be desirable: the strong positive focusing created by temperature gradients at the beam waist

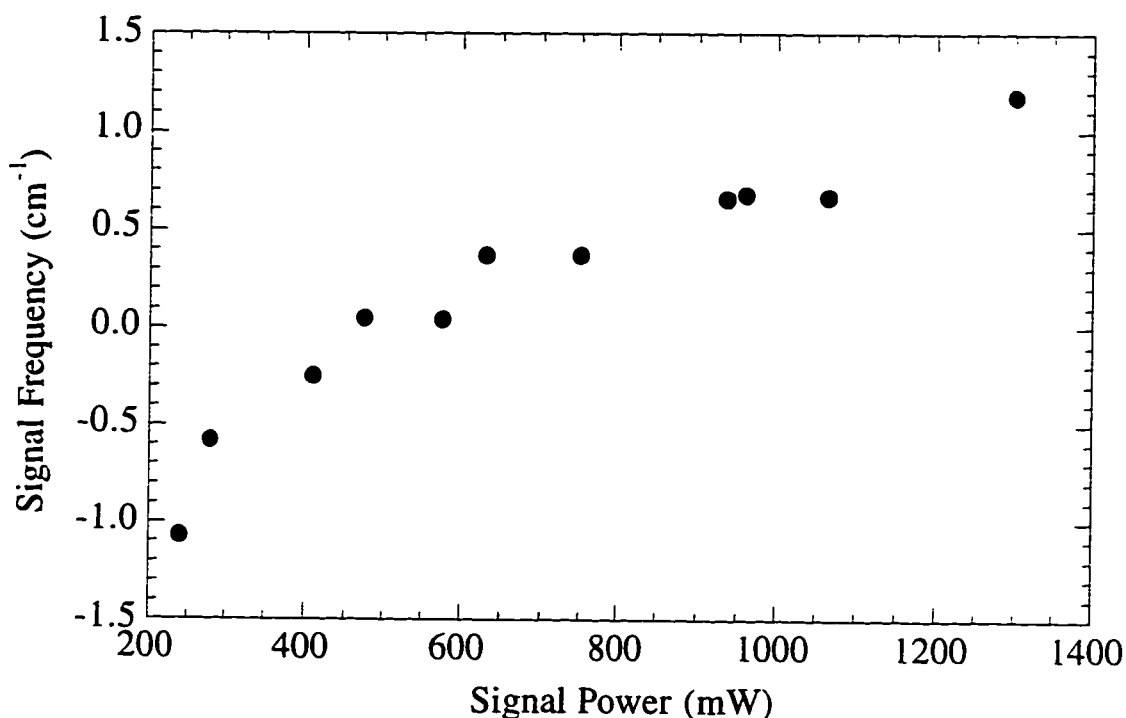


Figure 4.7 - Frequency Offset versus Signal Power

may confine the wave fronts and extend the near field region, thus increasing the effective parametric interaction length.

The phase matching is also affected by thermal effects caused by visible laser absorption. In Figure 4.7 the signal frequency required to maintain maximum IR output power is plotted as a function of the signal laser input power. These data were recorded simultaneously with the IR output powers presented in Figure 4.6. Note the nearly linear increase in ν_{signal} with P_{signal} .

The phase matching measurements depicted in Figure 4.7 primarily reflect the thermal steady-state established between heat flowing into the crystal by absorption of the pump beam and heat being lost to the surroundings. The phase mismatch is related to the crystal temperature in

the parametric interaction region through the temperature dependence displayed by n_p , n_s , and n_i , the refraction indices. A linear least squares evaluation of the data in Figure 4.7 yields $dv/dP = 1.8 \text{ cm}^{-1}/\text{W}$. We can estimate the power induced temperature change, dT/dP , using the value of $dv/dT = 0.417 \text{ cm}^{-1}/^\circ\text{C}$ previously determined [157] for the temperature dependence of the phase matching conditions.

$$\frac{dT}{dP} = \frac{\left(\frac{dv}{dP}\right)}{\left(\frac{dv}{dT}\right)} = \frac{(1.8/0.82) \frac{\text{cm}^{-1}}{\text{W}}}{0.417 \frac{\text{cm}^{-1}}{^\circ\text{C}}} = 5.29 \frac{^\circ\text{C}}{\text{W}} \quad (4.7.2)$$

where we divide by 0.82 to account for Fresnel loss at the front surface of the crystal.

The radial temperature change in the crystal caused by the incident laser power is [190]

$$\begin{aligned} \frac{d(T(r) - T(r_b))}{dP} &= \frac{\alpha}{4 \cdot \pi \cdot K_c} \left(\ln\left(\frac{r_b^2}{r^2}\right) + E_1\left(\frac{2r_b^2}{\omega_p^2}\right) - E_1\left(\frac{2r^2}{\omega_p^2}\right) \right) \\ &= 2.77 \frac{^\circ\text{C}}{\text{W}} \end{aligned} \quad (4.7.3)$$

where α ($= 0.05 \text{ cm}^{-1}$) is the signal power absorption coefficient, r_b is the crystal radius, K_c ($= 0.014 \text{ W}/(\text{cm K})$) is the thermal conductivity coefficient, ω_p ($= 29 \text{ } \mu\text{m}$) is the beam waist, and $E_1(x)$ is the exponential integral. This equation assumes that the crystal is a cylinder with a 2 mm radius (our crystal has a $(4 \times 4) \text{ mm}^2$ square cross section). In our experimental arrangement the crystal is exposed to air on two sides and

pressed against a thin Al housing by Teflon screws on the other two sides. We believe that the temperature at the surfaces of the crystal must be rising by about $2.5\text{ }^{\circ}\text{C/W}$ to account for the discrepancy between the phase matching temperature rise of $5.29\text{ }^{\circ}\text{C/W}$ of Equation 4.7.2 and the smaller estimated rise of $2.77\text{ }^{\circ}\text{C/W}$ from Equation 4.7.3. The thermal conductivity of air is only $0.00025\text{ W/(cm}\cdot\text{K)}$ compared with $0.014\text{ W/(cm}\cdot\text{K)}$ for AgGaS_2 .

There have been reports of similar thermal lensing behavior in the related chalcopyrite material AgGaSe_2 [191-193]. Marquardt *et al.* [191] have recently demonstrated that the thermal lensing effects in a AgGaSe_2 OPO pumped at kilohertz repetition rates can be virtually eliminated by cooling the crystal to liquid nitrogen temperatures. We plan to explore the thermal behavior of DFG in AgGaS_2 at cryogenic temperatures, although this is a negative design consideration in our quest for an "ideal" IRKS source.

4.7.4 Conclusions

We have constructed a cw DFG source based on AgGaS_2 as the central element in a IRKS apparatus achieving output powers of $10 - 30\text{ }\mu\text{W}$ and have explored the parametric conversion efficiency as a function of focusing conditions and input powers. We observed reasonable agreement between experimental and theoretical IR yields for the limiting case of DFG with plane waves, but the optimized experimental yields for DFG from focused beams was a factor of 3 to 5 lower than the theory

predicted. Thermal loading in the AgGaS₂ crystal was observed for all focusing conditions. Because we have more titanium:sapphire power available (up to 4 Watts) and the IR output power begins to turn over at 800 mW, it is clear that residual absorptions in the AgGaS₂ crystal are limiting our ultimate IR power production.

There are two improvements which we clearly must make to increase the IR output power of our AgGaS₂ DFG source. Firstly, the thermal loading effects in the crystal must be eliminated or significantly reduced. State of the art AgGaS₂ crystals currently have residual absorptions of less than 0.1% cm⁻¹ compared to ~3.0% cm⁻¹ for our crystal. Using more transparent AgGaS₂ bars should permit the use of higher pumping powers without thermal loading. Voronin *et. al.* [194] found no drop in SFG conversion efficiency (10.6 μm + 1.064 μm) using a crystal with $\alpha < 0.1 \text{ cm}^{-1}$. With these more transparent materials, the effective pumping power can be further increased by AR coating the front surface of the crystal and loss of IR at the exit surface can be reduced by IR AR coating that surface. Without such coatings Fresnel losses at the entrance and exit surfaces would reduce the IR output power to 55% of its potential value.

4.7.5 Corrections to the above

There were fundamental problems in the above study which will be discussed at this time.

Because the laser power meter used (Coherent 212 Power Meter) employs a silicon photodiode as its active element, the responsivity of the detector is wavelength dependent. This was not taken into account in the above mentioned paper. The responsivity at 666.076 nm and 762.776 nm is too high by a factor of 1.11 and 1.30 respectively and thus the product of the incident powers should be scaled by a factor of $1/(1.11 + 1.30)$ or 0.69 and the theoretical power decreased by the same factor. This correction accounts for 31% of the discrepancy of experimental versus theoretical power.

The newly developed theory (Section 2.4) shows that the maximum infrared power does not coincide with the perfect phasematching frequencies (see Figure 4.3). Thus, the theoretical power is higher than previously calculated and the conversion efficiencies appropriately decreased.

The transimpedance amplifier used in the experiment to increase the signal voltage from the infrared detector begins to saturate at 1 volt [195]. Though the brochure from the detector manufacturer specifies 7 volts as the saturation level, the signal visibly flattens out at this level and EG&G personnel confirm that the 7 volt specification is in error. To avoid nonlinearity, laser power is increased until a 1 volt response from the detector is approached. A measurement of the detector response before and after the addition of an attenuator placed immediately in front of the detector at the same infrared power level determines a scaling factor that can be applied to all subsequent measurements at higher power levels as long as the attenuator remains undisturbed. In this laboratory, neutral

density filters proved a simple way to attenuate the IR (sheets of plastic or other semi-transparent IR materials could also be used), though the attenuation factors printed on the neutral density filters cannot be used for the mid-infrared. After the addition of appropriate attenuation, the infrared power can again be increased.

Because absorbed light from the pump and signal lasers changes the ordinary and extraordinary indices of refraction by heating the crystal, the frequencies necessary to optimize the infrared power are input power dependent. Figure 4.7 illustrates the effect. The measurements presented in Figure 4.5 held the frequencies of the two lasers fixed at the frequencies which maximized the infrared power for 0.5 Watt incident upon the crystal from each laser. Thus, Figure 4.5 is a convolution of the peak power scaling (where the idler power is proportional to the product of the pump and signal powers) and the phasematching condition (the sinc^2 curve) and it might be expected that there would be a regime of increasing slope (crystal heating causes the wavevector mismatch to decrease and approaches the top of the sinc^2 function), an area of constant slope (the top of the curve), and an area wherein the power did not scale linearly with the power product (the phasematching was "moving off" the top of the sinc^2 curve).

It can be seen that as light crosses a boundary from a lower to a higher index material, the wavefronts will be turned towards the normal. This moves the focus farther from the focusing lens than the position calculated from vacuum propagation. It can be shown by the use of ABCD matrices that this displacement is approximately eighteen millimeters, while

empirically it was found that the correct displacement for maximum power was approximately ten millimeters. Experimentally, it can be shown that correct placement of the focusing and collimating lenses can increase infrared production by a factor of at least seven over the previous studies. In addition, thermal lensing in the crystal causes a change in the far-field divergence of the beam that forces optimization of the lens positions as a function of the total input laser powers. The lens positions were not optimized in the previous study. This could contribute to the power rolloff in Figure 4.6.

In an attempt to verify the nonlinearity of the infrared power as a function of the product of the input powers, a second series of measurements were taken. This time, the idler was centered around 2470 cm^{-1} . The pump and signal waves required to produce IR at this frequency are $\nu_{\text{pump}} = 13717\text{ cm}^{-1}$ and $\nu_{\text{signal}} = 11243.31\text{ cm}^{-1}$, allowing the use of two Ti:Sapphire lasers. The above mentioned deficiencies were corrected and the measurements with $F=100\text{ mm}$ repeated.

Figure 4.8 depicts the measured IR power as a function of the product of the input powers. It should be noted that the conversion efficiency at 0.15 Watt^2 is 59% of the theoretical power. The curve still exhibits the three regimes seen earlier, and in fact the infrared power marginally decreases with increasing pump powers above 0.20 Watt^2 . This turnover indicates that pumping with greater than 0.5 Watt / laser is counterproductive with the present crystal in this wavelength regime

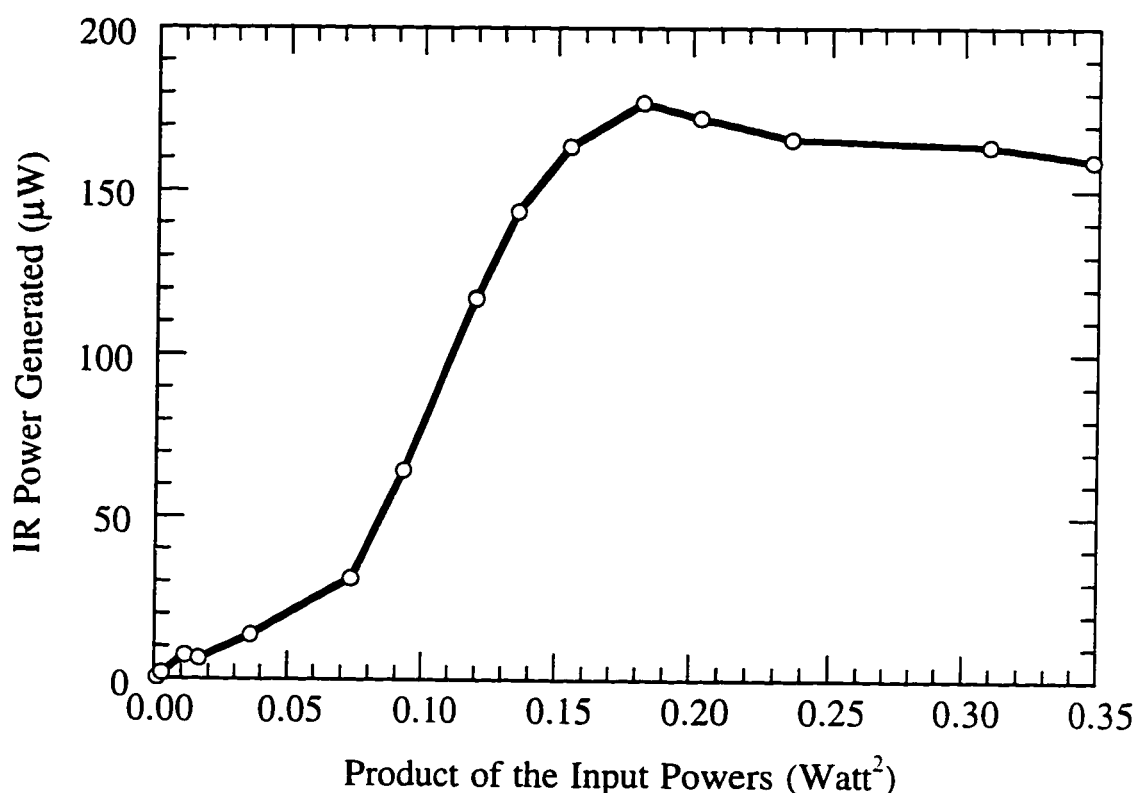


Figure 4.8 - Infrared Power Generation versus Input Power in AgGaS₂

because as the total input power exceeds one watt, thermal effects are destroying the confocal parameter and decreasing conversion efficiency.

The low slope value evident at low pump powers may be due to the neutral density filters used to attenuate the pump beam power. It has been seen that the use of some of these filters decreases infrared conversion more than others for the same transmitted power. The filters are old and burn marks are apparent on the surface of many - it is possible that the transmitted transverse intensity is no longer gaussian even when using apparently unburned portions of the filter. Therefore, the infrared power can no longer be expected to follow assumptions based on TEM₀₀ modes. This effect is more apparent at low pump powers when three or more

filters are used simultaneously to adjust the infrared power and because some of the most burned filters are those with the highest attenuation factors. This would account for the apparent low conversion efficiencies in Table 4.4, which were calculated by measuring the slope of the line for low pump powers in both the signal and pump lasers. Attempts to characterize the transverse profile with a razor blade and the power meter have been inconclusive, but projecting an expanded beam upon the laboratory wall does indeed show transverse intensity variations inconsistent with a gaussian distribution.

Figure 4.9 depicts the frequency offset in the pump beam to maintain peak phasematching efficiency versus the pump laser power. The signal laser power was held fixed at 660 mW (the highest power achievable that day and considerably higher than that used in Figure 4.7). If thermal effects were present, they would manifest themselves at the highest possible total input powers. The negative slope of the line is due to the fact that the pump laser was tuned to maximize the infrared signal. As was found in Figure 4.7, the offset is linear with respect to the pump power, indicating that there is no thermal runaway, which should manifest itself as negative curvature.

The conclusion of the latest studies is that it is indeed a thermal effect that is causing the nonlinear scaling of the infrared power with the product of the two input powers. The $4 \times 4 \times 45 \text{ mm}^3$ crystal currently used in the system typically absorbs 5% / cm while those recently produced by Cleveland Crystals absorb less than 0.25% / cm [186]. It would be greatly

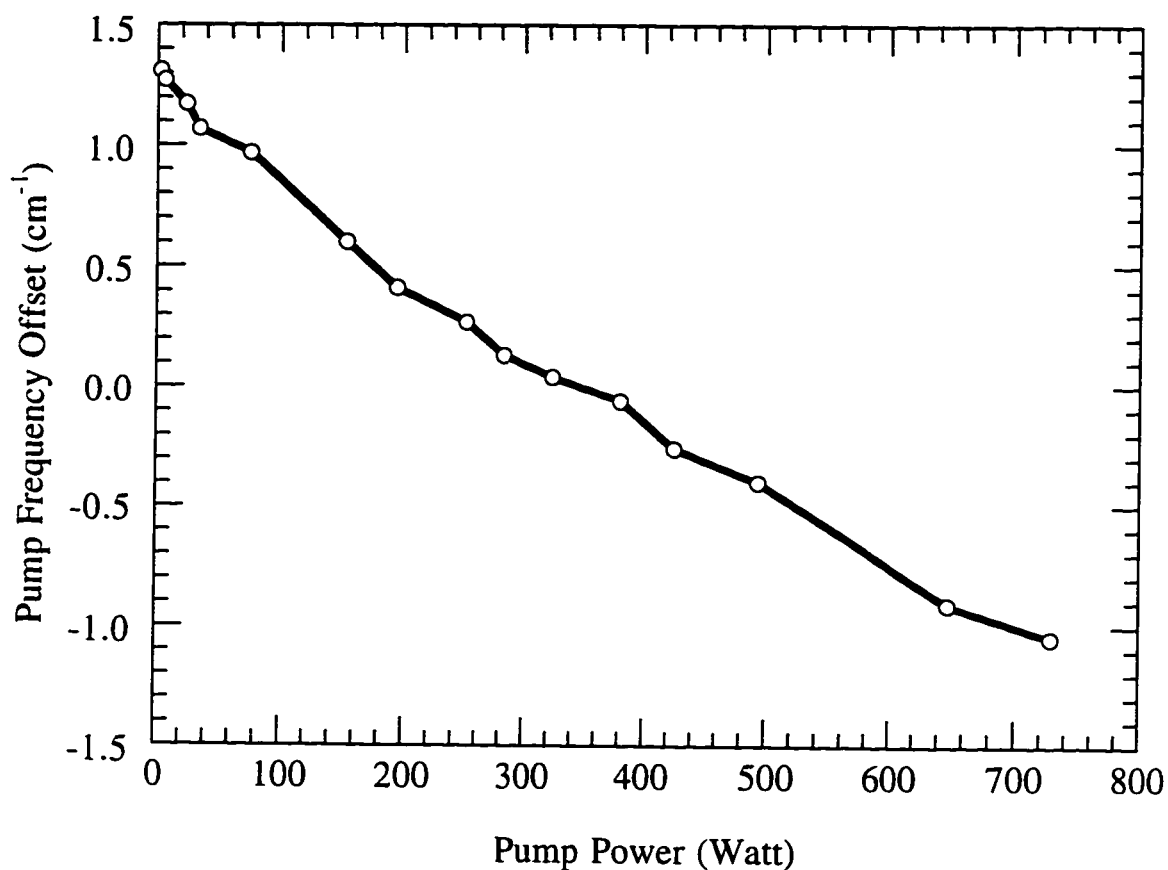


Figure 4.9 - Peak Phasematching Frequency Offset versus Input Power

advantageous to purchase one of these newer crystals, should such an opportunity present itself.

4.8 Noise and sensitivity in the AgGaS₂ System

Because the performance characteristics of the IR probe almost exclusively determine the feasibility of any experiments we desire to conduct, it seems appropriate to discuss the noise and sensitivity at this time.

A balanced detection scheme is used to reduce or eliminate the fluctuations in the source intensity. Indium Antimonide (InSb) detectors are photovoltaic and are to be preferred over photoconductive mercury cadmium telluride (MCT) detectors because they ordinarily have a detectivity level ten times that of the MCT. InSb detectors can only be used at wavelengths shorter than $5.3\text{ }\mu\text{m}$, however. A slightly different procedure has been developed for balancing both type of detectors.

4.8.1 Balancing with photovoltaic detectors

To use a balanced detector noise reduction scheme, a silicon beamsplitter is placed in the main path of the infrared beam (Figure 3.2). One side of the beamsplitter is broad-band antireflective coated and the other side left uncoated. Fresnel losses at a 45° angle of incidence equal approximately thirty percent. The transmitted beam passes through the multipass cell and is focused into a detector, while the reflected beam is attenuated with a MgF_2 Rochan polarizer and focused into a second detector. This second detector has reversed polarity with respect to the first (with increasing infrared power it has a response current that is opposite in sign to the response of the first detector). As the infrared power fluctuates due to noise in the pump lasers, one detector yields a positive signal and the other a negative signal. When the infrared power incident upon each detector multiplied by the responsivity is equal in magnitude but opposite in sign to that of the other detector:

$$P_1(\theta) \cdot R_1 = - (P_2 \cdot R_2) \quad (4.8.1)$$

fluctuations in the source power can be canceled by connecting the detectors in series to a single transimpedance amplifier (the currents simply add to zero for fluctuations in the source power). By adjusting the rotation angle of the polarizer (θ), the power incident on one of the detectors can be adjusted and the signals nulled out.

For optimum results, a pair of matched detectors should be used so that their risetimes and responsivity are equivalent. In practice we use a pair of detectors (EG&G Judson and Infrared Associates) that are reasonably well matched in risetimes but not in responsivity (differing by a factor of three). This means that the balancing detector receives three times less light than the signal detector because it is three times more responsive.

Because the detectors become unbalanced during frequency scans due to etalon effects within the system and precursor absorptions, a Rochan polarizer is manually adjusted during a scan to visually reduce the noise on an oscilloscope. The effects of the balanced detection scheme can quite clearly be seen in Figure 4.10. Each trace is a sampling of two thousand data points spaced five hundred nanoseconds apart with offsets added to the two uppermost traces to make them more legible. (Please note: these were three discrete traces and were not taken simultaneously.) The standard deviation of the single detector signal is five times that of the balanced detector. The standard deviations of the detector noise and the balanced detectors were identical ($\sigma = 7.8 \text{ mV}$) and indicate that in the case of

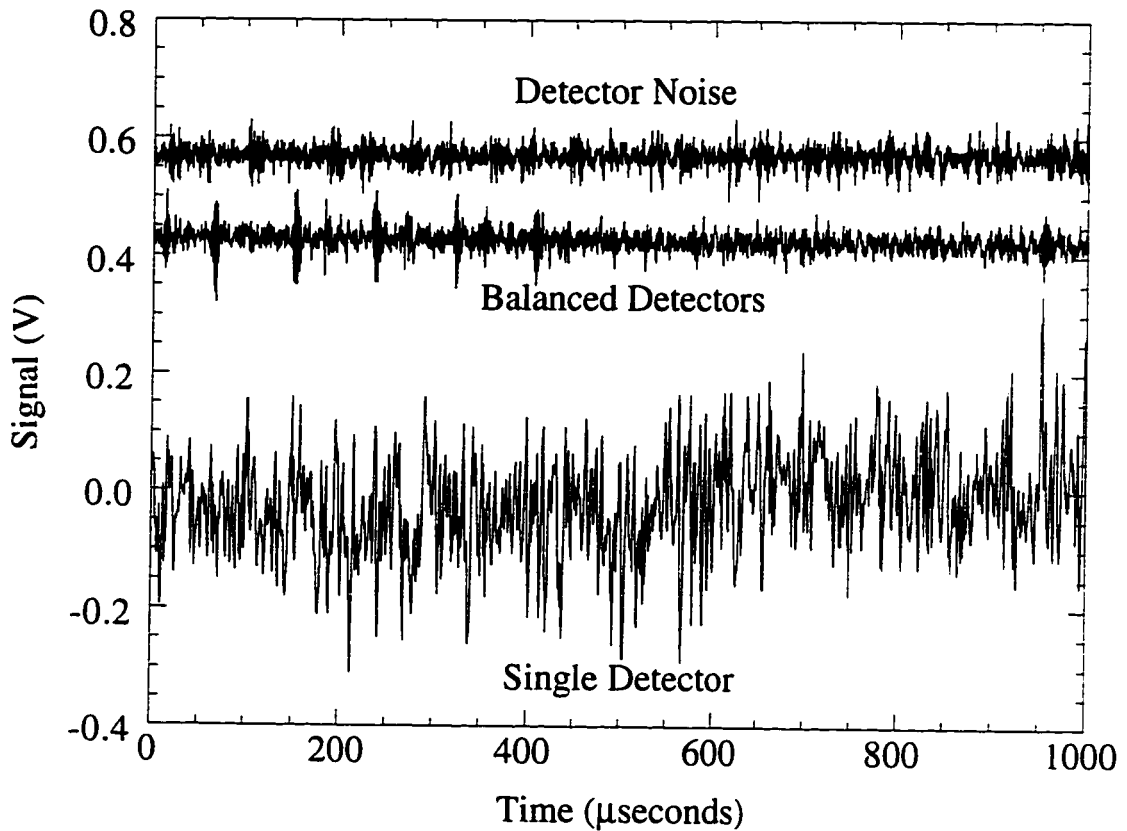


Figure 4.10 - Comparison of Detector, Laser, and Balanced Detection Noise

perfectly balanced detectors, the noise originates entirely in the detector/preamplifier. The standard deviation of the unbalanced detectors is approximately 0.1% of the signal when extrapolated for linear response in the preamplifier, matching the stability of the ring lasers as measured with a silicon photodiode (Coherent specifications for the laser are 0.8%).

By calculating the Fourier transform of the noise, an estimation of the power spectra of signals is obtained and narrow-band signals buried in broadband noise can be detected, but because a noise spectrum is often incoherent the fluctuations at a given frequency fade out and reappear with different phases, leading to erroneous results when one transforms the raw

signal [196,197]. To compensate for this, one first calculates the correlation function of the spectrum:

$$\psi(\tau) = \frac{1}{T} \sum_{\tau=0}^T I(t) I(t + \tau) \quad \text{where } T = \text{the time to complete half the scan}$$

(4.8.2)

and calculates the Fourier transform of this function. The Nyquist frequency is one quarter the original sampling frequency because only half the time data is used in the Fourier transform after the application of the correlation function. Figure 4.11 displays the results of these calculations on the data presented in Figure 4.10. It can again be seen that the noise due to fluctuations in the infrared power is completely canceled out and that most noise is originating at a relatively low frequency.

4.8.2 Balancing Photoconductive Detectors

Mercury Cadmium Telluride (MCT or HgCdTe) detectors operate on the principle that photons with energy greater than the semiconductor band-gap energy excite electrons into the conduction band, increasing the conductivity of the material. The signal output by the preamplifier is ac-coupled and therefore oscillates around the ground voltage.

Theoretically, it should be possible to balance MCT detectors in the same fashion as InSb detectors. Matched MCT detectors are not available in this laboratory so one detector with an active area of 1 mm² and the other 0.25 mm² were balanced. The time response of a detector is

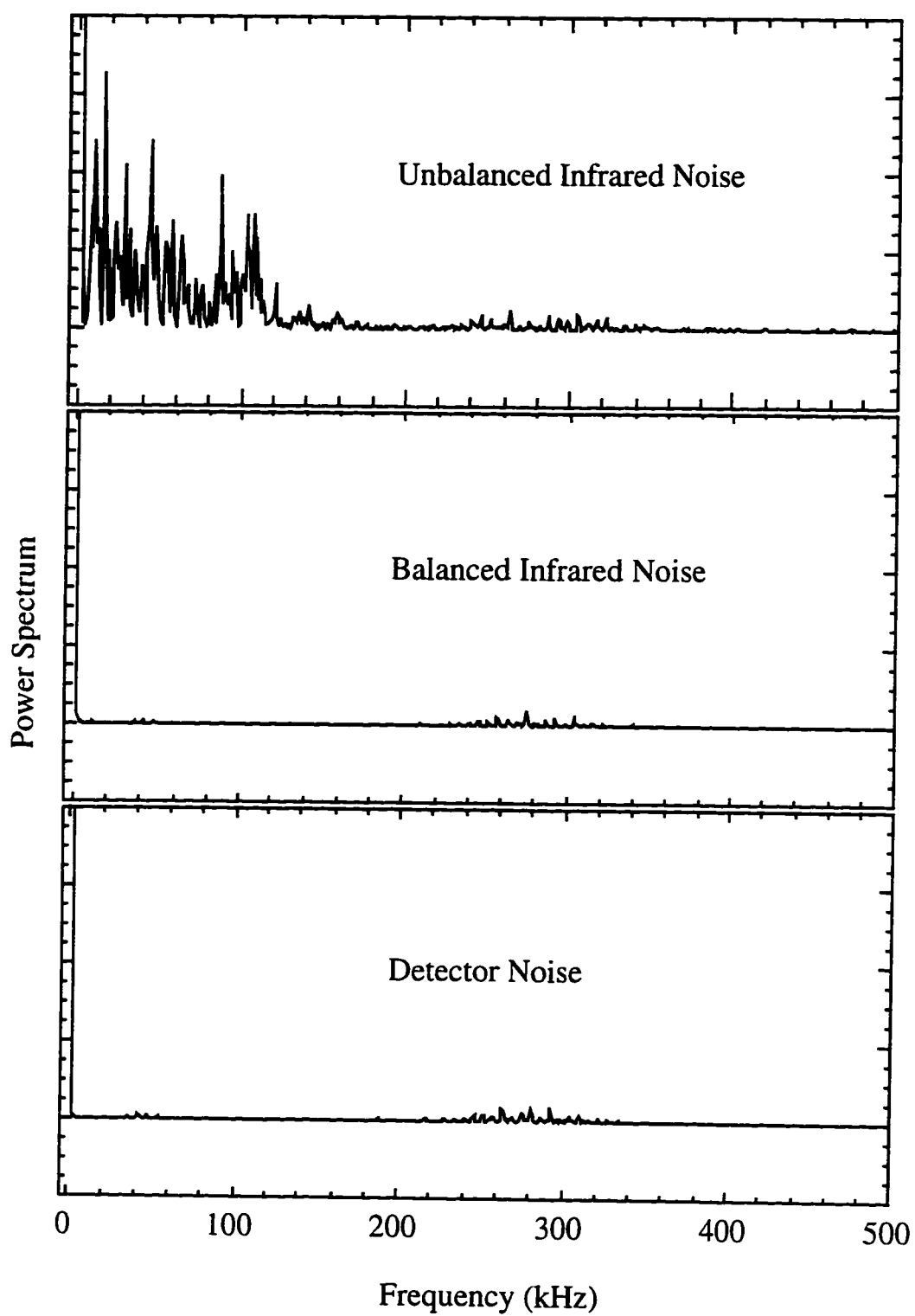


Figure 4.11 - Noise Power Spectrum. The y-axis scale of all three spectra are identical.

expected to be directly proportional to the active area so it is predicted that the detectors would not respond proportionally to fluctuations in the infrared power. In practice, however, it was found that these detectors reacted with virtually the same time response in a rather special fashion. Figure 4.12 displays a time trace of both detectors collected simultaneously on the transient digitizer. A careful inspection of the two detector traces indicates that there is a time delay of $0.51 \mu\text{seconds}$ between the two detectors. While direct subtraction of the detectors does improve the S/N ratio by a factor of seven, delaying the 1 mm^2 detector signal by $0.51 \mu\text{seconds}$ improves the S/N by a factor of 10 as shown in Figure 4.13.

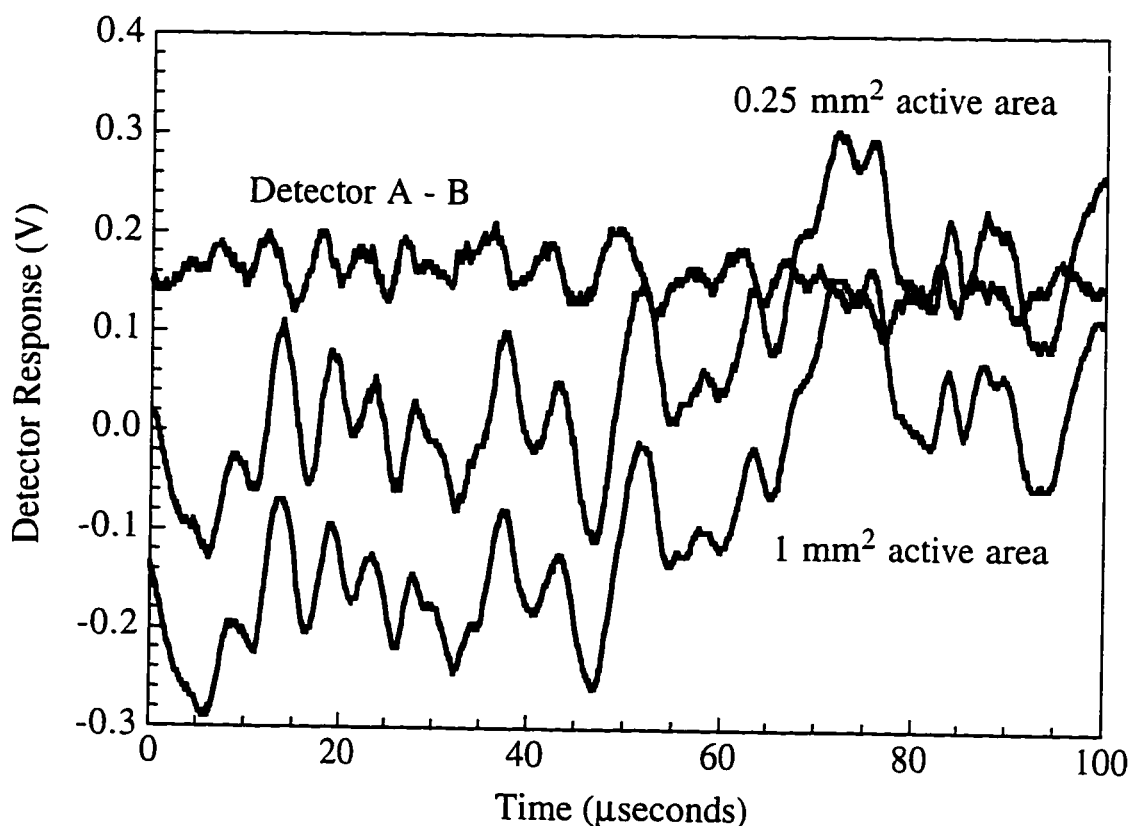


Figure 4.12 - Noise in Mercury Cadmium Telluride Detectors

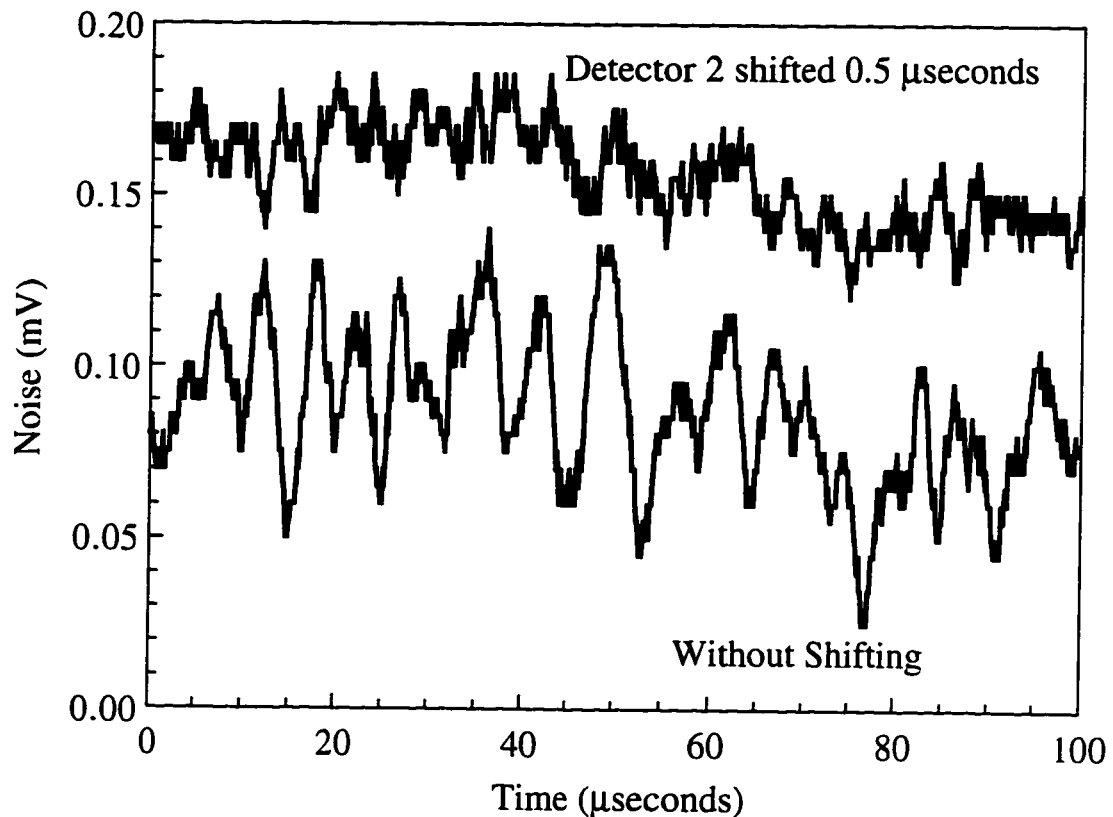


Figure 4.13 - Effect of Time Delay in Mercury Cadmium Telluride Detectors

To properly balance these two detectors, an effective delay between the detectors must be implemented. One possible solution involves the collection of temporal information from both detectors simultaneously, shifting one channel with respect to the other, and then subtracting them. Though the transient digitizer (WAAG II) is technically incapable of acquiring two channels simultaneously, it can collect them in an interlaced fashion: acquisition between channels alternates at rates of up to 25 ns. This does not pose difficulties in our experiment because the detector/preamplifier has no response at this 40 MHz frequency.

4.8.3 Excimer Noise

There are a numbers of problems inherent to excimer laser use that have rather profound effects upon the noise in an infrared kinetic spectroscopy.

The high voltage necessary in excimer lasers produces significant amounts of electrical interference upon discharge. This is detected by the system as electrical radio-frequency ringing and a damping ($1/e$) time of three to four microseconds. The actual duration of the radio pulse is ~ 0.3 μsec . Though the effect of this pulse can be severely reduced by proper shielding of the excimer cavity and power supply, it cannot always be eliminated. With the present experimental setup, most of the electrical coupling between the excimer and the data collection systems occurs through a BNC cable directly connected from the excimer trigger output signal to the trigger of the transient digitizer board that triggers the data acquisition. This problem will be solved in the future by triggering the digitizer upon a photodiode signal measuring the scatter of the UV light off the beam block in the White cell (Figure 3.3).

4.8.4 Infrared Emissions

Of a much larger concern in infrared kinetic spectroscopy experiments to date has been the interference of infrared light emanating from the excimer laser itself, the optics through which it passes, and the fluorescence of the precursor gas in the absorption cell.

Infrared fluorescence arises in the excimer laser and scatters off both the output coupler of the laser and the input window to the multipass cell. This could be eliminated with the introduction of a UV-selective filter in front of the excimer laser, but such filters are easily susceptible to radiation damage. While an iris placed in front of the detector does eliminate some of the scattered light, it cannot entirely eliminate it. One improvement would be to obtain wavelength selective elements (either filters or a monochromator) and to place them immediately before the infrared detector. While it is known that the emissions from the optics exist somewhere between 3 and 4 μm [198], the exact wavelengths are unknown. This would argue in favor of using the greater wavelength discrimination capability of a monochromator and their generally superior transmission characteristics (85-95% for vertically polarized light over the entire tuning range capability of the instrument).

Some precursor gases fluoresce in the infrared, and this signal can interfere with a transient signal for tens of microseconds. More will be said of this in Chapter 6 when the spectroscopy of the propargyl radical is discussed.

4.8.5 Theoretical noise limitations

It will be instructive to calculate the ultimate sensitivity of the system, assuming the only sources of noise in the system are quantum noise and detector noise.

Calculations are complicated by the fact that the infrared power varies by a factor of three or four during the course of a scan, but for the sake of clarity we will assume that the average power across a scan and transmitted through the multipass cell is 40 μ Watts (valid only for infrared frequencies near 2400 cm^{-1} - see Figure 4.4). This corresponds to $8.4 \cdot 10^{14}$ photons per second. If we assume a data collection window 10 μ seconds long, $8.4 \cdot 10^9$ infrared photons are produced during a single excimer shot.

D^* is a measure of detector noise at a particular electrical frequency in a 1 Hz bandwidth when 1 Watt of radiant power is incident on a 1 cm^2 active area detector.

$$D^* = \frac{\sqrt{\text{Area in cm}^2 \cdot \text{Measurement Bandwidth in Hz}}}{\text{NEP}} \quad (4.8.4)$$

Here, NEP is short for Noise Equivalent Power (the radiant power that produces a signal-to-noise ratio of one). Noise arises from a variety of sources: thermal noise caused by thermal radiation impinging upon the detector, Johnson noise due to the random thermal movements of carriers in a substance, and shot noise which is dependent upon the current flowing through the diode. Shot noise is the major contributor in both the InSb and MCT detectors.

Since the bandwidth is equal to $(2\pi\tau)^{-1}$ where τ is equal to the observation time (typically 10 μ seconds for each excimer shot), and typical values for the signal InSb detector are: $D^* = 1.7 \cdot 10^{11} \text{ cm} \cdot \text{Hz}^{0.5} \cdot \text{W}^{-1}$ at 2400 cm^{-1} and Area = 0.01 cm^2 ,

$$\begin{aligned}
 \text{NEP} &= \frac{1}{D^*} \sqrt{\frac{\text{Area in cm}^2}{2\pi\tau}} \\
 &= \frac{1}{2 \cdot 10^{11} \text{ cm} \cdot \text{Hz}^{0.5} \cdot \text{W}^{-1}} \sqrt{\frac{0.01 \text{ cm}^2}{2\pi \cdot 10^{-5} \text{ seconds}}} \\
 &= 63 \text{ pW}
 \end{aligned} \tag{4.8.5}$$

We are using two detectors in series and their noise will both be contributing to any measurements, so we must increase this NEP by multiplying it by $\sqrt{2}$ to obtain an effective NEP of 89 pW for the system. Another way to express this is that fluctuations of in the infrared probe of $1.9 \cdot 10^4$ photons per 10 μ second channel will just equal the noise inherent to the detectors.

The quantum noise of the system may be calculated in the following manner. The standard deviation of the quantum noise for a photovoltaic detector is given by the square root of the number of carriers generated in a time interval Δt [199] :

$$\Delta C = \sqrt{\eta \cdot \frac{P \cdot \Delta t}{h\nu}} \tag{4.8.6}$$

where η is the quantum efficiency of the detector and P is the total power. Though the quantum efficiency of the detector is unknown, the specifications included with the detector indicate the responsivity of the detector is 0.483 A/W. Therefore,

$$\eta = \frac{0.483 \text{ A/W} \cdot h\nu}{e} = 14\% \tag{4.8.7}$$

if we assume one carrier is generated for each photon. With 40 μ Watts of continuous power, 19.3 μ A is generated and in a 10 μ second time span $1.2 \cdot 10^9$ carriers are generated (193 pC). Taking the square root of this number, we find that the quantum limit of the system is $3.5 \cdot 10^4$ "counts" per 10 μ second period. Incidentally, Equation 4.8.6 must be multiplied by two for photoconductive detectors (like MCT) because noise in the photoconductive detector includes statistical fluctuation of the current due to random recombination of photogenerated carriers [200].

In the preceding sections, the effects of dark current have been neglected. Dark current is the current through a photodiode when a specific reverse bias voltage is applied with no incident radiant power. The dark current I_d is calculated from Equation 4.8.8 [201]

$$I_d = I_b + \frac{V_{os}}{R_d} \quad (4.8.8)$$

where I_b is the preamp input bias current, V_{os} is the preamp input offset voltage, and R_d is the detector shunt resistance. As InSb detectors typically are unbiased and have a low offset voltage, the dark current is negligible.

Infrared detectors generate a current due to detection of the background radiation present in any laboratory. Typically, with a 60° field-of-view (FOV), this background current is 7 μ A [201]. This value is already built into the D^* value and only becomes important in determining the maximum shunt resistance that can be used in the transimpedance amplifier.

From the above calculations it appears the system is in a regime in which both quantum and detector noise contribute are comparable. From the last series of calculations, we might expect to be able to measure a difference in transmission of 0.0004% ($3.4 \cdot 10^4 / 8.4 \cdot 10^9$) for a single excimer shot, 0.0001% averaged for 16 shots. A difference in transmission of 0.01% is the practical limit, however. (see Section 6.3). The difference between theory and experiment is possibly due to difficulties in keeping the system "balanced" due to precursor absorptions and optical interference in the system or is due to noise generated in the preamplifier.

4.8.6 Sensitivity of the AgGaS₂ DFG spectrometer

The absorption of the IR can be calculated using the Beer-Lambert Law:

$$I = I_0 e^{-\sigma_{\text{IR}} \cdot c \cdot L} \quad (4.8.9)$$

where

- I is the transmitted IR intensity
- I_0 is the IR intensity incident upon the cell
- σ_{IR} is the IR cross-section of the absorbing species
- c is the concentration of the absorbing species
- L is the total UV/IR overlap region

A typical infrared cross-section is $1 \cdot 10^{-19} \text{ cm}^2$ and the usual UV/IR overlap length L is 12 m (40 passes across the cell at 30 cm UV/IR

overlap per pass). To solve for the concentration that will yield a signal-to-noise of 1, we set $I = (1-0.0001) \cdot I_0 = 0.9999 \cdot I_0$. Rearranging the above equation, we solve for the absorbing species concentration:

$$c = \frac{-\ln\left(\frac{I}{I_0}\right)}{\sigma_{\text{IR}} \cdot L} = 8 \cdot 10^{13} \text{ molecules} \cdot \text{cm}^{-3} \quad (4.8.10)$$

To this point we have assumed a uniform concentration of absorbing species in the multipass cell across the UV/IR overlap region.

In order to determine the concentration of free radicals generated in a 150 mJ excimer laser pulse at 193 nm, use the following equation

$$c(z) \cdot dz = \left(\frac{-\eta \cdot dE}{A(z) \cdot h \cdot \nu_{\text{UV}}} \right) \quad (4.8.11)$$

$A(z)$ is the area of the beam as a function of the distance down the multipass cell

η is the quantum yield for formation of the IR absorber from 193 nm photolysis of its precursor

E is the energy of the excimer laser

ν_{UV} is the frequency of the excimer laser

z is the distance from the excimer beam entrance window

dE/dz can be calculated using Beer's Law:

$$E(z) = E_0 e^{-\sigma_{\text{UV}} \cdot c_{\text{pre}} \cdot z} \quad (4.8.12)$$

where c_{pre} is the concentration of the precursor.

$$dE(z) = -\sigma_{UV} \cdot c_{pre} \cdot E_0 \cdot e^{-\sigma_{UV} \cdot c_{pre} \cdot z} \cdot dz \quad (4.8.13)$$

To make the calculations simpler, we will assume the divergence of the excimer beam is negligible and therefore the transverse area of the beam is invariant with z , that the quantum yield η of the photolysis reaction to the desired free radical is unity, and that the initial excimer energy E_0 is 100 mJ. We therefore arrive at equation 4.8.15

$$c(z) = \frac{\eta \cdot \sigma_{UV} \cdot c_{pre} \cdot E_0 \cdot e^{-\sigma_{UV} \cdot c_{pre} \cdot z}}{A \cdot h \cdot \nu_{UV}} \quad (4.8.14)$$

From Equation 4.8.15 it is quite simple to display the concentration c as a function of the distance z down the White Cell for varying values of the parameter

$$\beta = \sigma_{UV} \cdot c_{pre} \quad (4.8.15)$$

Figure 4.14 displays the concentration of the free radical for four different combinations of the β parameter. It can be seen that as β is increased that the proportion of free radicals that are generated in the first few centimeters of the White Cell increases dramatically at the cost of decreased concentrations farther down in the cell due to depletion of the excimer beam. It is also apparent that for nearly all values of the B parameter, the AgGaS₂ spectrometer has sufficient sensitivity for measurement of the infrared transitions.

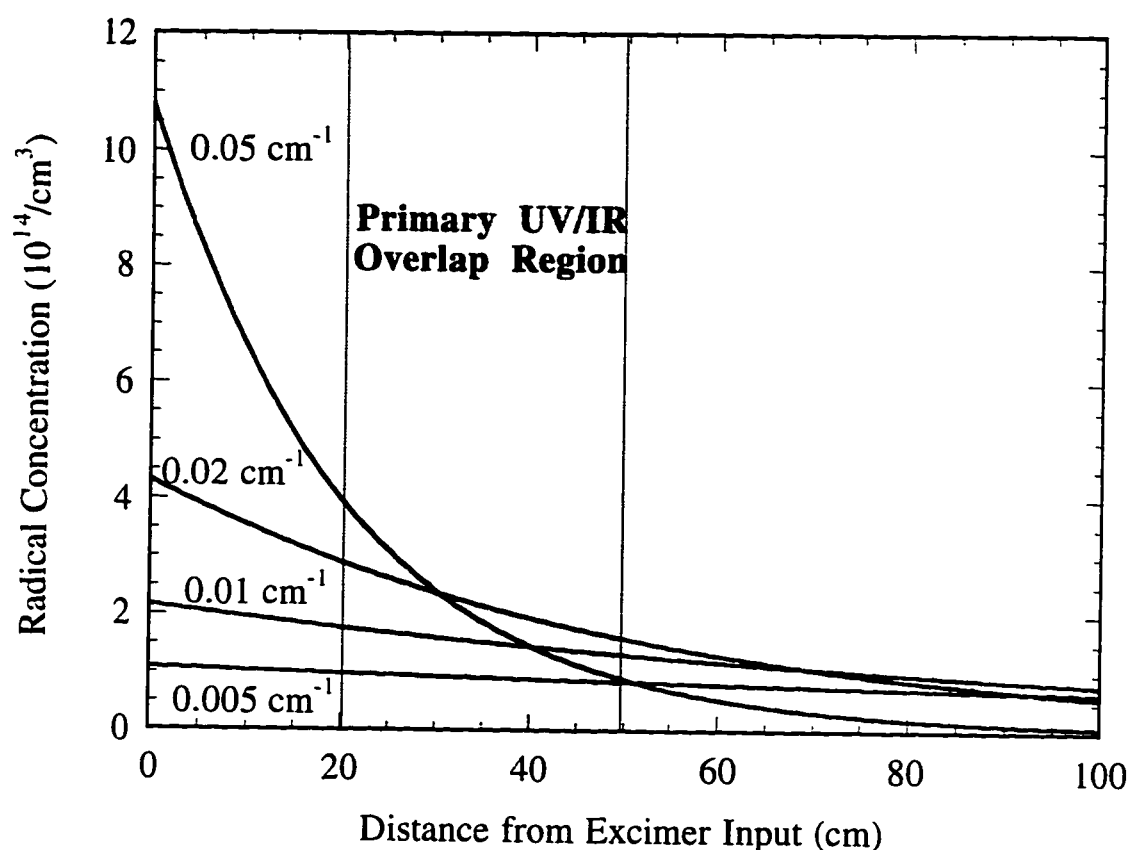


Figure 4.14 - Spatial Concentration of Radicals in the White Cell

A complete analysis of the absorption of the infrared beam involves a rather complicated function involving the mode structure of the White Cell, the divergence of the excimer beam, the exact geometry of the cell and the overlap region, etc. To a fair approximation, however, most of the UV/IR overlap occurs in the region between 20 and 50 cm from the excimer entrance window to the White Cell and we might assume perfect overlap in this region and no overlap for the rest of the cell. Therefore, to calculate the most effective pressure for any given UV cross section σ_{UV} , it is only necessary to integrate Equation 4.8.14 over the overlap region shaded in Figure 4.16. The left axis of Figure 4.15 displays the result of

this integrated concentration versus $\sigma_{\text{UV}} \cdot c_{\text{pre}}$. It can be seen that with the present White Cell geometry the optimum value is 0.03 cm^{-1} . From the right axis of this figure it can be seen that this corresponds to 95% absorption of the UV light. If we assume a typical UV cross-section of 10^{-18} cm^2 , this corresponds to a precursor concentration of $3 \cdot 10^{16} \text{ molecules / cm}^3$ or a pressure of just under 1 torr.

4.9 Summary of the AgGaS₂ Spectrometer

The infrared spectrometer constructed in this laboratory is a widely tunable source capable of measuring free radicals lasting only microseconds. With a linewidth of 1 MHz, it is capable of measuring the Doppler limited profile of these molecules and frequency calibration of

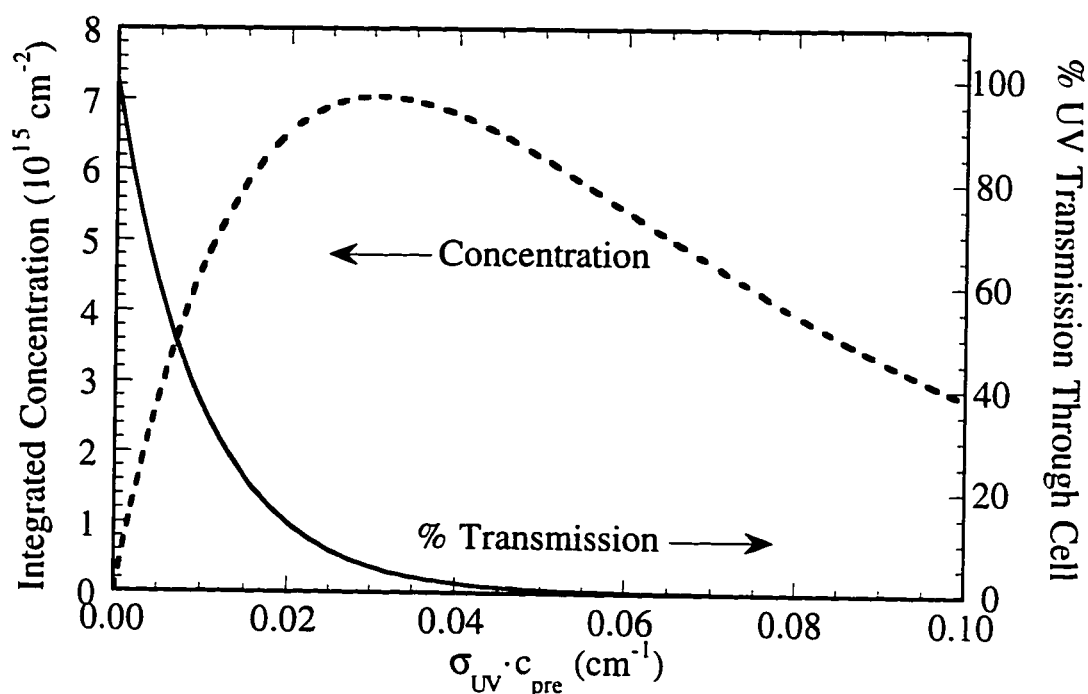


Figure 4.15 - Optimization of the $\sigma_{\text{UV}} \cdot c_{\text{pre}}$ Parameter

0.001 cm⁻¹ is routine. These points will be illustrated in Chapter 6 with the spectroscopy of the monodeuterated propargyl radical (CH₂CCD)

Chapter 5 -Difference Frequency Generation in GaSe

Much of the following text appears in the publication "A continuously tunable long-wavelength cw IR source for high-resolution spectroscopy and trace-gas detection." [202].

A new widely tunable source in the infrared for use in high-resolution spectroscopy and trace gas detection is described. This spectroscopic source is based on difference frequency generation (DFG) in Gallium Selenide (GaSe) and is continuously tunable in the 8.8-15.0 micron wavelength region. Such a DFG source operates at room temperature which makes it a useful alternative to a lead-salt diode laser-based detection system requiring cryogenic temperatures and numerous individual diode lasers.

5.1. Background

There is considerable interest in developing convenient methods for selective and sensitive measurements of trace gas concentrations. As virtually all fundamental vibrational modes of molecules and molecular ions lie in the 2 to 20 μm wavelength region, infrared spectroscopy provides a convenient and real time method of detection for most gases. Hence, it is important to develop compact and reliable diode laser based sources in this spectral region.

Diode-based cw DFG spectroscopic sources have recently been demonstrated in the 3-5 μm region with periodically poled LiNbO_3 [181] and AgGaS_2 [182]. The present work aims to explore the feasibility of similar cw sources at wavelengths from 5-18 microns by mixing two visible lasers in the nonlinear crystal GaSe. Although the work described here uses two cw Ti:Sapphire lasers in order to explore the characteristics of the nonlinear optical material, it is envisioned that the pump lasers will ultimately be high power visible/near infrared diode lasers to create a rugged portable IR source for gas monitoring.

Gallium selenide has been tested previously in pulsed DFG sources in the 4-19 μm region [150,203-207]. In addition, Vodopyanov *et al.* [61,208] have measured the spontaneous parametric emission from GaSe pumped by a mode-locked Er:YAG (2.94 μm) laser. In all these experiments, pulsed lasers operating at wavelengths longer than 1 μm were used to generate the tunable infrared radiation. In the only previous reported work with visible pumps, Abdullaev and coworkers used the pulsed output of a ruby laser and dye laser (715 - 750 nm) in a DFG source to generate pulsed radiation in the 9-18 μm region [56].

A good summary of the above experiments and many others can be found within the review article by N. C. Fernelius [209].

2. Experimental

The equipment used throughout the experiment has been described in Chapter 3 and a simple summary will here be presented.

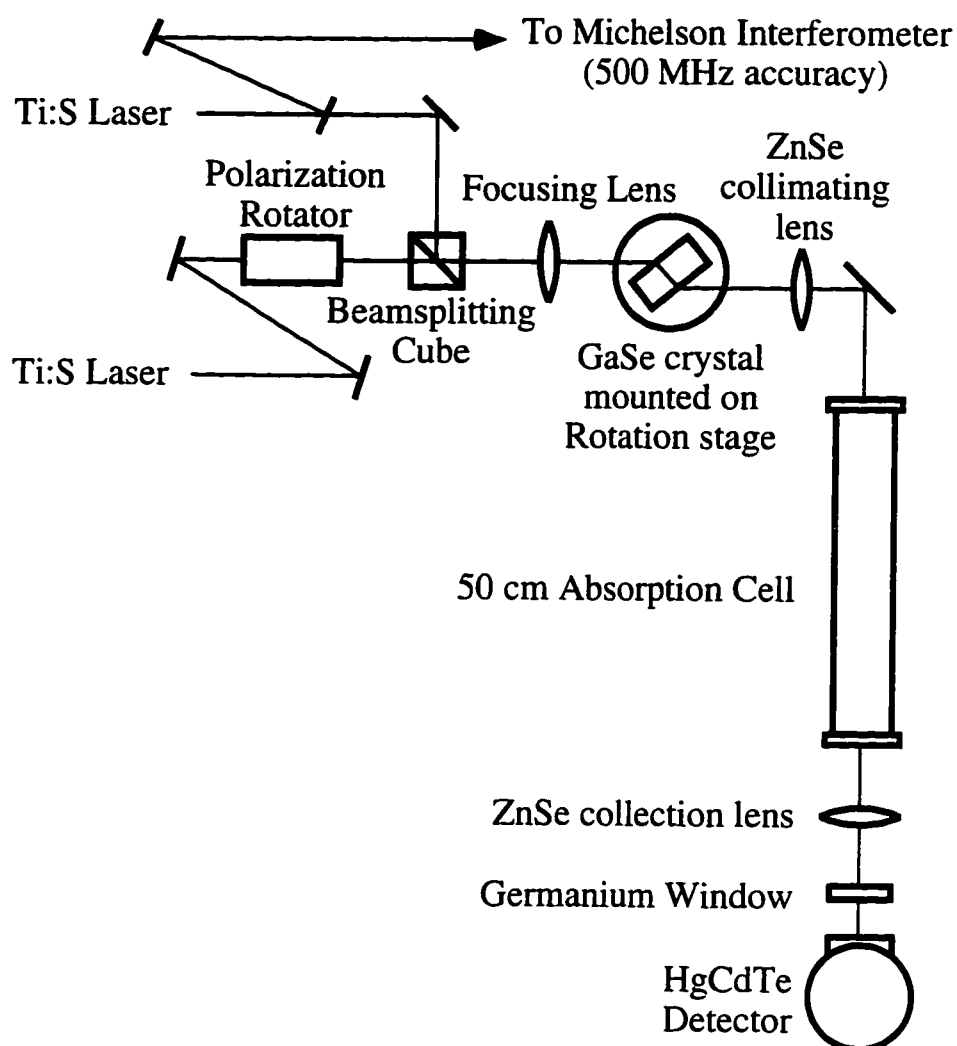


Figure 5.1 - Schematic Diagram of a DFG Spectroscopic Source Based on GaSe Crystal

The cw infrared spectroscopic source, shown in Figure 5.1, used the 20 Watt all lines output of an argon ion laser to pump simultaneously two single frequency cw Titanium:Sapphire ring lasers (Coherent Model 899-21 and 899-29). These lasers are actively frequency stabilized by locking to external etalons, and linewidths in the near IR of 500 kHz are typical. Titanium:Sapphire lasers were used in this experiment because of

their superior wavelength tuning, transverse mode quality, and output power characteristics. The output from each laser was attenuated to less than 300 mW using linearly variable filters to avoid optical damage of the GaSe crystal. The two beams were spatially overlapped by rotating the polarization of the pump beam orthogonal to the signal and overlapping them in a polarization cube to provide Type-I phasematching. Type-I phasematching was chosen in GaSe because the required external angle and walkoff effects are smaller than for Type-II (See Figures 2.11 and 2.12). The two beams are chopped and focused with a 100 mm lens into a GaSe crystal 5 mm in length and 10 mm in diameter mounted on a rotation stage. The infrared light generated in the GaSe crystal was collected and refocused with a single ZnSe lens onto a 1mm diameter liquid nitrogen cooled HgCdTe detector. A broad band antireflective coated (3-13 μm) Ge flat is placed immediately in front of the detector to block the two pump beams. The output of the detector is monitored by a lock-in amplifier and recorded by a computer. A 50 cm long absorption cell equipped with ZnSe windows was used for absorption experiments.

To date, we have generated continuously tunable light from 8.8 to 15.0 μm by tuning the wavelength of the two pump lasers and the angle of the crystal. We are not fundamentally limited to this tuning range and could extend the range to 6 μm with larger crystal angles, but the present crystal mount restricts the GaSe external angle to less than 60°. We expected to be able to tune to the 18 μm absorption edge of the crystal but did not obtain significant IR power at wavelengths longer than 15 μm . Within the current 45 to 60° range of external angles it is possible to

continuously tune over a 6.2 μm IR range using only a 25 nm tuning range of one of the visible/near IR pump lasers.

The published Sellmeier coefficients [55,58-60,210-212] were found to be inadequate for accurately describing the combination of input wavelengths and crystal angles to generate infrared light. Figure 5.2 graphically illustrates this, displaying the index of refraction of the above authors. Compare this with the excellent agreement between the dispersion relations of AgGaS₂ (Figure 4.1). Figure 5.3 displays the phasematching predictions of the three Sellmeier coefficients valid over entire tuning range of the pump, signal, and idler wavelengths. The predicted pump wavelengths for a given external crystal angle and signal wavelength are too low by about 3% or 20-25 nm, which confirms the observations of the Abdullaev [210] and Bhar [213] groups. Abdullaev

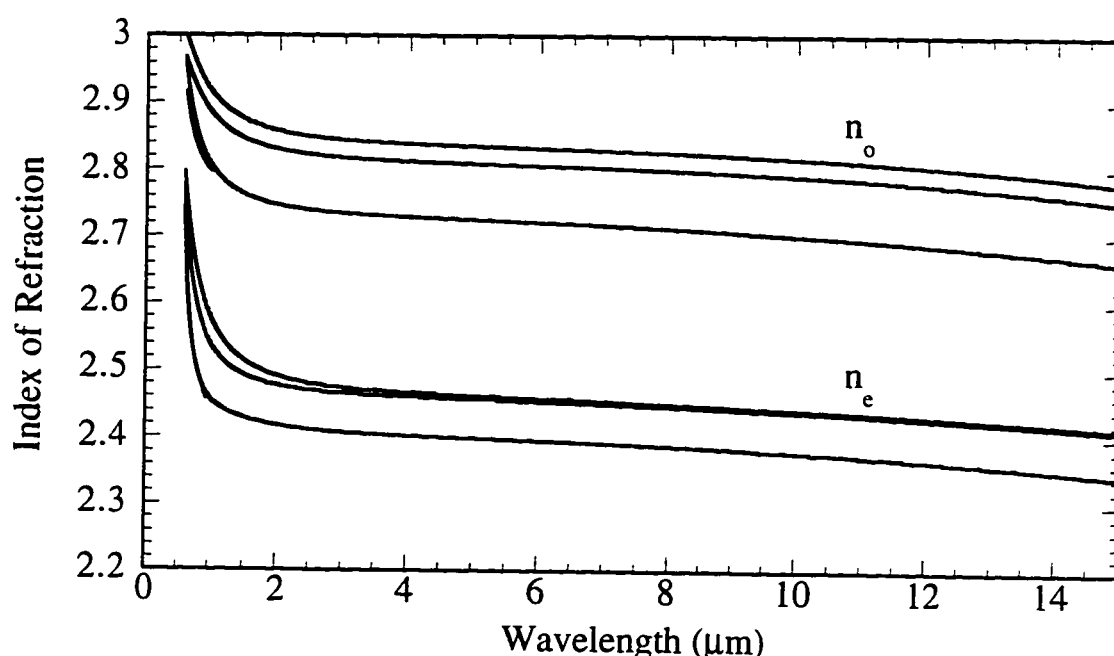


Figure 5.2 - Comparison of the Index of Refraction versus Wavelength for Published Dispersion Relations

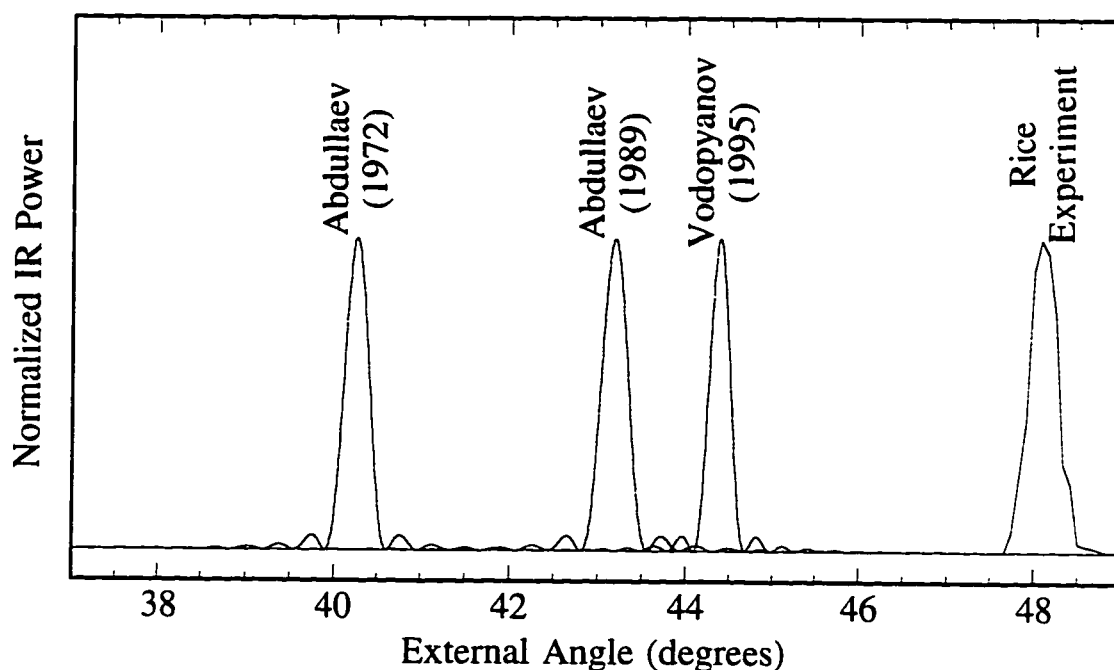


Figure 5.3 - Relative infrared power as a function of external crystal angle: theory versus experiment. The pump wavelength was held fixed at 793.210 nm and the signal wavelength fixed at 841.925 nm. The theoretical predictions are based on the dispersion relations proposed by the authors listed above the peaks.

attributed these errors to inaccuracies in the ordinary index of refraction near the short-wavelength edge of the absorption band. The results of our systematic investigation for optimized phasematched conditions are given in Figure 5.4 and Table 5.1. We obtained each data point by fixing the crystal angle and the signal wavelength and by scanning the pump laser wavelength. The results of one such scan is shown in Figure 5.5. The noise in the trace is a result of limiting the input power of each beam to 25 mW average at the crystal to avoid possible thermal effects due to absorption. The phasematching FWHM was found to be 0.706 nm (10.967 cm^{-1}) for a pump laser scan with the signal laser wavelength fixed at

Table 5.1 - Experimentally determined conditions that optimize the GaSe infrared power

External Angle (°)	Pump (nm)	Wavelengths Signal (nm)	Idler (μm)	Frequency Idler (cm ⁻¹)
45.5	802.847	848.408	14.950	668.898
48.0	798.324	848.408	13.523	739.468
48.0	806.474	858.868	13.220	756.417
48.0	803.603	855.080	13.348	749.148
48.0	795.802	845.123	13.636	733.343
48.0	793.213	841.867	13.725	728.589
48.0	801.008	851.744	13.447	743.653
48.0	808.844	861.831	13.156	760.127
51.2	805.593	865.428	11.652	858.243
51.2	794.791	851.352	11.963	835.907
51.2	802.937	862.015	11.716	853.554
51.2	800.391	858.621	11.802	847.318
51.2	797.762	855.262	11.866	842.737
51.2	792.234	848.047	12.038	830.731
51.2	807.406	868.318	11.510	868.822
54.0	795.805	858.623	10.877	919.334
54.0	798.346	862.017	10.808	925.201
54.0	788.127	848.047	11.154	896.510
54.0	790.311	851.355	11.022	907.259
54.0	793.296	855.263	10.949	913.320
57.0	783.863	848.592	10.276	973.103
57.0	803.005	868.319	10.676	936.714
57.0	800.925	865.434	10.745	930.664
57.0	800.768	871.793	9.829	1017.397
57.0	786.299	851.904	10.210	979.388
57.0	796.142	865.435	9.943	1005.687
57.0	791.102	858.713	10.048	995.266
57.0	793.614	862.020	10.001	999.921
57.0	798.257	868.319	9.893	1010.795
57.0	788.647	855.245	10.128	987.385
60.0	810.774	891.469	8.957	1116.450
60.0	815.532	898.229	8.858	1128.922
60.0	803.585	881.859	9.053	1104.549
60.0	806.110	885.476	8.994	1111.890
60.0	787.285	858.617	9.476	1055.244

Table 5.1 - (continued)

External Angle (°)	Pump (nm)	Wavelengths Signal (nm)	Idler (μm)	Frequency Idler (cm^{-1})
60.0	789.790	862.083	9.418	1061.779
60.0	784.913	855.248	9.544	1047.754
60.0	780.015	848.592	9.652	1036.043
60.0	782.462	851.911	9.598	1041.864
60.0	799.325	875.361	9.202	1086.692
60.0	801.070	878.328	9.107	1098.031
60.0	796.859	871.851	9.264	1079.420
60.0	792.274	865.502	9.364	1067.912
60.0	794.385	868.382	9.322	1072.680

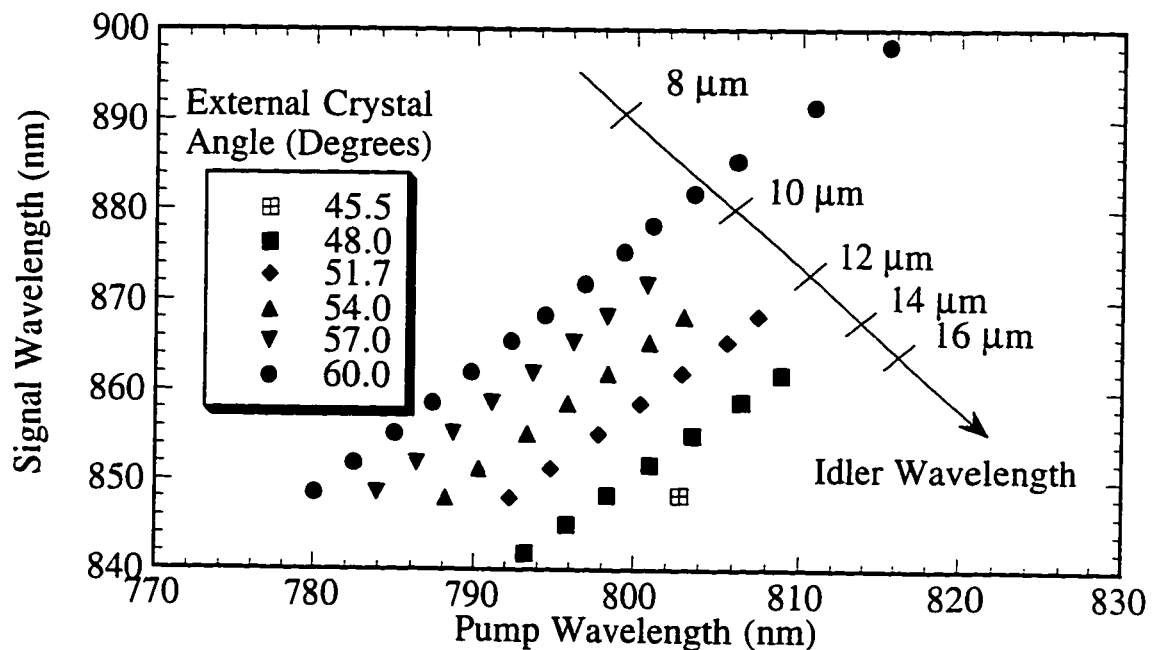


Figure 5.4 - Experimental phase-matching angles and wavelengths for a GaSe crystal in the 780-880 nm region. Individual points represent combinations of external angles and pump wavelengths that optimize the IR DFG power. IR wavelengths are given by projecting the data points onto the diagonal axis labeled "idler wavelength".

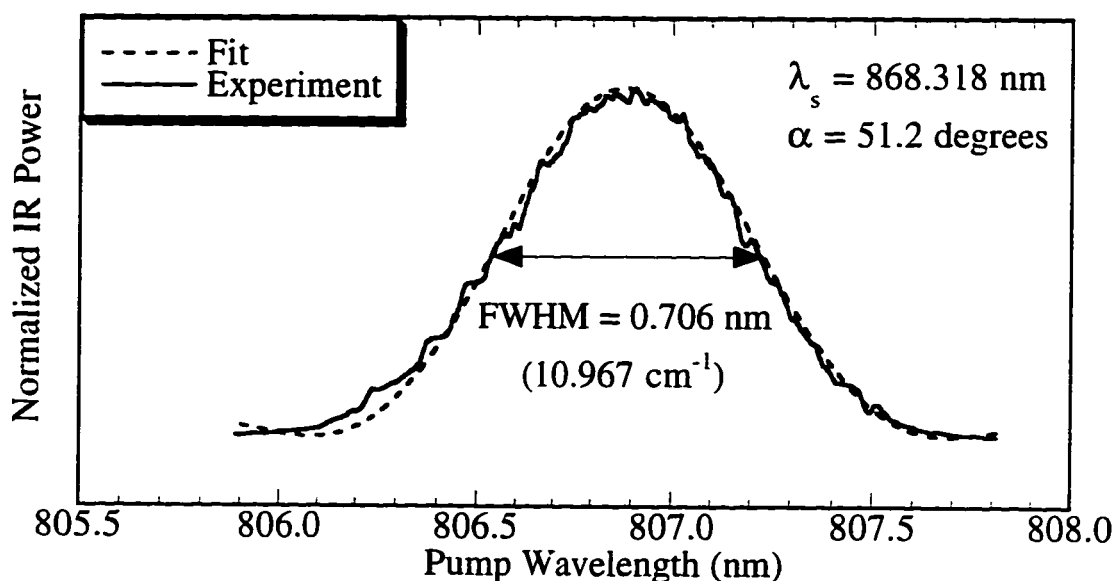


Figure 5.5 - Wavelength dependence of the IR power with fixed signal laser wavelength of 868.318 nm and fixed GaSe crystal external angle of 51.2°.

868.318 nm and the external crystal angle fixed at 51.2°.

We attempted to reoptimize the Sellmeier coefficients and found that the mathematical system was underdetermined. There were numerous solutions that fit our experimental data and some of these deviated from the previously published index of refraction dispersion relations. We therefore have chosen to present our data on predicting the GaSe crystal external angle in a manner that makes no reference to the index of refraction so that no confusion results. The external crystal angle in degrees was fitted with a quadratic function of the pump wavelength (λ_p) in nanometers and the idler frequency (ν_i) in wavenumbers.

$$\text{External Angle} = 49.4 - 1.84 \cdot 10^{-5} \cdot \lambda_p^2 + 4.70 \cdot 10^{-5} \cdot \nu_i^2 - 4.37 \cdot 10^{-11} \cdot \lambda_p^2 \cdot \nu_i^2$$

The fit to our 44 data points has a standard deviation of 0.12° . There is a high relative uncertainty in all the coefficients due to a linear dependence between variables that is not easily removed without transforming the observed variables of wavelength and frequency to nonintuitive units. The main source of experimental uncertainty was the measurement of the zero crystal angle. We were able to measure the back reflection at the polarization cube from normal incidence with respect to the GaSe crystal to within two millimeters which yielded an angular resolution of 0.2° . The uncertainty in the pump and signal wavelengths are orders of magnitude below this angular uncertainty.

Under the plane wave approximation, the phasematching bandwidth is a simple function of the effective coherence length and the wavevector mismatch. The output power can be regarded as proportional to $\text{sinc}^2((\Delta k \cdot L_{\text{eff}}) / 2)$. Assuming all three indices of refraction are constant during a scan and $\Delta k = 0$ at the peak of the infrared production, the Δk term can be approximated by Equation 5.1,

$$\Delta k = 2\pi \cdot \left(\frac{1}{\lambda_p} - \frac{1}{\lambda_p^0} \right) (n_p - n_i) \quad (5.1)$$

where λ_p is the pump wavelength, λ_p^0 is the pump wavelength at which the output IR power is maximized, and n_p and n_i are the indices of refraction at the pump and idler wavelengths, respectively. In this fashion, only the difference between the indices of refraction are necessary to compute the wavevector mismatch and is relatively insensitive to the choice of Sellmeier constants. The wavevector mismatch is assumed to be equal to zero at the

centroid of the experimental curve based on the observation that the curve does not exhibit the asymmetry shown in systems where the maximum output power and $\Delta k=0$ do not coincide (see Boyd and Kleinman [21] for an example in the case of second harmonic generation). The phasematching bandwidth for unfocused and focused beams is found to be nearly identical so long as the beams are not in the overfocused condition. In this experiment, we deliberately underfocused the input beams by using an $f=100$ mm lens instead of the $f=66$ mm called for by theory. By fitting the observed spectrum with Equation 1 where L_{eff} is the adjustable variable it is possible to obtain agreement between theory and experiment. The value of L_{eff} determined from this fit is 2.9 mm - in agreement with the work of Bianchi *et. al.* [203] in which an L_{eff} value of 3.2 mm was obtained.

As a further test of our fitting, the L_{eff} parameter can be estimated by:

$$L_{\text{eff}} = \frac{\lambda_p}{2 \cdot \Delta n}$$

where Δn is the change in index of the pump beam in turning the crystal to reduce the IR power to 40.5% of the peak value or when the accumulated phase error is equal to 180° . The value of Δn is calculated from the dispersion relations, and again it is found to be largely invariant to the choice of Sellmeier coefficients. The resulting L_{eff} is 2.9 mm. Both our results imply that the coherence length is determining the power output and

not the crystal length; thus it would be not be advantageous to obtain GaSe crystals in excess of 5 mm in length in order to obtain more IR power.

The effect of high input powers on the parametric conversion process was measured. Linearly variable neutral density filters were used to vary the input powers and the generated infrared power plotted versus their product in Figure 5.6. Thermal lensing can be a problem in the nonlinear optical conversion process - especially in the case of intense cw input beams [188]. This effect can cause the IR power to scale less than linearly with the product of the input powers but was not observed in GaSe as shown in Figure 5.6. The experimental conversion efficiency derived from the slope of the fitted line in the figure is 28% of the calculated value obtained with a nonlinear coefficient $d_{22} = 54.4$ pm/V [55] at the specific wavelengths used in Figure 6.4. Our best estimate of the detector calibration is +/- 20%. Fresnel losses at all uncoated surfaces were calculated and the calculated IR power scaled appropriately. A component of the discrepancy is the transverse distortion of the beam into an oval shape with non-normal incidence upon the GaSe crystal surface. This could be corrected with the use of a cylindrical focusing lens. A second explanation of the missing power is the possibility that the two input beams were focused at different longitudinal positions. We assumed the lasers were operating to manufacturers specifications and thus the foci were in the same location, but telescopes could be inserted in the beam path to verify this condition.

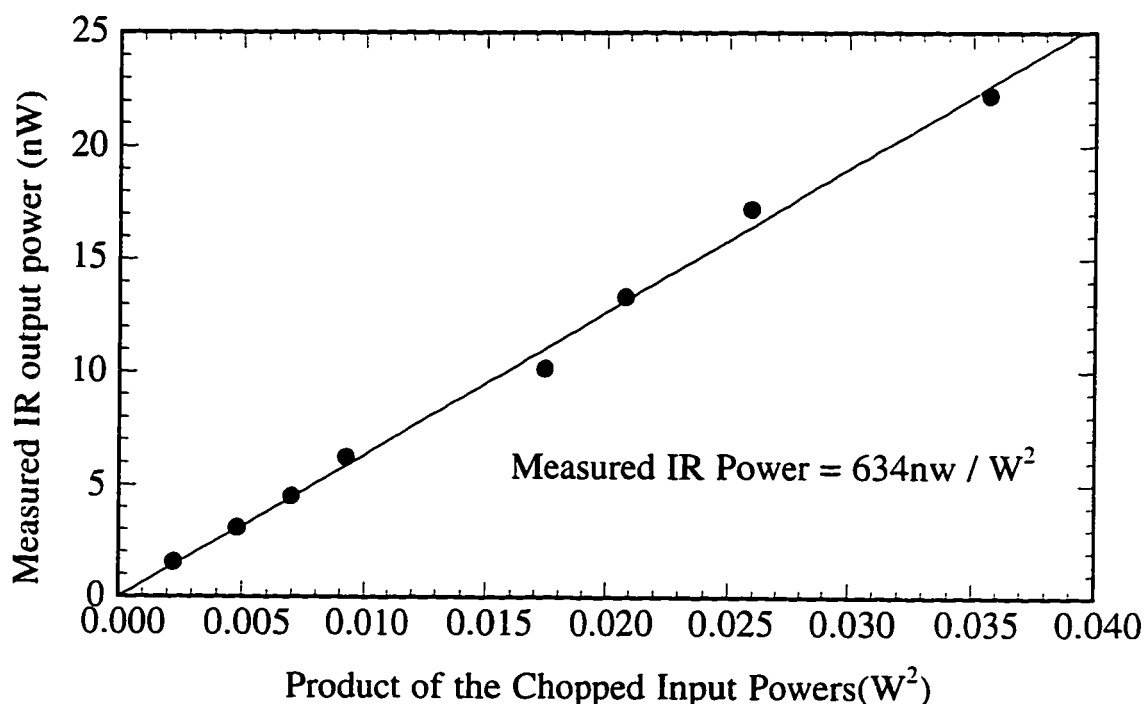


Figure 5.6 - IR DFG Power vs the product of two input drive lasers. The line is a least-squares fit to the data. The idler, pump, and signal wavelengths were 13.708 μm , 793.210 nm, and 841.925 nm, respectively, and the external angle was 48.3°.

5.3 Spectroscopy of Ethylene (C_2H_4)

The maximum mid-infrared output measured by the present system is about 30 nW, which is sufficient for spectroscopic detection of many gases. It is feasible to design a mid-IR absorption based gas sensor based on the mixing of two visible high power laser diodes (in master oscillator-power amplifier geometries at the 0.5 to 1 Watt level) in GaSe. This sensor would be capable of detecting numerous gases of interest in atmospheric monitoring - including but not limited to such species as hydrogen cyanide, acetylene, ethylene, ammonia, nitric acid, phosphine, ozone, methane, and nitrous oxide. Figure 5.7 is a survey spectrum of a

sampling of gases important to atmospheric chemistry. It should be possible to monitor all gases listed with a single sensor unit.

Ethylene is a very interesting botanical molecule. It has been found to play a role in many developmental processes in plants: ripening of fruits, wilting of flowers, and the emergence from dormancy in some seeds and bulbs [214-216]. Environmental stresses, such as excessive water loss, mechanical damage, and lack of sufficient light all stimulate the production of increased levels of C_2H_4 [217]. Ethylene concentrations have been monitored by gas chromatography and by photoacoustic detection using a carbon dioxide laser [218-220], though neither method is readily portable. Using difference frequency generation, it appears feasible to construct an

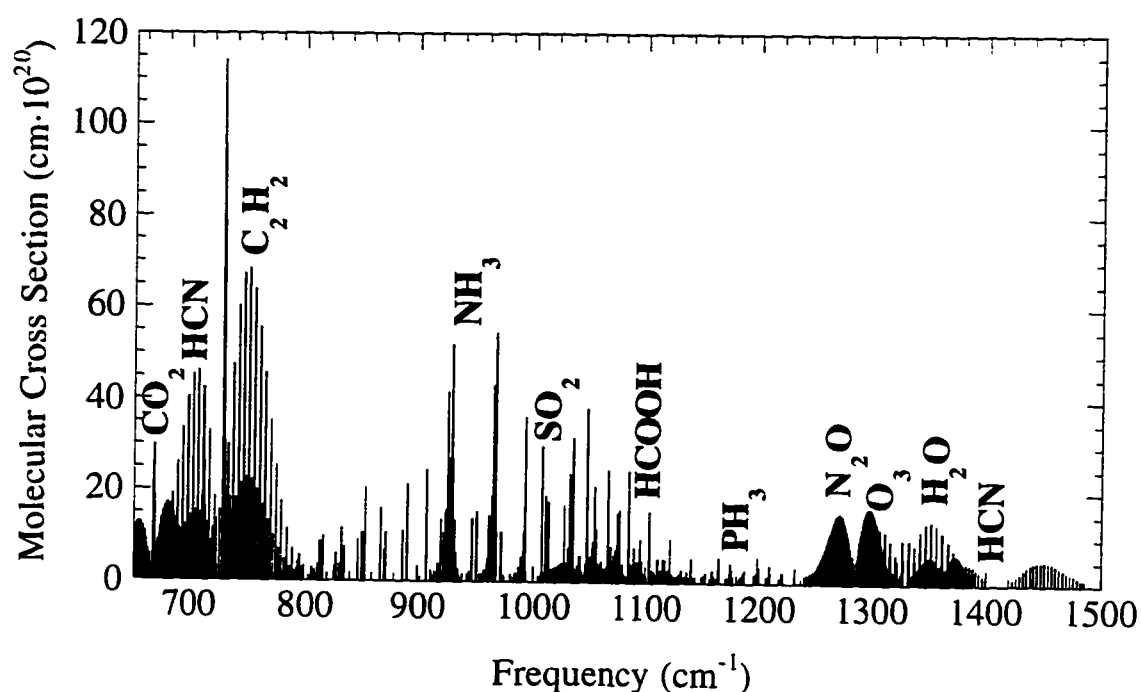


Figure 5.7 - Survey spectrum of a sampling of gases important to atmospheric chemistry.

ethylene sensor that is compact and battery driven.

In the 10- μm region, the absorption of ethylene gas is essentially due to the intense ν_7 C-type perpendicular infrared band which presents a strong Q-branch near 950 cm^{-1} . The P and R branches cover the region from 800 to 1100 cm^{-1} . Much in the way of high-resolution spectroscopy has been conducted on this band [221-223]. Nearly all the lines in this region have been assigned and their positions known to sub-Doppler accuracy.

A 20 cm^{-1} scan of ethylene taken with the experimental apparatus is shown in Figure 5.8. The inset spectrum is a blowup of 0.5 cm^{-1} centered around the most intense absorption lines. The total path length is 50 cm and the ethylene pressure is 20 mTorr. The scan was taken by fixing the signal laser at 868.750 nm, the external angle to 55.5 degrees, and scanning the pump laser from 802.195 nm to 803.484 nm in 20 MHz steps. The lock-in amplifier was set to a 100 msec time constant with a 12 dB/octave rolloff. Because of etalon effects within the 3 mm thick ZnSe flats used as windows for the absorption cell, the cell was pumped out and scanned to provide normalization.

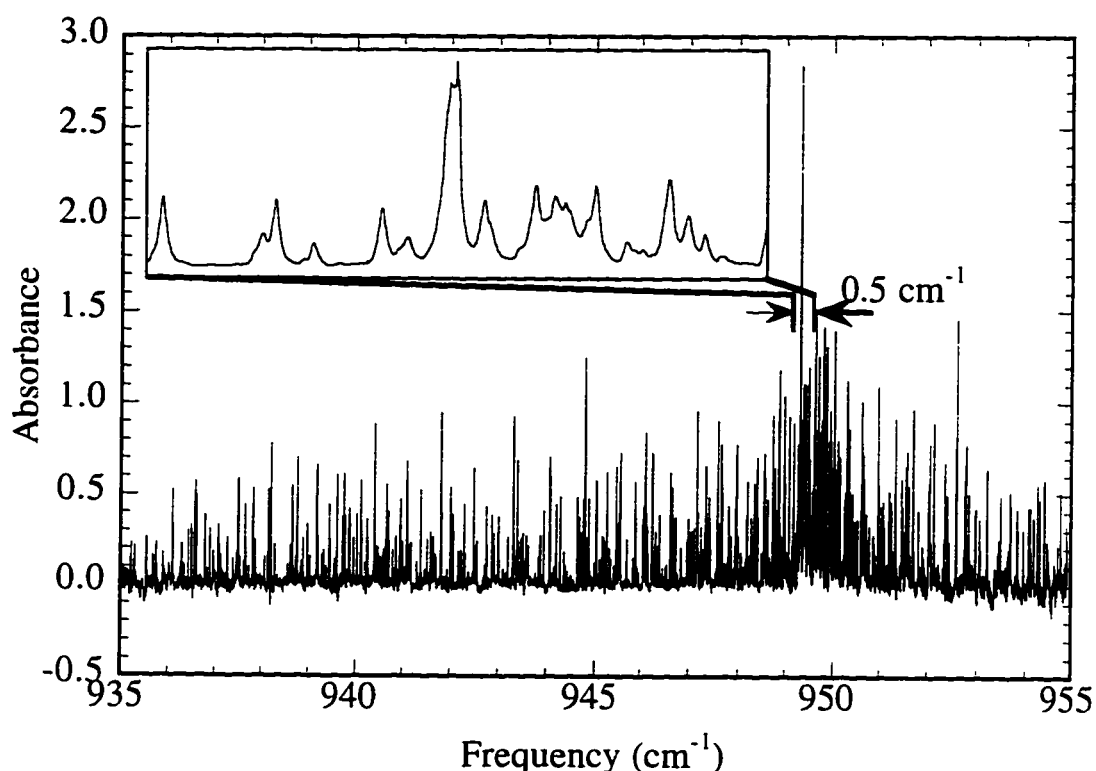


Figure 5.8 - A sample spectrum of the ethylene molecule near 945 cm^{-1} . This was taken with a path length of 50 cm and a pressure of 20 mTorr. The inset is a 0.5 cm^{-1} blowup centered on the strongest absorption lines in the lower scan.

5.4 Conclusion

In this work we have investigated the characteristics of using 780 - 900 nm pump sources to generate narrow bandwidth infrared radiation which is continuously tunable from 8.8 to $15\text{ }\mu\text{m}$ in the nonlinear optical crystal GaSe. No thermal lensing effects are observed with chopped input powers of up to half a watt cw. It is now possible to predict the phasematching angle in GaSe with an error that is less than the phasematching angular bandwidth, thus assuring IR generation for a given

combination of input wavelengths and calculated external angle. Such a tunable DFG IR source has the potential of becoming a valuable tool for environmental sensing, as demonstrated by the detection of ethylene.

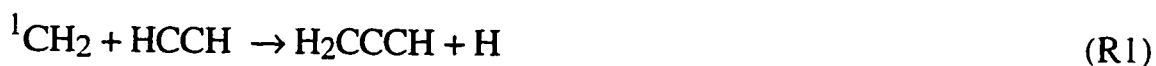
Chapter 6 - The ν_1 Stretch of the Monodeuterated Propargyl Radical (CH_2CCD)

The high-resolution infrared spectrum of the monodeuterated propargyl radical (CH_2CCD) has been obtained in the region of its acetylenic C-D stretch. Lower state rotational constants were determined for the molecule but perturbations in the upper state precluded evaluations of the upper state constants.

6.1 Propargyl Background

The propargyl radical ($\text{H}_2\text{C}-\text{C}\equiv\text{CH}$) has attracted interest as one of the simplest possible conjugated organic free radicals. Observed in abundance in pyrolysis and oxidation processes [224-232], it is thought to play an important role in the combustion and soot formation processes [233-235].

Miller and Melius [236] proposed that propargyl radicals formed from the reaction



initiate benzene ring formation, and hence the formation of polycyclic aromatic hydrocarbons (PAH), via the propargyl self-reaction



However, the ab initio calculations by Walch [237] indicate that the reaction



is responsible for propargyl radical formation and that R1 leads to the production of the stable molecules cyclopropene, allene, and propyne. Recent experiments by Adamson *et al.* [238] followed the growth and decay of H₂CCCH produced in R1 using infrared kinetic spectroscopy. The rate constant observed for R1 indicated greater than 95% yield of propargyl from this reaction and provides conclusive support for the Miller and Melius mechanism. Morter *et al.* [239] measured the rate of the propargyl self-reaction (R2) but were unable to follow product formation. More work is clearly needed to ascertain the correct mechanism of PAH formation

Spectroscopic detection of propargyl was first reported by Ramsay and Thistlewhite who observed the radical after flash photolysis of propargyl bromide, allene, and methyl acetylene [240]. They identified H₂CCCH as the carrier of an electronic transition with its origin near 30,000 cm⁻¹ that contained diffuse rotational structure based on the isotopic shifts of different vibronic bands; the spectra and identification were confirmed by Dubois and LeClerq [241]. The ESR measurements of Kasai demonstrated that the vibrationally averaged ground state propargyl radical is symmetric about a C-C≡C-H axis [242] and this conclusion has been supported by numerous theoretical calculations [243-250]. The ESR spectrum was tentatively assigned to the $\pi \leftarrow \pi$ ($^2B_1 \leftarrow ^2B_1$) transition and

was based on a C_{2v} structure for the radical. Vibrational frequencies for several of the ground state fundamentals have been determined for the normal and deuterated isotopomers from the matrix isolation infrared spectra of Jacox and Milligan [251], Mal'tsev [252], and Huang and Graham [253].

Despite its possible importance in the combustion process and subsequent soot formation, gas-phase spectroscopic data on propargyl remain scarce. Morter *et al* [254] reported the first rotationally resolved spectrum in their paper on the ν_1 absorption band near 3322 cm^{-1} . The extremely small change in the A rotational constant between the ground state and ν_1 made it possible to determine only the B and C constants for both states and precluded an experimental estimate of the molecular structure. Work by Tanaka and coworkers [255-257] on the CH_2 wagging band near 698 cm^{-1} and the microwave spectrum have provided a complete set of rotational and quartic centrifugal distortion constants for the ground state. The experimental values are in good agreement with those determined from the ab initio calculations of Botschwina *et. al.* [250].

Motivated by the importance of propargyl in combustion systems and its properties as the smallest, conjugated free radical, we have investigated the ν_1 spectrum of the H_2CCCD radical near 2555 cm^{-1} using the AgGaS₂ spectrometer described in Chapters 3 and 4. The ability to follow the time dependence of H_2CCCD concentrations in chemical reactions will be valuable in tracing the mechanism of propargyl formation in combustion systems through isotopic labelling. Monitoring H_2CCCD will also help verify mechanisms: propargyl is formed by the reaction of $^1\text{CH}_2$ with

acetylene but it is not known whether $^1\text{CH}_2$ attacks the CC bond to form a cyclic intermediate or the CH bond. This could be determined by deuterio isotopic substitution studies. Additionally, this study provides the first rotational information for any propargyl isotopomer and is an important step towards determining the substitution structure.

6.2 Experimental

We report the high resolution spectrum of the ν_1 vibrational band of the monodeuterated propargyl radical (CH_2CCD) using the technique of infrared kinetic spectroscopy. In this method, approximately 8 mTorr of 3d-propargyl bromide (a description of the synthetic route to this precursor is provided in Appendix 3) in the presence of about 7.5 Torr of He buffer gas flows into an absorption cell. Though it would have been desirable to use higher precursor pressures (see Section 4.8.6), the photolysis reaction created enough soot to clog the valves in the vacuum system. When heating the valves proved ineffective in reducing the rate of obstruction, it proved necessary to lower the precursor pressure so that operation of at least a one hour span was possible.

The propargyl radical was produced by flash photolysis of the precursor at 193 nm by the output of an ArF excimer laser. The time dependent infrared absorption spectrum of the transient was observed with the tunable single frequency cw infrared source based on difference frequency generation in AgGaS_2 with a total infrared path length of 40 meters.

6.3 Results and Discussion

A sample of the ν_1 acetylenic stretch spectrum is shown in Figure 6.1. The most intense lines represent approximately 0.3%

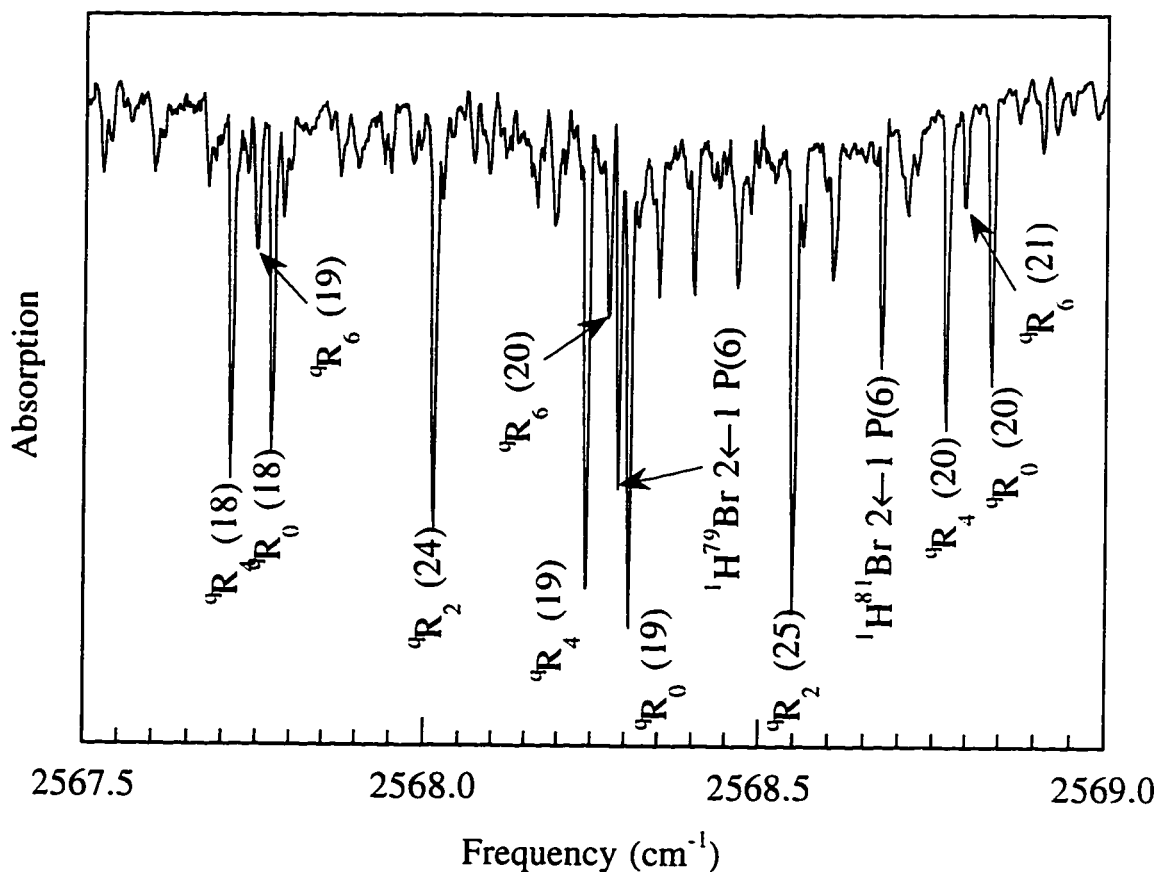


Figure 6.1 - Sample Spectrum of the Propargyl Radical.

absorption of the infrared probe. Figure 6.2 displays the vibrational origin region near 2553 cm^{-1} and illustrates the spectral resolution capable with this instrument. The final spectrum covers the range from 2535 to 2585 cm^{-1} and contains over 500 observed transient absorption features. Tables 6.1 through 6.4 list the assigned transition frequencies. From

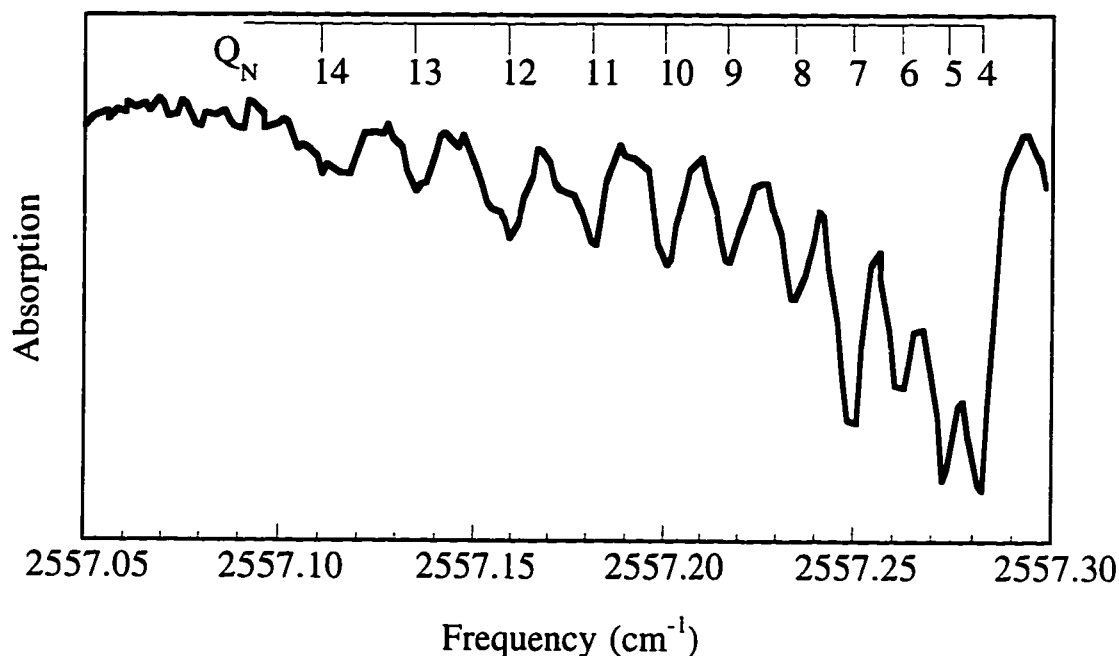


Figure 6.2 - Q-Branch of the $K_a = 4$ Subband

Figure 6.1, it seems clear that the instrument is matching our expectations and is measuring absorptions as low as 0.01% (Section 4.8.5).

As a basis for comparison, a sample of the acetylenic C-H stretch in the CH_2CCH molecule has been reproduced from Morter *et. al.* [254] in Figure 6.3. In the normal species, the K_a structure is not resolved in the normal molecule because the A , Δ_K , and Δ_{NK} rotational constants do not change much from the lower to the upper state. Thus, there is a single dominant series which runs through the central portion of the band consisting of overlapped and unresolved K_a components where all but the $K_a = 1$ bands overlap. In contrast, for CH_2CCD , the K_a structure of the C-D stretch is very well resolved.

The deuterated species spectrum displays the structure characteristic of parallel transitions ($\Delta K_a = 0$) of a nearly symmetric prolate rotor.

Table 6.1 Observed $K_a = 0 \leftarrow 0$ Frequencies (cm^{-1})

N	P(N)	R(N)
3		2559.589
4		2560.146
5	2554.482	2560.703
6	2553.905	2561.257
7	2553.330	2561.811
8	2552.752	2562.362
9	2552.170	2562.913
10	2551.589	2563.461
11	2551.006	2564.008
12	2550.422	2564.554
13	2549.835	2565.100
14	2549.250	2565.652
15	2548.662	2566.138
16		2566.695
17	2547.437	2567.235
18	2546.860	2567.772
19	2546.271	2568.306
20	2545.677	2568.838
21	2545.078	2569.366
22	2544.480	2569.897
23	2543.881	2570.424
24	2543.280	2570.950
25	2542.677	2571.477
26	2542.072	2571.969
27	2541.471	2572.513
28	2540.838	2573.037
29	2540.246	2573.559
30	2539.650	2574.085
31	2539.043	2574.619
32	2538.442	2575.179
33	2537.848	2575.691
34		2576.100
35		2576.625
36		2577.148
37		2577.673
38		2578.203

Table 6.2 - Observed $K_a = 2 \leftarrow 2$ Frequencies (cm^{-1})

N	P($N_2(N-2)$)	P($N_2(N-1)$)	Q(N)	R($N_2(N-2)$)	R($N_2(N-1)$)
2			2554.726		
3			2554.715	2556.989	
4	2552.456		2554.703	2557.552	
5	2551.887			2558.112	
6	2551.315			2558.673	
7	2550.740			2559.232	
8	2550.166			2559.790	
9	2549.592			2560.347	
10	2549.016			2560.904	
11	2548.439			2561.458	
12				2562.012	
13	2547.283			2562.564	
14	2546.703			2563.117	
15	2546.123			2563.666	
16	2545.538	2545.542		2564.215	
17	2544.950	2544.957		2564.761	
18	2544.367	2544.376		2565.307	
19	2543.779	2543.789		2565.851	
20	2543.190	2543.200		2566.394	
21	2542.596	2542.613		2566.935	
22	2542.004	2542.023		2567.475	
23	2541.408	2541.435		2568.013	
24	2540.814	2540.838		2568.550	
25	2540.214	2540.246		2569.084	
26	2539.616	2539.650		2569.617	
27	2539.016	2539.054		2570.141	2570.152
28	2538.410	2538.456			
29	2537.800	2537.856		2571.203	2571.214
30					2571.740
31				2572.261	2572.272
32				2572.798	2572.811

Note: in the above notation $N_2(N-2)$ $N_2(N-1)$ denotes the transition originating from the $NK_{\text{pro}}K_{\text{obl}}$ level (the E^+ and E^- matrix elements, respectively). Below $N=16$ on the P-Branch side and $N=27$ on the R-Branch sides, the splitting was unresolved and only a single frequency is listed.

Table 6.3 - Observed $K_a = 4 \leftarrow 4$ Frequencies (cm^{-1})

N	P(N)	Q(N)	R(N)
4		2557.284	2560.101
5		2557.275	
6		2557.264	2561.213
7	2553.298	2557.251	2561.770
8	2552.713	2557.236	2562.319
9	2552.135	2557.219	2562.868
10	2551.552	2557.201	2563.416
11	2550.967	2557.182	2563.960
12	2550.380	2557.159	2564.500
13	2549.791	2557.138	2565.049
14	2549.203	2557.116	
15	2548.616	2557.096	2566.106
16			2566.646
17	2547.407		2567.179
18	2546.812		2567.712
19	2546.214		2568.242
20	2545.615		2568.770
21	2545.011		2569.296
22	2544.408		2569.821
23	2543.801		2570.345
24	2543.190		2570.865
25	2542.581		2571.386
26	2541.971		2571.904
27	2541.357		2572.423
28	2540.746		2572.947
29			2573.502
30	2539.525		
31	2538.947		2574.517
32	2538.278		
33	2537.696		

Table 6.4 - Observed $K_a = 6 \leftarrow 6$ Frequencies (cm^{-1})

N	P(N)	Q(N)	R(N)
6		2556.791	
7		2556.778	
8		2556.763	
9		2556.746	2562.391
10	2551.085		2562.931
11	2550.500		2563.477
12	2549.911		2564.016
13	2549.319		2564.559
14			2565.091
15			2565.633
16	2547.542		2566.164
17	2546.949		2566.695
18	2546.346		2567.224
19	2545.748		2567.750
20	2545.144		2568.275
21	2544.541		2568.797
22	2543.936		2569.318
23	2543.325		
24	2542.715		2570.358
25	2542.104		2570.870
26	2541.491		2571.391
27	2540.874		2571.903
28	2540.251		2572.409
29	2539.640		2572.914
30	2539.016		2573.423
31	2538.394		2573.925
32	2537.769		2574.425
33			2574.928
34			2575.425
35			2575.922
36			2576.415
37			2576.910
38			2577.402
39			2577.894

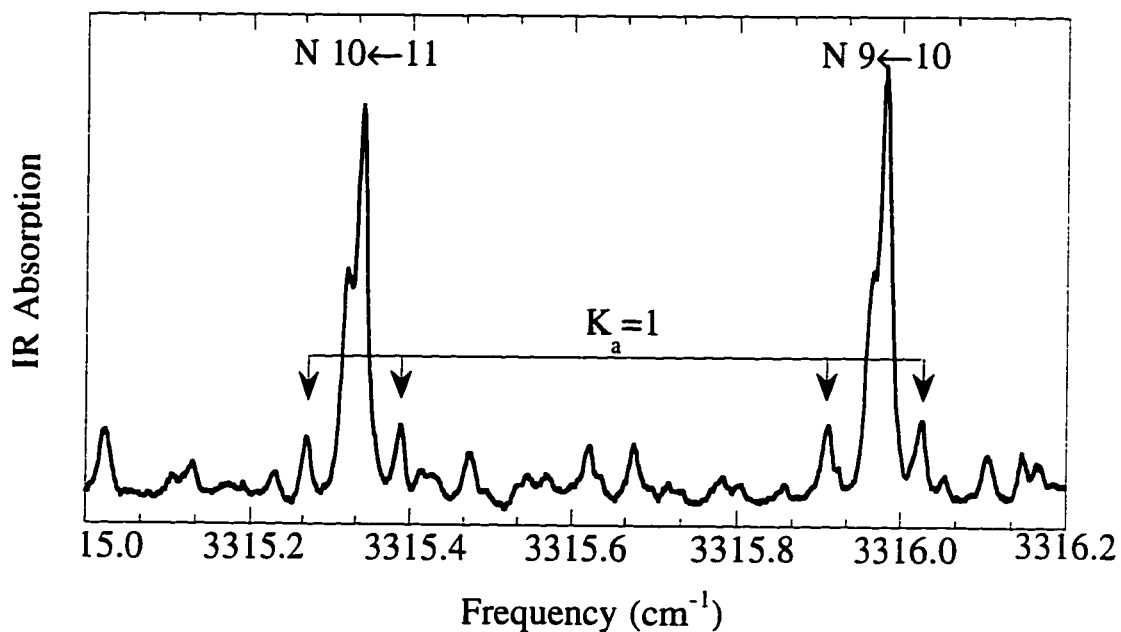


Figure 6.3 - Sample Spectrum of the Normal Propargyl Radical in the Acetylenic C-H Stretch Region

Sequences involving $K_a = 0, 2, 4,$ and 6 were positively assigned, but there were no obvious transitions associated with *any* odd K_a levels. If one assumes a C_{2v} symmetry and the $2B_1$ electronic configuration for H_2CCCD , the statistical weights of the even to odd levels are expected to be 3 to 1. This suggests that the individual components of the $K_a = 1$ and $K_a = 3$ should have comparable intensities to the $K_a = 6$ lines, which we could clearly follow

The HBr lines seen in Figure 6.1 indicate that the 193 nm photons used to photolyze the propargyl bromide may be creating trace amounts of propargylene ($CHCCD$). We would like to verify the time behavior of this reaction to determine whether propargylene is indeed a primary product of the flash photolysis or whether the HBr is generated from Br atom

extraction of hydrogen atoms from the precursor, but this is not currently feasible with the present experimental setup.

The reason for the inability to determine time behaviors can readily be seen in a time trace of the propargyl absorption line at 2550.740 cm^{-1} . Figure 6.4 was obtained by fixing the infrared frequency to the absorption line at 2565.851 cm^{-1} and averaging the signal as a function of time for 512 excimer shots. Infrared emission from the excimer laser saturates the transient digitizer for the first 6 microseconds (the signal actually reaches 600 mV) and effectively blinds the instrument during this time. The source of the emission was verified by firing the excimer laser into an evacuated White Cell without infrared light. After the excimer emission has abated, the propargyl bromide precursor continues to fluoresce until at

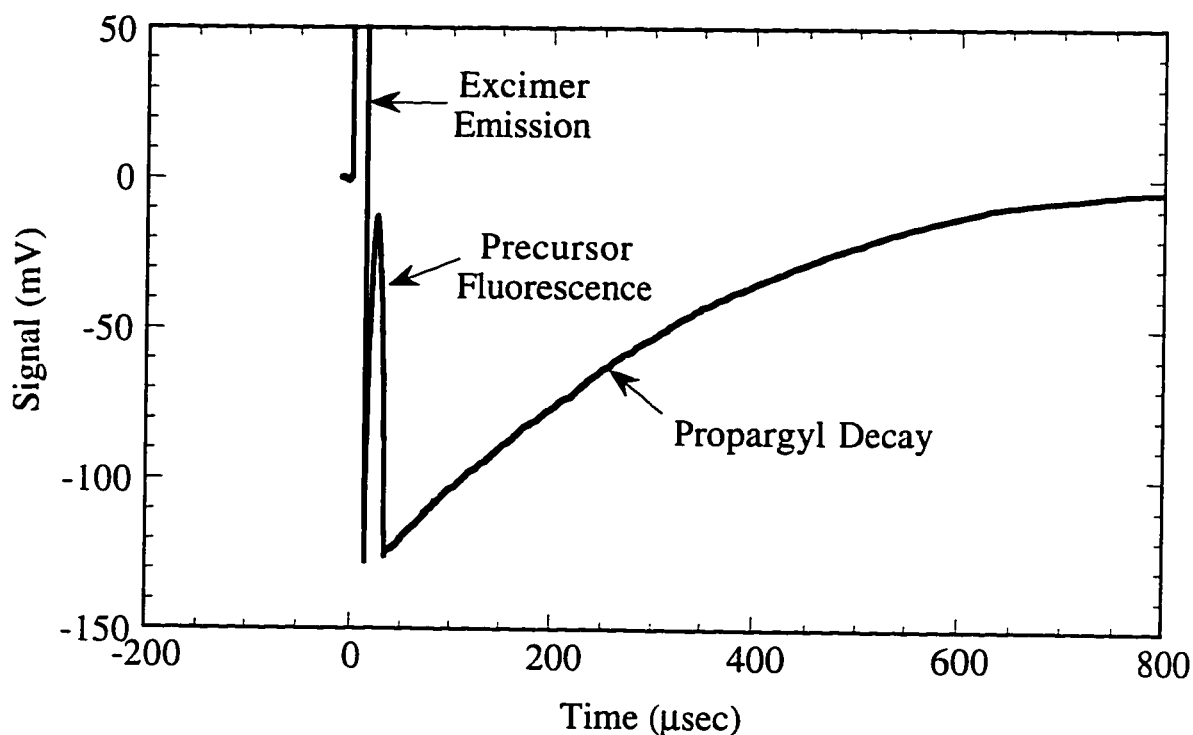


Figure 6.4 - Propargyl Time Trace

least 35 μ seconds after the excimer pulse (verified by blocking the infrared beam and taking a time trace of the excimer photolysis of the precursor). The clearest spectra were obtained by integrating the signal from 35 to 45 μ seconds after the photolysis reaction.

Upon trying to fit the assigned transitions, it rapidly became apparent that the upper state energy levels were perturbed. Therefore, ground state combination differences were fitted using Watson's A-reduced Hamiltonian. Because the $K_a=1$ lines were not assigned and only parallel transitions were observed, A, B-C, δ_N , and δ_K are heavily correlated and only the change from the lower to the upper state is well determined. The fit error associated with the $K_a = 0$ subband are seen in Figure 6.5 while the standard deviation of all fitting residuals for the ground state is 0.0009 cm^{-1} . To date, the most advanced theoretical structure for this

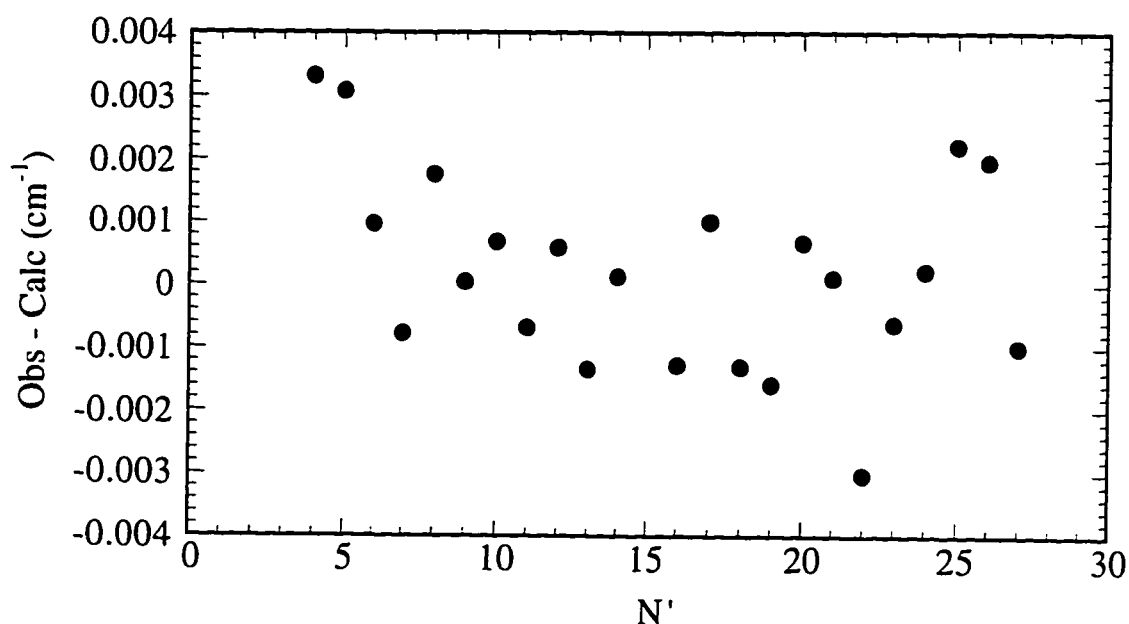


Figure 6.5 - Residuals of the $K_a = 0$ Ground State Combination Differences

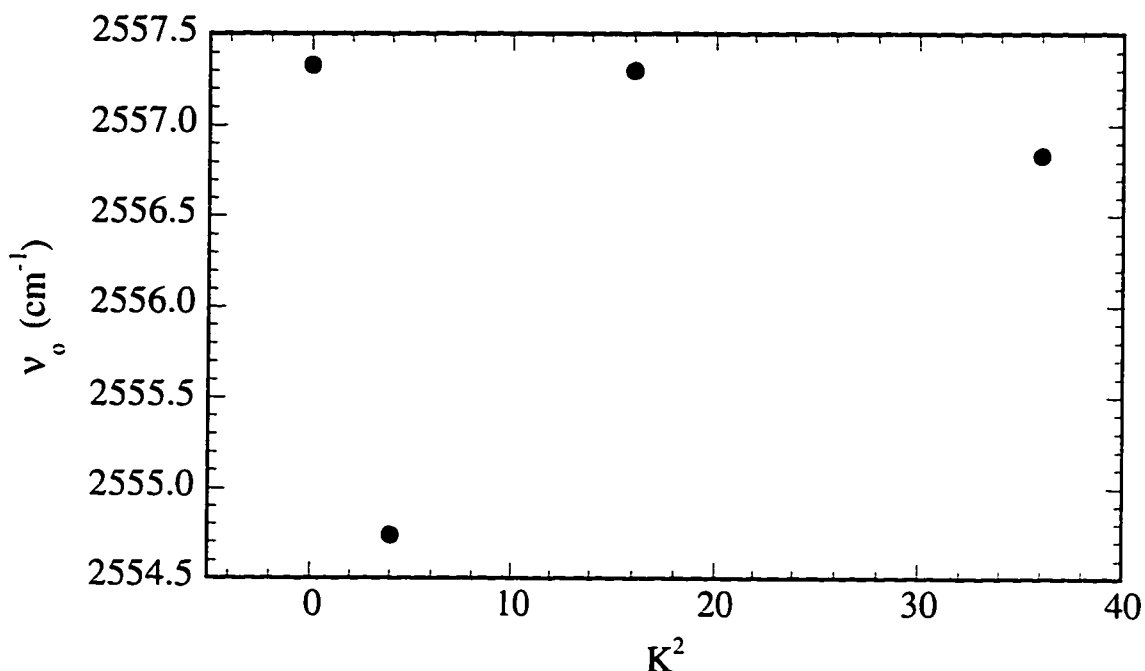


Figure 6.6 - Subband Origins in the CH₂CCD Spectrum

molecule is that of Botschwina *et. al.* [250]. The rotational constants determined from this *ab initio* geometry are given also given in Table 6.5 for comparison. The calculated rotational constants do not match the experimental numbers very well as they are different by as much as 10%.

Isotopic substitution at the acetylenic H atom should produce no change in the A'' rotational constant; therefore we fixed A'' to the value of 9.60847 cm⁻¹ determined by Tanaka and coworkers [256] for the undeuterated molecule. The resulting rotational constants are listed in Table 6.5.

The upper state energy levels were determined by adding the calculated lower state energy to the observed frequency. However, fitting many of the lines in the upper state proved impossible because of strong perturbations throughout the spectrum. Figure 6.6 shows the origins of the

Table 6.5 - Rotational Constants of the Propargyl Radical

Parameter	This Experiment C-D stretch (cm ⁻¹)	Tanaka C-H stretch [256] (cm ⁻¹)	Botschwina C-D stretch [250,258] (cm ⁻¹)
A''	9.60847(Fixed)	9.60847 (36)	9.66265
B''	0.287879(16)	0.317674 (24)	0.28664
C''	0.279211(17)	0.307098 (24)	0.27838
Δ_N''	$8.42 \cdot 10^{-8}$ (25)	$7.35 \cdot 10^{-8}$ (243)	$7.47 \cdot 10^{-8}$
Δ_{NK}''	$1.183 \cdot 10^{-5}$ (10)	$1.282 \cdot 10^{-5}$ (69)	$8.08 \cdot 10^{-6}$
Δ_K''	$7.59 \cdot 10^{-4}$ (34)	$7.546 \cdot 10^{-4}$ (137)	$7.16 \cdot 10^{-4}$
δ_N''	Undetermined	$3.45 \cdot 10^{-8}$ (167)	$2.28 \cdot 10^{-8}$
δ_K''	$5.254 \cdot 10^{-6}$ (Fixed)	$5.254 \cdot 10^{-6}$ (Fixed)	$4.453 \cdot 10^{-6}$
A'	9.614803(29)		
B'	0.286219(12)		
C'	0.279078(11)		
Δ_N'	$7.77 \cdot 10^{-8}$ (79)		
Δ_{NK}'	$1.3799 \cdot 10^{-5}$ (43)		
Δ_K'	$-1.34474 \cdot 10^{-3}$ (78)		
δ_N'	$2.78 \cdot 10^{-9}$ (33)		
δ_K'	$5.24029 \cdot 10^{-6}$ (33)		
ν_1	2557.33826(29)		

Note: The number in parenthesis is 2 standard deviations. The decimal point should be placed such that the last digit in the uncertainty matches the last digit in the experimental value.

K_a subbands in the ν_1 region, with the $K_a = 2$ subband origin displaced approximately 2.5 cm^{-1} from its expected position. Figure 6.7 shows that the $(B_{\text{eff}}' - \Delta_{NK}' \cdot K^2)$ value ($B_{\text{eff}}' = (B+C)/2$) is also perturbed: a plot of the $(B_{\text{eff}}' - \Delta_{NK}' \cdot K^2)$ values for the subbands versus K^2 should yield a straight line. The perturbation in the $K_a = 2$ subband could be caused by either a Fermi resonance or a P_a -type Coriolis interaction, but at this time we lack sufficient understanding of the possible interacting states to attempt

a detailed analysis. Our inability to assign the $K_a = 1$ and $K_a = 3$ subbands probably results from similar perturbations in their subband origins. Fits of the $K_a = 0, 4$, and 6 levels were performed to obtain effective spectroscopic constants for the upper state, but these effort were hampered by a large number of Coriolis interactions. Figure 6.8 shows the effect of three separate level crossings in the $K_a = 0$ subband. The final upper state fits employed a three standard deviation rejection limit.

It should be noted that there is a great degree of uncertainty in the values of these upper state constants that is not evident in the standard deviations. With only three subbands included in the fit and three parameters that determine the subband origins, it is impossible to determine whether any of these subband origins are perturbed. Therefore, while we can satisfactorily fit the observed lines, **we cannot be sure that the results of those fits has physical significance.**

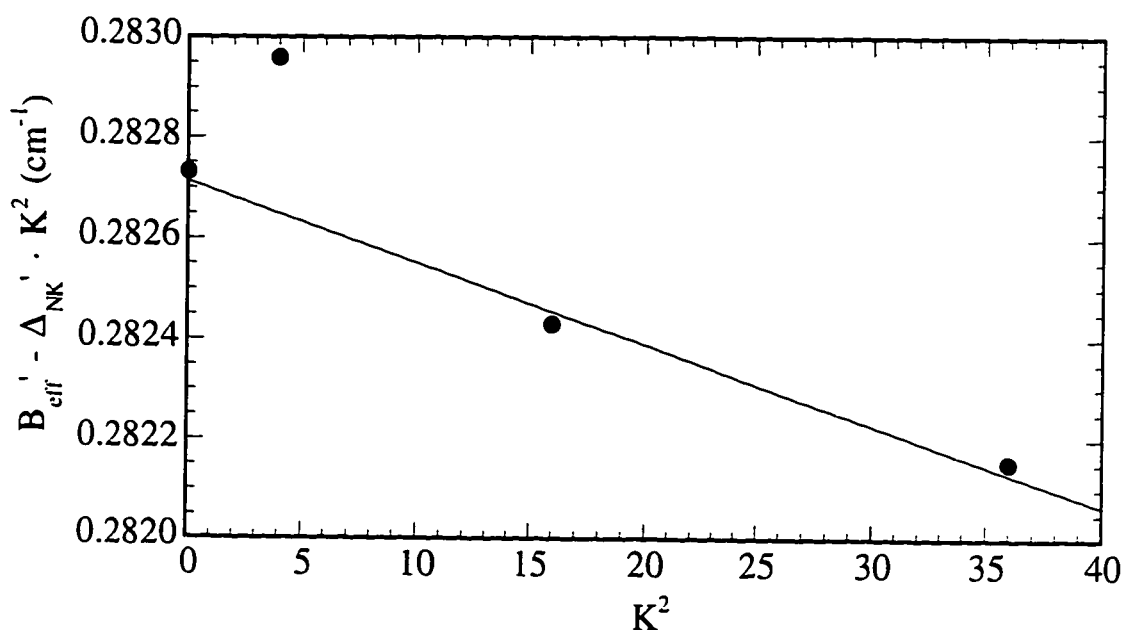


Figure 6.7 - $(B_{eff}' - D_{NK}' \cdot K^2)$ vs. K^2

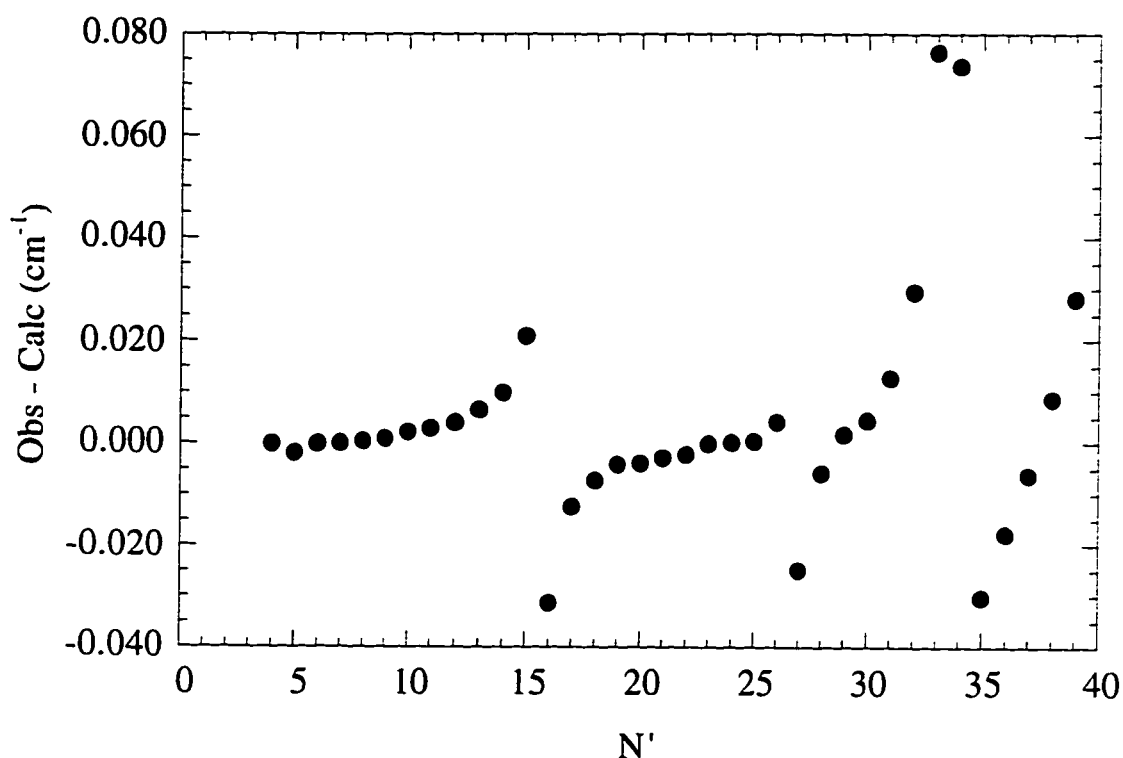


Figure 6.8 - Perturbations in the $K_a = 0$ Subband

As seen in Figure 6.1, there are as of yet many unassigned lines that could be due to the odd K_a levels as well as hot bands arising from low-lying vibrational states. A systematic study of approximately 250 unassigned lines (listed in Table 6.6) was implemented in an effort to identify the two $K_a = 1$ and the $K_a = 3$ subbands. Using the A rotational constant determined by Tanaka *et. al.* [256] and the rotational constants determined in this study, a computer program was written to calculate values of the lower state combination differences and add them to all observed lines. The presence of corresponding R-Branch transitions was noted. Estimates of the rotational constants were used to subtract the rotational energies from the observed transition frequencies and the results

plotted versus $N(N+1)$. The missing subbands should have been exhibited as straight lines on this plot but were not visually apparent (see Figure 6.9 for the results of trying to fit the lines in Table 6.6 to the $K_a = 3$ subband). Another computer program was written that fitted all possible pairs of points and calculated the sum squares due to error (SSE) of all data points based on that line, but no positive assignments were made.

6.4 Conclusions on the Propargyl Radical

Though the upper states of the propargyl radical are perturbed and thus far have not yielded reliable upper state rotational constants for the vibrational band, both the lower and upper state constants have been fit and

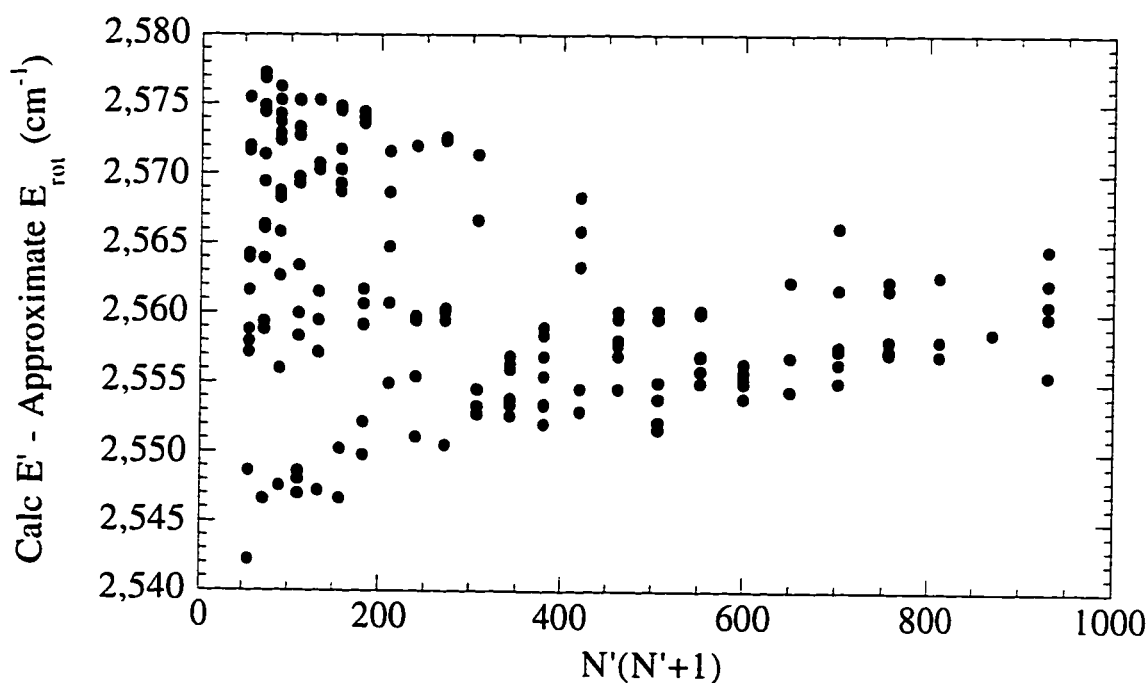


Figure 6.9 - Attempted Fit of the $K_a = 3$ Subband

several hundred transitions have been identified. The information thus gained should be of use in future kinetics work.

Table 6.6 - Unassigned Lines in the ν_1 Region of the Deuterated Propargyl Spectrum. Lines positions measured in cm^{-1}

2537.286	2537.603	2537.667	2538.209
2538.755	2538.762	2539.190	2539.283
2539.947	2540.325	2540.437	2540.542
2540.680	2540.692	2540.914	2540.961
2541.014	2541.138	2541.230	2541.471
2541.539	2541.563	2541.589	2541.623
2541.732	2541.747	2541.827	2542.212
2542.321	2542.740	2542.835	2542.912
2543.670	2543.841	2544.094	2544.889
2545.268	2545.599	2545.853	2545.892
2546.167	2546.195	2546.288	2546.746
2546.773	2547.020	2547.326	2547.348
2549.647	2550.221	2550.288	2550.289
2550.494	2551.074	2551.106	2552.031
2552.596	2552.871	2553.364	2553.641
2553.652	2554.221	2554.482	2554.637
2556.098	2556.196	2556.908	2557.040
2558.765	2559.399	2559.690	2560.008
2560.030	2560.074	2560.937	2560.958
2561.060	2561.102	2561.148	2561.206
2561.755	2561.862	2562.162	2562.307
2562.405	2562.503	2562.538	2562.695
2562.711	2562.728	2562.752	2562.774
2562.856	2562.952	2562.967	2563.039
2563.052	2563.262	2563.289	2563.329
2563.405	2563.470	2563.497	2563.542
2563.599	2563.685	2563.710	2563.741
2563.803	2563.854	2563.894	2563.931
2564.266	2565.091	2565.321	2565.545
2565.557	2565.633	2565.707	2565.742
2565.864	2565.944	2566.115	2566.241
2566.310	2566.321	2566.376	2566.409
2566.477	2566.498	2566.670	2566.773
2566.810	2566.821	2566.884	2566.900
2566.922	2566.948	2567.009	2567.054
2567.090	2567.158	2567.297	2567.345
2567.367	2567.373	2567.422	2567.487

Table 6.6 (continued)

2567.527	2567.600	2567.678	2567.790
2567.876	2567.903	2567.946	2567.981
2568.025	2568.070	2568.093	2568.157
2568.167	2568.195	2568.350	2568.401
2568.467	2568.562	2568.605	2568.710
2568.876	2568.910	2568.928	2568.949
2568.987	2569.063	2569.097	2569.195
2569.223	2569.261	2569.273	2569.277
2569.451	2569.468	2569.500	2569.509
2569.550	2569.635	2569.682	2569.740
2569.773	2570.028	2570.175	2570.525
2570.576	2570.840	2570.900	2571.031
2571.141	2571.152	2571.168	2571.510
2571.670	2571.696	2571.785	2571.850
2572.085	2572.094	2572.253	2572.274
2572.535	2572.756	2572.798	2572.809
2572.822	2573.090	2573.166	2573.261
2573.268	2573.360	2573.543	2573.651
2573.700	2573.806	2573.816	2573.902
2574.301	2574.328	2574.345	2574.468
2574.553	2574.845	2574.859	2574.985
2575.360	2575.373	2575.567	2575.595
2575.873	2575.888	2575.922	2576.037
2576.385	2576.442	2576.803	2576.891
2576.941	2577.026	2577.438	2577.900
2577.931	2578.281	2578.407	2578.425
2578.439	2578.751	2578.918	2579.337
2579.405	2579.462	2579.892	2580.325
2580.771	2580.810	2580.850	2581.222
2581.248	2581.293	2581.333	2581.437
2581.479	2581.514	2581.718	2581.816
2581.869	2582.770		

Chapter 7 - Concluding Remarks

7.1 Advances in Difference Frequency Generation

The theory of difference frequency generation has been advanced in this text. Derived from basic principles, the equations predicting the power of the generated infrared wave have been shown to accurately predict physical systems. Not only does the theory reproduce the results of the plane wave theory [19] and Chu and Broyer's formulation [27], but it overcomes their limitations. Critically phasematched difference frequency generation can now be modeled and the effects of double refraction and the ellipticity of the drive beams caused by non-normal incidence of the beams upon the crystal calculated. This work has lifted the requirement that the two drive beams be focused into the center of the crystal and have an equal confocal parameter in order to determine the expected power. The results of these calculations will be the focus of a future paper.

A mid-infrared spectrometer based on titanium:sapphire pumped difference frequency generation in silver thiogallate (AgGaS_2) has been constructed in order to conduct high resolution spectroscopy on free radicals. The tuning range of this instrument has been dramatically increased in the last three years with the introduction of the second titanium-sapphire laser. Noise in the infrared source has been reduced by almost two orders of magnitude by enclosing the argon ion laser pump beam and systematically optimizing the focusing conditions in the titanium:sapphire lasers. By carefully adjusting the focusing parameters in

the DFG process as a function of the total drive power, the wavelength independent infrared power measured by the instrument has been increased by a factor of seven over previous studies. With the introduction of a balanced detection scheme, noise in the detection of free radicals has been reduced by another factor of seven and detector limited sensitivity has been demonstrated with an estimated source bandwidth of 0.00003 cm^{-1} and an absolute sensitivity of 0.01% to changes in the infrared signal. The process used to calibrate scans has been improved so that a calibration accuracy of 0.001 cm^{-1} is now routine. The software used to control data acquisition has been rewritten and now can accurately acquire spectroscopic and kinetic data.

With the silver thiogallate spectrometer, the infrared spectrum of the monodeuterated propargyl radical (CH_2CCD) has been acquired. Approximately 250 lines have been positively identified and assigned to the ν_1 C-D stretch in the region between 2300 cm^{-1} and 2400 cm^{-1} . The spectrum consists of a-type transitions ($\Delta K_a = 0$) with a fully resolved K subband structure, in contrast to the CH stretch of the normal radical. The resolved structure may be due to a P_a -type Coriolis interaction or a Fermi resonance in the molecule, though it is also possible that the difference between species is due to an accidental cancellation in the normal species. The interactions in the deuterated molecule may be responsible for the fact that we were unable to identify the odd K subbands, though positive identification of the $K_a = 0, 2, 4$, and 6 subbands were made and used to determine rotational constants for the radical.

A spectrometer based on difference frequency generation in gallium selenide (GaSe) has been constructed. Precise phasematching characteristics have been determined as well as the potential power produced in the process. The instrument is continuously tunable in the 8.8 - 15.0 μm wavelength region. While the infrared power produced by this instrument is insufficient for the study of free radicals, it is an important development for the study of atmospheric trace gases.

7.2 Future Directions

In spite of the great advances made in the system over the past several years, there remains considerable work to be done in order to make the system live up to its full capabilities.

At present, it is not possible to follow the kinetics of reactions. The excimer laser emits infrared radiation in the 3 - 4 μm spectral region that blinds the detector for the first few microseconds. Often, the precursors used in photolysis reactions fluoresce in the infrared and interfere with kinetics studies for the first several tens of microseconds of a reaction (see Figure 6.4 for an example of both these effects in the case of the propargyl radical). A straightforward solution to the problem is to install an infrared monochromator immediately before the transient detector in order to select the specific wavelength under study. It would be desirable to have a monochromator of relatively low resolution so that adjustment of this element during the course of a scan would be unnecessary. A typical commercially available one eighth meter monochromator would have a

resolution of around 10 cm^{-1} and a transmission greater than 95% for vertically polarized light over the entire tuning range of the difference frequency generation instrument.

Spectroscopic studies would be made easier if the phasematching bandwidth could be increased. With the 45 mm AgGaS₂ crystal, scan lengths are limited to less than 2 cm^{-1} , often making wavelength calibration challenging. It is possible to use limited temperature tuning to extend the phasematching bandwidth and to remove the frequency dependence of the infrared power (see Figure 4.3). Canarelli *et. al.* [157] have determined a temperature tuning value of $0.65\text{ cm}^{-1} / ^\circ\text{C}$ for noncritical phasematching near 1300 cm^{-1} . Since this tuning value is not expected to be appreciably different in other spectral regions, this would imply that in order to conduct a 10 cm^{-1} scan at peak phasematching, it would only be necessary to change the temperature of the crystal by $6.5\text{ }^\circ\text{C}$ over the course of three hours (16 excimer shots per data point at a 10 Hz repetition rate with 50 MHz frequency steps) - well within the thermal limits of the crystal and achievable with simple thermoelectric coolers (Peltier elements). Because of the relatively low thermal tuning value, the temperature tolerances would be rather large: if the crystal temperature was ramped up by $6.8\text{ }^\circ\text{C}$ instead of $6.5\text{ }^\circ\text{C}$ over a 10 cm^{-1} scan, the infrared power would only drop in half. A properly adjusted temperature controller is capable of controlling the temperature of the crystal to well within $0.01\text{ }^\circ\text{C}$ and the change in infrared power due to this error in temperature would be unnoticeable.

Because the infrared source is on a "floating" table and the multipass cell is not, noise can be introduced into the system when the floating table is jarred. It is possible to move the infrared beam completely off the detector simply by rearranging objects on the optical table. This problem can be eliminated by yoking two optical tables together and placing all optical elements on this surface but would involve a substantial rearrangement of the laboratory.

At present, it is difficult to conduct spectroscopic studies in regions of the spectrum where the atmosphere absorbs infrared light. The region around 6 μm is particularly troublesome, where water vapor often absorbs all radiation in paths longer than a few centimeters. An earlier study by this author and others [259] of the high-resolution spectrum of the HCCN radical was greatly hampered by these lines. To combat this difficulty, the infrared beam should be entirely shielded from the atmosphere with either a vacuum system or dry nitrogen purge lines.

When the precursors used in experiments have a low cross-section to the photolysis wavelength, it is difficult to generate high concentrations of free radicals. By reflecting the transmitted excimer beam back through the multipass cell, it would be possible to increase the photolysis product concentrations. In the past, it was found that standard excimer wavelength mirrors were damaged when placed in evacuated cells because of the deposition of soot on the mirror surface that was impossible to remove. There was also insufficient cooling of the dielectric surface under vacuum that resulted in ablation of the mirrors. However, it should be possible to employ the rear reflector of an excimer laser in this environment. The

reflective silver or aluminum coating is placed on the side of the optic removed from the photolysis region and the ultraviolet light passes through the mirror substrate. If the optic were mounted on the multipass cell such that the reflective surface was exposed to the atmosphere, heat dissipation would no longer be problematic. A sooty mirror surface would be cleaned in the same way that excimer windows or the input window to the multipass cell is cleaned - titanium oxide rubbing compound.

7.3 Conclusion

The applicability of two difference frequency generation spectrometers have been demonstrated in this laboratory and the theory behind their use furthered. It is to be hoped that this work has allowed the instruments to move beyond feasibility studies and that they have become useful scientific instruments in the studies of gas-phase molecules.

Appendix 1 - Derivation of the Power Generated in the Difference Frequency Generation Process

The theory of power generation in the difference frequency conversion process generally starts with the paraxial wave equation (Equation 2.3.14) and with the Gaussian envelope of the drive lasers. In the present formulation we have chosen the Gaussian envelope (Equation 2.3.15) to allow ellipticity in the beams, birefringent walkoff, differing confocal parameters between the two drive lasers, and adjustable focal positions for both the vertical and horizontal dimensions of each beam. The study was undertaken because there is experimental evidence [260-262] that elliptical focusing in the presence of double refraction can increase the parametric amplification and lower the threshold power for Optical Parametric Oscillators. In previous analyses the theory for difference frequency generation have assumed cylindrical beams. Here we consider the parametric interaction of two waves - one of which undergoes double refraction.

To calculate the power produced in a single pass through a optical parametric amplifier (the typical difference frequency generation setup), one solves the for the following form of Equation 2.3.22.

$$P_i = \frac{n_i \cdot c}{2 \cdot \epsilon_0} \left(\frac{j \cdot \omega_i \cdot d_{eff}}{\epsilon_0 \cdot c \cdot n_i} \right)^2 \int_{-\infty}^{\infty} dz \cdot \int_{-\infty}^{\infty} dx \cdot dy \cdot A_p(x, y, z) \cdot A_s^*(x, y, z) \cdot e^{-j\Delta k z}.$$

$$\int_0^z dz' \cdot \int_{-\infty}^{\infty} dx' dy' \cdot G^*(x, x', y, y', z, z') \cdot A_p^*(x', y', z') \cdot A_s(x', y', z') \cdot e^{-j\Delta k z'} \quad (A1.1)$$

$$G_i(x, x', y, y', z, z') = \frac{-j \cdot k_i}{2\pi(z-z')} \exp\left(\frac{j \cdot k_i}{2\pi(z-z')} \{(x-x')^2 + (y-y')^2\}\right) \quad (A1.2)$$

$$A_a(x, y, z) = \frac{A_{a0}}{(1+j \cdot (\tau_{ax} - \tau_{ax}^0)) \cdot (1+j \cdot (\tau_{ay} - \tau_{ay}^0))} \cdot \exp\left(\frac{-\{x - \rho_a(z - z_{ax}^0) - x_0\}^2}{w_{ax}^2 \cdot (1+j \cdot (\tau_{ax} - \tau_{ax}^0))} + \frac{-y^2}{w_{ay}^2 \cdot (1+j \cdot (\tau_{ay} - \tau_{ay}^0))}\right) \quad (A1.3)$$

where the definitions of the variables contained within the equations are given in the text of Chapter 2.

The radiation density ρ is given by the square of the electric field (Equation A1.3) divided by the permittivity of free space and the intensity of the beam I_a is given by the radiation density multiplied by

the group velocity of light ($n_a \cdot c$) at the input frequency. An integration of the intensity across the transverse coordinates at any arbitrary location z will equal the total power P_a in the beam. Note: we have explicitly used the undepleted pump (and signal) approximation so that the peak amplitude A_{a0} is invariant with respect to z). It is simplest to integrate this function at the focus of the beam ($z=z_{ax}^0$ so that $\tau_{ax} = \tau_{ax}^0$, $\tau_{ay} = \tau_{ay}^0$, etc.). By calculating the peak amplitude term from vacuum propagation, we can set the double refraction angle ρ_a to zero (the form of the wave function has to be valid for vacuum propagation as well as in the nonlinear medium). Thus:

$$P_a = \int_{-\infty}^{\infty} dx \cdot dy \cdot I = \frac{n_a \cdot c}{\epsilon_0} \int_{-\infty}^{\infty} dx \cdot dy \cdot \rho_a \quad (A1.4)$$

$$= \frac{n_a \cdot c}{\epsilon_0} \cdot \int_{-\infty}^{\infty} dx \cdot dy \cdot \left\{ \frac{A_{a0}}{(1) \cdot (1)} \cdot \exp \left(\frac{-x^2}{w_{ax}^2 \cdot (1)} + \frac{-y^2}{w_{ay}^2 \cdot (1)} \right) \right\}^2$$

$$= \frac{n_a \cdot c \cdot A_{a0}^2}{\epsilon_0} \cdot \int_{-\infty}^{\infty} dx \cdot dy \cdot \left\{ \exp \left(\frac{-x^2}{w_{ax}^2} + \frac{-y^2}{w_{ay}^2} \right) \right\}^2$$

$$\begin{aligned}
&= \frac{n_a \cdot c \cdot A_a 0^2}{\epsilon_0} \cdot \left(\frac{\sqrt{\pi}}{2 \cdot \sqrt{\frac{2}{w_{ax}^2}}} \right) \left(\frac{\sqrt{\pi}}{2 \cdot \sqrt{\frac{2}{w_{ay}^2}}} \right) \\
&= \frac{\pi \cdot n_a \cdot c \cdot A_a 0^2 \cdot w_{ax} \cdot w_{ay}}{8 \cdot \epsilon_0} \\
A_a 0^2 &= \frac{8 \cdot \epsilon_0 \cdot P_a}{\pi \cdot n_a \cdot c \cdot w_{ax} \cdot w_{ay}}
\end{aligned} \tag{A1.5}$$

In the interest of saving space we will stop writing the explicit dependence of the amplitude on the Cartesian coordinates in the interest of space and will simply have to remember the dependence. Interchange the order of integration of Equation A1.1 and rearrange slightly to give:

$$P_i = \frac{d_{eff}^2 \cdot \omega_i^2}{2 \cdot \epsilon_0^3 \cdot c \cdot n_i} \cdot \text{Im} \left[j \cdot \int_0^L dz \cdot \int_0^z dz' \cdot e^{-j\Delta k(z-z')} \int_{-\infty}^{+\infty} dx dx' dy dy' A_p A_s^* G_i^* \cdot A_p^{'} \cdot A_s^{'} \right] \tag{A1.6}$$

Separation of the x from the y coordinates is relatively straightforward. Define the kernel of the transformation as

$$K(z,z') = \int_{-\infty}^{+\infty} dx dx' dy dy' A_p A_s^* G_i^* \cdot A_p^{i*} A_s' \quad (A1.7)$$

This kernel can be factored into an x and y kernel

$$K(z,z') = \frac{-j \cdot A_{p0}^2 \cdot A_{s0}^2 \cdot k_i}{2\pi(z-z')} \cdot K_x(z,z') \cdot K_y(z,z') \text{ where} \quad (A1.8)$$

$$K_x(z,z') = \int_{-\infty}^{+\infty} dx dx' A_{px}(x,z) A_{sx}^*(x,z) G_{ix}^*(x,x',z,z') A_{px}^{i*}(x',z') A_{sx}'(x',z') \quad (A1.9)$$

$$A_{px}(x,z) = \frac{1}{\sqrt{(1+j \cdot (\tau_{px} - \tau_{px}^0))}} \cdot \exp \left\{ \frac{(x - \rho_{px}(z - z_{px}^0) + x_{p0})^2}{w_{px}^2 \cdot (1+j \cdot (\tau_{px} - \tau_{px}^0))} \right\} \quad (A1.10)$$

$$A_{sx}(x,z) = \frac{1}{\sqrt{(1+j \cdot (\tau_{sx} - \tau_{sx}^0))}} \cdot \exp \left\{ \frac{(x - \rho_{sx}(z - z_{sx}) + x_{s0})^2}{w_{sx}^2 \cdot (1+j \cdot (\tau_{sx} - \tau_{sx}^0))} \right\} \quad (A1.11)$$

$$G_{ix}(x,x',z,z') = \exp \left\{ \frac{j \cdot k_i \cdot (x - x')}{2(z - z')} \right\} \quad (A1.12)$$

$$K_y(z,z') = \int_{-\infty}^{+\infty} dx dx' A_{py}(x,z) A_{sy}^*(x,z) G_{iy}^*(y,y',z,z') A_{py}'(y',z') A_{sy}'(y',z') \quad (A1.13)$$

$$A_{py}(y,z) = \frac{1}{\sqrt{(1+j(\tau_{py} - \tau_{py0}))}} \cdot \exp \left\{ \frac{(y - \rho_{py}(z - z_{py})^0)^2}{w_{py}^2 \cdot (1+j(\tau_{py} - \tau_{py}^0))} \right\} \quad (A1.14)$$

$$A_{sy}(y,z) = \frac{1}{\sqrt{(1+j(\tau_{sy} - \tau_{sy})^0))}} \cdot \exp \left\{ \frac{(y - \rho_{sy}(z - z_{sy})^0)^2}{w_{sy}^2 \cdot (1+j(\tau_{sy} - \tau_{sy}^0))} \right\} \quad (A1.15)$$

$$G_{iy}(y,y',z,z') = \exp \left\{ \frac{j \cdot k_i \cdot (y - y')}{2(z - z')} \right\} \quad (A1.16)$$

We can now write:

$$P_i = \frac{d_{\text{eff}}^2 \cdot \omega_j^2}{2 \cdot e_0^3 \cdot c \cdot n_i} \cdot \text{Im} \left(j \cdot \int_0^L dz' \int_0^z dz'' e^{-j\Delta k(z-z')} K(z, z') \right) \quad (\text{A1.17})$$

and all the transverse dependence of the beam is included in the kernel K. Integration across these four coordinates is all tied into the exponents and is a Fourier Transform of a Gaussian function that has an exact analytical solution. To put this integration into a more manageable form, will make several further substitutions. Integration across the transverse coordinates leaves the preexponential terms in Equation A1.9 unaffected and thus they can be brought out from the integral. Collect all the preexponential terms from A_{px} , A_{sx}^* , A_{px}'' , and A_{sx}' in Equation A1.9 into a single term.

$$C_x = \frac{1}{\sqrt{\{1+j(\tau_{px}-\tau_{px0})\} \{1-j(\tau_{sx}-\tau_{sx0})\} \{1-j(\tau_{px}'-\tau_{px0})\} \{1+j(\tau_{sx}'-\tau_{sx0})\}}} \quad (\text{A1.18})$$

Collect the similar terms from the y-coordinates in Equation A1.13

$$C_y = \frac{1}{\sqrt{\{1+j(\tau_{py}-\tau_{py0})\} \{1-j(\tau_{sy}-\tau_{sy0})\} \{1-j(\tau_{py}'-\tau_{py0})\} \{1+j(\tau_{sy}'-\tau_{sy0})\}}} \quad (\text{A1.19})$$

Collect the exponential terms from Equations A1.9.

$$\exp \left\{ \left(\frac{-y^2}{w_{py}^2 \cdot (1+j \cdot (\tau_{py} - \tau_{py}^0))} \right) + \left(\frac{-\left(x - \rho_{sx}(z - z_{sx}^0) + x_{s0} \right)^2}{w_{sx}^2 \cdot (1+j \cdot (\tau_{sx} - \tau_{sx}^0))} \right) + \right. \\ \left. \left(\frac{-y^2}{w_{py}^2 \cdot (1-j \cdot (\tau_{py}' - \tau_{py}^0))} \right) + \left(\frac{-\left(x - \rho_{sx}(z - z_{sx}^0) + x_{p0} \right)^2}{w_{sx}^2 \cdot (1-j \cdot (\tau_{sx}' - \tau_{sx}^0))} \right) \frac{j \cdot k_i}{2(z - z')} \right\} \quad (A1.20)$$

Integration of the x and x' coordinates is now equivalent to an integration of Equation A1.20. The problem can be simplified if we make the following substitutions.

$$a_x = \frac{1}{w_{sx}^2 \cdot (1+j \cdot (\tau_{sx} - \tau_{sx}^0))} \quad (A1.21)$$

$$b_x = \frac{1}{w_{px}^2 \cdot (1-j \cdot (\tau_{px} - \tau_{px}^0))} \quad (A1.22)$$

$$c_x = \frac{1}{w_{sx}^2 \cdot (1-j \cdot (\tau_{sx}' - \tau_{sx}^0))} \quad (A1.23)$$

$$d_x = \frac{1}{w_{px}^2 \cdot (1+j \cdot (\tau_{px}' - \tau_{px}^0))} \quad (A1.24)$$

$$E = \frac{j \cdot k_i}{2(z-z')} \quad (A1.25)$$

$$\delta_0 = \rho_x(z-z_{px})^0 - x_{p0} - x_{s0} \quad (A1.26)$$

$$\delta_1 = \rho_x(z'-z_{px})^0 - x_{p0} - x_{s0} \quad (A1.27)$$

Integration across Equation A1.20 can now be written in the more friendly form of

$$\int_{-\infty}^{+\infty} dx dx' \exp \{ -a_x x^2 - b_x (x - \delta_0)^2 - c_x x'^2 - d_x (x - \delta_1)^2 + jE(x - x')^2 \} \quad (A1.28)$$

where a, b, c, and d have positive real components and E is entirely real. With some rearrangement the exponent in A2.28 is -1 times

$$(a_x + b_x - jE)x^2 + (c_x + d_x - jE)x'^2 + 2jExx' - 2b_x \delta_0 \delta_1 - 2d_x \delta_0 \delta_1 + b_x \delta_0^2 + d_x \delta_1^2 \quad (A1.29)$$

Let M be the matrix

$$M_x = \begin{bmatrix} a_x + b_x - jE & jE \\ jE & c_x + d_x - jE \end{bmatrix} \quad (A1.30)$$

Then Equation A1.28 is transformed to

$$\exp(-b_x \delta_0^2 - d_x \delta_1^2) \int_{-\infty}^{+\infty} dx' dx \cdot \exp\left(-[x \ x'] \cdot \mathbf{M}_x \cdot \begin{bmatrix} x \\ x' \end{bmatrix}\right) \cdot \exp\left\{-[x \ x'] \cdot \begin{bmatrix} 2b_x \delta_0 \\ 2d_x \delta_1 \end{bmatrix}\right\} \quad (\text{A1.31})$$

The analytical solution of this integral is known and will be used without further explanation. The reader is urged to consult Hörmander [263] for details of the solution. We finally end up with the integration of Equation A1.6 across the x coordinate.

$$I_x = \frac{\pi}{\sqrt{|\mathbf{M}_x|}} \exp\{-b_x \delta_0^2 - d_x \delta_1^2\} \exp\left\{-[b_x \delta_0 \ d_x \delta_1] \cdot \mathbf{M}_x^{-1} \cdot \begin{bmatrix} b_x \delta_0 \\ d_x \delta_1 \end{bmatrix}\right\} \quad (\text{A1.32})$$

In a similar manner, we can derive the same form for the y dimension by replacing all the x's in Equations A1.21 - A1.32 with y's. The form of Equation A1.34 is different than that of A1.32 because of the absence of double refraction effects by our definition of the coordinate axes.

$$\mathbf{M}_y = \begin{bmatrix} a_y + b_y - jE & jE \\ jE & c_y + d_y - jE \end{bmatrix} \quad (\text{A1.33})$$

$$I_y = \frac{\pi}{\sqrt{|\mathbf{M}_y|}} \quad (\text{A1.34})$$

$$a_y = \frac{1}{w_{sy}^2 \cdot (1+j \cdot (\tau_{sy} - \tau_{sy}^0))} \quad (\text{A1.35})$$

$$b_y = \frac{1}{w_{py}^2 \cdot (1-j \cdot (\tau_{py} - \tau_{py}^0))} \quad (\text{A1.36})$$

$$c_y = \frac{1}{w_{sy}^2 \cdot (1-j \cdot (\tau_{sy}' - \tau_{sy}^0))} \quad (\text{A1.37})$$

$$d_y = \frac{1}{w_{py}^2 \cdot (1+j \cdot (\tau_{py}' - \tau_{py}^0))} \quad (\text{A1.38})$$

Looking back, all that remains is to collect the terms derived above. We can see that

$$K_x(z, z') = C_x \cdot I_x \quad (\text{A1.39})$$

$$K_y(z, z') = C_y \cdot I_y$$

$$K(z,z') = \frac{-j \cdot A_p^2 \cdot A_s^2 \cdot k_i}{2\pi(z-z')} \cdot C_x C_y I_x I_y = \frac{-64 \cdot j \cdot \epsilon_0^3 \cdot P_p \cdot P_s \cdot k_i}{2\pi^3 \cdot n_p \cdot n_s \cdot c^2 \cdot w_{px} \cdot w_{py} \cdot w_{sx} \cdot w_{sy} \cdot (z-z')} \cdot C_x C_y I_x I_y \quad (A1.40)$$

$$P_i = \frac{-\omega_i^2 \cdot d_{eff}^2}{2 \cdot \epsilon_0^3 \cdot c \cdot n_i} \cdot \text{Im} \left(j \cdot \int_0^L dz \int_0^z dz' \cdot e^{-j\Delta k(z-z')} \frac{-64 \cdot j \cdot \epsilon_0^3 \cdot P_p \cdot P_s \cdot k_i}{2\pi^3 \cdot n_p \cdot n_s \cdot c^2 \cdot w_{px} \cdot w_{py} \cdot w_{sx} \cdot w_{sy} \cdot (z-z')} \cdot C_x C_y I_x I_y \right) \quad (A1.41)$$

$$P_i = \frac{16 P_p P_s k_i \omega_i^2 d_{eff}^2}{\pi^3 \epsilon_0 n_p n_s n_i c^3 w_{px} w_{py} w_{sx} w_{sy}} \cdot \text{Im} \left(j \cdot \int_0^L \int_0^z \frac{C_x \cdot C_y \cdot I_x \cdot I_y \cdot e^{-j\Delta k(z-z')}}{2(z-z')} dz' dz \right) \quad (A1.42)$$

Lemma 1 - The existence of $|M|^{-1/2}$

Equations A1.32 and A1.34 are only valid if $|M|$ is not a purely real negative number. This can be verified in the following manner. Note that the form of $|M|$ (minus the subscripts) equals

$$(a+b)(c+d) - (a+b+c+d)jE$$

$$\text{write } a + b = \alpha + jB \quad \alpha > 0$$

$$(A1.43)$$

$$c + d = \gamma + j\delta \quad \gamma > 0$$

substitute the above equations into A2.33

$$(\alpha + jB)(\gamma + j\delta) - (\alpha + \gamma)jE + (\beta + \delta)E = \alpha\gamma - \beta\delta + (\beta + \delta)E + j \cdot (B\gamma + \alpha\delta - \alpha E - \gamma E) \quad (A1.44)$$

If the above is a real number, then

$$E = \frac{\beta\gamma + \alpha\delta}{\alpha + \delta} \quad (A1.45)$$

so the real part equals $1/(\alpha + \delta)$ times

$$\begin{aligned} (\alpha + \gamma)(\alpha\gamma - \beta\delta) + (\beta + \delta)(\beta\gamma + \alpha\delta) = \\ (\alpha + \gamma) \cdot \alpha\gamma - (\alpha + \delta)\beta\delta + \beta^2\gamma + \alpha\delta^2 + \beta\alpha\delta + \delta\beta\gamma = \\ (\alpha + \gamma)\alpha\gamma + \beta^2\gamma + \delta^2\alpha \end{aligned} \quad (A1.46)$$

This last term is greater or equal to

$$(\alpha + \gamma)\alpha\gamma$$

which is greater than zero by definition in A1.43. Thus, the determinant of **M** is not a purely negative real number and we can take the principal square root.

Appendix 2 - The Index of Refraction in Silver Thiogallate

Note: All dispersion equations in this work assume the wavelength is presented in microns.

First studied by the Hobden group [167], the index of refraction in AgGaS₂ was determined using the minimum deviation technique with polished AgGaS₂ prism and the output of He and Hg lamps in the 480 to 670 nm range. The published values for the index of refraction have been fitted to pseudo-Sellmeier equations by Bhar and Smith [135]:

$$\begin{aligned} n_o^2 &= 5.728 + \frac{0.2410 \lambda}{\lambda^2 - 0.0870} - 0.00210 \lambda^2 \\ n_e^2 &= 5.497 + \frac{0.2026 \lambda}{\lambda^2 - 0.1307} - 0.00233 \lambda^2 \end{aligned} \quad (\text{A.2.1})$$

Bhar and Smith used a simple least squares algorithm to fit published index data to the above form.

Boyd *et. al.* [154] remeasured the dispersion of AgGaS₂ in the 0.490 - 12.000 μm range with the same minimum deviation prisms method and their data was also fit by Bhar and Smith [135]:

$$\begin{aligned} n_o^2 &= 2.6149 + \frac{3.1769 \lambda}{\lambda - 0.0739} + \frac{2.1328 \lambda}{\lambda - 950} \\ n_e^2 &= 3.0398 + \frac{2.4973 \lambda}{\lambda - 0.0912} + \frac{2.1040 \lambda}{\lambda - 950} \end{aligned} \quad (\text{A.2.2})$$

Bhar and Smith [135] measured the index of refraction in the visible range (485 - 700 nm) using a small angle prism. They have obtained results similar to the previous works:

$$\begin{aligned} n_o^2 &= 4.6187 + \frac{1.3758 \lambda}{\lambda - 0.1205} + \frac{199.28 \lambda}{\lambda - 950} \\ n_e^2 &= 5.5373 + \frac{0.5685 \lambda}{\lambda - 0.1725} + \frac{636.85 \lambda}{\lambda - 950} \end{aligned} \quad (\text{A.2.3})$$

Fan *et al.* [109] modified the Sellmeier coefficients by adjusting both ultraviolet [sic] and infrared poles independently for the two indices to obtain a least squares fit to the dispersion data of Boyd *et al.* [154].

$$\begin{aligned} n_o^2 &= 3.3970 + \frac{1.3758 \lambda^2}{\lambda^2 - 0.009311} + \frac{2.1640 \lambda^2}{\lambda^2 - 950} \\ n_e^2 &= 3.5873 + \frac{1.9533 \lambda^2}{\lambda^2 - 0.11066} + \frac{2.3391 \lambda^2}{\lambda^2 - 1030.7} \end{aligned} \quad (\text{A.2.4})$$

The Bhar group [168] revisited the dispersion problem with new crystals and paid particular attention to the 8.8 - 10.8 μm wavelength range, though the results were not cast in the form of a dispersion relation but were presented in Figure 1 of their paper.

Dave Roberts, in the most recently published work [104] has assembled birefringence and phasematching data from a variety of sources (including all the above studies). Using a least-squares optimization technique applied simultaneously to all the data, the following equations describing the index of refraction have been proposed:

$$\begin{aligned}
 n_o^2 = & 5.814100 + \frac{0.0867547}{\lambda^{3.156983} - 0.0356502} + \\
 & \frac{0.0821721}{\lambda^{4.430430} + 0.315646} + \frac{0.506566}{\lambda^{6.604280} + 6.582197} + \frac{176380}{1 - \frac{112586195}{\lambda^{2.225043}}} \\
 & \qquad \qquad \qquad (A.2.5) \\
 n_e^2 = & 5.530050 + \frac{0.0510941}{\lambda^{2.359877} - 0.141109} + \\
 & \frac{0.195314}{\lambda^{2.566664} + 0.0910735} + \frac{4253.78}{1 - \frac{4304924}{\lambda^{2.383834}}}
 \end{aligned}$$

The above is not cast in the traditional form of a Sellmeier equation with the second electronic term (the third term) in both equations and a second ionic term in the ordinary index of refraction (the fourth term) as well as the optimized exponents. With this assemblage of terms, Roberts has been able to reproduce most of the available data on silver thiogallate from various experiments within experimental errors for the wavelength ranges 0.490 - 12.000 μm .

Appendix 3 - Synthesis of 3-*d* Propargyl Bromide

General. Ether refers to diethyl ether. Ether, propargyl alcohol, and pyridine were distilled before use. An inert atmosphere was maintained during all reactions and distillations.

3-*d* Propyn-1-*d*-ol

To a stirred solution of K₂CO₃ (8.0g, 0.058 mol, anhydrous) in D₂O (50 mL, 2.76 mol) at room temperature was added propargyl alcohol (15 mL, 0.26 mol) via syringe over one minute. The progress of the equilibration was monitored by ¹H NMR (250 MHz, D₂O).

After two days, 25 mL of ether was added to the stirred solution. Solid NaCl was then added in portions until the aqueous phase was saturated. The mixture was then transferred to a 1 L separatory funnel for extraction with ether (5 x 100 mL). The combined organic layers were dried with MgSO₄, filtered, and distilled (24/40 30 cm Vigreux) down to about 25 mL. Removal of solvent *in vacuo* is more convenient but results in slightly lowered yields. The residue was transferred with dry ether rinsings to a 100 mL round-bottom flask and fractionally distilled (14/20 12.5 cm Vigreux) to yield 3-*d* propyn-1-*d*-ol (12.64g, 0.217 mol, 84%, b.p. 114 °C). Deuterium incorporation at C-3 was 91% based on normalized ¹H NMR integration ratios of hydrogen on C-3 and C-1.

3-*d* Propargyl Bromide

A 3-necked 500 mL round-bottomed flask was charged with triphenyl phosphite (62.8 mL, 0.24 mol) and equipped with an overhead stirrer. Two dropping addition funnels were installed. One dropping funnel was charged with bromine (11.8 mL, 0.23 mol), and the other with a solution of pyridine (19.3 mL, 0.24 mol) and 3-*d* propyn-1-*d*-ol (12.64g, 0.22 mol). *Note*: pyridine and propargyl alcohol generate heat upon mixing.

Efficient stirring was maintained during all additions. Bromine was introduced over 15 minutes while the flask was periodically cooled in an ice water bath to keep the reaction below room temperature. The mixture was stirred for 10 minutes after all the bromine had been added. The pyridine/propynol solution was then added over 15 minutes with cooling as required. After complete addition, the reaction was stirred for 3 hours at room temperature. The addition funnels were removed and one of the necks stoppered. The crude bromide was removed *in vacuo* (2.0 torr) and condensed in a cold trap submerged in Dry Ice/acetone. The contents of the trap were fractionally distilled (12.5 cm glass helices) to provide 3-*d* propargyl bromide (20.05g, 77 %, b.p. 40 °C / 140 torr). The material was stored over MgO.

Bibliography

1. G. Phillips, P. Hinske, W. Demtröder, K. Möllmann, and R. Beigang, "*NaCl Color Center Laser with Birefringent Tuning*" Appl. Phys. B., 47 (1988) 127-133.
2. Clifford Raymond Pollock, *Color Center Lasers for Infrared Spectroscopy*, Doctor of Philosophy (1981), Rice University, Houston.
3. Ch. Hornberger, M. König, S. B. Rai, and W. Demtröder, "*Sensitive photoacoustic overtone spectroscopy of acetylene with a multipass photoacoustic cell and a colour centre laser at 1.5 μm* " J. Chem. Phys., 100 (1994) 171-177.
4. C. K. N. Patel, "*Linewidth of Tunable Stimulated Raman Scattering*" Phys. Rev. Lett., 28(11) (1972) 649-652.
5. C. K. N. Patel, "*Stimulated Second Stokes Spin-Flip Raman Scattering in InSb*" Appl. Phys. Lett., 18(7) (1971) 274-276.
6. A. Mooradian, S. R. J. Brueck, and F. A. Blum, "*Continuous Stimulated Spin-Flip Raman Scattering in InSb*" Appl. Phys. Lett., 17(11) (1970) 481-483.
7. S. R. J. Brueck and A. Mooradian, "*Efficient, Single-Mode, cw, Tunable Spin-Flip Raman Laser*" Appl. Phys. Lett., 18(6) (1971) 229-230.
8. R. L. Aggarwal, B. Lax, C. E. Chase, C. R. Pidgeon, D. Limbert, and F. Brown, "*High-Intensity Tunable InSb Spin-Flip Raman Laser*" Appl. Phys. Lett., 18(9) (1971) 383-385.
9. C. K. N. Patel and E. D. Shaw, "*Tunable Stimulated Raman Scattering from Conduction Electrons in InSb*" Phys. Rev. Lett., 24(9) (1970) 451-455.
10. C. K. N. Patel, E. D. Shaw, and R. J. Kerl, "*Tunable Spin-Flip Laser and Infrared Spectroscopy*" Phys. Rev. Lett., 25(1) (1970) 8-11.
11. Shin-Chu Hsu, Richard H. Schwendeman, and Gottfried Magerl, "*Infrared microwave sideband laser spectroscopy in the CO laser region*" IEEE J. Quantum Electron., 24 (1988) 2294-2301.

12. Gottfried Magerl, Walter Schupita, and Ernst Bonek, "A Tunable CO_2 Laser Sideband Spectrometer" IEEE J. Quantum Electron., QE-18 (1982) 1214-1220.
13. Philippe Repond and Markus W. Sigrist, "Continuously Tunable High-Pressure CO_2 Laser for Spectroscopic Studies on Trace Gases" IEEE J. Quantum Electron., QE-32(9) (1996) 1549-1559.
14. H. Weidner and R. E. Peale, "Time-resolved Fourier spectroscopy for activated optical materials" Appl. Opt., 35(16) (1996) 2849-2856.
15. C. A. Carere, W. S. Neil, and J. J. Sloan, "Fast time-resolved Fourier-transform spectroscopy for the study of transient chemical reactions" Appl. Opt., 35(16) (1996) 2857-2866.
16. *Monitoring of Gaseous Pollutants by Tunable Diode Lasers*, ed. R. Grisar, et al. 1989, Dordrecht, The Netherlands: Kluwer.
17. W. R. Bosenberg, A. Drobshoff, Jason I. Alexander, L. E. Myers, W. Tulloch, and R. L. Byer. *cw singly-resonant optical parametric oscillator based on periodically poled LiNbO₃*. in *Conference on Lasers and Electro-Optics*. 1996. Anaheim, California: Optical Society of America.
18. W. H. Flygare, *Molecular Structure and Dynamics*. 1978, Englewood Cliffs, NJ: Prentice-Hall, Inc.
19. Robert W. Boyd, *Nonlinear Optics*. 1992, San Diego: Academic Press, Inc.
20. J. E. Midwinter and J. Warner, "The effects of phase matching method and of uniaxial crystal symmetry on the polar distributions of second-order non-linear optical polarization" Brit. J. Appl. Phys., 16 (1965) 1135-1142.
21. G. D. Boyd and D. A. Kleinman, "Parametric Interaction of Focused Gaussian Light Beams" J. Appl. Phys., 9(4) (1968) 3597-3639.
22. R. Fischer, P. V. Nickles, Tran Bá Chu, and L. -W. Wiczorek, "Optimum Conditions for Elliptical Focusing in Singly Resonant Parametric Oscillators with Hemispherical Resonator" Annalen der Physik, 39(4) (1982) 287-294.

23. D. A. Kleinman, A. Ashkin, and G. D. Boyd, "*Second-Harmonic Generation of Light by Focused Laser Beams*" Phys. Rev., 145(1) (1966) 338-379.
24. G. D. Boyd, A. Ashkin, J. M. Dziedzic, and D. A. Kleinman, "*Second-Harmonic Generation of Light with Double Refraction*" Phys. Rev., 137(4A) (1964) 1305-1320.
25. D. A. Kleinman and R. C. Miller, "*Dependence of Second-Harmonic Generation on the Position of the Focus*" Phys. Rev., 148(1) (1966) 302-312.
26. G. D. Boyd and A. Ashkin, "*Theory of Parametric Oscillator Threshold with Single-Mode Optical Masers and Observation of Amplification in LiNbO₃*" Phys. Rev., 146(1) (1966) 187-198.
27. Tran-Ba-Chu and M. Broyer, "*Intracavity cw difference frequency generation by mixing three photons and using Gaussian laser beams*" J. de Physique, 46 (1985) 523-533.
28. G. Lera and M. Nieto-Vesperinas, "*Non-Paraxial Method for Non-Linear Optical Problems: Far-Infrared Generation with Depletion and Diffraction*" J. Optics (Paris), 20(4) (1989) 169-179.
29. Martin M. Fejer, G. A. Magel, Dieter H. Jundt, and Robert L. Byer, "*Quasi-Phase-Matched Second Harmonic Generation: Tuning and Tolerances*" J. Quant. Electron., 28(11) (1992) 2631-2654.
30. J. A. Armstrong, N. Bloembergen, J. Ducuing, and P. S. Pershan, "*Interactions between Light Waves in a Nonlinear Dielectric*" Phys. Rev., 127(6) (1962) 1918-1939.
31. Richard A. Baumgartner and Robert L. Byer, "*Optical Parametric Amplification*" IEEE J. Quant. Electron., QE-15(6) (1979) 432-444.
32. Lew Goldberg, W. K. Burns, and R. W. McElhanon, "*Wide acceptance bandwidth difference frequency generation in QPM-LiNbO₃*" Appl. Phys. Lett., 67(20) (1995) 2910-2912.
33. L Goldberg, W. K. Burns, and R. W. McElhanon, "*Difference-frequency generation of tunable mid-infrared radiation in bulk periodically poled LiNbO₃*" Opt. Lett., 20(11) (1995) 1280-1282.

34. R. L. Byer, H. Kildal, and R. S. Feigelson, "*CdGeAs₂ - A New Nonlinear Crystal Phasematchable at 10.6 μm* " Appl. Phys. Lett., 19(7) (1971) 237-240.
35. Kug Sun Hong, R. F. Speyer, and Sr. R. A. Condrate, "*Infrared Reflectance and Transmission Spectra of II-IV-V₂ Semiconducting Compounds: CdGeAs₂*" J. Phys. Chem. Solids, 51(8) (1990) 969-976.
36. H. Kildal and J. C. Mikkelsen, "*Efficient Doubling and CW Difference Frequency Mixing in the Infrared using the Chalcopyrite CdGeAs₂*" Opt. Commun., 10(4) (1974) 306-309.
37. Gary D. Boyd, Ernest Buehler, Frederick G. Storz, and Jack H. Wernick, "*Linear and Nonlinear Optical Properties of Ternary AII BIV C₂V Chalcopyrite Semiconductors*" IEEE J. Quantum Electron., QE-8(4) (1972) 419-426.
38. Gopal Bhar, "*Refractive index interpolation in phase-matching*" Appl. Opt., 15(2) (1976) 305-307.
39. Martin S. Piltch, John Rink, and Charles Tallman, "*Pulsed Infrared Difference Frequency Generation in CdGeAs₂*" Opt. Commun., 15(1) (1975) 112-114.
40. A. A. Davydov, L. A. Kulevskii, A. M. Prokhorov, A. D. Savel'ev, and V. V. Smirnov, "*Parametric Generation with CdSe Crystal Pumped by CaF₂:Dy²⁺ Laser*" JETP Lett., 15 (1972) 513-514.
41. R. L. Herbst and R. L. Byer, "*Singly resonant CdSe infrared parametric oscillator*" Appl. Phys. Lett., 21(5) (1972) 189-191.
42. Gopal C. Bhar and G. C. Ghosh, "*Temperature Dependent Phase-Matched Nonlinear Optical Devices Using CdSe and ZnGeP₂*" IEEE J. Quantum Electron., QE-16(8) (1980) 838-843.
43. R. L. Herbst and R. L. Byer, "*CdSe Infrared Parametric Oscillator*" IEEE J. Quantum Electron., QE-8 (1972) 575.
44. A. A. Davydov, L. A. Kulevskii, A. M. Prokhorov, A. D. Savel'ev, V. V. Smirnov, and A. V. Shirkov, "*A Tunable Infrared Parametric Oscillator in a CdSe Crystal*" Opt. Commun., 9(3) (1973) 234-236.

45. Joel A. Weiss and Lawrence S. Goldberg, "*Single resonant CdSe parametric oscillator pumped by an HF laser*" Appl. Phys. Lett., 24(8) (1974) 389-391.
46. Robert G. Wenzel and George P. Arnold, "*Parametric oscillator: HF oscillator-amplifier pumped CdSe parametric oscillator tunable from 14.1 μm to 16.4 μm* " Appl. Opt., 15(5) (1976) 1322-1326.
47. D. C. Hanna, B. Luther-Davies, R. C. Smith, and R. Wyatt, "*CdSe down-converter tuned from 9.5 to 24 μm* " Appl. Phys. Lett., 25(3) (1974) 142-144.
48. D. Andreou, "*16 μm Tunable Source Using Parametric Processes in Non-Linear Crystals*" Opt. Commun., 23(1) (1977) 37-43.
49. A. Dhirani and P. Guyot-Sionnest, "*Efficient generation of infrared picosecond pulsus from 10 to 20 μm* " Opt. Lett., 20(10) (1995) 1104-1106.
50. P. J. Kupecek, D. S. Chemla, and H. Le Person, "*Étude des Propriétés et de la Qualité de Cristaux de Cinabre Synthétique en vue D'Applications en Optique non Linéaire*" Revue de Physique Appliquée, 11 (1976) 285-291.
51. D. C. Hanna, B. Luther-Davies, H. N. Rutt, R. C. Smith, and C. R. Stanley, "*Q-Switched Laser Damage of Infrared Nonlinear Materials*" J. Quantum Electron., QE-8(3) (1972) 317-324.
52. W. L. Bond, G. D. Boyd, and H. L. Carter Jr., "*Refractive Indices of HgS (Cinnabar) between 0.62 and 11 μm* " J. Appl. Phys., 38 (1967) 4090-4091.
53. B. Ayrault, H. Langlois, M. C. Lecocq-Mayer, and F. Lefin, "*Indices et biréfringence du cinabre*" Phys. Stat. Sol. A, 17 (1973) 665-676.
54. Gary D. Boyd, Thomas J. Bridges, and E. Gardner Burkhardt, "*Up-Conversion of 10.6 μ Radiation to the Visible and Second Harmonic Generation in HgS*" IEEE J. Quantum Electron., QE-4(9) (1968) 515-519.
55. G. B. Abdullaev, L. A. Kulevskii, A. M. Prokhorov, A. D. Savel'ev, E. Yu. Salaev, and V. V. Smirnov, "*GaSe, A New Effective Material for Nonlinear Optics*" JETP Lett., 16 (1972) 90-92.

56. G. B. Abdullaev, L. A. Kulevskii, P. V. Nikles, A. M. Prokhorov, A. D. Savel'ev, E. Yu. Salaev, and V. V. Smirnov, "*Difference frequency generation in a GaSe crystal with continuous tuning in the 560-1050 cm⁻¹ range*" Sov. J. Quant. Electron., 6(1) (1976) 88-90.
57. P. Kupecek, E. Batifol, and A. Kuhn, "*Optical frequency conversion in gallium selenide (GaSe)*" Opt. Commun., 11(3) (1974) 291-295.
58. Sadao Adachi and Yoichi Shindo, "*Optical constants of GaSe*" J. Appl. Phys., 71(1) (1992) 428-431.
59. N. Piccioli, R. Le Toullec, M. Mejatty, and M. Balkanski, "*Refractive index of GaSe between 0.45 μ m and 330 μ m*" Appl. Opt., 16(5) (1977) 1236-1238.
60. G. B. Abdullaev, K. R. Allakhverdiev, L. A. Kulevskii, A. M. Prokhorov, E. Yu. Salaev, A. D. Savel'ev, and V. V. Smirnov, "*Parametric conversion of infrared radiation in a GaSe crystal*" Sov. J. Quant. Electron., 5(6) (1975) 665-668.
61. K. L. Vodopyanov, L. A. Kulevskii, V. G. Voevodin, A. I. Gribenyukov, K. R. Allakhverdiev, and T. A. Kerimov, "*High efficiency middle IR parametric superradiance in ZnGeP₂ and GaSe crystals pumped by an erbium laser*" Opt. Comm., 83(5) (1991) 322-326.
62. Donald E. McCarthy, "*The Reflection and Transmission of Infrared Materials. V: Spectra from 2 μ to 50 μ* " Appl. Opt., 7(10) (1968) 1997-2000.
63. F. Zernike, "*Temperature-Dependent Phase Matching for Far-Infrared Difference-Frequency Generation in InSb*" Phys. Rev. Lett., 22(18) (1969) 931-933.
64. Frits Zernike, "*Quasi cw Generation of Far-Infrared Difference Frequencies*" Bull. Am. Phy. Soc., 12(5) (1967) 687.
65. U. Chatterjee, A. M. Rudra, and G. C. Bhar, "*Widely tunable difference frequency generation (2.6 - 7.7 μ m) in lithium iodate*" Opt. Commun., 118 (1995) 367-374.
66. A. I. Izrailenko, A. I. Kovrigin, and P. V. Nikles, "*Parametric Generation of Light in High-Efficiency Nonlinear LiIO₃ and alpha-HIO₃ Crystals*" JETP Lett., 12 (1970) 331-333.

67. U. Deserno and G. Nath, "*A New Stable High Power Giant-Pulse Laser at $0.53\ \mu$ Using LiIO_3* " Phys. Lett. A, 30(8) (1969) 483-484.
68. P. G. Kryukov, Yu. A. Matveets, D. N. Nikogosyan, A. V. Sharkov, E. M. Gordeev, and S. D. Fanchenko, "*Generation of frequency-tunable single ultrashort light pulsus in an LiIO_3 crystal*" Sov. J. Quantum Electron., 7(1) (1977) 127-128.
69. G. Nath and H. Mehmanesch, "*Efficient Conversion of a Ruby Laser to $0.347\ \mu$ in Low Loss Lithium Iodate*" Appl. Phys. Lett., 17(7) (1970) 286-287.
70. Michael M. Choy and Robert L. Byer, "*Accurate second-order susceptibility measurements of visible and infrared nonlinear crystals*" Phys. Rev. B, 14(4) (1976) 1693-1706.
71. V. I. Kabelka, A. S. Piskarskas, A. Yu. Stabinis, and R. L. Sher, "*Group matching of interacting light pulses in nonlinear crystals*" Sov. J. Quantum Electron., 5(2) (1975) 255-256.
72. B. F. Levine and C. G. Bethea, "*Nonlinear Susceptibility of GaP; Relative Measurement and Use of measured Values to Determine a Better Absolute Value*" Appl. Phys. Lett., 20(8) (1972) 272-275.
73. G. D. Boyd, Robert C. Miller, K. Nassau, W. L. Bond, and A. Savage, " *LiNbO_3 : An Efficient Phase Matchable Nonlinear Optical Material*" Appl. Phys. Lett., 5(11) (1964) 234-236.
74. Takashi Kushida, Yuichi Tanaka, Masahiro Ojima, and Yasunori Nakazaki, "*Generation of Widely Tunable Pico-Second Pulses by Optical Parametric Effect*" Jpn. J. Appl. Phys., 14(7) (1975) 1097-1098.
75. Martin Lawrence, "*A temperature-dependent dispersion equation for congruently grown lithium niobate*" Opt. and Quantum Electron., 16 (1984) 373-374.
76. U. Schlarb and K. Betzler, "*Refractive indices of lithium niobate as a function of wavelength and composition*" J. Appl. Phys., 73(7) (1992) 3472-3476.
77. U. Schlarb and K. Betzler, "*Refractive indices of lithium niobate as a function of temperature, wavelength, and composition: A generalized fit*" Phys. Rev. B, 48(21) (1993) 15613-15619.

78. G. D. Boyd, W. L. Bond, and H. L. Carter, "*Refractive Index as a Function of Temperature in LiNbO_3* " J. Appl. Phys., 38(4) (1967) 1941-1943.
79. D. S. Smith, H. D. Riccius, and R. P. Edwin, "*Refractive Indices of Lithium Niobate*" Opt. Commun., 17(3) (1976) 332-335.
80. A. Ashkin, G. D. Boyd, J. M. Dziedzic, R. G. Smith, A. A. Ballman, J. J. Levinstein, and K. Nassau, "*Optically-Induced Refractive Index Inhomogeneities in LiNbO_3 and LiTaO_3* " Appl. Phys. Lett., 9(1) (1966) 72-74.
81. A. S. Pine, "*Doppler-limited molecular spectroscopy by difference-frequency mixing*" J. Opt. Soc. Am., 64(12) (1974) 1683-1690.
82. M. Yamada, N. Nada, M. Saitoh, and K. Watanabe, "*First-order quasi-phase matched LiNbO_3 waveguide periodically poled by applying an external field for efficient blue second-harmonic generation*" Appl. Phys. Lett., 62(5) (1993) 435-436.
83. B. F. Levine, C. G. Bethea, H. M. Kasper, and F. A. Thiel, "*Nonlinear Optical Susceptibility of HgGa_2S_4* " IEEE J. Quantum Electron, QE-12 (1976) 367-368.
84. Victor Zhorin, Personal Communication.
85. V. V. Badikov, I. N. Matveev, S. M. Pshenichnikov, O. V. Rychik, N. K. Trotsenko, N. D. Ustinov, and S. I. Shcherbakov, "*Growth and nonlinear properties of HgGa_2S_4* " Sov. J. Quantum Electron., 10(10) (1980) 1300-1301.
86. V. V. Badikov, I. N. Matveev, V. L. Panyutin, S. M. Pshenichnikov, T. M. Repyakhova, O. V. Rychik, A. E. Rozenson, N. K. Trotsenko, and N. D. Ustinov, "*Growth and optical properties of mercury thiogallate*" Sov. J. Quantum Electron., 9(8) (1980) 1068-1069.
87. K. F. Hulme, O. Jones, P. H. Davies, and M. V. Hobden, "*Synthetic Proustite (Ag_3AsS_3): A New Crystal for Optical Mixing*" Appl. Phys. Lett., 10(4) (1967) 133-135.
88. L. M. Guseva, I. G. Ganeev, A. V. Dronov, and I. S. Rez, "*Proustite and Pyrargyrite as Optical Materials for the Infrared*" Optics and Spectroscopy, 24(2) (1968) 156-157.

89. D. S. Chemla, Ph. J. Kupecek, and C. A. Schwartz, "*Redetermination of the Nonlinear Optical Coefficients of Proustite by Comparison with Pyrargyrite and Gallium Arsenide*" *Opt. Commun.*, 7(3) (1973) 225-228.
90. M. V. Hobden, "*The Dispersion of the Refractive Indices of Proustite (Ag_3AsS_3)*" *Opto-Electronics*, 1 (1969) 159.
91. R. F. Lucy, "*Infrared to Visible Parametric Upconversion*" *Appl. Opt.*, 11(6) (1972) 1329-1336.
92. C. D. Decker and F. K. Tittel, "*High-Power broadly tunable difference-frequency generation in proustite*" *Appl. Phys. Lett.*, 22(8) (1973) 411-413.
93. P. E. Oettinger, "*Difference-Frequency Power Generation in the 6.7-10.5 μm Spectral Region in Very Thin Proustite Crystals*" *J. Quant. Spectrosc. Radiat. Transfer*, 18(4) (1977) 369-371.
94. L. O. Hocker and C. F. Dewey Jr., "*Difference Frequency Generation in Proustite from 11 to 23 μm* " *Appl. Phys.*, 11 (1976) 137-140.
95. J. D. Feichtner, R. Johannes, and G. W. Roland, "*Growth and Optical Properties of Single Crystal Pyrargyrite (Ag_3SbS_3)*" *Appl. Opt.*, 9(7) (1970) 1716-1717.
96. E. L. Zorina, L. D. Popova, I. S. Kovaleva, L. G. Voinova, and A. S. Kanishcheva, "*Light Absorption in Pyrargyrite and its Amorphous Films*" *Optics and Spectroscopy*, 33(5) (1972) 505-508.
97. J. D. Feichtner and G. W. Roland, "*Optical Properties of a New Nonlinear Optical Material: Tl_3AsSe_3* " *Appl. Opt.*, 11(5) (1972) 993-998.
98. W. B. Gandrud and G. D. Boyd, "*Photomultiplier Detection of 10.6 μm Radiation Using Sum-Mixing in Ag_3SbS_3* " *Opt. Commun.*, 1(4) (1969) 187-190.
99. D. N. Nikogosyan, "*Nonlinear optics crystals - review and summary of data*" *Sov. J. Quantum. Electron.*, 7 (1977) 1-13.
100. B. C. Ziegler and K. L. Schepler, "*Transmission and damage-threshold measurement in AgGaSe_2 at 2.1 μm* " *Appl. Opt.*, 30 (1991) 5077-5080.

101. R. S. Feigelson and R. K. Route, *"Recent developments in the growth of chalcopyrite crystals for nonlinear infrared applications"* Opt. Eng., 26(2) (1987) 113-119.
102. Ulrich Simon, Zsolt Benko, Markus W. Sigrist, Robert F. Curl, and Frank K. Tittel, *"Design considerations of an infrared spectrometer based on difference-frequency generation in AgGaSe₂"* Appl. Opt., 32(33) (1993) 6650-6655.
103. R. C. Eckardt, Y. X. Fan, R. L. Byer, C. L. Marquardt, M. E. Storm, and L. Esterowitz, *"Broadly tunable infrared parametric oscillator using AgGaSe₂"* Appl. Phys. Lett., 49(11) (1986) 608-610.
104. David A. Roberts, *"Dispersion Equations for Nonlinear Optical Crystals: KDP, AgGaSe₂ and AgGaS₂"* Appl. Opt., 35(24) (1996) 4677-4688.
105. H. Komine, J. M. Fukumoto, W. H. Long Jr., and E. A. Stappaerts, *"Noncritically phase matched mid-infrared generation in AgGaSe₂"* IEEE J. of Select. Topics in Quantum Electron., 1(1) (1995) 44-49.
106. K. P. Petrov, R. F. Curl, F. K. Tittel, and L. Goldberg, *"Continuous-wave tunable 8.7- μ m spectroscopic source pump by fiber-coupled communications lasers"* Opt. Lett., 21(18) (1996) Accepted for publication.
107. D. S. Chemla, P. J. Kupecek, D. S. Robertson, and R. C. Smith, *"Silver Thiogallate. A New Material with Potential for Infrared Devices"* Opt. Commun., 3(1) (1971) 29-31.
108. J. -J. Zondy, D. Touahri, and O. Acef, *"Measurement of the d_{36} Nonlinear Coefficient of AgGaS₂ from Second-Harmonic, Sum and Difference Frequency Generations"* (To be published) .
109. Yuan Zuan Fan, R. C. Eckhardt, R. L. Byer, R. K. Route, and R. S. Feigelson, *"AgGaS₂ infrared parametric oscillator"* Appl. Phys. Lett., 45(4) (1984) 313-315.
110. J. H. McFee, G. D. Boyd, and P. H. Schmidt, *"Redetermination of the Nonlinear Optical Coefficients of Te and GaAs by Comparison with Ag₃SbS₃"* Appl. Phys. Lett., 17(2) (1970) 57-59.

111. Glenn Howard Sherman and Paul D. Coleman, "*Absolute Measurement of the Second-Harmonic Generation Nonlinear Susceptibility of Tellurium at 28.0 μm* " IEEE J. Quantum Electron, QE-9(3) (1973) 403-409.
112. T. J. Bridges, V. T. Nguyen, E. G. Burkhardt, and C. K. N. Patel, "*Tunable cw difference-frequency generation in tellurium at $\sim 11 \mu\text{m}$* " Appl. Phys. Lett., 27(11) (1975) 600-602.
113. G. D. Boyd, E. Buehler, and F. Storz, "*Linear and Nonlinear Optical Properties of ZnGeP_2 and CdSe* " Appl. Phys. Lett., 18(7) (1971) 301-304.
114. Yu. M. Andreev, V. G. Voevodin, A. I. Gribenyukov, O. Ya. Zyryanov, I. I. Ippolitov, A. N. Morozov, A. V. Sosnin, and G. S. Khmel'nitskii, "*Efficient generation of the second harmonic of tunable CO_2 laser radiation in ZnGeP_2* " Sov. J. Quant. Electron., 14(8) (1984) 1021-1022.
115. K. L. Vodopyanov and V. G. Voevodin, "*Type I and II ZnGeP_2 traveling-wave optical parametric generator tunable between 3.9 and 10 μm* " Opt. Commun., 117 (1995) 277-282.
116. John U. White, "*Long Optical Paths of Large Aperature*" J. Opt. Soc. Am., 32 (1942) 285-288.
117. W. Bruce Olson, "*Minizization of volume and astigmatism in White cells for use with circular sources and aperatures*" Appl. Opt., 23(10) (1984) 1580-1585.
118. Paul Hannan, "*White cell design considerations*" Opt. Eng., 28(11) (1989) 1180-1184.
119. H. W. Kohn, "*Astigmatism and White cells: theoretical considerations on the construction of an anastigmatic White cell*" Appl. Opt., 31(31) (1992) 6757-6764.
120. Jeffrey I. Steinfeld, Steven M. Adler-Golden, and Jean W. Gallagher, "*Critical Survey of Data on the Spectroscopy and Kinetics of Ozone in the Mesosphere and Thermosphere*" J. Phys. Chem. Ref. Data., 16(4) (1987) 709.
121. Coherent Laser Group, *Operator's Manual: The Coherent 899-21 Titanium:Sapphire Ring Laser*, . 1990, Coherent Laser Group: USA.

122. Coherent Laser Group, *Operator's Manual - Autoscan - PC Version*. 1991.
123. J. L. Hall and S. A. Lee, "Interferometric real-time display of cw dye laser wavelength with sub-Doppler accuracy" *App. Phys. Lett.*, 29(5) (1976) 367-369.
124. F. V. Kowalski, R. T. Hawkins, and A. L. Schawlow, "Digital wavemeter for cw lasers" *J. Opt. Soc. Am. Lett.*, 66(9) (1976) 965-966.
125. F. V. Kowalski, R. E. Tects, W. Demtroder, and A. L. Schawlow, "An improved wavemeter for cw lasers" *J. Opt. Soc. Am. Lett.*, 68(11) (1978) 1611-1613.
126. J. Cachenout, C. Man, P. Cerez, A. Brillet, F. Stoeckel, A. Jourdon, and F. Hartman, "Description and accuracy tests of an improved lambdameter" *Revue de Physique Appliquee*, 14 (1979) 685-688.
127. R. Balhorn, H. Kunzmann, and F. Lebowsky, "Frequency Stabilization of Internal-Mirror Helium-Neon Lasers" *Appl. Opt.*, 11(4) (1972) 742-744.
128. T. M. Niebauer, James E. Faller, H. M. Godwin, John L. Hall, and R. L. Barger, "Frequency stability measurements on polarization-stabilized He-Ne lasers" *Appl. Opt.*, 27(7) (1988) 1285-1289.
129. Coherent Laser Group, *Model 200 Single Frequency HeNe Laser Operation Manual*. 1991.
130. G. M. Jurisch, W. A. Von Drasek, R. K. Brimacombs, and J. Reid, "Gas contaminant effects in discharge-excited KrF lasers" *Appl. Opt.*, 31(12) (1992) 1975-1981.
131. G. M. Jurisch, W. A. Von Drasek, K. Mulderink, V. Olchowka, J. Reid, and R. K. Brimacombs, "The effects of gas contaminants in excimer lasers" *Proc. SPIE*, 1412 (1991) 115-119.
132. Qihong Lou, Takashi Yagi, Kaoru Igarishi, and Hideaki Saito, "The effects of F₂ concentration on discharge pumped KrF laser characteristics" *J. Appl. Phys.*, 68(6) (1990) 2572-2576.

133. M. C. Gower, A. J. Kearsley, and C. E. Webb, "*Gas Composition and Lifetime Studies of Discharge Excited Rare-Gas Halide Lasers*" IEEE J. Quant. Electron., QE-16 (1980) 231-235.
134. R. E. Stevens, C. Y. Yung, C. Kittrell, and J. L. Kinsey, "*A simple and efficient external gas filtration and trapping system for excimer lasers*" Rev. Sci. Instrum., 65(8) (1994) 2464-2469.
135. G. C. Bhar and R. C. Smith, "*Silver Thiogallate (AgGaS_2) - Part II: Linear Optical Properties*" IEEE J. Quantum Electron, QE-10 (1974) 546-550.
136. G. Brandt, A. Rauber, and J. Schneider, "*ESR and X-ray analysis of the ternary semiconductors CuAlS_2 , SnInS_2 , and AgGaS_2* " Solid State Commun., 12 (1973) 481-483.
137. G. H. Bhar and R. C. Smith, "*Optical Properties of II-IV-V₂ and I-III-VI₂ Crystals with Particular Reference to Transmission Limits*" Phys. Status Solidi A, 13 (1972) 157-168.
138. B. Tell and H. M. Kasper, "*Optical and electrical properties of AgGaS_2 and AgGaSe_2* " Phys. Rev. B., 4(12) (1971) 4455-4459.
139. B. Tell, J. L. Shay, and H. M. Kasper, "*Electroreflectance and Absorption-Edge Studies of AgGaS_2 and AgGaSe_2* " Phys. Rev. B, 6(8) (1972) 3008-3012.
140. P. W. Yu, W. J. Anderson, and Y. S. Park, "*Anomalous Temperature Dependence on the Energy Gap of AgGaS_2* " Solid State Commun., 13 (1973) 1883-1887.
141. G. D. Holah, H. Montgomery, and J. S. Webb, "*Lattice dynamics of AgGaS_2* " J. Phys. C, 7(21) (1974) 3875-3890.
142. G. D. Holah, "*Infrared dielectric dispersion of silver thiogallate*" Opt. Commun., 5(10-13) (1972) 10.
143. M. V. Hobden, "*Optical Activity in a Non-enantiomorphous Crystal Silver Gallium Sulphide*" Nature, 216 (1967) 678.
144. L. M. Suslikov, Z. P. Gadmasi, and Yu. A. Khazitarkhanov, "*Gyrotropy of AgGaS_2 crystals*" Opt. Spectrosc., 62(4) (1987) 491-493.

145. O. G. Vlokh and V. A. Gradovskii, "*Temperature dependence of the optical rotation dispersion of silver thiogallate*" Opt. Spectrosc. (USSR), 64(6) (1988) 779-781.
146. J. F. Nye, *Physical Properties of Crystals*. 1964, London: Oxford Univ. Press.
147. D. C. Hanna, V. V. Rampal, and R. C. Smith, "*Tunable Medium Infrared Generation in Silver Thiogallate (AgGaS_2) by Down-Conversion of Flash-Pumped Dye-Laser Radiation*" IEEE J. Quantum Electron., QE-10 (1974) 461-462.
148. D. C. Hanna, V. V. Rampal, and R. C. Smith, "*Tunable Infrared Down-Conversion in Silver Thiogallate*" Opt. Commun., 8(2) (1973) 151-153.
149. S. A. Andreev, I. N. Matveev, I. P. Nekrasov, S. M. Pshenichnikov, and N. P. Sopina, "*Parametric conversion of infrared radiation in an AgGaS_2 crystal*" Sov. J. Quantum Electron., 7(3) (1977) 366-368.
150. T. Dahinten, U. Plodereder, A. Seilmeier, K. L. Vodopyanov, K. R. Allakhverdiev, and Z. A. Ibragimov, "*Infrared Pulses of 1 Picosecond Duration Tunable Between 4 μm and 18 μm* " IEEE J. Quantum Electron., 29(7) (1993) 2245-2250.
151. A. G. Yodh, H. W. K. Tom, G. D. Aumiller, and R. S. Miranda, "*Generation of tunable mid-infrared picosecond pulses at 76 MHz*" J. Opt. Soc. Amer. B, 8(8) (1991) 1663-1667.
152. Jean-Jacques Zondy, Mohamed Abed, and André Clairon, "*Type-II frequency doubling at $\lambda=1.30 \mu\text{m}$ and $\lambda=2.53 \mu\text{m}$ in flux grown potassium titanyl phosphate*" J. Opt. Soc. Am. B, 11(10) (1994) 2004-2008.
153. K. Kato, "*High-Power Difference-Frequency Generation at 5-11 μm in AgGaS_2* " IEEE J. Quantum Electron., QE-20 (1984) 698-699.
154. G. D. Boyd, H. Kasper, and J. H. McFee, "*Linear and Nonlinear Optical Properties of AgGaS_2 , CuGaS_2 , CuInS_2 , and Theory of the Wedge Technique for the Measurement of Nonlinear Coefficients*" IEEE J. Quantum Electron., QE-7 (1971) 563-573.

155. P. J. Kupecek, C. A. Schwartz, and D. S. Chemla, "*Silver Thiogallate (AgGaS₂) - Part I: Nonlinear Optical Properties*" IEEE J. Quantum Electron., QE-10(7) (1974) 540-545.
156. E. C. Cheung, Karl Koch, and Gerald T. Moore, "*Measurement of second-order nonlinear optical coefficients from the spectral brightness of parametric fluorescence*" Opt. Lett., 19(3) (1994) 168-170.
157. P. Canerelli, Z. Benko, A. H. Hielscher, R. F. Curl, and F. K. Tittel, "*Measurement of Nonlinear Coefficient and Phase Matching Characteristics of AgGaS₂*" IEEE J. Quantum Electron., 28 (1992) 52-55.
158. R. C. Miller, "*Optical Second Harmonic Generation in Piezoelectric Crystals*" Appl. Phys. Lett., 5(1) (1964) 17-19.
159. Herman Vanherzeele and John D. Bierlein, "*Magnitude of the nonlinear coefficients of KTiOPO₄*" Opt. Lett., 17(14) (1992) 982-984.
160. B. Boulanger, J. Ph. Fève, G. Mernier, B. Menaert, and X. Cabirol, "*Relative sign and absolute magnitude of the $\chi^{(2)}$ coefficients of KTP by SHG measurements*" J. Opt. Soc. Am. B, 11(5) (1994) 750-757.
161. G. C. Bhar, D. K. Ghosh, P. S. Ghosh, and D. Schmitt, "*Temperature effects in AgGaS₂ nonlinear devices*" Appl. Opt., 22(16) (1983) 2492-2494.
162. G. C. Bhar and R. C. Smith, "*Optical properties of II-IV-V₂ and I-III-VI₂ crystals with particular reference to transmission limits*" Phys. Status Solidi. A, 13(1) (1972) 157-168.
163. H. A. Chedzey, D. J. Marshall, H. T. Parfitt, and D. S. Robertson, "*A study of the melt growth of single-crystal thiogallates*" J. Phys. D, 4(9) (1971) 1320-1324.
164. H. M. Kasper, "*Crystal growth and properties of some I-III-IV₂ compounds*" Nat. Bur. Std. (U.S.) Spec. Publ., 364 (1972) 671-679.
165. P. Korczak and C. B. Staff, "*Liquid encapsulated Czochralski growth of silver thiogallate*" J. Cryst. Growth, 24 (1974) 386-389.
166. H. Matthes, R. Viehmann, and N. Marshall, "*Improved optical quality of AgGaS₂*" Appl. Phys. Lett., 26(5) (1975) 237-239.

167. M. V. Hobden, *"Optical Activity in a Non-enantiomorphous Crystal: AgGaS₂"* Acta Crystal., A 24 (1968) 676-680.
168. G. C. Bhar, S. Das, D. K. Ghosh, and L. K. Samanta, *"Phasematching of Infrared Nonlinear Laser Devices Using AgGaS₂"* IEEE J. Quantum Electron., 24(8) (1988) 1492-1494.
169. M. Born and E. Wolf, *Principles of Optics*. 6 ed. 1986, Oxford: Pergamon Press.
170. C. G. Bethea, *"Megawatt Power at 1.318 μ in Nd³⁺:YAG and Simultaneous Oscillation at Both 1.06 and 1.318 μ "* IEEE J. Quantum Electron., QE-9 (1973) 254.
171. T. Elsaesser, H. Lobentanzer, and A. Seilmeier, *"Generation of tunable picosecond pulses in the medium infrared by down-conversion in AgGaS₂"* Opt. Comm., 52(5) (1985) 355-359.
172. K. Kato, *"High-Power Difference-Frequency Deneration at 5-11 μ m in AgGaS₂"* IEEE J. Quantum Electron., QE-20 (1984) 698-699.
173. H. J. Krause and W. Daum, *"High-Power Source of Coherent Picosecond Light Pulses Tunable from 0.41 to 12.9 μ m"* Appl. Phys. B, 56 (1993) 8-13.
174. Kazuyuki Akagawa, Satoshi Wada, Akira Nakamura, and Hideo Tashiro, *"Synchronization of pulsed Ti:sapphire lasers and its application to difference frequency mixing for tunable infrared generation"* Appl. Opt., 35(15) (1996) 2570-2575.
175. R. J. Seymour and F. Zernike, *"Infrared radiation tuable from 5.5 to 18.3 μ m generated by mixing in AgGaS₂"* Appl. Phys. Lett., 29(11) (1976) 705-707.
176. P. Canerelli, Z. Benko, R. F. Curl, and F. K. Tittel, *"A Continuous-wave Infrared Laser Spectrometer Based on Difference Frequency Generation in AgGaS₂ for High Resolution Spectroscopy"* J. Opt. Soc. Am. B, 9 (1992) 197-202.
177. A. H. Hielscher, C. E. Miller, D. C. Bayard, U. Simon, K. P. Smolka, R. F. Curl, and F. K. Tittel, *"Optimization of a midinfrared high-resolution difference-frequency laser spectrometer"* J. Opt. Soc. Am. B, 9(11) (1992) 1962-1967.

178. T. Elsaesser, A. Seilmeier, W. Kaiser, P. Koidl, and G. Brandt, "*Parametric generation of tunable picosecond pulsus in the medium infrared using AgGaS₂ crystals*" Appl. Phys. Lett., 44(4) (1984) 383-385.
179. H. J. Bakker, J. T. M. Kennis, H. J. Kop, and A. Legendijk, "*Generation of intense picosecond pulses tunable between 1.2 and 8.7 μm* " Opt. Commun., 86(1) (1991) 58-64.
180. E. C. Cheung, Karl Koch, and Gerald T. Moore, "*Silver thiogallate, singly resonant optical parametric oscillator pumped by a continuous-wave mode-locked Nd:YAG laser*" Opt. Lett., 19(9) (1994) 631-633.
181. Konstantin Petrov, *Application of Diode-Laser-Pumped Difference-Frequency Generation to Spectroscopic Trace Gas Detection in the Atmosphere*, Master of Science (1995), Rice University, Houston, TX.
182. K. P. Petrov, S. Waltman, U. Simon, R. F. Curl, F. K. Tittel, E. J. Dlugokensky, and L. Hollberg, "*Detection of methane in air using diode-laser pumped difference-frequency generation near 3.2 μm* " Appl. Phys. B, 61 (1995) 553-558.
183. U. Simon, S. Waltman, I. Loa, F. K. Tittel, and L. Hollberg, "*External-cavity difference-frequency source near 3.2 μm , based on combining a tunable diode laser with a diode-pumped Nd:YAG laser in AgGaS₂*" J. Opt. Soc. Am. B, 12(2) (1995) 323-327.
184. Ulrich Simon, Frank K. Tittel, and Lew Goldberg, "*Difference-frequency mixing in AgGaS₂ by use of a high-power GaAlAs tapered semiconductor amplifier at 860 nm*" Opt. Lett., 18(22) (1993) 1931-1933.
185. U. Simon, C. E. Miller, C. C. Bradley, R. G. Hulet, R. F. Curl, and F. K. Tittel, "*Difference-frequency generation in AgGaS₂ by use of single-mode diode-laser pump sources*" Opt. Lett., 18(13) (1993) 1062-1064.
186. G. C. Catella, *Cleveland Crystals*, Personal Communication.
187. Anthony E. Siegman, *Lasers*. 1986, Mill Valley, California: University Science Books.

188. Charles E. Miller, Wade C. Eckhoff, Ulrich Simon, Frank K. Tittel, and Robert F. Curl. *CW difference frequency generation using AgGaS₂: problems encountered in power scaling*. in *Nonlinear Optics for High-Speed Electronics and Optical Frequency Conversion*. 1994. Los Angeles, CA: SPIE - The International Society for Optical Engineering.
189. T. F. Johnson and M. W. Sasnett. *The Effect of Pump Laser Mode Quality on the Mode Quality of the CW Dye Laser*. in *Laser Energy Distribution Profiles: Measurement and Applications*. 1993.
190. M. E. Innocenzi, H. T. Yura, C. L. Fincher, and R. A. Fields, "Thermal Modeling of Continuous-wave End-pumped Solid-State Lasers" *Appl. Phys. Lett.*, 56 (1990) 1831-1833.
191. C. L. Marquardt, D. G. Cooper, P. A. Budni, M. G. Knights, K. L. Schepler, R. DeDomenico, and G. C. Catella, "Thermal lensing in silver gallium selenide parametric oscillator crystals" *Appl. Opt.*, 33(5) (1994) 3192-3197.
192. P. A. Budni, M. G. Knights, E. P. Chicklis, and K. L. Schepler, "Kilohertz pumped Optical Parametric Oscillator Pumped at 2 μm " *Opt. Lett.*, 18 (1993) 1068-1070.
193. G. C. Catella, L. R. Shiozawa, J. R. Hietanen, R. C. Eckardt, R. K. Route, R. S. Feigelson, D. G. Cooper, and C. L. Marquardt, "Mid-IR Absorption in AgGaSe₂ Optical Parametric Oscillator Crystals" *Appl. Opt.*, 32 (1993) 3948-3950.
194. E. S. Voronin, V. S. Solomatin, N. I. Cherepov, V. V. Shuvalov, V. V. Badikov, and O. N. Pivovarov, "Conversion of infrared radiation in an AgGaS₂ crystal" *Sov. J. Quant. Electron.*, 5(5) (1975) 597-598.
195. Ron Hopwood, *EG & G Judson Inc.*, Personal Communication.
196. S. O. Rice, *Mathematical Analysis of Random Noise*, in *Noise & Stochastic Processes*, N. Wax, Editor. 1954, Dover Publications: New York.
197. R. W. Harris and T. J. Ledwidge, *Introduction to Noise Analysis*. 1974, London: Pion Limited.
198. Jeffrey Louis Hall, *Infrared Kinetic Spectroscopy Using a Color Center Laser*, Doctor of Philosophy (1986), Rice University, Houston.

199. Koichi Shimoda, "*Limits of Sensitivity of Laser Spectrometers*" Appl. Phys., 1 (1973) 77-86.
200. R. J. Keyes and T. M. Quist, *Low-Level Coherent and Incoherent Detection in the Infrared*, in *Semiconductors and semimetals*, R.K. Willardson and A.C. Beer, Editors. 1970, Academic: New York. p. 321-359.
201. EG&G Judson, *Infrared Detectors Catalog*, . 1992.
202. Wade C. Eckhoff, Roger S. Putnam, Shunxi Wang, Robert F. Curl, and Frank K. Tittel, "*A continuously tunable long-wavelength cw IR source for high-resolution spectroscopy and trace-gas detection*" Appl. Phys. B, 63 (1996) 437-441.
203. A. Bianchi, A. Ferrario, and M. Musci, "*4-12 μm Tunable Down-Conversion in GaSe from a LiNbO₃ Parametric Oscillator*" Opt. Commun., 25(2) (1978) 256-258.
204. A. Bianchi and M. Garbi, "*Down-Conversion in the 4-18 μm Range with GaSe and AgGaSe₂ Nonlinear Crystals*" Opt. Comm., 30(1) (1979) 122-124.
205. J. L. Oudar, Ph. J. Kupecek, and D. S. Chemla, "*Medium Infrared Tunable Down Conversion of a YAG-Pumped Infrared Dye Laser in Gallium Selenide*" Opt. Comm., 29(1) (1979) 119-122.
206. Yu. A. Gusev, A. V. Kirpichnikov, S. N. Konoplin, S. I. Marennikov, P. V. Nikles, Yu. N. Polivanov, A. M. Prokhorov, A. D. Savel'ev, R. Sh. Sayakhov, V. V. Smirnov, and V. P. Chebotaev, "*Tunable mid-IR difference frequency generator*" Sov. Tech. Phys. Lett, 6(10) (1980) 541-542.
207. A. Suda and H. Tashiro. *High Power Mid-infrared Difference Frequency Generation in a GaSe Crystal*. in *16th Annual Meeting of the Laser Society*. 1996. Japan.
208. K. L. Vodopyanov, "*Parametric generation of tunable infrared radiation in ZnGeP₂ and GaSe pumped at 3 μm* " J. Opt. Soc. Am. B, 10(9) (1993) 1723-1729.
209. N. C. Fernelius, *Properties of Gallium Selenide Single Crystal*. Prog. Crystal. Growth and Charact. Vol. 28. 1994: Pergamon. 275-353.

210. G. B. Abdullaev, K. R. Allakhverdiev, M. E. Karasev, V. I. Konov, L. A. Kulevskii, N. B. Mustafaev, P. P. Pashinin, A. M. Prokhorov, Yu. M. Starodumov, and N. I. Chapliev, "*Efficient generation of the second harmonic of CO₂ laser radiation in a GaSe crystal*" Sov. J. Quantum Electron., 19(4) (1989) 494-498.
211. K. L. Vodopyanov and L. A. Kulevskii, "*New dispersion relationships for GaSe in the 0.65-18 μ m spectral region*" Opt. Comm., 118 (1995) 375-378.
212. T. A. McMath and J. C. Irwin, "*Indices of Refraction of GaS and GaSe*" Phys. Stat. Sol. A, 38 (1976) 731-738.
213. G. C. Bhar, S. Das, and K. L. Vodopyanov, "*Nonlinear optical laser devices using GaSe*" Appl. Phys. B, 61 (1995) 187-190.
214. S. F. Yang and N. E. Hoffman, "*Ethylene Biosynthesis and its Regulation in Higher Plants*" Annu. Rev. Plant Physiol., 35 (1984) 155-189.
215. F. B. Ables, *Ethylene in Plant Biology*. 1973, London: Academic Press.
216. M. B. Jackson, *Ethylene and the Responses of Plants to Excess Water in their Environment - A Review*, in *Ethylene and Plant Development*, J.A. Roberts and G.A. Tucker, Editors. 1985, Butterworths: London.
217. H. Mehlhorn and A. R. Wellburn, "*Stress ethylene formation determines plant sensitivity to ozone*" Nature, 327 (1987) 417-418.
218. L. B. Kreuzer, N. D. Kenyon, and C. K. N. Patel, "*Air Pollution: Sensitive Detection of Ten Pollutant Gases by Carbon Monoxide and Carbon Dioxide Lasers*" Nature, 177 (1972) 347-349.
219. D. Bicanic, F. Harren, J. Reuss, E. Woltering, J. Snel, L. A. C. J. Voesenek, B. Zuidberg, H. Jalink, F. Bijnen, C. W. P. M. Blom, H. Sauren, M. Kooijman, L. van Hove, and W. Tonk, *Trace Detection in Agriculture and Biology*, in *Photoacoustic, Photothermal and Photochemical Processes in Gases*, P. Hess, Editor. 1989, Springer: New York. p. 213-245.

220. C. Brand, A. Winkler, P. Hess, A. Miklos, Z. Bozoki, and J. Sneider, "*Pulsed-laser excitation of acoustic modes in open high-Q photoacoustic resonators for trace gas monitoring: results for C₂H₄*" *Appl. Opt.*, 34(18) (1995) 3257-3266.
221. W. L. Smith and I. M. Mills, "*Coriolis Perturbations in the Infrared Spectrum of Ethylene*" *J. Chem. Phys.*, 40(8) (1964) 2095-2109.
222. Ch. Lambeau, A. Fayt, J. L. Duncan, and T. Nakagawa, "*The Absorption of Ethylene in the 10- μ m Region*" *J. Mol. Spect.*, 81 (1980) 227-247.
223. F. Herlemont, M. Lyszyk, and J. Lemaire, "*Laser Spectroscopy of Ethylene with Waveguide CO₂ and N₂O Lasers*" *J. Mol. Spect.*, 74 (1979) 400-408.
224. Richard D. Smith, "*Formation of Radicals and Complex Organic Compounds by High-Temperature Pyrolysis: The Pyrolysis of Toluene*" *Combust. Flame*, 35 (1979) 179-190.
225. Richard D. Smith, "*A Direct Mass Spectrometric Study of the Mechanism of Toluene Pyrolysis at High Temperatures*" *J. Phys. Chem.*, 83(12) (1979) 1553-1563.
226. J. M. Goodings, D. K. Bohme, and C. K. Ng, "*Detailed Ion Chemistry in Methane-Oxygen Flames. I. Positive Ions*" *Combust. Flame*, 36 (1979) 27-43.
227. J. D. Bittner and J. B. Howard, "*Composition Profiles and Reaction Mechanisms in a Near-Sooting Premixed Benzene/Oxygen/Argon Flame*" Eighteenth Symposium (International) on Combustion, (1981) 1105-1116.
228. Richard D. Smith and Allen L. Johnson, "*Mass Spectroscopic Study of the High Temperature Chemistry of Benzene*" *Combust. Flame*, 51 (1983) 1-22.
229. J. D. Bittner and J. B. Howard, "*Mechanism of Hydrocarbon Decay in Fuel-Rich Secondary Reaction Zones*" Nineteenth Symposium (International) on Combustion, (1983) 211-221.
230. J. A. Cole, J. D. Bittner, J. P. Longwell, and J. B. Howard, "*Formation Mechanisms of Aromatic Compounds in Aliphatic Flames*" *Combust. Flame*, 56 (1984) 51-70.

231. G. Rotzoll, "*Molecular Beam Sampling Mass-Spectroscopic Study of High-Temperature Benzene Oxidation*" Intern. J. Chem. Kinetics, 17 (1985) 637-653.
232. Philip R. Westmoreland, Jack B. Howard, and John P. Longwell. *Tests of Published Mechanisms by Comparison with Measured Laminar Flame Structure in Fuel-Rich Acetylene Combustion*. in *Twenty-first Symposium (International) on Combustion*. 1986: The Combustion Institute.
233. Philip R. Westmoreland, Anthony M. Dean, Jack B. Howard, and John O. Longwell, "*Forming Benzene in Flames by Chemically Activated Isomerization*" J. Phys. Chem., 93 (1989) 8171-8180.
234. Stephen E. Stein, James A. Walker, Mahendra M. Suryan, and Askar Fahr. *A New Path to Benzene in Flames*. in *Twenty-third Symposium (International) on Combustion*. 1990: The Combustion Institute.
235. R. D. Kern, H. Chen, J. H. Kiefer, and P. S. Mudipalli, "*Thermal Decomposition of Propargyl Bromide and the Subsequent Formation of Benzene*" Combust. Flame, 100 (1995) 177-184.
236. James A. Miller and Carl F. Melius, "*Kinetic and Thermodynamic Issues in the Formation of Aromatic Compounds in Flames of Aliphatic Fuels*" Combustion and Flame, 91 (1992) 21-39.
237. Walch, "*Characterization of the minimum energy paths for the reactions of CH_2 and $^1\text{CH}_2$ with C_2H_2* " J. Chem. Phys., 103 (1995) 7064-7071.
238. J. D. Adamson, C. L. Morter, J. D. DeSain, G. P. Glass, and R. F. Curl, "*Propargyl from the Reaction of Singlet Methylene with Acetylene*" J. Phys. Chem., 100(6) (1996) 2125-2128.
239. C. L. Morter, S. K. Farhat, J. D. Adamson, G. P. Glass, and R. F. Curl, "*Rate Constant Measurement of the Recombination Reaction $\text{C}_3\text{H}_3 + \text{C}_3\text{H}_3$* " J. Phys. Chem., 98(28) (1994) 7029-7035.
240. D. A. Ramsey and P. Thistlewaite, "*The Electronic Absorption Spectrum of the Propargyl Radical*" Can. J. Phys., 44 (1966) 1381-1386.
241. I. Dubois and H. LeClercq, "*New Electronic Transition of the Propargyl Radical*" Can. J. Phys., 49 (1971) 174-176.

242. Paul H. Kasai, "*Electron Spin Resonance Studies of Vinyl, Propargyl, and Butatrienyl Radicals Isolated in Argon Matrices*" J. Am. Chem. Soc., 94(17) (1972) 5950-5956.
243. Fernando Bernardi, Nicolaos D. Epiotis, William. Cherry, H. Bernard Schlegel, Myung-Hwan H. Whangbo, and Saul Wolfe, "*A Molecular Orbital Interpretation of the Static, Dynamic, and Chemical Properties of CH₂X Radicals*" J. Am. Chem. Soc., 98(2) (1976) 469-478.
244. Fernando Bernardi, Carlo Maurizio Camaggi, and Marcello Tiecco, "*ab initio Molecular Orbital Investigations of Free Radicals. Part I. Structure and Reactivity of the 'Open-chain' C₃H₃ Radical*" J. Chem. Soc. - Perkin Trans. II, 2 (1974) 518-520.
245. Alan Hinchliffe, "*The Electronic Structure of the CH₂CCH Radical*" J. Mol. Struct., 36 (1977) 162-164.
246. Alan Hinchliffe, "*The Electronic Structure of the CH₂CCH Radical - an ab initio SCF-MO Study*" J. Mol. Struct., 37 (1977) 295-298.
247. N. Colin Baird, Rashmi R. Gupta, and Kathleen F. Taylor, "*On Geometry Predictions for Conjugated Free Radicals Containing Three π Electrons Using ab Initio MO Theory*" J. Am. Chem. Soc., 101(16) (1979) 4531-4533.
248. Daniel M. Chipman and Kristine E. Miller, "*Theoretical Study of the Cyclopropenyl Radical*" J. Am. Chem. Soc., 106(21) (1984) 6236-6242.
249. H. Honjou, M. Yoshimine, and J. Pacansky, "*Theoretical Studies on the Ground State and Low-Lying Doublet Excited States of the Propargyl Radical*" J. Phys. Chem., 91(17) (1987) 4455-4459.
250. P. Botschwina, R. Oswald, J. Flugge, and M. Horn, "*A Theoretical Investigation of the Propargyl Radical and its Cation*" Zeit. fur Phys. Chem., 188 (1995) 29-43.
251. Marilyn E. Jacox and Dolphus E. Milligan, "*Matrix Isolation Study of the Vacuum Ultraviolet Photolysis of Allene and Methylacetylene. Vibrational and Electronic Spectra of the Species C₃, C₃H, C₃H₂, and C₃H₃*" Chem. Phys., 4 (1974) 45-61.

252. V. A. Korolev, A. K. Mal'tsev, and O. M. Nefedov, *"Infrared Spectroscopic Investigation of Propargyl Radicals Stabilized in Low-Temperature Argon Matrix"* Bulletin of the Academy of Sciences of the USSR Division of Chemistry, 38 (1989) 957-964.
253. J. W. Huang and W. R. M. Graham, *"Fourier transform infrared study of tricarbon hydride radicals trapped in Ar at 10 K"* J. Chem. Phys., 93(3) (1990) 1583-1595.
254. C. L. Morter, C. Domingo, S. K. Farhat, E. Cartwright, G. P. Glass, and R. F. Curl, *"Rotationally resolved spectrum of the ν_1 CH stretch of the propargyl radical (H_2CCCH)"* Chem. Phys. Lett., 195(4) (1992) 316-321.
255. Yoshihiro Sumiyoshi, Takashi Imajo, Keiichi Tanaka, and Takehiko Tanaka, *"Infrared diode laser spectroscopic detection of the propargyl radical produced in a supersonic jet expansion by UV laser photolysis"* Chem. Phys. Lett., 231 (1994) 569-573.
256. Keiichi Tanaka, Takeshi Harada, Kouichi Sakaguchi, Kensuke Harada, and Takehiko Tanaka, *"Time-resolved diode laser spectroscopy of the ν_6 band of propargyl produced by the UV photolysis of allene"* J. Chem. Phys., 103(15) (1995) 6450-6458.
257. K. Tanaka, Y. Oshima, and Y. Endo. *Fourier-Transform Microwave Spectroscopy of the Propargyl Radical*. in *The Ohio State University 49th International Symposium on Molecular Spectroscopy*. 1994. Columbus, Ohio: The Ohio State University.
258. P. Botschwina, *Based on recent unpublished CEPA-1 Calculations*, Personal Communication.
259. C. E. Miller, W. C. Eckhoff, and R. F. Curl, *"Quasi-linearity in HCCN: effects of the ν_2 fundamental"* J. Mol. Struct., 352/353 (1995) 435-446.
260. V. D. Volosov, *"The influence of the parameters of the radiation of a laser and a non-linear medium on the effectiveness of the generation of the second optical harmonic"* Sov. J. Tech. Phys., 39(12) (1970) 2188-2197.
261. F. M. Librecht and J. A. Simons, *"Second-harmonic generation in birefringent crystals by a Gaussian beam with an elliptical cross section"* IEEE J. Quantum Electron., QE 11 (1975) 850-852.

262. D. J. Kuizenga, "*Optimum focusing conditions for parametric gain in crystals with double refraction*" *Appl. Phys. Lett.*, 21 (1972) 570-572.
263. Lars Hörmander, *The Analysis of Linear Partial Differential Operators I*. Grundlehren der mathematischen Wissenschaften. Vol. 256. 1983, Berlin: Springer-Verlag.